Parametric Study of the Performance of a Biplane Joined at the Tips

Thesis

Submitted to

The School of Engineering of the

UNIVERSITY OF DAYTON

In Partial Fulfillment of the Requirements for

The Degree

Master of Science in Aerospace Engineering

by

Nicola Genco

UNIVERSITY OF DAYTON

Dayton, Ohio

May, 2008

APPROVED BY:

Aaron Altman, Ph.D.
Advisory Committee Chairman
Assistant Professor,
Department of
Mechanical and Aerospace
Engineering

Raymond Kolonay, Ph.D.
Committee Member
Adjunct Professor,
Department of
Mechanical and Aerospace
Engineering

Cale Zeune
Committee Member
Aerospace Engineer,
Air Force Research Laboratory
Air Vehicles Directorate

Malcolm W. Daniels, Ph.D.
Associate Dean,
School of Engineering

Joseph E. Saliba, Ph.D., P.E.
Dean,
School of Engineering

ABSTRACT

PARAMETRIC STUDY OF THE PERFORMANCE
OF A BIPLANE JOINED AT THE TIPS

Name: Nicola Genco
University of Dayton

Advisor: Dr. Aaron Altman

This thesis investigates the impact on performance of stagger and gap on a biplane wing joined at the tips by endplates. The effects due to these parameters on the aerodynamic performance of the biplane will be discussed in this thesis to better understand the interaction between the two wings. The experimental integrated force data were obtained from wind tunnel tests performed in the University of Dayton Low Speed Wind Tunnel (LSWT) at two different Reynolds numbers. Test conditions varied angle of attack from -2° to 25° in 0.25° increments. The computational study used the Athena Vortex Lattice (AVL) code based on the Vortex Lattice Method (VLM). Then, the computed results were verified by comparison with the experimental data and the two were found to compare well under some conditions, and not well under other conditions. The results show that both gap and stagger have positive effects on the coefficient of lift and aerodynamic efficiency. These effects become less important at higher values of gap, due to the smaller interactions between the two wings. The models with positive stagger show higher lift coefficient and higher aerodynamic efficiency

compared to the models with negative stagger. Curves of lift coefficient versus angle of attack show a change in the lift slope, $dC_L/d\alpha$, around the angle of attack of maximum aerodynamic efficiency. These interesting results will be discussed in this thesis as well as a more profound analysis of the aerodynamic performance using both experimental and theoretical results.

ACKNOWLEDGMENTS

I would like to offer thanks to my faculty advisor, Dr. Aaron Altman, for his direction, help and support throughout the course of this thesis effort. I revised this thesis incorporating the valuable comments and suggestions from many people to whom I am grateful. They include: Abhishek Bichal, Dr. Hantae Kang, Giuseppe Landolfo, Jonathan Raush, and Dan Stanley. It was a pleasure working with you. I especially thank Giuseppe Landolfo for sharing this wonderful experience in the United States, for walking next to me throughout the difficult journey of my professional life, and for being such a good friend. I would like to express my sincere appreciation to Dr. Raymond Kolonay for his great teaching ability that made me appreciate every single day of my studies. Thanks to my extended family for their sincere encouragement, despite having no actual interest in the subject. My mom Rosa, my dad Angelo, and my sisters Maddalena e Marica, I thank you for making me a rich, rich man. I never walked alone. Special thanks to the Cardinal Achille Silvestrini, for making my dreams a reality. I would like to thank all my friends in the United States and in Italy, for their friendship, big support, and amazing moments when I was not working on this thesis. Last, but not least, I would like to thank a special person for her love and fondest affection.

Nicola Genco

TABLE OF CONTENTS

LIST OF FIGURES

LIST OF TABLES

NOMENCLATURE

AR	aspect ratio
b	length of semi-span
c	mean chord length
C_D	coefficient of drag
C_{Do}	drag coefficient at zero lift
C_L	lift coefficient
C_f	skin friction coefficient
D_i	induced drag
$D_{interference}$	interference drag
$D_{parasite}$	parasite drag
$D_{skinfriction}$	skin friction drag
D_{total}	total Drag force
e	span efficiency factor
g	gap
L	lift force
L/D	lift over drag ratio
k_i	Munk's Equivalent Span Factor
Re	Reynolds Number
S	wing area
SVP	saturation vapor pressure for a given temperature T
s	stagger
V_∞	freestream velocity
α	angle of attack
α_i	lift induced angle of attack
Γ	circulation strength
ΔH	manometer reading
μ	dynamic viscosity of the fluid
ρ	density of the fluid

σ	coefficient of mutual influence
ϕ	velocity potential (scalar)
ω_z	vorticity vector in two dimensional flow about z-axis
$\nabla\times$	curl
$\nabla\cdot$	divergence
∇	gradient
Λ	biplane's geometric parameter
ξ_i	biplane's geometric parameter
ζ_i	strength of a vortex i

PARAMETRIC STUDY OF THE PERFORMANCE OF A BIPLANE JOINED AT THE TIPS

I. Introduction

1.1 Background

The science of aerodynamics is concerned with the motion of air and of bodies moving through air. The airflow around an aircraft is a highly complex phenomenon. To study it, in the present state of our knowledge, demands simplifying assumptions. These must be based, at least partly, on experimental observations. Making mathematical deductions and predictions belong to the theoretical side. To arrive at the knowledge of such mathematical laws, Galileo says, we must make use of sense and reason, by passing through three stages:

- The observation of the facts which fall within our experience;
- The elaboration of a mathematical hypothesis as a presumed explanation of the phenomena under observation;
- Verification of the hypothesis through new facts of experience. If the verification of experience agrees, the hypothesis becomes law.

The aim of this thesis is therefore to lay bare the behavior of airflow around a biplane joined at the tips by endplates, using the observation of the facts, elaborating hypotheses, and verifying these hypotheses using an experimental approach.

Airflow around a biplane is a complex study. It is important, as a first step, to understand which factors influence the performance of a biplane and

furthermore, a biplane joined at the tips by endplates. This report will take into account the influence of stagger and gap on the performance of a biplane joined at the tips by endplates.

1.2 Biplane

The first successful powered, piloted airplanes in history were biplane designs, with the Wright brothers' planes being the earliest example (Figure 1.1). The biplane is an aircraft with two sets of wings, an upper set and a lower set, separated by struts and wires and connected to the upper and lower parts of the fuselage. The reason for this was structural. Airplanes were initially quite fragile.

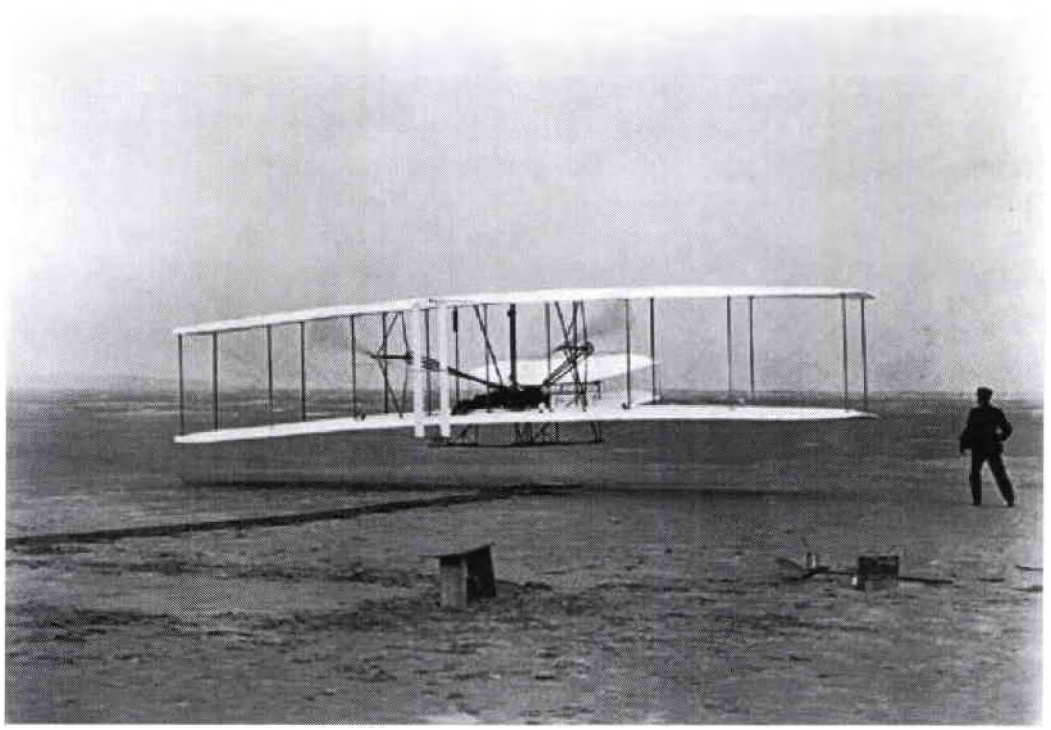

Figure 1.1: The beginning of the first flight, December 17, 1903.
Credits - Library of Congress

The reason airplanes were so fragile had to do with the difficulty of flight in the early days. For the first decade or so of flight, because of low-powered engines and designs that created a lot of drag, airplanes could barely make it into the air at all. Planes therefore were constructed of the lightest materials, such as fabric and wood, and built in such a way that they used as little of the heaviest materials as possible. As a result, their wings were not capable of supporting much weight or handling wind gusts without crumpling in flight. Early airplanes had more than one wing because this reduced the wing loading, or amount of weight that the wing had to support in flight. With an upper and lower set of wings, the wings had to support less weight and the structural fittings between them, such as struts and wires, could reinforce them (Figure 1.2). While the biplane was the primary aircraft during the early days of flight, its design also led to its downfall. The primary shortcoming of the biplane design lies in the fact that the two wings interfere with each other from an aerodynamic standpoint. In short, the two sets of wings on a biplane produce more drag and less lift than does the lone set of wings on a monoplane. The triplane, a plane with three sets of wings, is even worse in this regard. Once designers were able to make stronger, thicker wings, removing the need for the bracing and stabilizers common to biplanes, monoplanes quickly became the norm. While biplanes are not often seen today, they are still used at air shows and for agricultural purposes.

Figure 1.2: Pitts S1s Aerobatic biplane in flight

Some parameters that determine the efficiency of a biplane configuration are the stagger of the wings, and the gap distance between the two biplane wings (Figure 1.3). The biplane has significant advantages over other configurations in terms of the weight of the finished aircraft. If spanwise, as well as vertical bracing is used between the wings, the combined pair can be treated much like a single beam with each individual wing carrying bending loads and the bracing carrying shear loads. If lateral inter-wing bracing is not used, smaller weight advantages can still be realized. The use of only inboard and outboard inter-wing struts/plates gives the aircraft wings much higher torsional stiffness compared to unbraced wings of comparable weight and design. This is because the wings and bracing now form an open box when viewed from the aircraft front. If the end plates/braces on the wings can carry bending moments at the wing/brace joint then some additional weight savings can be realized because now the braces carry shear loads between the two wings.

Figure 1.3 shows the section of a two-dimensional biplane by a plane perpendicular to the span, giving two profiles, 1 and 2, whose chords are inclined at the angle δ called the *dècalage*, which is assumed positive when the upper wing is at greater incidence than the lower, as in the diagram.

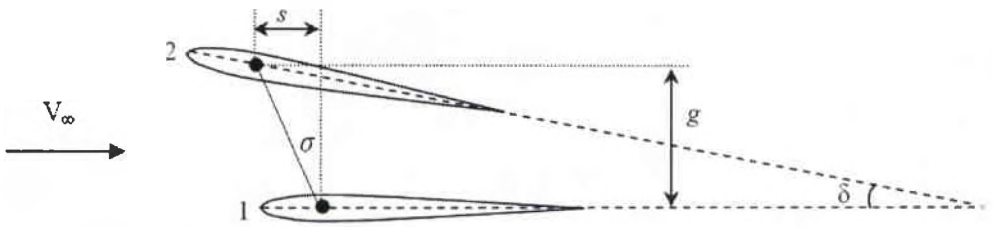

Figure 1.3: Biplane Parameters: Dècalage, Stagger, and Gap

The gap g is defined as the vertical distance between the quarter chords of the two wings perpendicular to the freestream, and stagger s is the distance between the quarter chords of the two wings parallel to the freestream. The stagger can be also defined by the angle σ between the line perpendicular to the freestream and the line joining the quarter chords of the wings, and it is equal to:

$$\sigma = \tan^{-1}\frac{s}{g} \tag{1.1}$$

There is no defined convention for positive stagger. In this report, the stagger is assumed positive when the upper wing is fore of the lower wing. Both gap and stagger are referred to the chord length of the model. The effect of dècalage is not taken into account for this experimental study. However, it has minimal effect on overall lift efficiency [1].

1.3 Joined Wings

The joined wing concept was first introduced as Patent 4,365,773 by Julian Wolkovitch of Stanford University in 1980. He states in his article [2],

> "The joined-wing airplane may be defined as an airplane that incorporates tandem wings arranged to form diamond shapes in both plan and front views".

The joined wing has two wings, a front wing that is swept to the rear, and a back wing that is swept toward the front. The back wing is mounted at the top of the vertical tail and extends downward at a substantial anhedral angle (negative dihedral), meeting the attaching to the front wing. From the front this has a triangular shape, whereas from the top, a diamond shape. Area ruling is employed at the place of the attachment, where the back wing begins behind the maximum thickness point of the front wing. An example of a joined-wing aircraft can be seen in Figure 1.4

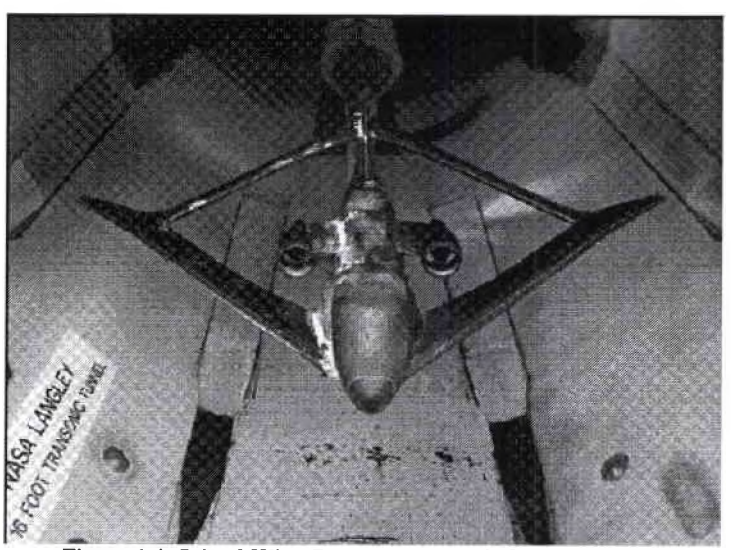

Figure 1.4: Joined Wing Demonstrator (wind tunnel model)
NASA Langley Research Center

Compared to an aircraft with the same wing-span, an optimally configured joined-wing aircraft may have some advantages. Unlike normal biplanes, such an arrangement can have good transonic and aerodynamic characteristics. Additional tails are probably not required, and trailing edge surfaces on both wings provide pitch and roll and can provide direct lift and side force, if desired. The main benefit, though, is the substantial reduction in wing structural weight that is achievable, on the order of 30%. On the negative side, it is difficult to get a trimmed maximum lift coefficient equal to a normal wing-tail configuration, and there can be excess wetted area and interference drag with so many component intersections [3].

1.4 Problem Statement

The root question that will be answered at the conclusion of this report is what is the best configuration in terms of aerodynamic efficiency across different models where each model has different values of stagger and gap. How does the interference between wings behave with changes in stagger and gap? Furthermore, can this interference between wings be used to optimize the aerodynamic efficiency?

II. Literature Review

2.1 Chapter Overview

Before improvements can be made, the fundamentals of flight must first be understood. This work assumes prior knowledge of fluid dynamics in general, and aerodynamics in particular, referred to a single-wing system. Therefore this chapter includes the fundamentals of flight for a biplane that will be the basis of discussion throughout the paper.

2.2 Lift for a Biplane

By definition, lift is the component of the aerodynamic force that is perpendicular to the relative wind.

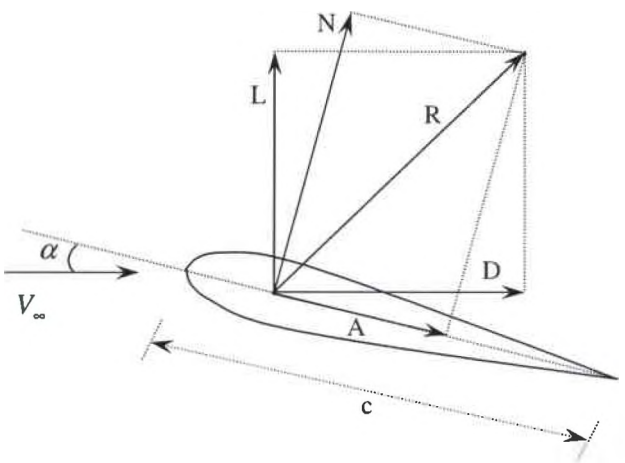

Figure 2.1: Resultant aerodynamic force and the components into which it splits (Reproduced from [4])

In , V_∞ is the relative wind, defined as the flow velocity far ahead of the body, and is also called the freestream velocity, c is the chord, defined as the linear

distance from the leading edge to the trailing edge of the body, α is the angle of attack defined as the angle between c and V_∞, R is the resultant aerodynamic force which is sometimes split into components perpendicular and parallel to the chord. By definition, N is the normal force, component of R perpendicular to c, A is the axial force, component of R parallel to c. Lift is therefore equal to:

$$Lift \equiv L = N\cos\alpha - A\sin\alpha \tag{2.1}$$

For an incompressible, potential flow (irrotational velocity field), the lift per unit span L' on the airfoil is given by the Kutta Joukowski Theorem:

$$L' = \rho_\infty V_\infty \Gamma \tag{2.2}$$

It states that the lift per unit span is directly proportional to circulation Γ. It allows us to determine the lift generated by a body in the flow without considering the physical sources of the forces on the body, which are pressure and shear stresses.

The Kutta-Joukowski Theorem is simply an alternative way of expressing the consequences of the surface pressure distribution. In the theory of incompressible, potential flow, it is generally easier to determine circulation around the body rather than calculate the detailed surface pressure distribution. Under these assumptions, the drag generated by a body in an inviscid, incompressible flow is zero, regardless of whether or not the flow has circulation about the body. The inviscid flow assumed in the Kutta-Joukowski Theorem does not model the proper physics for drag calculation. On the other hand, the prediction of lift via equation is quite realistic.

We suppose the biplane wings consist of thin airfoils of small camber, as shown in Figure 2.2. To a first approximation the effect of one wing on the other can be calculated by means of a substitution vortex of strength ζ_1 for the upper wing and ζ_2 for the lower wing, placed at the quarter point of the chord of each wing [5]. The chords of the airfoils are represented by c_1, c_2. The stagger is represented by s, the angle of attack by α, the dècalage by δ, the gap by g, and the freestream velocity by V_∞.

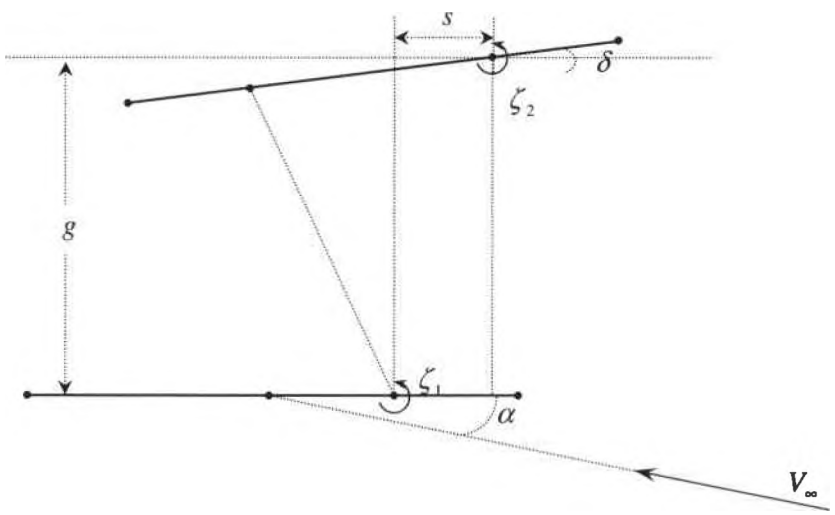

Figure 2.2: thin airfoils with vortex locations (Reproduced from [5])

In this general case we get:

$$\zeta_1 = \frac{1}{2} c_1 V_\infty \left(\frac{\alpha - \xi_2(\alpha + \delta)}{1 - \xi_1 \xi_2} \right) \tag{2.3}$$

$$\zeta_2 = \frac{1}{2} c_2 V_\infty \left(\frac{\alpha + \delta - \xi_1 \alpha}{1 - \xi_1 \xi_2} \right) \tag{2.4}$$

where, if we introduce the mean chord $c = \frac{1}{2}(c_1 + c_2)$,

$$\xi_1 = \frac{\frac{1}{2}c_1\left(\frac{1}{2}c - s - g\delta\right)}{g^2 + \left(\frac{1}{2}c - s\right)^2 - \frac{1}{2}c_2 g\delta} \tag{2.5}$$

$$\xi_2 = \frac{\frac{1}{2}c_2\left(\frac{1}{2}c + s\right)}{g^2 + \left(\frac{1}{2}c + s\right)^2 + \frac{1}{2}c_2 g\delta} \tag{2.6}$$

and the lift on the biplane system is

$$L = 2\pi(\zeta_1 + \zeta_2)\rho_\infty V_\infty \tag{2.7}$$

In the case of a biplane without dècalage, and same chord length for both wings, we have:

$$\xi_1 = \frac{\frac{1}{2}c\left(\frac{1}{2}c - s\right)}{g^2 + \left(\frac{1}{2}c - s\right)^2} \tag{2.8}$$

$$\xi_2 = \frac{\frac{1}{2}c\left(\frac{1}{2}c + s\right)}{g^2 + \left(\frac{1}{2}c + s\right)^2} \tag{2.9}$$

and the strength of the vortices are equal to:

$$\zeta_1 = \frac{1}{2}c\alpha V_\infty\left(\frac{1-\xi_2}{1-\xi_1\xi_2}\right) \tag{2.10}$$

$$\zeta_2 = \frac{1}{2}c\alpha V_\infty\left(\frac{1-\xi_1}{1-\xi_1\xi_2}\right) \tag{2.11}$$

the parameters ξ_1 and ξ_2 depend only on geometric parameters such as chord length, stagger, and gap.

Substituting (2.10) and (2.11) into (2.7) we get the lift of the biplane with same chord length for both wings, without dècalage:

$$L = c\pi\alpha\rho_\infty V_\infty^2\left(\frac{2-\xi_1-\xi_2}{1-\xi_1\xi_2}\right) = c\pi\alpha\rho_\infty V_\infty^2\Lambda \qquad (2.12)$$

Where Λ is a geometric parameter which depends on chord length, stagger and gap. Now consider that each plane is isolated. Allowing $(g \to \infty)$ in equations (2.8) and (2.9), we get:

$$L = 2c\pi\alpha\rho_\infty V_\infty^2 \qquad (2.13)$$

we would get the same result allowing $(s \to \infty)$ in equations (2.8) and (2.9).

2.3 Drag for a Biplane

By definition, drag is the component of the aerodynamic force that is parallel to the relative wind and retards the forward motion of the aircraft (see).

$$Drag \equiv D = N\sin\alpha + A\cos\alpha \qquad (2.14)$$

It is important to consider viscous flow to calculate the drag. In this case, at subsonic speeds, there are two kinds of drag: parasite drag and induced drag (see Figure 2.3):

$$D = D_p + D_i \qquad (2.15)$$

Parasite drag, D_p, is made up of three different components: skin friction drag ($D_{skinfriction}$), form drag (D_{form}), and interference drag ($D_{interference}$). Induced drag, D_i , also known as drag due to lift, is primarily caused by wing-tip vortices that form as the aircraft produces lift.

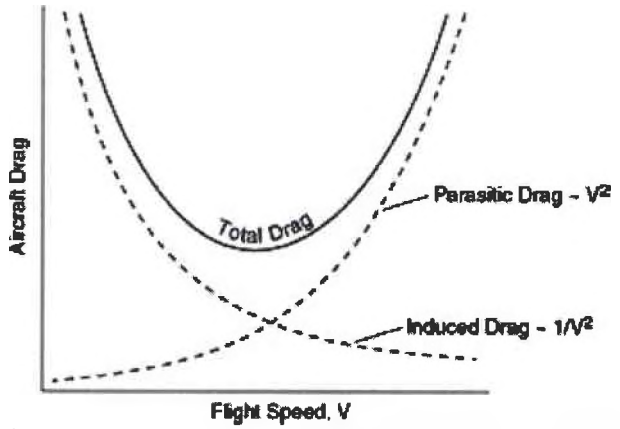

Figure 2.3: Shows the two components of Drag: Parasite Drag and Induced Drag as function of Flight Speed (Reproduced from [4])

Induced drag also includes the incremental change in pressure drag due to lift (due to the change in the angle of attack). Figure 2.4 shows the effect of induced drag on a finite wing.

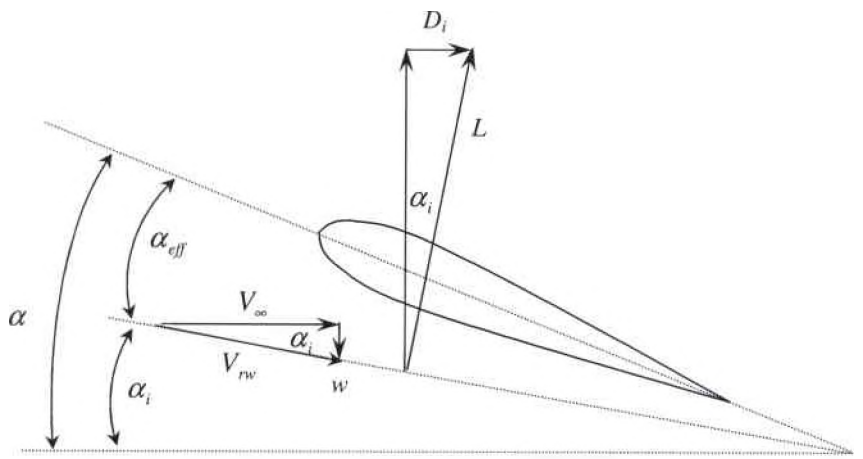

Figure 2.4: Effect of Induced Drag on Finite Wing (Reproduced from [4])

The angle between the chord line and the direction of V_∞ is the angle of attack α. We now define α as the geometric angle of attack. In Figure 2.4 the local relative wing is inclined below the direction of V_∞ by the angle α_i called the

induced angle of attack. This downward component of velocity is called downwash, denoted by the symbol w. The presence of downwash, and its effect on inclining the local relative wind in the downward direction, has two important effects on the local airfoil section:

1. The angle of attack actually seen by the local airfoil section is the angle between the chord line and the local relative wind. This angle is called effective angle of attack:

$$\alpha_{eff} = \alpha - \alpha_i$$

2. The local lift vector is aligned perpendicular to the local relative wind. Consequently, there is a component of the local lift vector in the direction of V_∞; that is, there is a drag created by the presence of downwash. This drag is defined as induced drag, denoted by D_i in Figure 2.4.

Induced drag is a function of the wing spanload only, and is independent of the details of the particular airfoil used in the wing. The additional profile drag is associated with the airfoil used in the wing. At low lift coefficients this drag should be small, only becoming important as flow separation starts to develop on the airfoil section. The additional profile drag becomes large as wing stall is approached.

Because of biplane lift interference effects, Munk studied the induced drag of a biplane due to the interference of one wing on the other. These studies led to a main conclusive theory [6]:

> "The total induced drag of any multiplane lifting system is unaltered if any of the lifting elements are moved in the direction of the motion provided that the attitude of the elements is adjusted to maintain the same lift distribution of lift among them."

This theorem is known as "Munk's Stagger Theorem", and basically states three important results:

1. If constant section lift is maintained, the chordwise pressure distribution does not affect the induced drag.
2. If the spanwise lift distribution is constant, there will be no effect on the induced drag from a change in biplane stagger or wing sweep.
3. The sum of all the lifting surfaces can be made equivalent to a single lifting element, enabling easier calculation of the induced drag.

Furthermore, Munk stated that if the two wings of the biplane are parallel and unstaggered, the downwash of each wing induced by the other wing is equal.

Munk then concludes with a formula for determining the induced drag coefficient of a biplane compared to that of a monoplane, where C_{D_1} and C_L are the induced drag and lift coefficients of the monoplane, respectively. The subscripts denote terms relating to the monoplane and biplane, and k denotes the "equivalent monoplane span" factor:

$$C_{D_2} = C_{D_1} - \frac{C_L^2}{\pi}\left[\frac{S_1}{b_1^2 k_1^2} - \frac{S_2}{b_2^2 k_2^2}\right] \tag{2.16}$$

where S is the entire area and b the greatest span. k_1 and k_2 are factors which depend merely on the gap/span ratio of the biplane and assume the value $k = 1$ for

a monoplane. If the two spans of a biplane are slightly different, an average span is to be substituted. The values of k are determined by Munk empirically as described in a former paper [6], and are given in Table 2.1 and Figure 2.5.

Table 2.1: values of Munk's k at different gap/span ratio

gap/span	k
0	1
0.05	1.02
0.1	1.05
0.15	1.09
0.2	1.15
0.3	1.21
0.4	1.25
0.5	1.27

The differences are not very great. In view of the fact that the comparison has been made with one wing section only, and that it is difficult to obtain exact values of k, these values are not very reliable and an average curve must be taken.

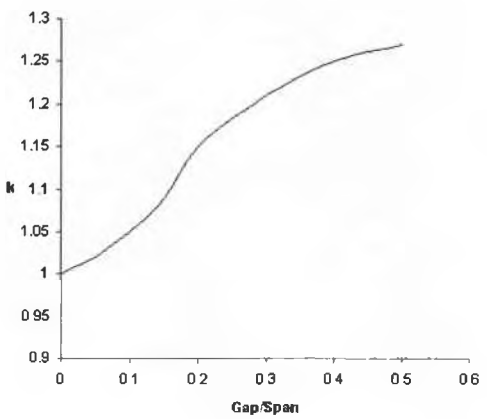

Figure 2.5: values of Munk's k plotted against the gap/span ratio

The result of the calculation of the drag coefficient is practically unaffected by this small change of k. For a rough estimate it is even sufficient to take $k = 1$ for all monoplanes and $k = 1.1$ for all biplanes. Equation (2.16) basically states that, at the same lift coefficient, the induced drag of a biplane will be smaller than that of a

monoplane with the same span. Munk then found that, due to induction and interference between the upper and lower wing sections, a biplane will experience an induced angle of attack, causing a greater angle of attack than that of a monoplane with the same lift coefficient.

For the same reasons of induction and interference Munk concluded that the shift in the center of pressure CP due to a change in the lift coefficient for the monoplane and the biplane were about the same, and when the shift is due to a change in the angle of attack, the CP travels an even smaller distance. Even though the difference in travel of the center of pressure between the two configurations is small, the biplane chord is only about half the length of a monoplane chord having the same airfoil section and lift, thus experiencing only about half the overall CP travel compared to the monoplane. This fact proves very advantageous in determining the stability characteristics of the biplane.

The final equation developed by Munk [6] for obtaining the induced drag coefficient, and that will be used in the theoretical and experimental comparison, is Equation (2.17)

$$C_{D_{iEM}} = \frac{C_L^2}{\pi} \frac{S}{b^2 k^2} \tag{2.17}$$

where the subscript EM is referred to the equivalent monoplane factor k.

Prandtl, then collaborating with Munk on biplane theory, reaffirmed Munk's stagger theorem by stating that the sum of the induced downwash between the two wings will remain constant, given any longitudinal change in geometry, and at angles of attack such that the lift is constant [7]. Prandtl states

that in an unstaggered wing system, the drag D_{12}, induced by wing 1 on wing 2, equals the drag D_{21} induced by wing 2 on wing 1. The drag D_{12} is due to the fact that wing 1 produces a downward air current toward wing 2. This value of D_{12} was found to be equal to:

$$D_{12} = D_{21} = \frac{\sigma}{\pi q}\frac{L_1}{b_1}\frac{L_2}{b_2} \tag{2.18}$$

where σ is the coefficient of mutual influence which depends upon gap/span ratio, and it is equal to:

$$\sigma \cong \frac{1 - 0.66\, g/b}{1.05 + 3.7\, g/b} \tag{2.19}$$

Values of σ are given in Figure 2.6 for different g/b and different $r = b_2/b_1$.

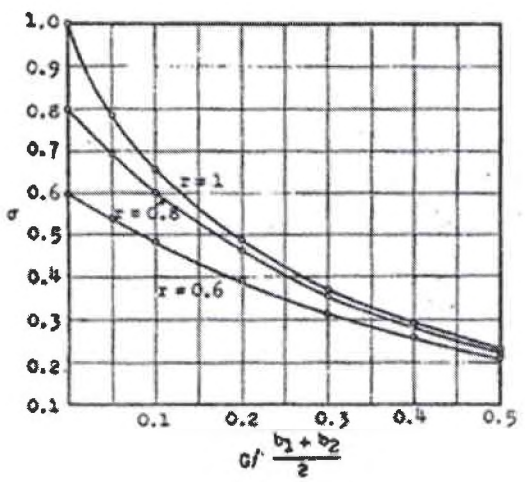

Figure 2.6: values of σ plotted against the gap/span ratio and different $r = b_2/b_1$ (Reproduced from [7])

The induced drag of the upper wing, for the unstaggered biplane, is

$$D_1 = D_{11} + D_{12} = \frac{1}{\pi q}\left(\frac{L_1^2}{b_1^2} + \sigma\frac{L_1}{b_1}\frac{L_2}{b_2}\right) \tag{2.20}$$

and that of the lower wing is

$$D_2 = D_{21} + D_{22} = \frac{1}{\pi q}\left(\sigma \frac{L_1}{b_1}\frac{L_2}{b_2} + \frac{L_2^2}{b_2^2}\right) \qquad (2.21)$$

where there is a positive stagger, the drag of the upper wing is diminished by the upward air currents produced by the lower wing; but, on the other hand, the drag of the lower wing is increased, by exactly the same extent, by the downward air current produced by the upper wing, so that the total drag is the same as in the case of the unstaggered biplane and is equal to:

$$D = D_1 + D_2 = \frac{1}{\pi q}\left(\frac{L_1^2}{b_1^2} + 2\sigma \frac{L_1}{b_1}\frac{L_2}{b_2} + \frac{L_2^2}{b_2^2}\right) \qquad (2.22)$$

Also Prandtl [7] gives a final equation for obtaining the induced drag coefficient, and that will be used in the theoretical and experimental comparison, that is Equation (2.23)

$$C_{D_{iOB}} = \frac{C_L^2}{\pi}\frac{S}{b^2}(1+\sigma) \qquad (2.23)$$

where the subscript OM is referred to the orthogonal biplane theory developed by Prandtl.

2.4 Wing-Tip Vortices

A finite wing is a three dimensional body, and consequently the flow over the finite wing is three dimensional; that is, there is a component of flow in the spanwise direction. Figure 2.7 gives the top view of a finite wing.

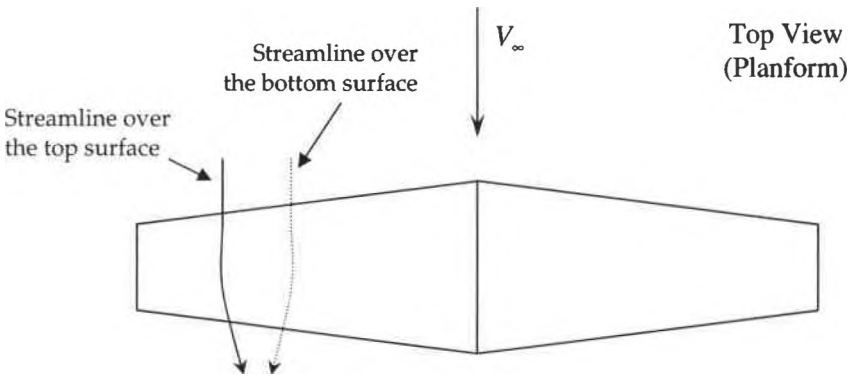

Figure 2.7: Finite wing Streamline Curvature (Reproduced from [4])

The primary cause for the formation of wing-tip vortices is lift. Lift, generated by a wing, results when there is a net pressure difference between the upper and lower surfaces of the wing. When the higher pressure exists on the lower surface of the wing, then positive lift is created. As a by-product of this pressure imbalance, the flow near the tips tends to curl around the tips. This generates on the top surface of the wing, a spanwise component of flow from the tip toward the root. Similarly, on the bottom surface of the wing, there is a spanwise component of flow from the root toward the tip, as shown in Figure 2.7. This flow establishes a circulatory motion that trails downstream of the wing; that is, a trailing vortex is created at each wing tip. These wing-tip vortices are sketched in Figure 2.8.

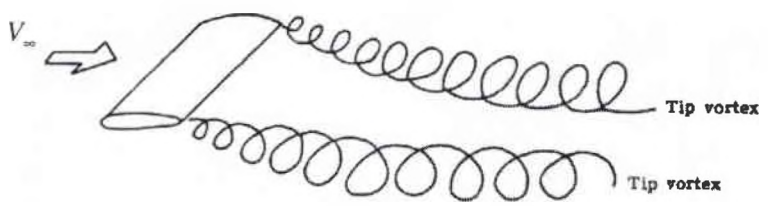

Figure 2.8: Schematic of wing-tip vortices (Reproduced from [4])

The aerodynamic theory of a finite wing now becomes more complicated, due to the three-dimensionality of the flow. The explanation of this theory can be found in the next section where the concepts of vortex filament, the Biot-Savart law, and Helmholtz's Theorem will be the tools by which obtaining analytical results using a Vortex Lattice Code called AVL (Athena Vortex Lattice) is made possible.

2.5 Vortex Lattice Method

2.5.1 Overview

The vortex lattice method is an extension of Prandtl's classical lifting line representation of a wing. Prandtl's classical lifting line theory gives reasonable results for straight wings at moderate to high aspect ratio. However, for low-aspect-ratio straight wings, swept wings, and delta wings, classical lifting line theory is inappropriate. For such planforms a more sophisticated model must be used. This model is called the Vortex Lattice Method. In this approach, the wing is represented by a series of lifting lines on the plane of the wing, at different chordwise and spanwise stations. Each vortex loop is located in each station and consisting of a bound vortex, infinitely long trailing vortex lines and a control point. The circulation Γ of the bound vortex generates a discontinuity in the tangential velocity component, corresponding to the velocity difference on the pressure and suction side of the wing. The lift force on the wing is calculated from

the strength of the bound vortex using the Kutta-Joukowski law, stated in Equation (2.2).

2.5.2 Introduction

The physical problem addressed was to find the aerodynamic forces acting on an aircraft flying at low subsonic speeds, below the stall limit. The governing equations used to solve the physical problem came from standard vortex lattice theory. The law of Biot-Savart was used to get the flowfield around a finite straight vortex line, one of the basic vortex segments needed for the lattice. These vortices induce a flow field in the air, and their strength was determined by the boundary conditions that no air should flow through the wings.

The forces acting on each vortex segment can be determined by employing the Kutta-Joukowski theorem. These forces may then be integrated to yield a composite force in three dimensions, which in turn may be used to compute aerodynamic coefficients. The computational problem is to create a good system for dealing with the mathematical results.

2.5.3 Physical Problem

As air flows around the airframe of an aircraft forces build up. These forces can be derived from pressure and friction acting on every free surface of the interface between the fluid (air) and the airframe (wings, body control surfaces etc.). The resulting force acting on the aircraft is given by integrating the distributed forces across the interface as shown in Figure 2.9

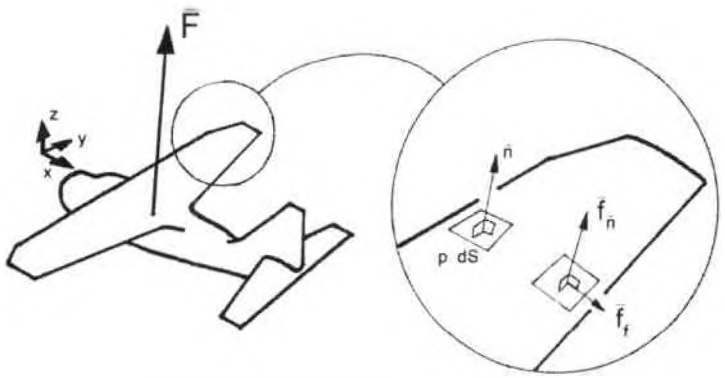

Figure 2.9: Showing aircraft with resulting force.
Partial blowup showing pressure and tangential forces.
(Reproduced from [23])

The force acting on an infinitesimal area of the interface can be divided into two components. One of them is perpendicular to the surface and the other is parallel. The physical interpretation being that the perpendicular force is a pressure force and the parallel force a shear, or friction, force.

The pressure forces are the forces acting along the normal of the interface. The total pressure in the fluid is constant and consisting of the static and the dynamic pressure. At rest, the total pressure is equal to the static pressure and constant at every point of the interface. Once in motion, the airframe creates a flow field in the air. As the interface is impenetrable the fluid must move to allow the passage of the airframe thus creating the flow field. The shape of this field is highly dependent of the shape of the interface. Thus parts of the airframe facing the wind experience a higher static pressure than areas parallel to the wind or on the off-wind side. This accounts for the pressure forces on the interface. At the microscopic level, the smallest divisions of air located closest to the skin of the

airframe must be stationary relative the airframe. If we move along the normal of the surface the tangential speed picks up and at a certain distance the tangential speed becomes constant along the rest of the normal. This distance constitutes the thickness of the boundary layer as shown in Figure 2.10. The viscous motion of the boundary layer is the source of the friction forces. The thickness of this boundary layer is often small in comparison with other typical lengths in the interface.

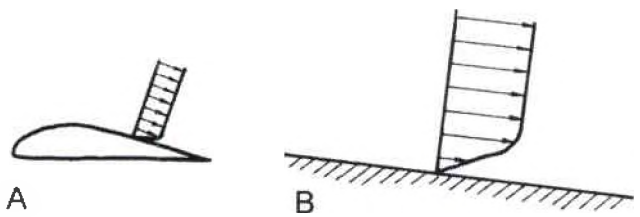

Figure 2.10: The boundary layer, tangential speed and viscous movement. The arrows are velocity vectors of the air. A shows the profile and B the local enlargement with visible boundary layer. (Reproduced from [23])

2.5.4 Mathematical Problem

Potential Flow

When considering a vector field where the rotation along any closed path is zero, the conclusion arises that the line integral between two points in the field is independent of the path. Such a flow field is called conservative. The concept of conservative fields allows the definition of the potential:

$$A = \nabla \phi \tag{2.24}$$

where ϕ equals the potential of A.

This mathematical theory can be, and is, applied to many physical problems. Among these are the theory of electric potential and the theory of velocity

potentials in flow fields. In the case of a fluid flow the field is defined as follows for an irrotational, inviscid, incompressible flow [4].

No mass is produced in the field so,

$$\nabla \cdot \vec{V} = 0 \tag{2.25}$$

Further, as the flow is irrotational,

$$\vec{V} = \nabla \phi \tag{2.26}$$

Hence,

$$\nabla \cdot (\nabla \phi) = 0 \tag{2.27}$$

or

$$\nabla^2 \phi = 0 \tag{2.28}$$

Equation (2.28) is Laplace's equation for which a number of solutions can be found.

Anderson [4] continues to evolve the matter and states that: "A complicated flow pattern for an irrotational, incompressible flow can be synthesized by adding together a number of elementary flows, which are also irrotational and incompressible." Such elementary flows may be the point source, the point sink, the doublet and the vortex line. These may be superpositioned in many ways including the formation of line sources, vortex sheets and so on. As one may use an arbitrary number of singularities the concept of using numerical methods is close at hand. Today, a wide variety of methods exist and one of them is the vortex lattice method (VLM).

Vortex Theorem

In using vortex singularities to model lifting surfaces, let review some properties of vortices. The key properties are defined by the so-called vortex theorems. These theorems are associated with the names of Kelvin and Helmholtz. Three important results are:

1. Along a vortex line (tube) the circulation, Γ, is constant.

2. A vortex filament (or line) cannot begin or end abruptly in a fluid. The vortex line must i) be closed, ii) extend to infinity, or iii) end at a solid boundary. Furthermore, the circulation, Γ, about any section is the vortex strength.

3. An initially irrotational, inviscid flow will remain irrotational.

Related to these theorems, an important result can be stated:

• A sheet of vortices can support a jump in tangential velocity [i.e. a force], while the normal velocity is continuous. This means that a vortex sheet can be used to represent a lifting surface.

2.6 AVL

Athena Vortex Lattice [8] (AVL) is a code developed by Youngren and Drela that utilizes vortex-lattice theory for aerodynamic and dynamic stability analysis of a given aircraft geometry. By changing parameters (C_L, C_D, α, etc.), an AVL model can be used to predict aircraft performance in real-world scenarios. To create a model, AVL requires a text file that defines the aircraft geometry.

An example of model created using AVL is shown in Figure 2.11

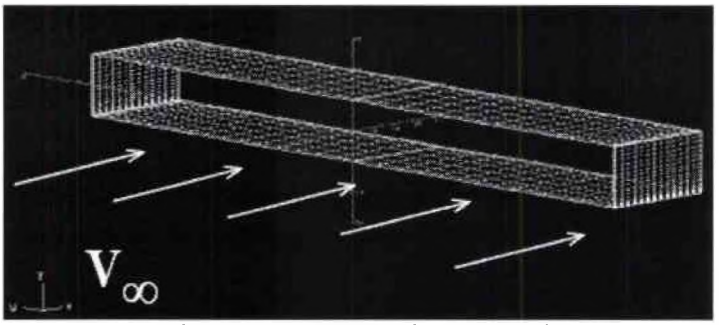

Figure 2.11: Example of AVL Model

2.7 Previous Experiments Conducted on Biplanes

2.7.1 Overview

Although these early theories are very important, they lacked experimental confirmation of their accuracy and did not take into account the effect of streamline curvature, non-elliptical lift distribution, or any geometrical variables. For these reasons, some discrepancy between the theories and actual biplane performance were encountered.

2.7.2 Early Experiments

Soon after Munk's biplane theories were published, J.C. Hunsaker performed an experimental analysis on the inherent longitudinal stability of a "typical" biplane. The aircraft he tested did not vary any geometric parameters, only the aircraft angle of attack was varied to determine the lift, drag, and pitching moment characteristics and their effect on the stability of the aircraft. His results showed that the biplane was an inherently unstable aircraft configuration at low speeds and high angles of attack [9].

In 1918, F.H. Norton conducted an investigation similar to Hunsaker's work utilizing a three-dimensional, non-symmetric biplane model to determine the effect of staggering the wings. All other variables held constant, Norton found that the maximum efficiency and lift are achieved at the highest degree of stagger possible. Furthermore, the travel of the CP was greatly reduced with large positive stagger, which could ease in solving the dynamic stability problem [10].

H. Glauert of the Royal Aircraft Establishment then incorporated a new variable into Munk's angle of incidence formula to include an improved method of determining the effect of streamline curvature [11]. His results showed accurate correlation with experiment for positive stagger but did not give good results at negative stagger.

As flight research and the biplane became more popular, studies became more prominent throughout the United States and Europe. New concepts had been formulated, old ones improved and many experimental tests had begun.

In 1929, a series of papers were written by Montgomery Knight and Richard W. Noyes [12] [13] [14]. They conducted wind tunnel tests on three dimensional asymmetrical biplane airfoils while varying the gap, stagger, decalage, dihedral, sweepback, overhang, and combinations thereof. Many useful results were obtained, some of which are as follows:

1. Increasing the gap or stagger in the positive direction tends to equalize the loads on the two wings, and also increases the maximum total lift coefficient of the biplane.

2. An increasing gap or lower sweep tends to decrease the travel of the center of pressure.
3. The deviation of decalage angle from zero tends to decrease the maximum lift coefficient when there is zero stagger.
4. With positive stagger, increasing the decalage angle tends to increase the maximum lift coefficient.

The last of these results may cause some confusion, but the reasoning is relatively straight-forward. To reach the maximum lift possible, the two wings of the biplane must stall at the same time. For this to occur, the wings must also be at the same effective angle of attack. When the wings are at positive stagger, there is an increased amount of downwash imposed by the upper wing onto the lower wing, causing a reduced effective angle of attack on the lower wing. Therefore, for the effective angles of attack to be equal, and hence stall at the same time, the lower wing's angle of incidence must be increased, creating a negative angle of decalage in the biplane wing configuration. These tests were all conducted at a low Reynolds number of 150,000.

Max Munk, still very interested in biplane theory, was influenced by the Bureau of Aeronautics of the Navy to conduct a series of tests on biplane and triplane models [15]. These tests were to determine the lift, drag, and pitching moment for different airfoils, systematically varying the gap and stagger, and then

to compare the results with the Army standards. The results of these tests were very interesting:

1. There was a general tendency of the upper wing to contribute more of the lift than the lower wing at positive stagger and less at negative stagger.
2. The gap/chord ratio had little effect on the relative lifts of the wings at high lift coefficients, but significant effects at low lift coefficients.
3. An increase in gap tends to equalize the lift of the wings over a wide range of angles of attack.
4. The gap/chord ratio had little effect on the positions of the center of pressures of the individual wings.
5. With an increase in positive stagger, the centers of pressure moved forward on the upper wing and aft on the lower wing, lying nearly together at zero stagger.

These results are very similar to the previous studies by Knight and Noyes, and would seem to verify the accuracy of both tests. Furthermore, Munk used two different airfoils, the RAF-15 and the USATS-5, to ensure that his own tests would give results unbiased to a given wing profile.

2.7.3 New Theories

While these extensive experimental tests were being performed, a few new theories on the biplane and its interference characteristics had been developed.

In 1930, Clark B. Millikan adopted a theory from Dr. Theodore Von Karman known as "Thin Airfoil Theory". In his paper, Millikan presented and used Von Karman's theory to develop a procedure for determining the characteristics of the individual wings of an arbitrary biplane configuration without sweepback or dihedral [16]. Although this process showed great success over current theories when compared with experimental data (at gap/chord ratios greater than ¾), the procedure was very tedious and cumbersome, and was therefore rarely incorporated into use by the designers of that day.

In 1933 Walter S. Diehl published a report on biplane theory [17]. His paper combined experimental and theoretical data by Fuchs and Hopf to obtain a series of curves from which the lift curves of the individual wings could be found. His results showed promise, but even Diehl agreed that:

> "Millikan's treatment of the biplane theory...appear to give somewhat better agreement with test data...but it is very difficult for an engineer to follow the steps required in a typical calculation."

2.8 Comparison of Monoplane and Biplane Results

In all of the aforementioned studies, the only comparison of biplane and monoplane performance characteristics was theoretical. Actual experimental testing of the biplane compared to the monoplane had not been done, but in July of 1974, E. Carl Olson wrote his M.S. on the improved aerodynamic characteristics of

a biplane over that of a monoplane by comparing experimental data [18]. Olson's experiments consisted of a three-dimensional asymmetrical airfoil biplane configuration, and incorporated the results of Nenadovitch by varying the geometry about his optimum point: a gap of one chord length, a stagger of one chord length, and a decalage angle of negative six degrees. Furthermore, Olson also tested a monoplane system using the same area and similar aspect ratio of the biplane configuration.

The aspect ratio considered in his report is equal to:

$$AR = \frac{b^2}{S} \frac{\mu^2(1+r)^2}{\mu^2 + 2\sigma \cdot r + r^2} \tag{2.29}$$

where S is the wing area, b the span of the upper wing, σ is the Prandtl interference factor defined in Equation (2.19), μ is the ratio of lower wing span over upper wing span, and r is the ratio lower wing area over upper wing area.

His tests were also conducted with and without a fuselage. The results obtained are probably the most significant to date.

In the first phase of testing, Olson concluded that the best range of decalage angles to continue testing at were between -5° and -7°, due to the high L/D and low C_D at these angles. Therefore, the remainder of his testing occurred between these angles.

In the second phase of his testing, a fuselage was incorporated into the configuration. In these tests, gap, stagger, and decalage angle were all varied, and

then the results of the biplane and monoplane configurations were compared and plotted against each other. There were many important conclusions obtained:

1. A substantial C_D reduction with respect to the monoplane over a wide range of angles of attack was obtained for most biplane configurations, the most efficient showing a 25% decrease in the C_D over the monoplane in a typical cruise condition.
2. A significant L/D ratio increase for the biplane configuration was obtained over a wide range of lift conditions with respect to the monoplane. The largest increase was 31.2% at the maximum L/D, with C_D being 21.4% lower than the monoplane at a C_L of 0.175.
3. The endurance of the biplane would be increased over a wide range of C_L over that of the monoplane due to the $L^{3/2}/D$ curve.
4. While creating higher interference drag, the biplane realized a substantial increase in efficiency over the monoplane due to a decreased induced drag and/or altered pressure distribution over the wings, creating an overall reduction in the total drag.
5. The most efficient overall biplane configuration increased L/D by 16.3%, reduced the C_D by 14.3% (at a C_L of 0.175), but had a 10.6% decrease in $C_{L\max}$ compared to the monoplane.
6. Increasing stagger tended to decrease the overall C_D.
7. Pitching moment characteristics of the biplane system were markedly improved over the monoplane system (a more negative moment curve slope).

Throughout all of the experimental testing and theoretical evaluations in the past, along with the recent studies, it is evident that a biplane wing configuration can hold many aerodynamic advantages over that of the monoplane.

2.9 Research Focus

The purpose of this report is to further investigate how gap and stagger influence the aerodynamic performance of a biplane joined at the tips by endplates. This parametric study has led to the selection of fourteen cases which have been test run first in the Athena Vortex Lattice (AVL) code, developed by Youngren and Drela, based on the Vortex Lattice Method (VLM). This method is based on solutions to Laplace's Equation and was used to estimate the inviscid aerodynamic coefficients and performance characteristics analytically. The fourteen different models selected for wind tunnel testing are represented in Table 2.2

Table 2.2: Model Configurations for wind tunnel testing

Models			
Gap	**Stagger**	**σ (°)**	**Chord Length (in)**
1c	0c	0	3.995
0.5c	0c	0	4.004
0.5c	0.5c	45	3.943
0.5c	1c	63.4	3.892
1c	0.5c	26.6	3.967
1c	1c	45	4.005
2c	1c	26.6	3.964
1c	1.5c	56.3	3.917
0.5c	-0.5c	-45	3.943
0.5c	-1c	-63.4	3.892
1c	-0.5c	-26.6	3.967
1c	-1c	-45	4.005
2c	-1c	-26.6	3.964
1c	-1.5c	-56.3	3.917

The wing is based on a flat plate airfoil section of thickness over chord ratio t/c =1.18%. A wing of 12" semi-span in a vertical orientation was used to match the size and Reynolds number with a full-sized UAV. Asymmetric flow is prevented by mounting the model on the floor.

Such an arrangement, though obviously unsuited for yaw tests, yields accurate pitch, lift, and downwash data at the maximum Reynolds number [19]. The gap between the half wing and the ground was measured to be 0.04" and it was filled with petroleum jelly to prevent interaction between the flow and the model in such a gap.

In order to achieve aerodynamic analyses of the models, the entire test matrix was repeated three times in the University of Dayton/University of Dayton Research Institute Low Speed Wind Tunnel (LSWT).

III. Methodology

3.1 Experimental Equipment

3.1.1 University of Dayton Low-Speed Wind Tunnel (LSWT)

The experimental integrated force data were obtained from wind-tunnel tests performed in the University of Dayton/University of Dayton Research Institute Low-Speed Wind Tunnel (LSWT) seen in Figure 3.1.

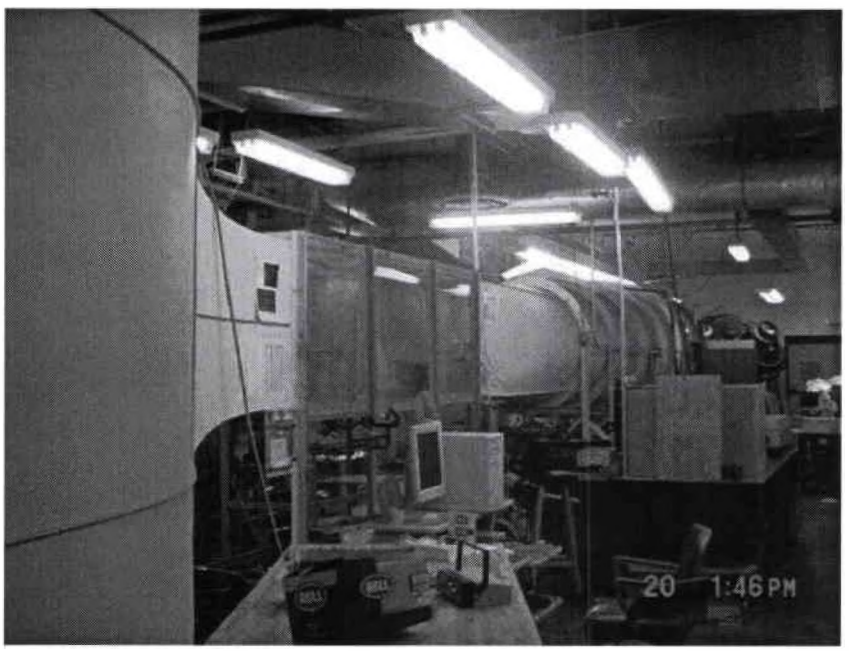

Figure 3.1: University of Dayton Low Speed Wind Tunnel (LSWT)

The DART CORPORATION constructed the tunnel in 1992. The LSWT is an Eiffel type with an 16:1 contraction ratio. The fan was designed and constructed by Hartzell and is driven by a 60 HP motor. The test section measures 30" X 30" X 90" (~0.75 X 0.75 X 2.3 m), and is easily exchanged with other test sections used for

demonstration and educational purposes to preserve the quality of the research test section. The LSWT has five anti-turbulence screens at the tunnel inlet.

The highest flow quality operable speed range of the LSWT is from 6.7 m/s (20 ft/s) to 36.7 m/s (120 ft/s). The tunnel has a turbulence intensity in the freestream direction of less than 0.1% throughout the test section (measured by hot wire anemometer), and less than 0.05% throughout the center portion of the test section utilized for testing the different models.

The test models are mounted on a rotary stage which is located on the top of a force balance. The connections between the model and the rotary stage, the rotary stage and the balance, the balance and the support were designed by the author. The system balance – rotary stage is fixed to a support located underneath the tunnel as shown in Figure 3.2.

Figure 3.2: Rotary stage and balance

3.1.2 LSWT 25 lb Strain Gage Balance

The force balance used to determine the forces on the models is based on an ATI Gamma F/T Transducer. Figure 3.3 shows the balance.

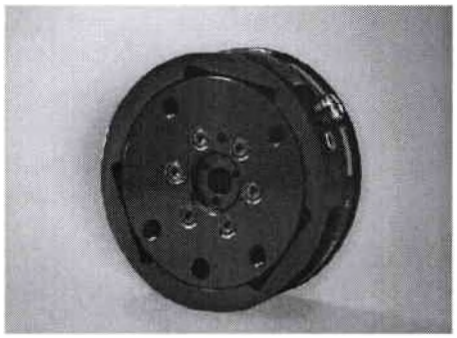

Figure 3.3: ATI Gamma F/T Transducer (Credit – ATI Industrial Automation)

The transducer senses applied loading with six degrees of freedom (Fx, Fy, Fz, Tx, Ty, and Tz) and it has the interface board inside the transducer. The transducer cable is attached with a connector and it is specially designed for noise immunity. This durable cable protects the transducer signals from electrical fields and mechanical stress. The controller interfaces with the transducer to process the transducer data into usable force and torque data and to provide high-level functions. The controller is powered by standard AC power. This controller communicates over an RS-232 serial port and can also output loads via analog voltages.

The interface board electronics receive transducer gauge signals and convert them to readable DAQ card signals using noise immunity technology. Each interface board is calibrated. The interface board is mounted within the sensor. Since the wind tunnel installed transducer output is uncalibrated, an in-house

high-resolution calibration was performed by the author and a calibration matrix subsequently created.

Figure 3.4 shows the axes of the sensor.

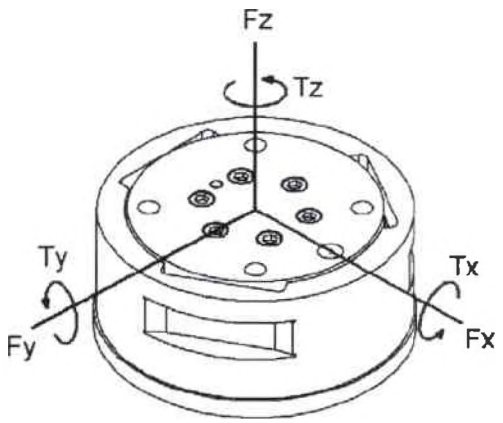

Figure 3.4: Axes of the sensor

A list of the maximum allowable forces and moments is listed in Table 3.1. If forces or moments exceed the allowable range then the balance could be damaged and thus invalidate the calibration. Sensing ranges and resolution (typical for a 16-bit data acquisition system) associated with the calibration matrix are listed in Table 3.2. The other dimensions of the balance can be seen in Appendix A.

Table 3.1: Max Allowable Forces and Moments for the Balance

Component	Max Load
Lift – F_X	±235 lb
Drag- F_Y	±235 lb
Side – F_Z	±736 lb
Yaw – T_X	±618 in-lb
Roll - T_Y	±618 in-lb
Pitch – T_Z	±727 in-lb

Table 3.2: Sensing ranges and Resolution

Component	Rated Sensing Ranges	Resolution
Lift – F_X	±7.5 lb	1/2560 lb
Drag- F_Y	±7.5 lb	1/2560 lb
Side – F_Z	±25 lb	1/1280 lb
Yaw – T_X	±25 in-lb	1/1280 in-lb
Roll - T_Y	±25 in-lb	1/1280 in-lb
Pitch – T_Z	±25 in-lb	1/1280 in-lb

3.1.3 LSWT 275 lb Rotary Stage

Due to the sidewall mount orientation of the model in the test section, a rotary stage Model RM-5 manufactured by Newmark was used to change the angle of attack of the models. The rotary stage is designed with a maximum load of ±275 lbs and it uses a single axis controller. It provides a resolution of 0.36 arc-sec and an accuracy of 60 arc-sec. Figure 3.5 shows the rotary stage.

Figure 3.5: Newmark RM-5 Rotary Stage (Credit –Newmark Systems Inc.)

The specifications are listed in Table 3.3

Table 3.3: Rotary Stage Specifications

Repeatability	5 arc - seconds
Resolution	0.36 arc - seconds
Accuracy	72 arc - seconds
Gear Ratio	72:1
Max. Load	275 lbs
Moment	260 in-lb
Max. Speed	1200 RPM
Travel	360° Continuos

The other dimensions of the rotary stage can be seen in Appendix B.

3.2 Collecting and Processing Data

3.2.1 Overview

Measurements can be taken by the balance once the wind tunnel reaches a desired velocity. Angle of attack can be accomplished by rotating the rotary stage and subsequent model using the angle control device. Data acquisition was performed on a Pentium IV PC running LabVIEW 8.0 and software written in-house driving a PCI 6281 performing simultaneous sampling at 1000 Hz passed through an SCXI Chassis and SCXI 1140 hardware filter. Ten thousand samples were recorded in each data sweep, and these values were acquired four times for any given angle of attack and tunnel speed to provide 40,000 samples per data point represented.

All data files for each test run were stored on the hard drive of the acquisition system and were later retrieved for data reduction. The acquisition recorded the following values: α, tunnel speed, lift force, drag force, side force,

pitch moment, yaw moment, roll moment, and relative standard deviations. All forces and moments were measured about the balance center. The balance records the force data by comparing voltage measurements to the calibrated voltage measurements. This comparison allows the forces that act on the balance to be determined.

The balance – rotary stage system is outside the wind tunnel test section (see Figure 3.2) but the support structure rises 0.04" from the bottom wall of the test section. For this reason, before and after testing each model, an aerodynamic tare was run on the support structure alone to account for the drag of the support. Between each change of airspeed during testing, the wind tunnel velocity was brought back to zero to account for any balance drift.

3.2.2 Density, Viscosity, and Velocity

In the LSWT, an Angle of Attack from -2° to 25° in steps of 0.25° was performed on the models at two different Reynolds Numbers. Tunnel temperature, atmospheric pressure and air humidity were measured numerous times during execution of the experiments and were used in the correction of calculated velocity to real tunnel velocity.

Each model has a different chord length as listed in Table 2.2. The Reynolds number was based on a chord length equal to $\bar{c} = 4"$ and is equal to:

$$\mathrm{Re} = \frac{V_{\infty} \cdot \bar{c} \cdot \rho_{air}}{\mu_{air}} \qquad (3.1)$$

The air density, ρ_{air}, is calculated using Equation (3.2):

$$\rho_{air} = 1.2929\left(\frac{273.15}{T+273.15}\right)\left(\frac{p_{atm} - SVP \cdot H}{760}\right) \tag{3.2}$$

Where T (°C) is the tunnel temperature, p_{atm} $(mmHg)$ is the atmospheric pressure, SVP $(mmHg)$ is the Saturation Vapor Pressure which depends on the temperature, and H is the air humidity.

The air viscosity, μ_{air}, is calculated using Sutherland's formula:

$$\mu_{air} = \mu_0 \frac{T_0 + C}{T + C}\left(\frac{T}{T_0}\right)^{3/2} \tag{3.3}$$

For standard air, μ_0 is the reference viscosity equal to $1.827 \cdot 10^{-5} Pa \cdot s$ at reference temperature T_0 (K) equal to 291.15K, C is the Sutherland's constant equal to 120, and T (K) is the input temperature. Once the Reynolds Number was chosen, the freestream velocity was obtained.

3.3 Test Plan

The test were performed on all the models in Table 2.2 at two different Reynolds numbers 60,000 and 120,000. Each model was placed in the LSWT and mounted on the rotary stage. Data were taken for all configurations for 109 different angles of attack, α, from -2° to 25° by 0.25° increments. Testing procedures were repeated for all models. The dates of the testing and the corresponding temperature, pressure, and humidity can be seen in Appendix C.

IV. Results and Analysis

4.1 Chapter Overview

In this chapter, results for the wind tunnel tests conducted on the fourteen biplane configurations will be shown. The aerodynamic data for all fourteen models in Table 2.2 can be seen in Appendix D for Reynolds number 60,000 and in Appendix E for Reynolds number 120,000.

The results will be divided into five main sections. The first section will compare the results of models of similar gap at each speed. The second section will compare the results of models of similar stagger at each speed. The third section will compare the differences between positive stagger and negative stagger for each model having stagger at each speed. The fourth section will describe the change in lift slope at each speed. The fifth section will discuss the aerodynamic hysteresis. The sixth section will compare analytical and experimental results. The seventh section will discuss the method by which obtaining uncertainty analysis on aerodynamic efficiency and lift coefficient is made possible.

4.2 Wind Tunnel Balance Data – Similar Gap Models

In this section the effect of stagger on the performance of the biplane joined at the tips will be presented. For this analysis, data from models having similar gap will be presented to better understand the behaviour of changes in stagger. The aerodynamic performance analyzed will be essentially the lift coefficient, the drag polar, and the aerodynamic efficiency of the different models.

4.2.1 Gap 0.5c

Summary

In the LSWT, an α sweep from -2° to 25° in steps of 0.25° was performed on the models having similar gap, g=0.5c, at two different speeds: $\mathrm{Re} = 60{,}000\ (\approx 9 m/s)$, $\mathrm{Re} = 120{,}000\ (\approx 18 m/s)$.

Lift Coefficient

The Reynolds number does not affect the variation of lift coefficient for the different models. For this reason, the section concerning the variation of lift coefficient changing the stagger, will be presented with the data at Reynolds number 60,000. At the end of the section, the percentage of variation of lift coefficient when changing the stagger will be presented for both Reynolds numbers.

Figure 4.1 and Figure 4.2 plot the lift coefficient, C_L, vs. α for models having gap 0.5c at two different stagger conditions and Reynolds number 60,000. Figure 4.1 plots the lift coefficient for the models having positive stagger from s = 0c to s = 1c, Figure 4.2 plots the lift coefficient the models having negative stagger from s = -1c to s = 0c. In both graphs, the curve of lift coefficient as function of angle of attack (lift curve) for the model having no stagger was plotted.

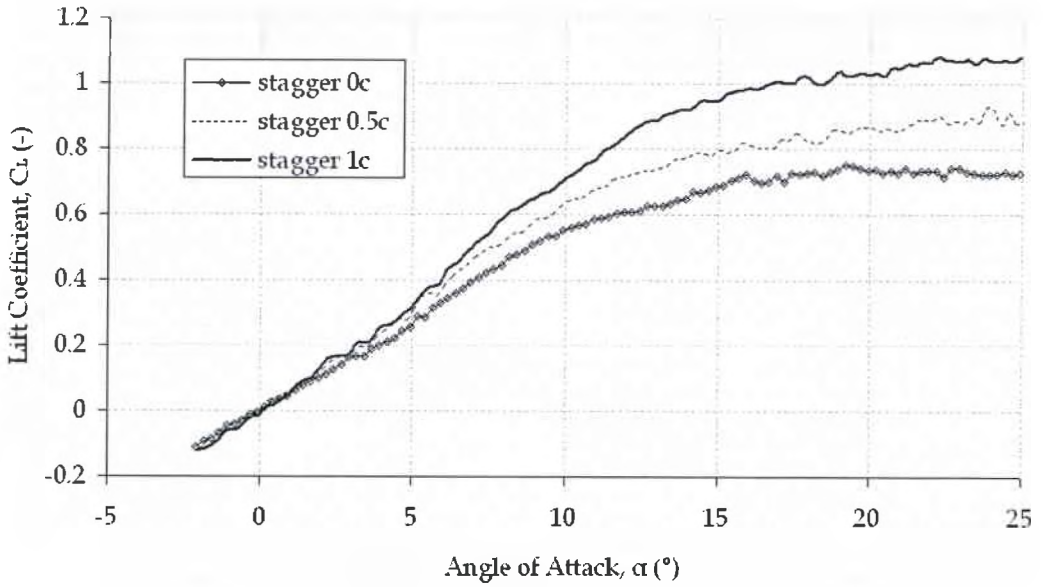

Figure 4.1: Comparison of Lift Curve with varying stagger in the positive direction and constant gap of 0.5c at Re=60,000

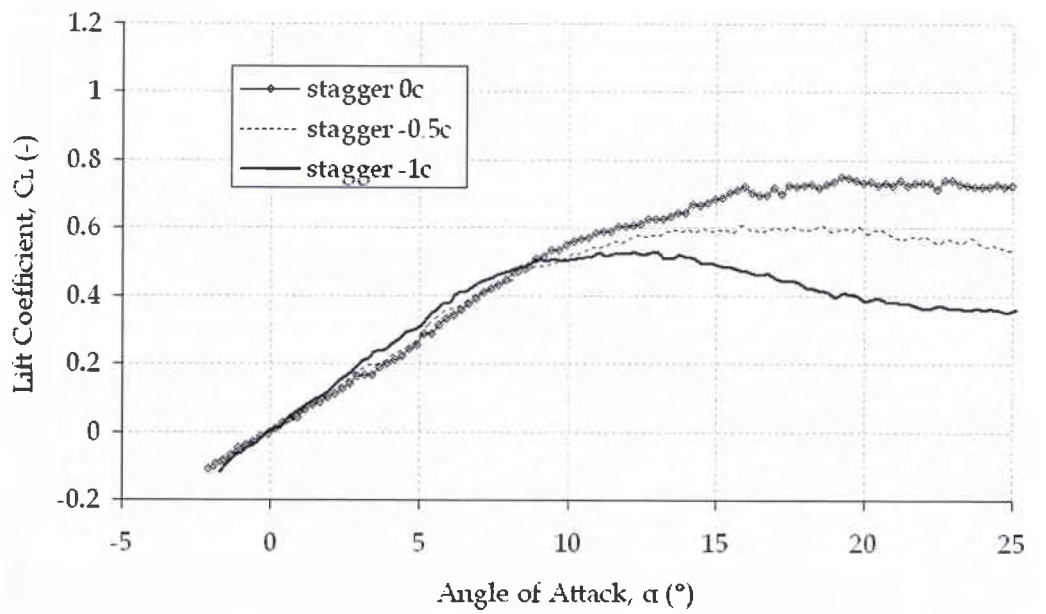

Figure 4.2: Comparison of Lift Curve with varying stagger in the negative direction and constant gap of 0.5c at Re=60,000

It can be seen that the lift coefficient increases when the stagger increases. Models with positive stagger do not show stall in the range of angle of attack

considered. They show a non linearity of the curve C_L vs. α between 10° and 15° angle of attack. To compare the different models having gap g = 0.5c and different stagger at the two different Reynolds numbers, the lift slope can be considered. Values of lift slope in the range of angle of attack between -2° and 8° are shown in Table 4.1 and in Table 4.2 where the comparison between the different models is expressed in terms of a percent variation which is referenced to the model having no stagger.

Table 4.1: Lift Slope for models having g=0.5c at Re 60,000

Models		Speed	Lift Slope	% Variation
Gap	Stagger	Re (-)	$C_{L\alpha}$ (-)	
0.5c	-1c	60,000	0.0613	11.45
	-0.5c	60,000	0.0572	4.01
	0c	60,000	0.0550	0.00
	0.5c	60,000	0.0634	15.31
	1c	60,000	0.0701	27.51

Table 4.2: Lift Slope for models having g=0.5c at Re 120,000

Models		Speed	Lift Slope	% Variation
Gap	Stagger	Re (-)	$C_{L\alpha}$ (-)	
0.5c	-1c	120,000	0.0598	8.22
	-0.5c	120,000	0.0569	2.89
	0c	120,000	0.0553	0.00
	0.5c	120,000	0.0625	13.04
	1c	120,000	0.0693	25.34

It can be seen from the graphs in Figure 4.1 and in Figure 4.2 of lift coefficient vs. angle of attack at Re 60,000 that the lift slope increases in both the positive and negative stagger direction. From Table 4.1 it can be seen that at Re 60,000 the lift slope increases by almost 5% for each 0.5c stagger increment in the

negative direction and it increases by almost 15% for each 0.5c stagger increment in the positive direction. Instead, from Table 4.2 at Re 120,000 the percentages of variation between different staggers is slightly different but the trend is the same. Figure 4.3 shows the lift slope variation vs. stagger for the different models at different Reynolds number, where, again, the percentage is referenced to the model having no stagger.

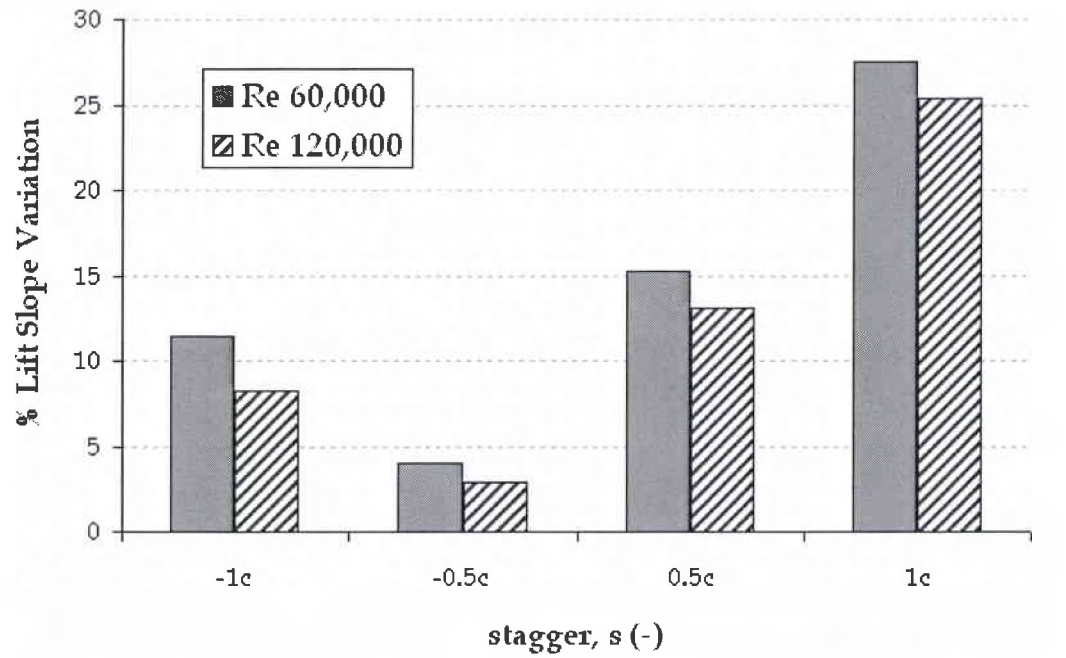

Figure 4.3: Shows the Lift Slope Variation with varying stagger and constant gap of 0.5c at both Reynolds numbers of 60,000 and 120,000

Aerodynamic Efficiency

Figure 4.4 and Figure 4.5 plot the aerodynamic efficiency, or lift over drag ratio, L/D, vs. α for the models having gap g=0.5c at two different stagger conditions and Reynolds number 60,000. As before, Figure 4.4 plots the aerodynamic efficiency for the models having positive stagger from s = 0c to s = 1c,

Figure 4.5 plots the aerodynamic efficiency for the models having negative stagger from s = -1c to s = 0c. In both graphs, the curve of aerodynamic efficiency as a function of angle of attack for the model having no stagger was plotted.

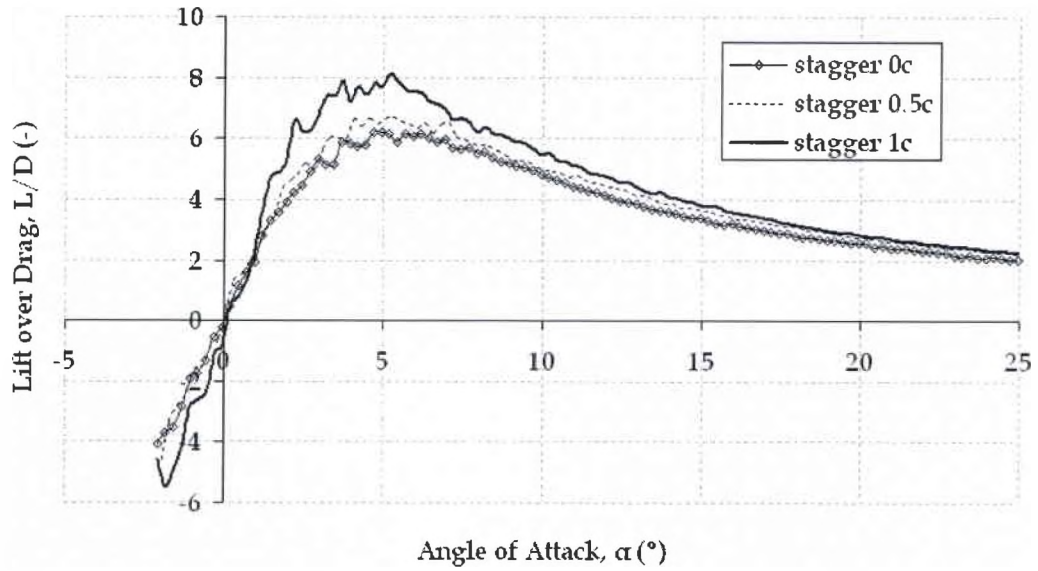

Figure 4.4: Comparison of Lift over Drag Ratio with varying stagger in the positive direction and constant gap of 0.5c at Re=60,000

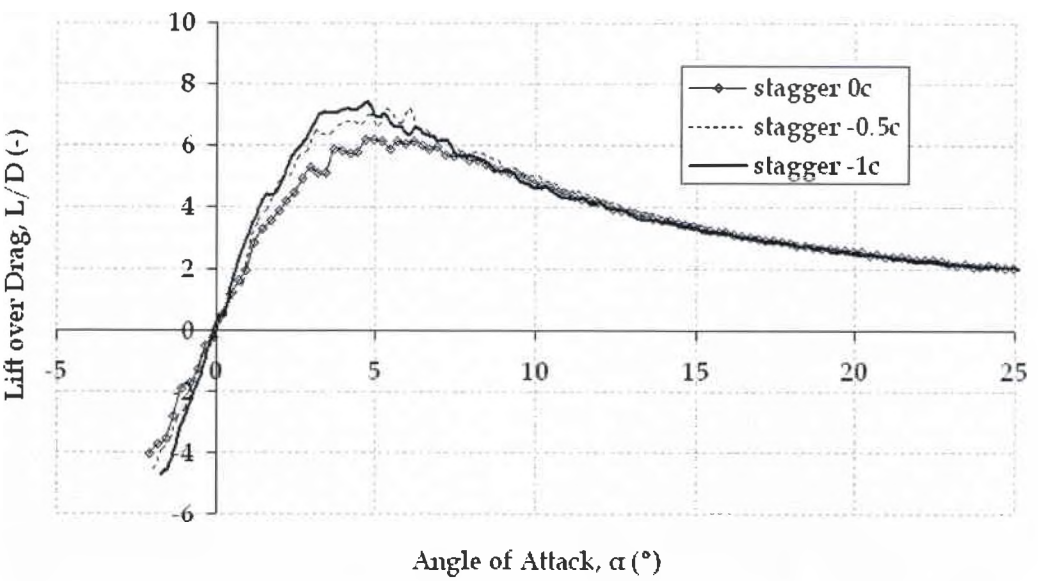

Figure 4.5: Comparison of Lift over Drag Ratio with varying stagger in the negative direction and constant gap of 0.5c at Re=60,000

It can be seen from the graphs of aerodynamic efficiency vs. angle of attack at Re 60,000 that models with larger stagger experience higher lift over drag ratio. Due to noise in the data around the value of maximum aerodynamic efficiency, the comparison between different models having same gap will be conducted considering the area underneath the curve of L/D vs. angle of attack. This procedure will allow to obtain values of area and the model with highest aerodynamic efficiency will be the model having highest area underneath the same curve keeping the angle of attack range constant across comparisons. Figure 4.6 shows an example of area underneath the curve of L/D vs. angle of attack that has been considered.

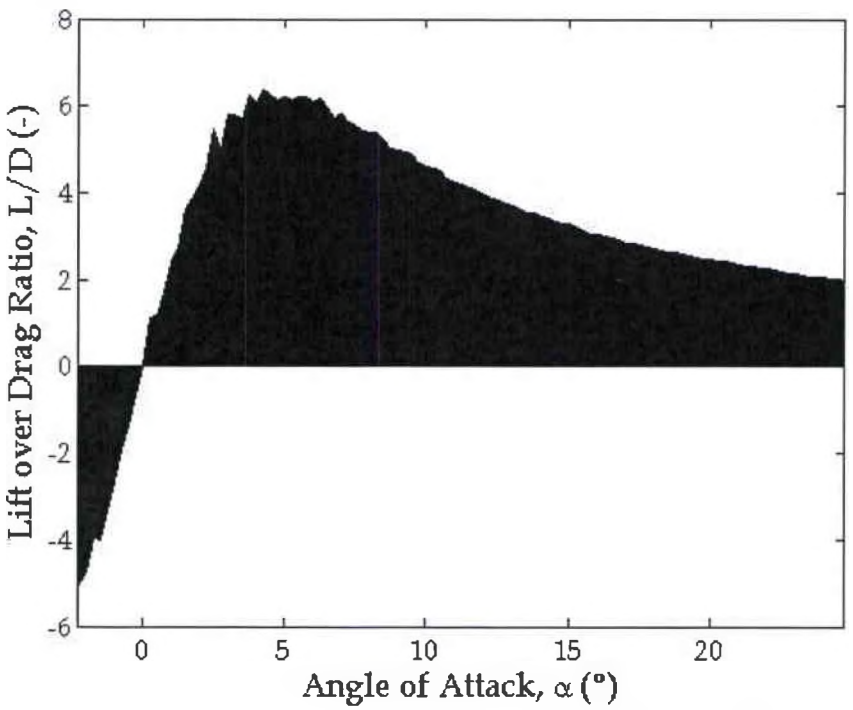

Figure 4.6: Shows an example of area underneath the curve L/D

This figure and the subsequent calculations were performed using the software Matlab and the calculation were carried out using the function trapz(x,y). This function computes an approximation of the integral of the function via the trapezoid rule. The error, if present, is declared to be equal to 1/1000 of the step size of the function. Because the step size in this case is equal to the increment of angle of attack which is equal to 0.25°, the error using this function will be equal to 0.025%. Also, in this section the comparison between areas, which means the largest total aerodynamic efficiency, of each model was performed by taking the percentage of variation referenced to the model with no stagger. This means that each calculation will be affected by the same error for each model and this error will not affect the final comparison between different models. Table 4.3 shows the variation of aerodynamic efficiency between different models at two different Reynolds numbers.

Table 4.3: Integrated Lift over Drag Ratio for models having g=0.5c at Re 60,000

Model		Speed	Integrated Lift over Drag Ratio	Speed	Integrated Lift over Drag Ratio
Gap	Stagger	Re (-)	% Variation	Re (-)	% Variation
0.5	-1	60,000	14.90	120,000	8.24
	-0.5	60,000	11.44	120,000	5.45
	0	60,000	0.00	120,000	0.00
	0.5	60,000	10.24	120,000	28.07
	1	60,000	21.18	120,000	34.48

From Table 4.3 it can be seen that at Re 60,000 the integrated lift over drag ratio increases by almost 10% for the first 0.5c stagger increment in the negative direction then it increases of another 5% for the second 0.5c stagger increment in the negative direction. For the positive stagger increment it can be seen that the

maximum lift over drag ratio increases by almost 10% for each 0.5c stagger increment in the positive direction. At Re 120,000 the percentages of variation between different staggers is slightly different but the trend is the same. As has been done before for the lift slope, the variation of aerodynamic efficiency at different Reynolds number as function of stagger, in Figure 4.7 is plotted.

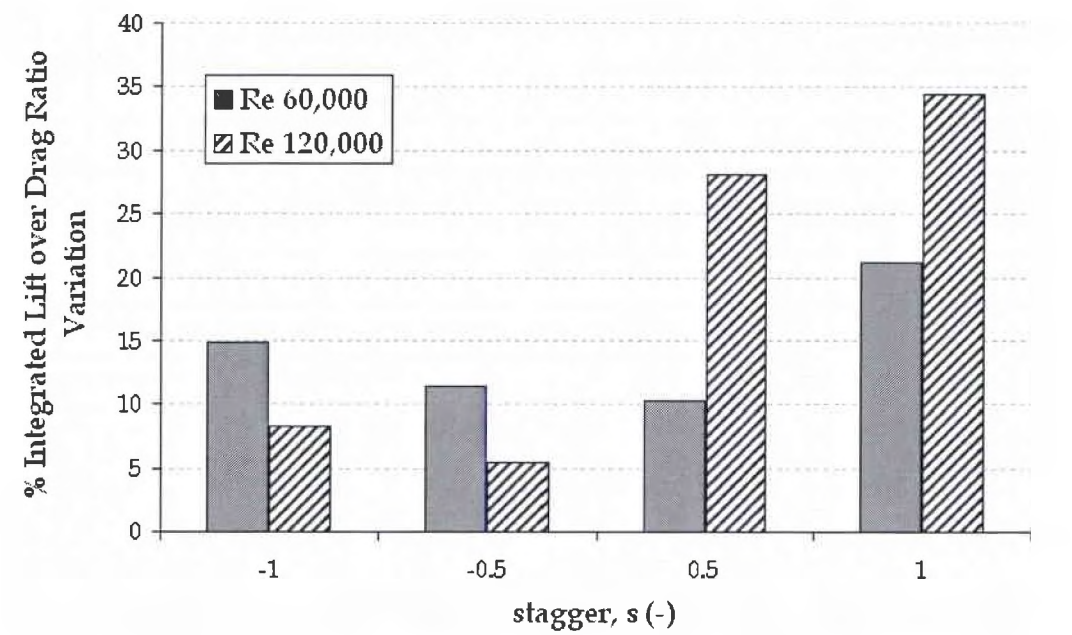

Figure 4.7: Shows the Integrated Lift over Drag Variation with varying stagger and constant gap of 0.5c at both Reynolds numbers of 60,000 and 120,000

Models with positive stagger at Re 120,000 show large variation in aerodynamic efficiency when the stagger changes from s = 0c to s = 1c. This variation at Re 120,000 is lower when considering negative stagger configurations. At Re 60,000 the models show almost the same variation in both negative and positive stagger configuration.

Drag Polar

Figure 4.8 and Figure 4.9 plot the drag polar, C_D vs. C_L, for the models with gap g = 0.5c at two different stagger conditions and Reynolds number 60,000.

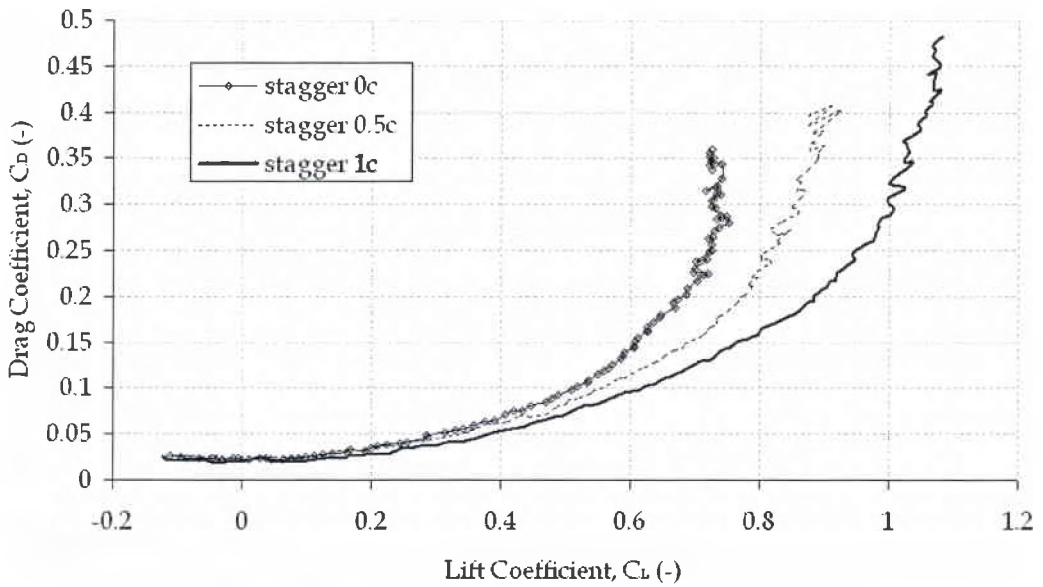

Figure 4.8: Comparison of Drag Polar with varying stagger in the positive direction and constant gap of 0.5c at Re=60,000

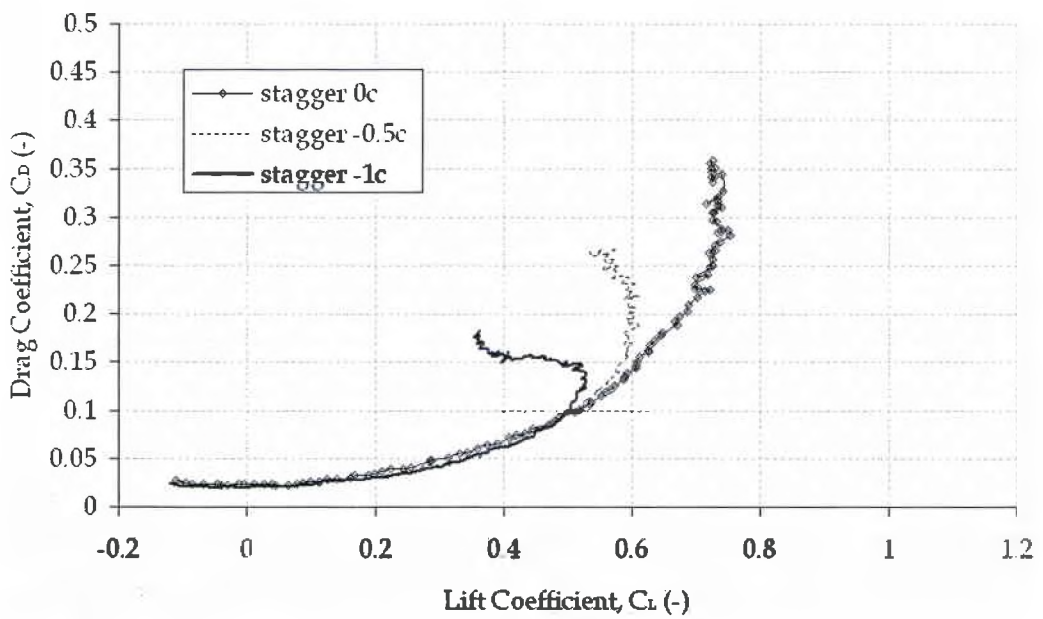

Figure 4.9: Comparison of Drag Polar with varying stagger in the negative direction and constant gap of 0.5c at Re=60,000

As before, Figure 4.8 plots the drag polar for the models having positive stagger from s = 0c to s = 1c, Figure 4.9 plots the drag polar for the models with negative stagger from s = -1c to s = 0c. In both graphs, the drag polar for the model having no stagger was plotted. From Figure 4.8 it can be seen that models with positive stagger have lower C_{Di} compared to the models with negative stagger in Figure 4.9. This means that positive stagger models perform better than the models with negative stagger.

Table 4.4 and Table 4.5 compare the induced and parasite drag between all configurations at Re 60,000 and Re 120,000.

Table 4.4: Induced Drag over Total Drag Ratio for models having g=0.5c at Re 60,000

Models		Speed	Drag Coefficients			
Gap	Stagger	Re (-)	C_D (-)	C_{D0} (-)	C_{Di} (-)	$\%C_{Di}/C_D$ (-)
0.5c	-1c	60,000	0.051	0.019	0.031	61.69
	-0.5c	60,000	0.040	0.019	0.021	53.04
	0c	60,000	0.041	0.022	0.019	46.03
	0.5c	60,000	0.052	0.024	0.028	54.01
	1c	60,000	0.042	0.018	0.024	57.38

Table 4.5: Induced Drag over Total Drag Ratio for models having g=0.5c at Re 120,000

Models		Speed	Drag Coefficients			
Gap	Stagger	Re (-)	C_D (-)	C_{D0} (-)	C_{Di} (-)	$\%C_{Di}/C_D$ (-)
0.5c	-1c	120,000	0.041	0.021	0.020	48.74
	-0.5c	120,000	0.033	0.022	0.012	35.58
	0c	120,000	0.034	0.019	0.014	42.38
	0.5c	120,000	0.031	0.021	0.010	32.33
	1c	120,000	0.043	0.018	0.025	57.67

Figure 4.10 plots the induced drag percentage of total drag for both Reynolds numbers versus stagger.

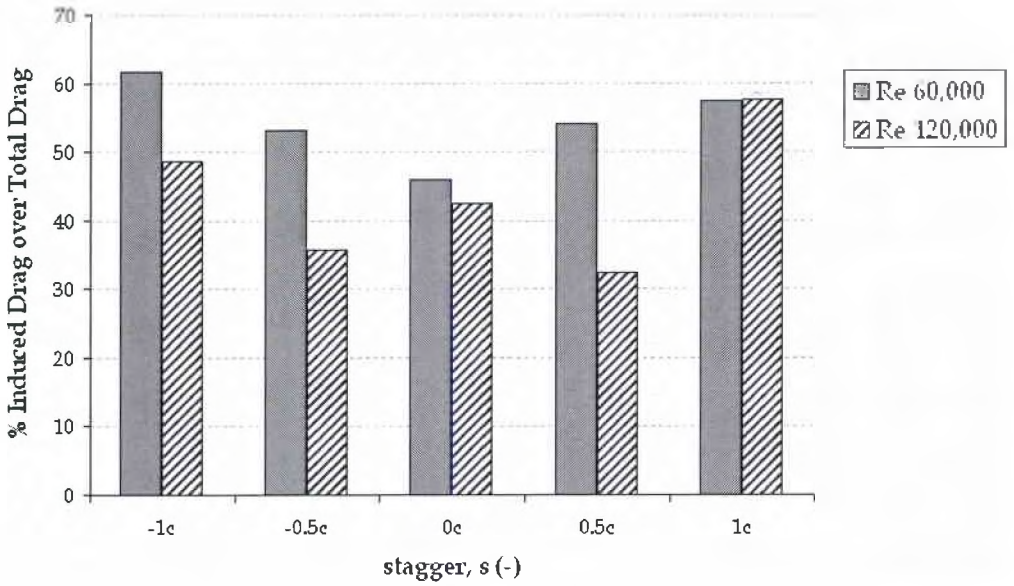

Figure 4.10: Shows the Induced Drag over Total Drag Ratio with varying stagger and constant gap of 0.5c at both Reynolds numbers of 60,000 and 120,000

It can be seen that at Re 60,000 the unstaggered model has the least amount of induced drag percentage of the total drag. At Re 120,000 the model with stagger s=0.5c is the one with the least amount of induced drag percentage of the total drag.

4.2.2 Gap 1c

Summary

In the LSWT, an α sweep from -2° to 25° in steps of 0.25° was performed on models with similar gap, g = 1c, at two different speeds: $\mathrm{Re} = 60{,}000\ (\approx 9 m/s)$, $\mathrm{Re} = 120{,}000\ (\approx 18 m/s)$.

Lift Coefficient

The Reynolds number does not affect the variation of lift coefficient for the different models. For this reason, the section concerning the variation of lift coefficient with change in stagger, will be presented with the data at Reynolds

number 60,000. At the end of the section, the percent variation in lift coefficient with changing stagger will be presented for both Reynolds numbers.

Figure 4.11 and Figure 4.12 plot the lift coefficient, C_L, vs. α for models with gap g = 1c at two different stagger conditions and Reynolds number 60,000. Figure 4.11 plots the lift coefficients for the models with positive stagger from s = 0c to s = 1.5c, Figure 4.12 plots the lift coefficient for the models with negative stagger from s = -1.5c to s = 0c. In both graphs, the curve of lift coefficient as a function of angle of attack for the model with no stagger was plotted.

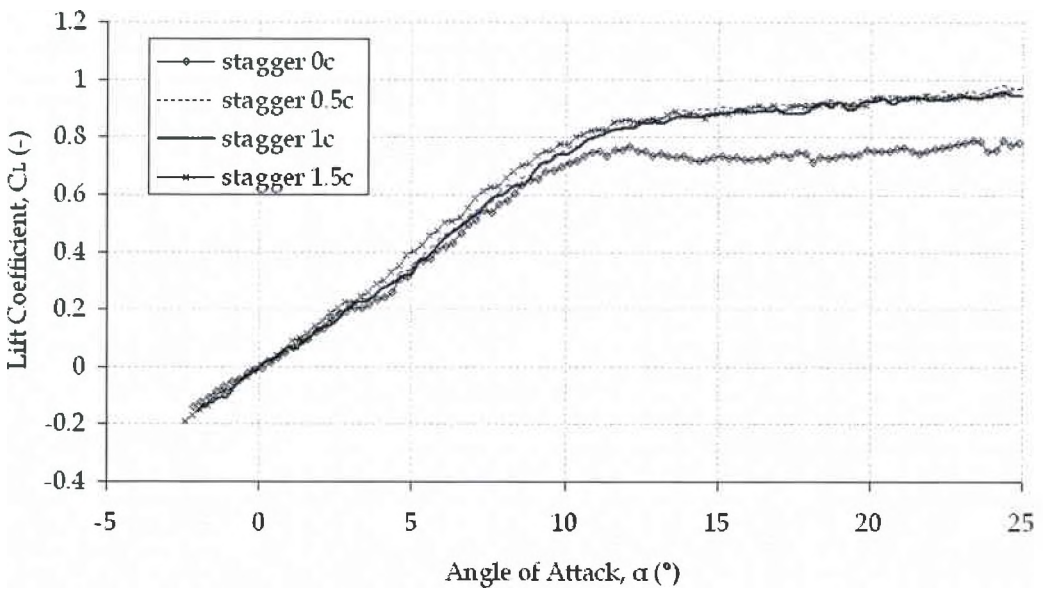

Figure 4.11: Comparison of Lift Curve with varying stagger in the positive direction and constant gap of 1c at Re=60,000

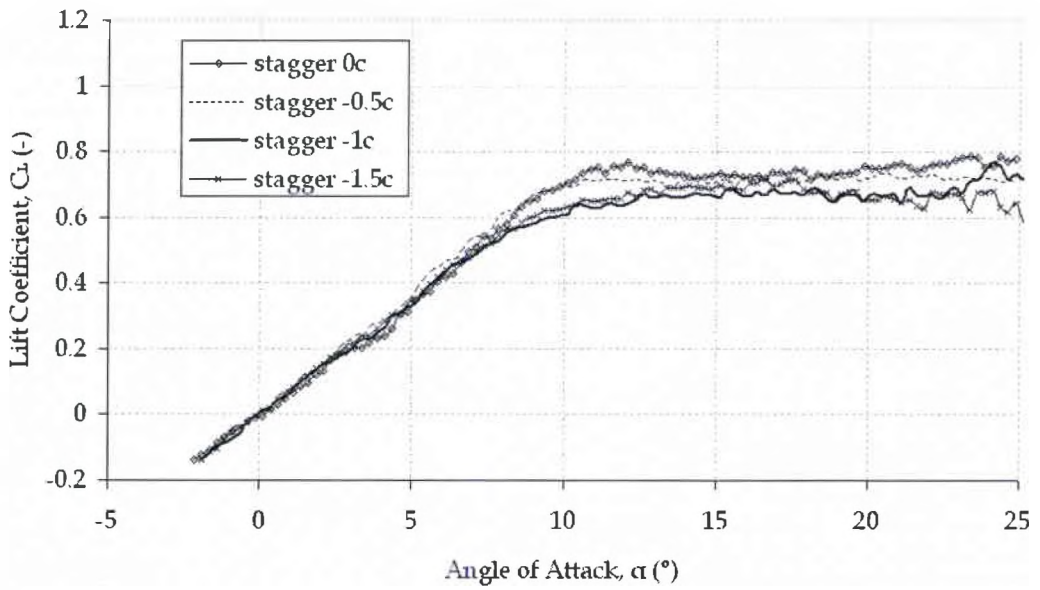

Figure 4.12: Comparison of Lift Curve with varying stagger in the negative direction and constant gap of 1c at Re=60,000

It can be seen from Figure 4.11 that the lift coefficient does not change when the stagger increases in the positive direction. Models with positive stagger do not show stall in the range of angle of attack considered. From Figure 4.12 it can be seen that models with negative stagger have different behavior than the models with positive stagger. In the negative stagger configurations each model presents a different lift coefficient vs. angle of attack curve. But nothing can be said about the models with gap g = 1c because the trend is not clear as it was in the case of gap g = 0.5c. This could be due to the fact that higher gap means less interference between the two wings. This yields essentially the same lift coefficient vs. angle of attack behavior for all models having similar gap g = 1c. Now compare the lift slope of the different models with gap g = 1c and different stagger at the two different Reynolds numbers. Values of lift slope in the range of angle of attack

between -2° and 8° are shown in Table 4.6 and Table 4.7 where the comparison between the different models is expressed in terms of a percentage referenced to the model having no stagger.

Table 4.6: Lift Slope for models having g = 1c at Re 60,000

Models		Speed	Lift Slope	% Variation
Gap	Stagger	Re (-)	$C_{L\alpha}$ (-)	
1c	-1.5c	60,000	0.0697	0.56
	-1c	60,000	0.0693	-0.10
	-0.5c	60,000	0.0737	6.32
	0c	60,000	0.0693	0.00
	0.5c	60,000	0.0748	7.83
	1c	60,000	0.0756	9.12
	1.5c	60,000	0.0803	15.89

Table 4.7: Lift Slope for models having g=1c at Re 120,000

Models		Speed	Lift Slope	% Variation
Gap	Stagger	Re (-)	$C_{L\alpha}$ (-)	
1c	-1.5c	120,000	0.0725	2.36
	-1c	120,000	0.0690	-2.59
	-0.5c	120,000	0.0712	0.58
	0c	120,000	0.0708	0.00
	0.5c	120,000	0.0719	1.59
	1c	120,000	0.0746	5.33
	1.5c	120,000	0.0803	13.49

Figure 4.13 shows the lift slope variation vs. stagger for the different models at different Reynolds number, where the percentage is referenced to the model having no stagger.

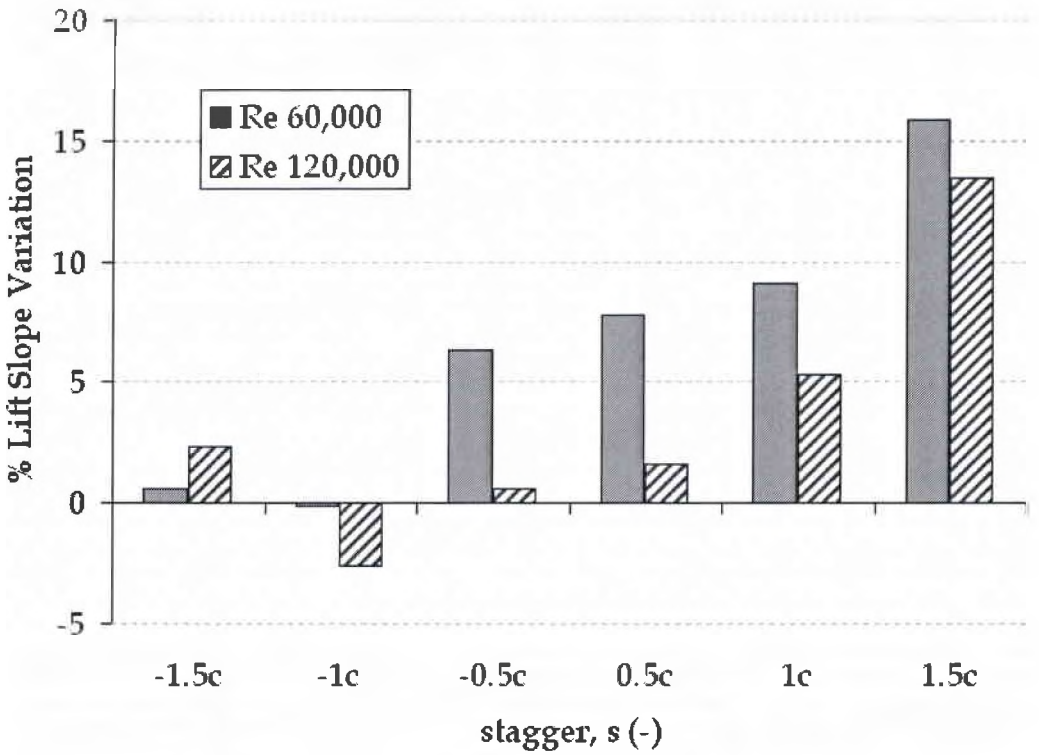

Figure 4.13: Shows the Lift Slope Variation with varying stagger and constant gap of 1c at both Reynolds numbers of 60,000 and 120,000

Looking at Figure 4.13 it can be seen that the lift slope of the models changes following a descendent trend going from stagger s = -1.5c to s = -1c at both Re 60,000 and Re 120,000. After a value of stagger equal to s = -1c, the lift slope starts to increase until it reaches its maximum value at the highest stagger configuration. Also, the only model that has lower lift slope compared to the model with no stagger is the model with stagger s = -0.5.

Aerodynamic Efficiency

Figure 4.14 and Figure 4.15 plot the aerodynamic efficiency, or lift over drag ratio, L/D, vs. α for the models having gap g = 1c at two different stagger conditions and Reynolds number 60,000.

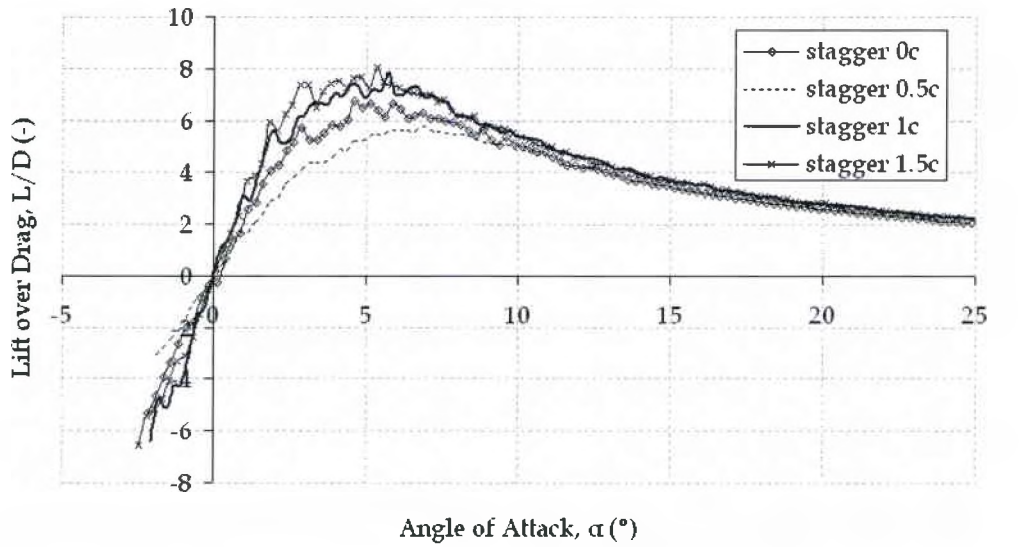

Figure 4.14: Comparison of Lift over Drag Ratio with varying stagger in the positive direction and constant gap of 1c at Re=60,000

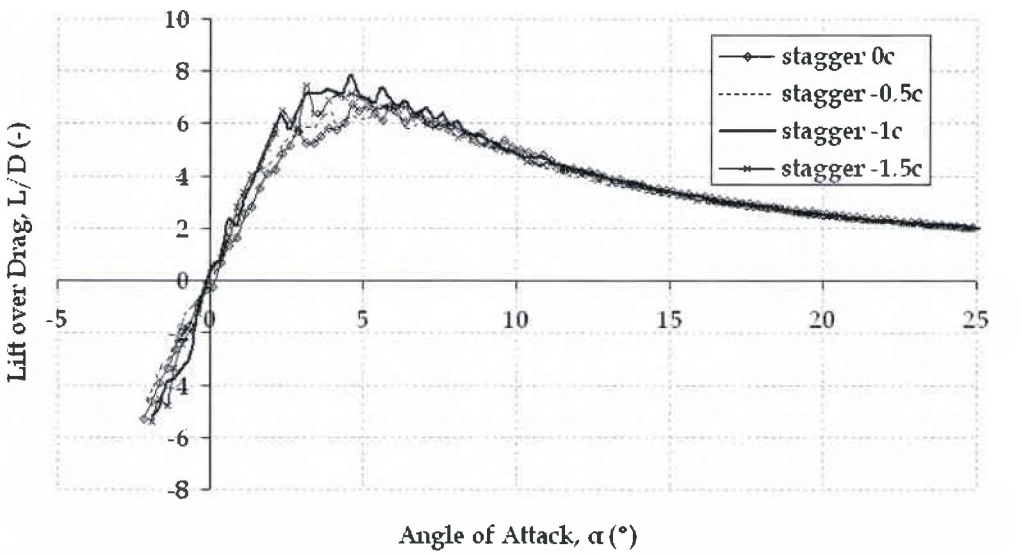

Figure 4.15: Comparison of Lift over Drag Ratio with varying stagger in the negative direction and constant gap of 1c at Re=60,000

As before, Figure 4.14 plots the aerodynamic efficiency for the models having positive stagger from s = 0c to s = 1.5c, Figure 4.15 plots the aerodynamic efficiency for the models having negative stagger from s = -1.5c to s = 0c. In both graphs, the curve of aerodynamic efficiency as a function of angle of attack for the model having no stagger was plotted.

To compare the different models in term of integrated efficiency the same method of computing the area beneath the curve of lift to drag ratio vs. angle of attack was used. This method, explained in the section concerning the models having similar gap g = 0.5c, gives, for these models with similar gap g = 1c, the following results represented in Table 4.8 where the variation of aerodynamic efficiency between different models is referenced to the model having no stagger at the two different Reynolds numbers.

Table 4.8: Integrated Lift over Drag Ratio for models having g=1c at Re 60,000

Model		Speed	Integrated Lift over Drag Ratio	Speed	Integrated Lift over Drag Ratio
Gap	Stagger	Re (-)	L/D_{max} (-)	Re (-)	L/D_{max} (-)
1	-1.5c	60,000	10.54	120,000	-13.43
	-1c	60,000	14.13	120,000	-12.98
	-0.5c	60,000	3.18	120,000	-18.22
	0c	60,000	0.00	120,000	0.00
	0.5c	60,000	-6.80	120,000	-11.82
	1c	60,000	13.83	120,000	-0.48
	1.5c	60,000	11.70	120,000	-2.46

As before for the lift slope, the variation of aerodynamic efficiency at different Reynolds number as function of stagger is plotted in Figure 4.16.

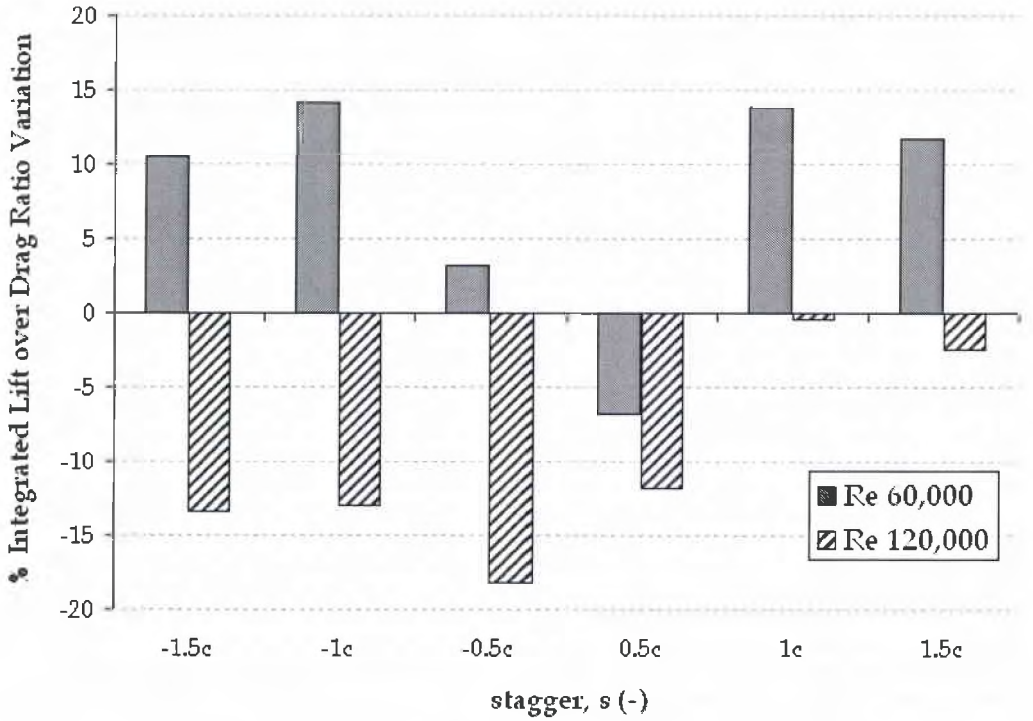

Figure 4.16: Shows the Integrated Lift over Drag Variation with varying stagger and constant gap of 1c at both Reynolds numbers of 60,000 and 120,000

From Table 4.8 and Figure 4.16 , it can be seen that at Re 60,000 the stagger has a positive effect on the aerodynamic efficiency, except in the case of stagger s = 0.5c where the integrated lift over drag ratio decreases by almost 7% compared to the unstaggered model. Also, models with stagger s = ±1c have higher lift over drag ratio than the models with stagger s = ±1.5c. It can also be seen that positive staggers s = 1c, and s = 1.5c have the same aerodynamic efficiency as the negative cases s = -1c, and s = -1.5 respectively. This means that at low Reynolds number the stagger could be positive or negative and it would affect the integrated aerodynamic efficiency in the same way. At Re 120,000 the stagger always has a negative effect on the aerodynamic efficiency. In this case, negative stagger has a

big deleterious effect on integrated aerodynamic efficiency compared to the positive stagger s = 1c and s = 1.5c where the effect of stagger is almost negligible. The model with stagger s = 0.5c does not follow this trend. But this model was also the only exception in the case of Re 60,000.

Drag Polar

Figure 4.17 and Figure 4.18 plot the drag polar, C_D vs. C_L, for the models with gap g = 1c at two different stagger conditions and Reynolds number 60,000. As before, Figure 4.17 plots the drag polar for the models having positive stagger from s = 0c to s = 1.5c, Figure 4.18 plots the drag polar for the models with negative stagger from s = -1.5c to s = 0c. In both graphs, the drag polar for the model with no stagger was plotted as a baseline reference.

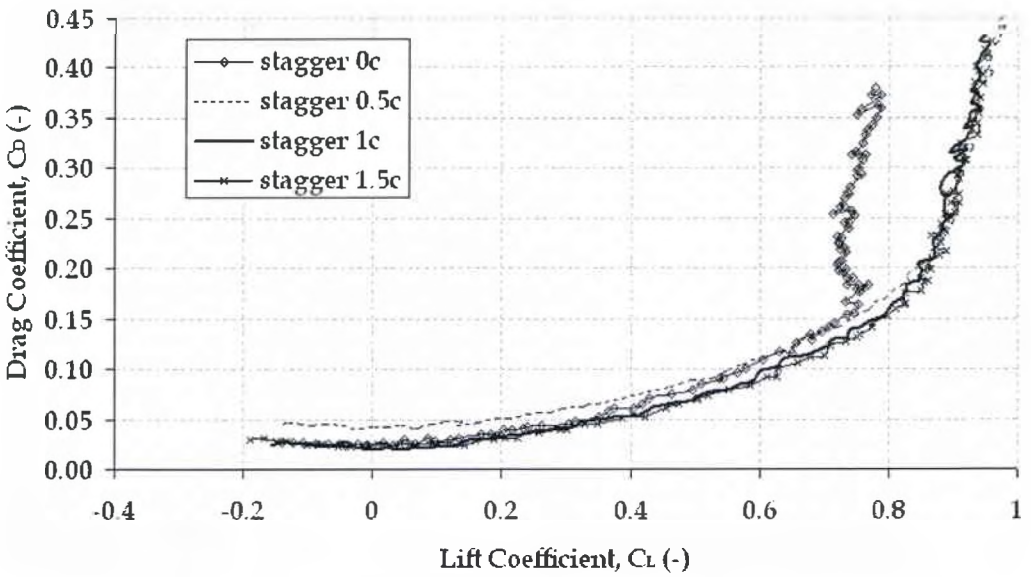

Figure 4.17: Comparison of Drag Polar with varying stagger in the positive direction and constant gap of 1c at Re=60,000

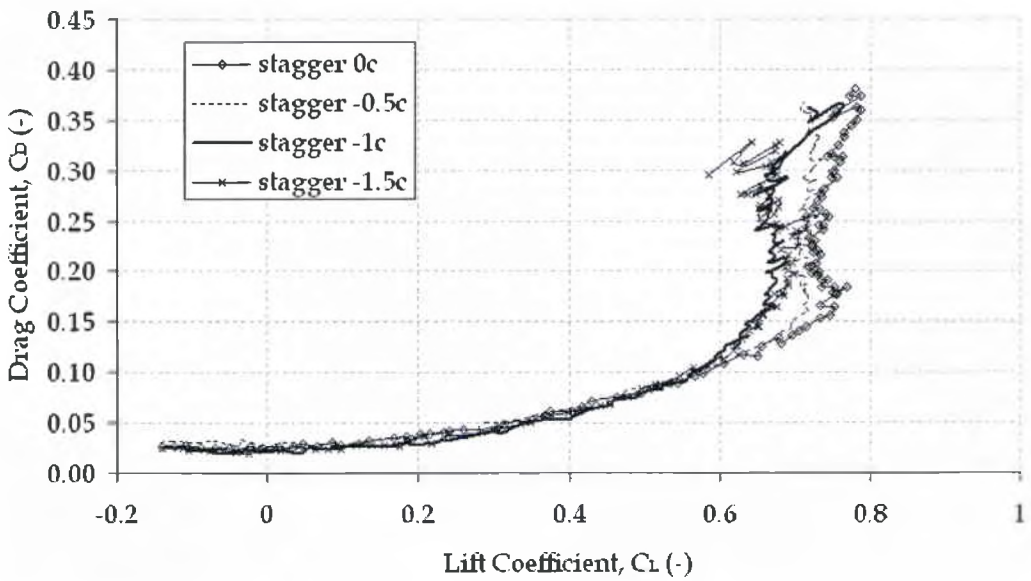

Figure 4.18: Comparison of Drag Polar with varying stagger in the negative direction and constant gap of 1c at Re=60,000

Also in the case of the drag polar, positive stagger models follow the same trend. Instead, from Figure 4.18 it can be seen that models with negative stagger have different behavior than the models with positive stagger. In the negative

stagger configurations each model presents a different drag polar. But nothing can be said about the models with gap g = 1c because the trend is not clear as it was in the case of gap g = 0.5c. And the reason is the same explained for the lift coefficient vs. angle of attack. The two wings interact more in the case of negative stagger than in the case of positive stagger. But still, high values of gap, which in this case means g = 1c, make the drag polar to be almost the same when changing the stagger. Table 4.9 and

Table 4.10 show the comparison between the induced and parasite drag of all the models at Re 60,000 and Re 120,000.

Table 4.9: Induced Drag over Total Drag Ratio for models having g=1c at Re 60,000

Models		Speed	Drag Coefficients			
Gap	Stagger	Re (-)	C_D (-)	C_{D0} (-)	C_{Di} (-)	$\%C_{Di}/C_D$ (-)
1c	-1.5c	60,000	0.029	0.019	0.010	35.19
	-1c	60,000	0.039	0.019	0.020	51.37
	-0.5c	60,000	0.066	0.027	0.039	59.63
	0c	60,000	0.045	0.024	0.021	47.13
	0.5c	60,000	0.091	0.041	0.050	55.37
	1c	60,000	0.052	0.020	0.032	61.79
	1.5c	60,000	0.053	0.022	0.030	57.87

Table 4.10: Induced Drag over Total Drag Ratio for models having g=1c at Re 120,000

Models		Speed	Drag Coefficients			
Gap	Stagger	Re (-)	C_D (-)	C_{D0} (-)	C_{Di} (-)	$\%C_{Di}/C_D$ (-)
1c	-1.5c	120,000	0.035	0.022	0.013	37.75
	-1c	120,000	0.039	0.018	0.021	53.68
	-0.5c	120,000	0.041	0.022	0.019	46.44
	0c	120,000	0.028	0.013	0.015	54.34
	0.5c	120,000	0.058	0.029	0.029	50.48
	1c	120,000	0.029	0.019	0.009	33.18
	1.5c	120,000	0.036	0.021	0.016	43.15

The induced drag percentage of total drag ratio for both Reynolds numbers versus stagger are plotted in Figure 4.19 providing:

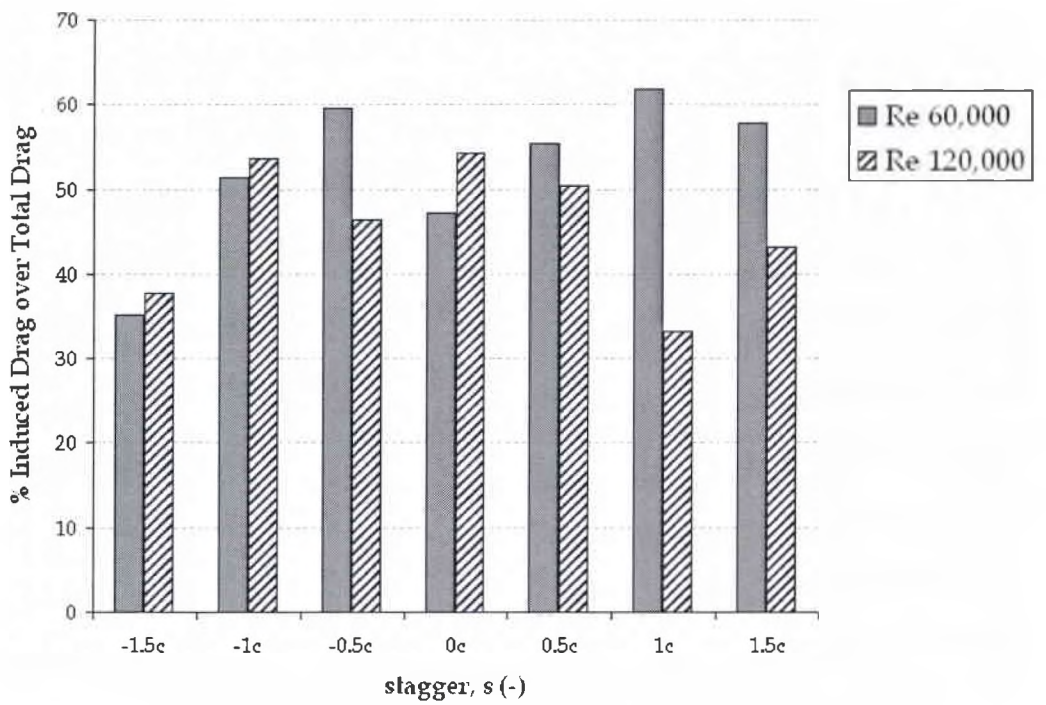

Figure 4.19: Shows the Induced Drag over Total Drag Ratio with varying stagger and constant gap of 1c at both Reynolds numbers of 60,000 and 120,000

It can be seen from Table 4.9 and Figure 4.19, that at Re 60,000 the model with stagger -1.5c has the least amount of induced drag percentage of the total drag. At Re 120,000 the model with stagger 1c has the least induced drag percentage of total drag.

4.2.3 Gap 2c

Summary

In the LSWT, an α sweep from -2° to 25° in steps of 0.25° was performed on the models with similar gap, g = 2c, at two different speeds: Re = 60,000 $(\approx 9 m/s)$, Re = 120,000 $(\approx 18 m/s)$.

Lift Coefficient

The Reynolds number does not affect the variation of lift coefficient for the different models. For this reason, the section concerning the variation of lift coefficient by varying the stagger, will be presented with the data at Reynolds number 60,000. At the end of the section, the percentage of variation in lift coefficient changing the stagger will be presented for both Reynolds numbers.

Figure 4.20 plots the lift coefficient, C_L, vs. α for the models with gap g = 2c at Reynolds number 60,000. The two different models with gap g = 2c have stagger s = ±1c. There were just two models with gap g = 2c. This will result in a more superficial comparison between different models, but these results can potentially verify the considerations about the effect of stagger on models having similar gap.

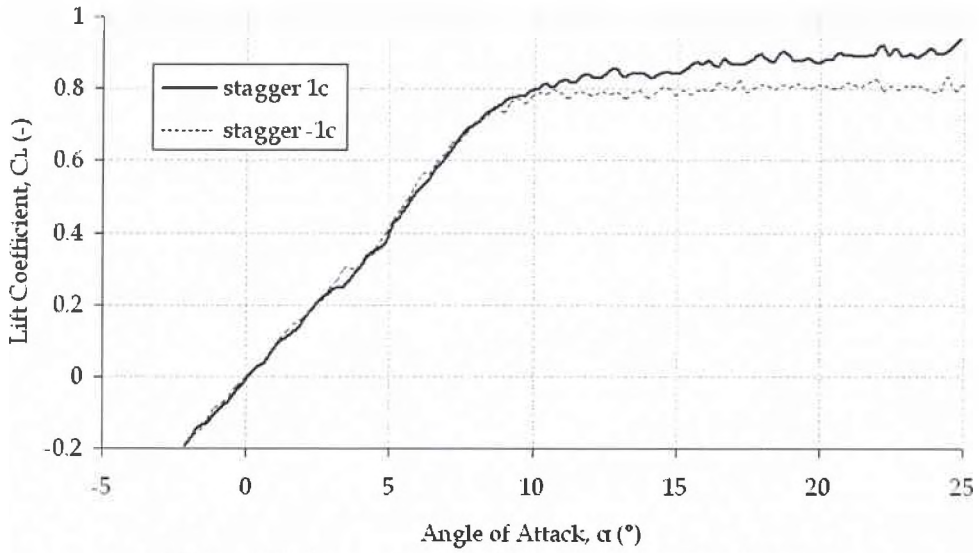

Figure 4.20: Comparison of Lift Curve with varying stagger and constant gap of 2c at Re=60,000

It can be seen that high values of gap means little interference between the two wings. The difference between positive stagger, s = 1c, and negative stagger, s = -1c, is negligible before an angle of attack equal of 10°. The two models also have the same lift slope, which is represented in Table 4.11 and Table 4.12 at both Reynolds numbers, and it is referenced to the model having negative stagger.

Table 4.11: Lift Slope for models having g=1c at Re 60,000

Models		Speed	Lift Slope	% Variation
Gap	Stagger	Re (-)	$C_{L\alpha}$ (-)	
2c	-1c	60,000	0.0881	0.00
	1c	60,000	0.0873	-0.89

Table 4.12: Lift Slope for models having g=1c at Re 120,000

Models		Speed	Lift Slope	% Variation
Gap	Stagger	Re (-)	$C_{L\alpha}$ (-)	
2c	-1c	120,000	0.0875	0.00
	1c	120,000	0.0874	-0.05

The variation of lift slope between the two models is almost negligible.

Aerodynamic Efficiency

Figure 4.21 plots the aerodynamic efficiency, or lift over drag ratio, L/D, vs. α for the models with gap 2c at two different stagger conditions and Reynolds number 60,000.

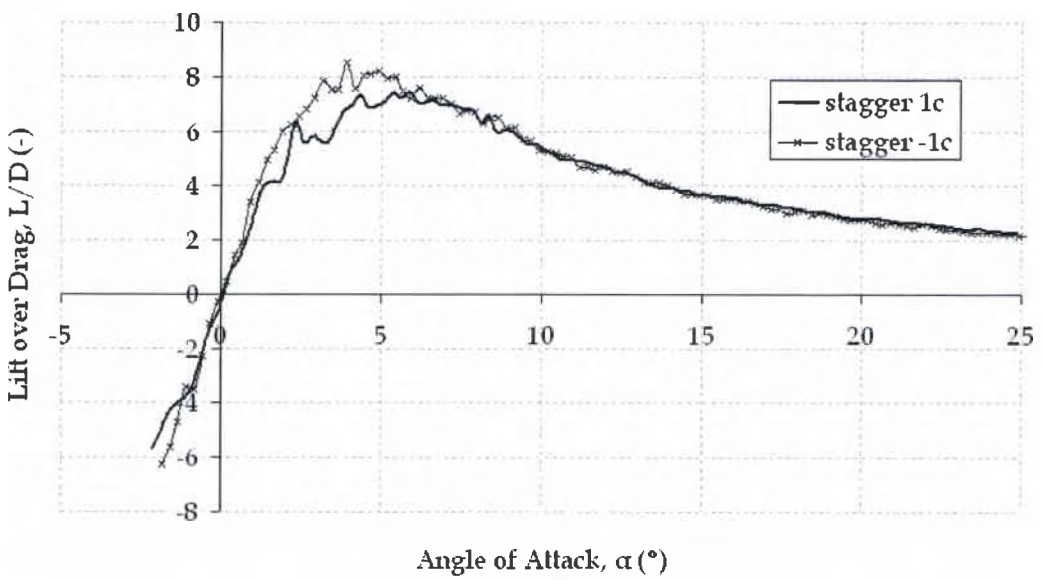

Figure 4.21: Comparison of Lift over Drag Ratio with varying stagger and constant gap of 2c at Re=60,000

The aerodynamic efficiency does not vary too much between the two models, except in the region of angle of attack between 2° and 6° where the aerodynamic efficiency reaches the maximum value. Table 4.13 shows the variation of aerodynamic efficiency for the two models referred to the model having negative stagger at both Reynolds numbers.

Table 4.13: Integrated Lift over Drag Ratio for models having g=0.5c at Re 60,000

Model		Speed	Integrated Lift over Drag Ratio	Speed	Integrated Lift over Drag Ratio
Gap	Stagger	Re (-)	L/D_{max} (-)	Re (-)	L/D_{max} (-)
2c	-1c	60,000	0.00	120,000	0.00
	1c	60,000	-12.12	120,000	-8.92

Negative stagger s = -1c has a higher aerodynamic efficiency than positive stagger s = 1c at both Reynolds numbers. It is interesting, for this configuration with a gap of g = 2c, to take a look at the lift over drag ratio as function of angle of attack in the case of Re 120,000. Figure 4.22 plots the aerodynamic efficiency, or lift over drag ratio, L/D, vs. α for the models with gap g = 2c at two different stagger conditions and a Reynolds number of 120,000.

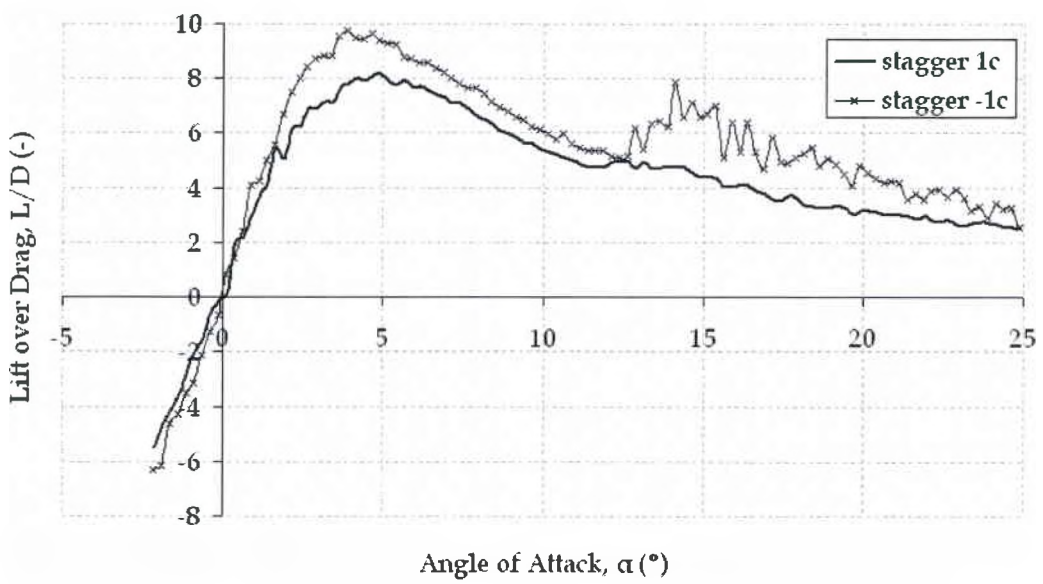

Figure 4.22: Comparison of Lift over Drag Ratio with varying stagger and constant gap of 2c at Re=120,000

In Figure 4.22, the two models show a interesting behavior beyond the angle of attack equal to 12°. It can be seen that this is the angle of stall for both models. This behavior will also be seen in the drag polar in the next section. This phenomenon is called stall flutter and it will be briefly explained in Appendix F.

Drag Polar

Figure 4.23 and Figure 4.24 plot the drag polar, C_D vs. C_L, for models with gap g = 2c at two different Reynolds numbers 60,000 and 120,000.

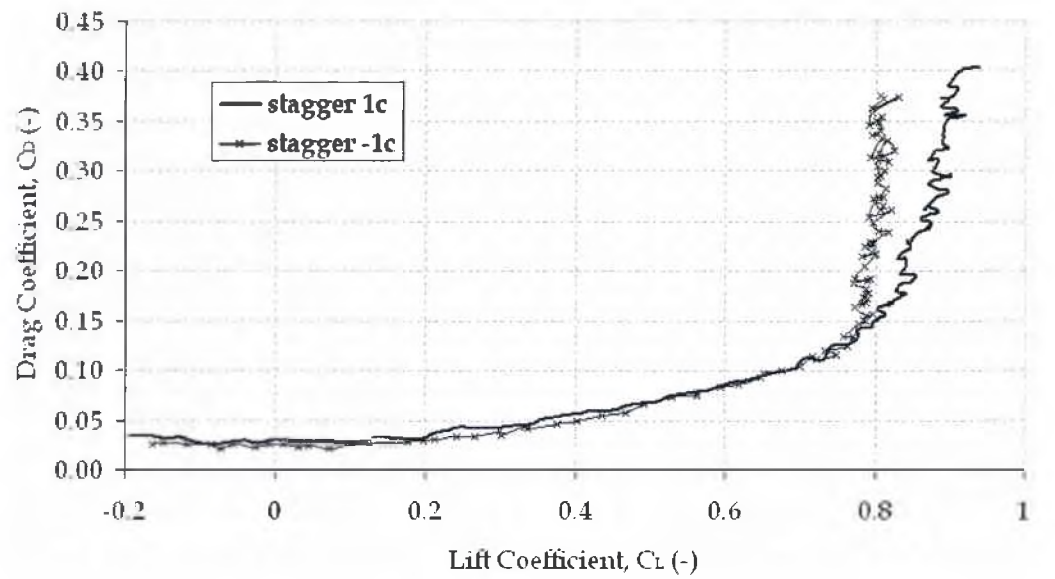

Figure 4.23: Comparison of Drag Polar with varying stagger and constant gap of 2c at Re=60,000

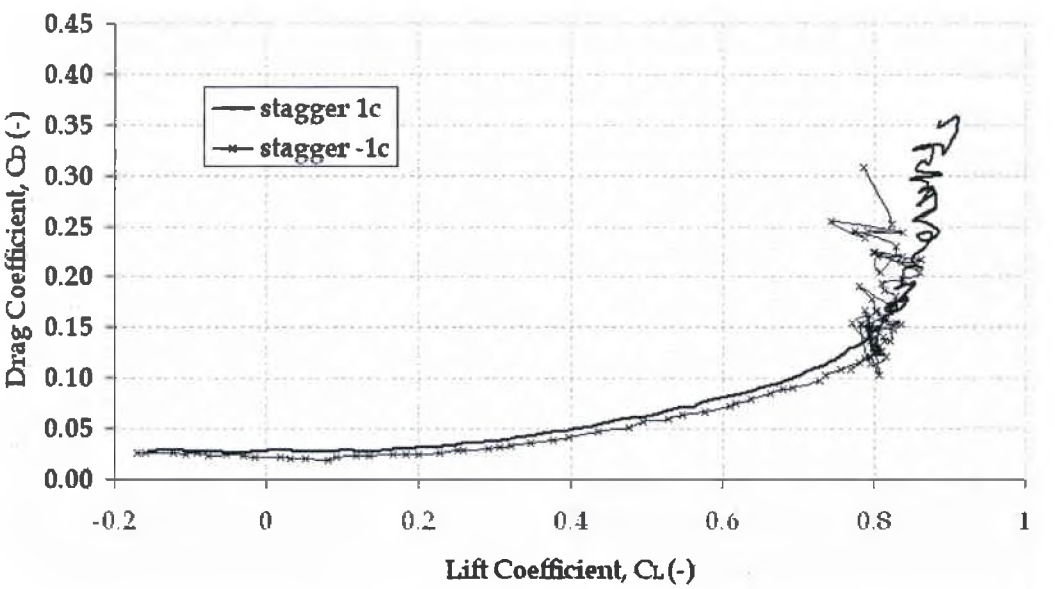

Figure 4.24: Comparison of Drag Polar with varying stagger and constant gap of 2c at Re=120,000

It can be seen from Figure 4.23 and Figure 4.24, that the drag polar is almost the same for both models at two different Reynolds numbers until a lift coefficient $C_L \cong 0.8$ then C_{Di} becomes lower for the positive stagger case, meaning that it performs better than the negative stagger case. Table 4.14 and Table 4.15 show the comparison between the induced and parasite drag of all the models at Re 60,000 and Re 120,000.

Table 4.14: Induced Drag over Total Drag Ratio for models having g=2c at Re 60,000

Models		Speed	Drag Coefficients			
Gap	Stagger	Re (-)	C_D (-)	C_{D0} (-)	C_{Di} (-)	$\%C_{Di}/C_D$ (-)
2c	-1c	60,000	0.036	0.020	0.015	42.44
	1c	60,000	0.060	0.026	0.034	56.33

Table 4.15: Induced Drag over Total Drag Ratio for models having g=2c at Re 120,000

Models		Speed	Drag Coefficients			
Gap	Stagger	Re (-)	C_D (-)	C_{D0} (-)	C_{Di} (-)	$\%C_{Di}/C_D$ (-)
2c	-1c	120,000	0.031	0.020	0.011	36.44
	1c	120,000	0.050	0.026	0.023	46.90

Plotting the ratio of induced drag over total drag for both Reynolds numbers versus stagger in Figure 4.25 we get:

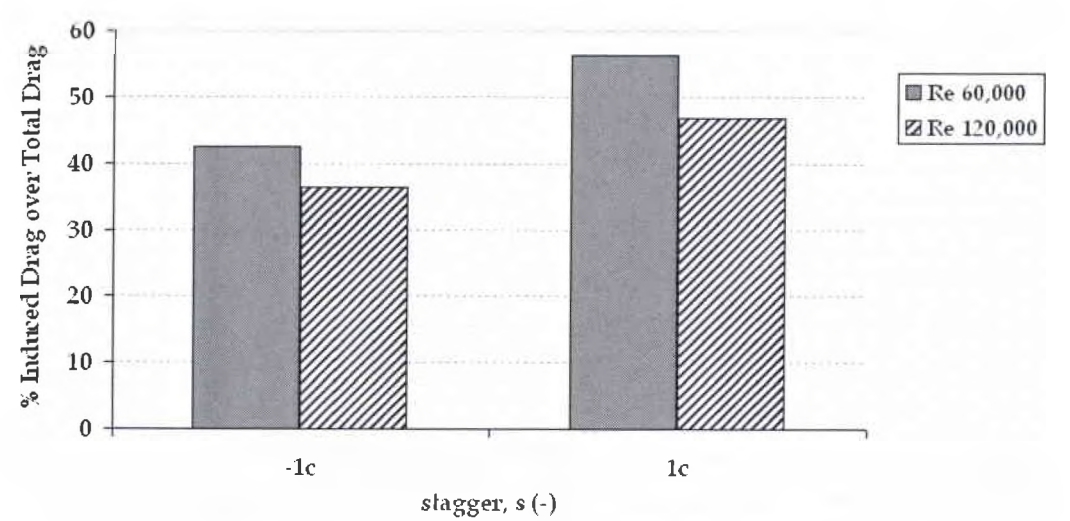

Figure 4.25: Shows the Induced Drag over Total Drag Ratio with varying stagger and constant gap of 2c at both Reynolds numbers of 60,000 and 120,000

It can be seen that the ratio induced drag over total drag of the positive stagger model is higher than the one with negative stagger at both Reynolds numbers.

4.3 Wind Tunnel Balance Data – Similar Stagger Models

In this section the effect of gap on the performance of the biplane joined at the tips will be presented. For this analysis, data from models having similar stagger will be presented to better understand the behaviour of such changes in gap. The aerodynamic performance analyzed will essentially be the lift coefficient, the drag polar, and the aerodynamic efficiency of the different models. In Table 2.2 it can be seen that there are five different stagger configurations, from s = -1.5c to s = 1.5c. In this section the effect of gap will be analyzed considering only two different stagger configurations: models having stagger 0c and the models having

stagger -1c. At the end of each section, results referenced to all the other configurations will be presented.

4.3.1 Stagger 0c

Summary

In the LSWT, an α sweep from -2° to 25° in steps of 0.25° was performed on the models having similar stagger, s=0c, at two different speeds: $\mathrm{Re} = 60{,}000\ (\approx 9 m/s)$, $\mathrm{Re} = 120{,}000\ (\approx 18 m/s)$.

Lift Coefficient

Figure 4.26 plots the lift coefficient, C_L vs. α for models having stagger 0c at Reynolds number 60,000.

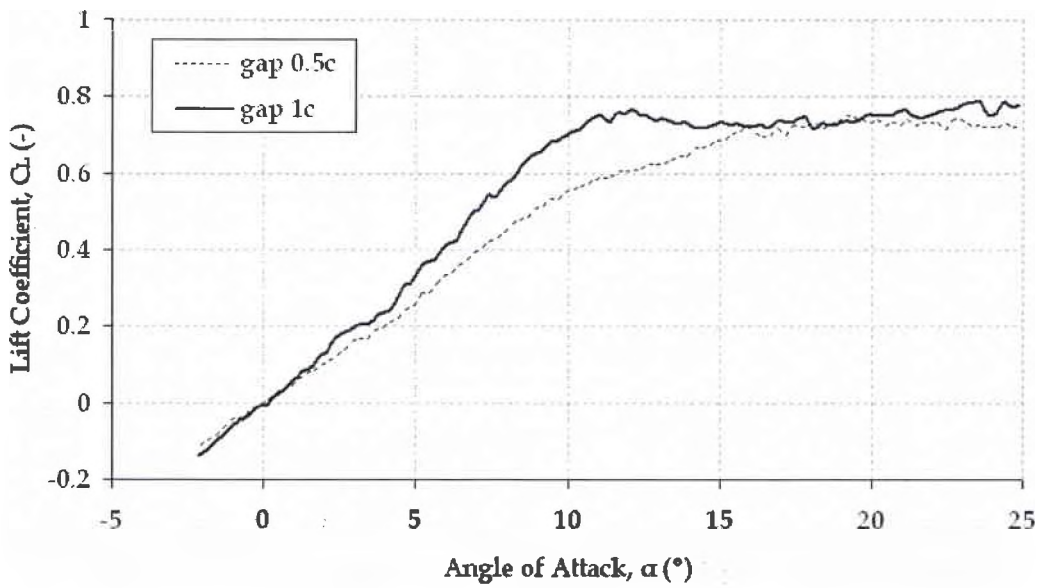

Figure 4.26: Comparison of Lift Curve with varying gap and constant stagger of 0c at Re=60,000

It can be seen that the lift coefficient increases mostly linearly until an angle of attack around 12°. The model with higher gap shows typical stall behavior, instead the model with lower gap does not show a clear stall break in the range of angle of attack considered. This means that low gap is a favourable condition for obtaining no stall. When the gap is higher, the interference between the two wings is less important and this yields a more common stall behavior. Taking a look now at the lift slope it can be seen that it increases when the gap increases. Values of lift slope in the range of angle of attack between -2° and 8° are shown in Table 4.16 and Table 4.17 at two Reynolds numbers 60,000 and 120,000. The comparison between the different models is expressed in terms of a percentage which is referenced to the model having a gap of 0.5c.

Table 4.16: Lift Slope for models having s=0c at Re 60,000

Models		Speed	Lift Slope	% Variation
Gap	Stagger	Re (-)	$C_{L\alpha}$ (-)	
0.5c	0c	60,000	0.0550	0.00
1c		60,000	0.0693	26.06

Table 4.17: Lift Slope for models having g=1c at Re 120,000

Models		Speed	Lift Slope	% Variation
Gap	Stagger	Re (-)	$C_{L\alpha}$ (-)	
0.5c	0c	120,000	0.0553	0.00
1c		120,000	0.0708	28.07

The lift slope of the model having gap g=1c is always higher than the lift slope of the model having gap g = 0.5 at both Reynolds numbers. The variation of lift slope is almost the same in both cases.

Aerodynamic Efficiency

Figure 4.27 and Figure 4.28 plot the aerodynamic efficiency, or lift over drag ratio vs. α for models with stagger 0c at Reynolds number 60,000 and Re 120,000.

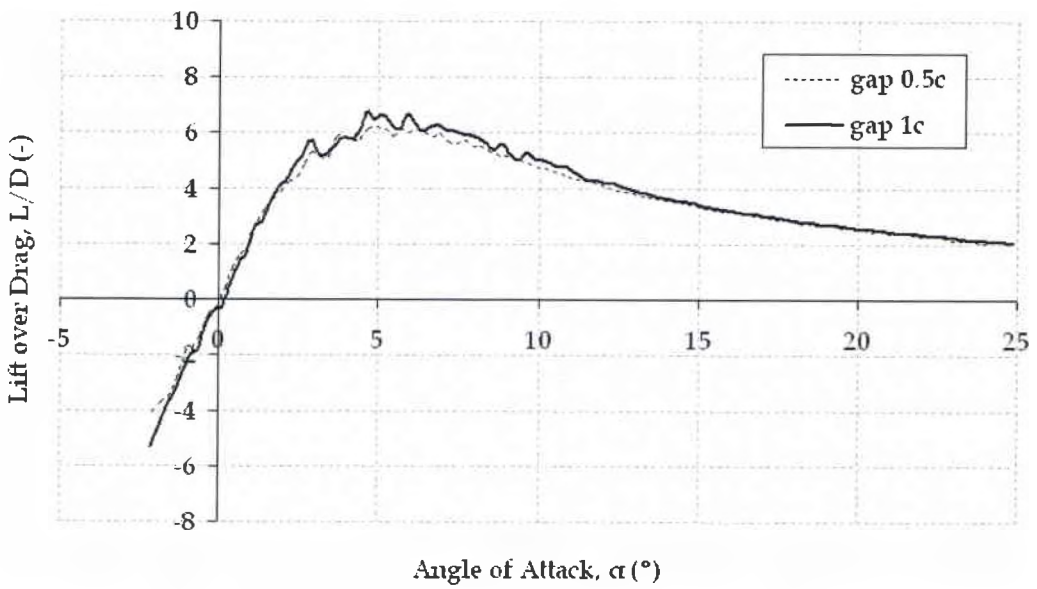

Figure 4.27: Comparison of Lift over Drag Ratio with varying gap and constant stagger of 0c at Re=60,000

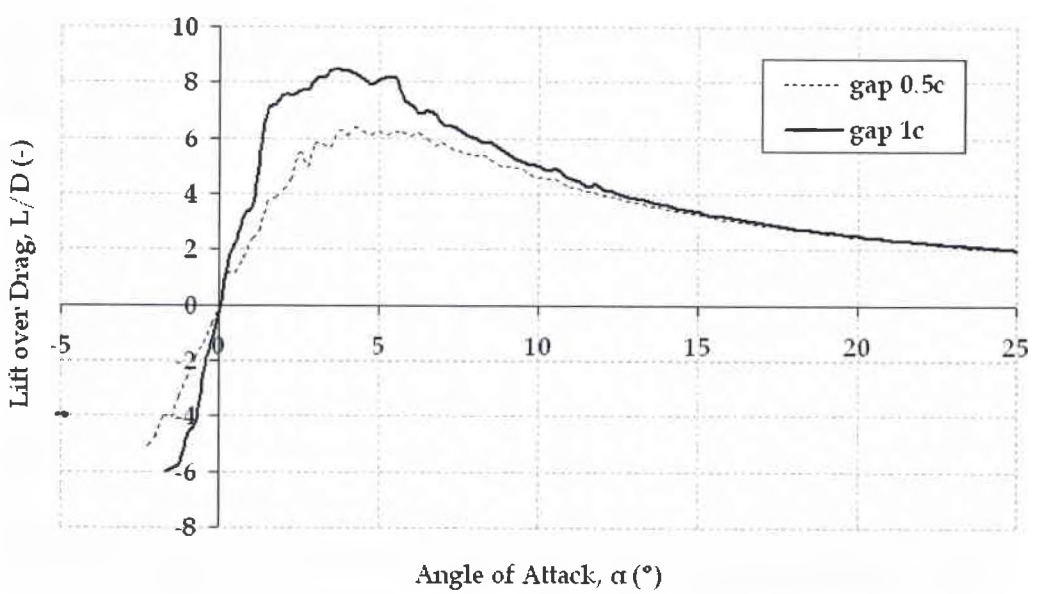

Figure 4.28: Comparison of Lift over Drag Ratio with varying gap and constant stagger of 0c at Re=120,000

It can be seen from the graphs of aerodynamic efficiency vs. angle of attack at Re 60,000 and Re 120,000 that models with larger gap experience higher lift over drag ratio. At higher Reynolds number this effect becomes important and it can be seen in Table 4.18 where the variation of aerodynamic efficiency is referenced to the model with stagger s = 0c:

Table 4.18: Integrated Lift over Drag Ratio for models having s=0c at Re 120,000

Model		Speed	Integrated Lift over Drag Ratio	Speed	Integrated Lift over Drag Ratio
Gap	Stagger	Re (-)	% Variation	Re (-)	% Variation
0.5c	0c	60,000	0.00	120,000	0.00
1c		60,000	1.48	120,000	34.92

At Re 120,000 the integrated lift over drag ratio of the model having gap g=1c is almost 35% higher than the integrated lift over drag ratio of the model with gap g=0.5c. This variation at Re 60,000 is equal to just 1.5%. This means that in terms of aerodynamic efficiency, the effect of changing the gap at higher Reynolds numbers is more important than the same effect at lower Reynolds numbers.

Drag Polar

Figure 4.29 and Figure 4.30 plot the drag polar, C_D vs. C_L, for the models having stagger s=0c at two different Reynolds number 60,000 and 120,000.

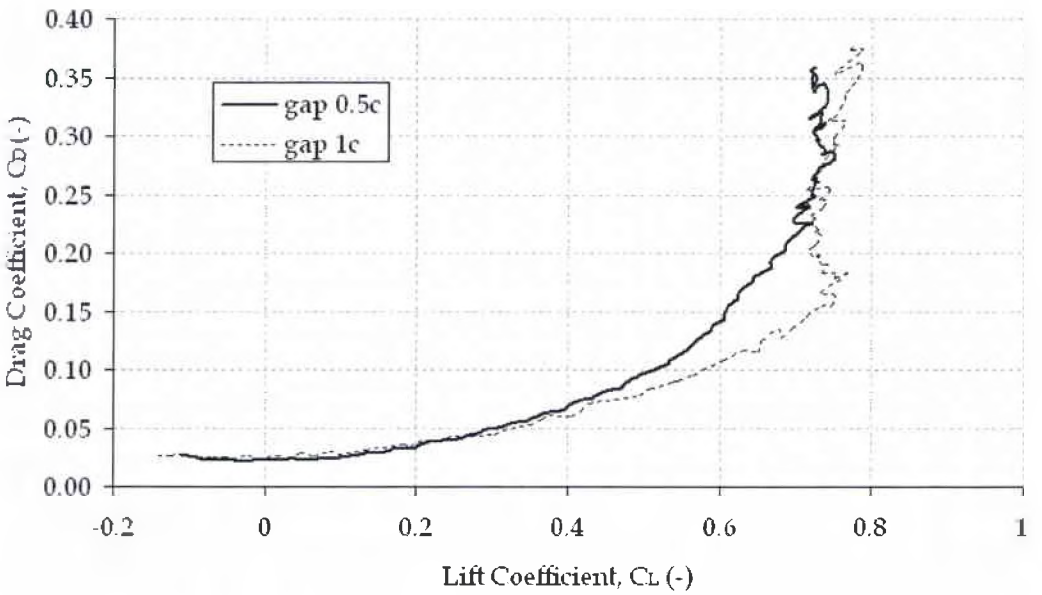

Figure 4.29: Comparison of Drag Polar with varying gap and constant stagger of 0c at Re=60,000

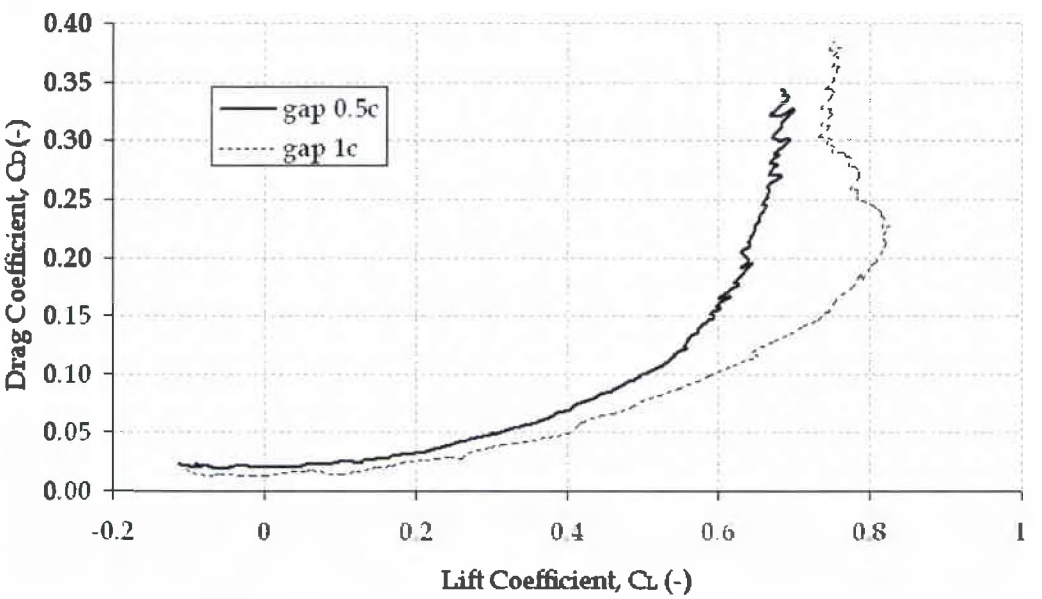

Figure 4.30: Comparison of Drag Polar with varying gap and constant stagger of 0c at Re=120,000

The drag polar is different at the two Reynolds numbers. This difference can be evaluated in terms of induced drag over total drag ratio. The values of this ratio are reported in Table 4.19 and Table 4.20 at two different Reynolds numbers.

Table 4.19: Induced Drag over Total Drag Ratio for models having s=0c at Re 60,000

Models		Speed	Drag Coefficients			
Gap	Stagger	Re (-)	C_D (-)	C_{D0} (-)	C_{Di} (-)	$\%C_{Di}/C_D$ (-)
0.5c	0c	60,000	0.041	0.022	0.019	46.03
1c		60,000	0.045	0.024	0.021	47.13

Table 4.20: Induced Drag over Total Drag Ratio for models having s=0c at Re 120,000

Models		Speed	Drag Coefficients			
Gap	Stagger	Re (-)	C_D (-)	C_{D0} (-)	C_{Di} (-)	$\%C_{Di}/C_D$ (-)
0.5c	0c	120,000	0.034	0.019	0.014	42.38
1c		120,000	0.029	0.013	0.016	56.25

It can be seen from Figure 4.29 and Figure 4.30, and from Table 4.19 and Table 4.20 that at Re 60,000 the gap has marginal effect on the induced drag. But at Re 120,000 it can be seen that model with gap g = 0.5 experiences less induced drag than the model with gap g = 1c.

4.3.2 Stagger -1c

Summary

In the LSWT, an α sweep from -2° to 25° in steps of 0.25° was performed on models with similar stagger, s = -1c, at two different speeds: Re = 60,000 $(\approx 9 m/s)$, Re = 120,000 $(\approx 18 m/s)$.

Lift Coefficient

Figure 4.31 plots the lift coefficient, C_L, vs. α for models with stagger s = -1c at Reynolds number 60,000.

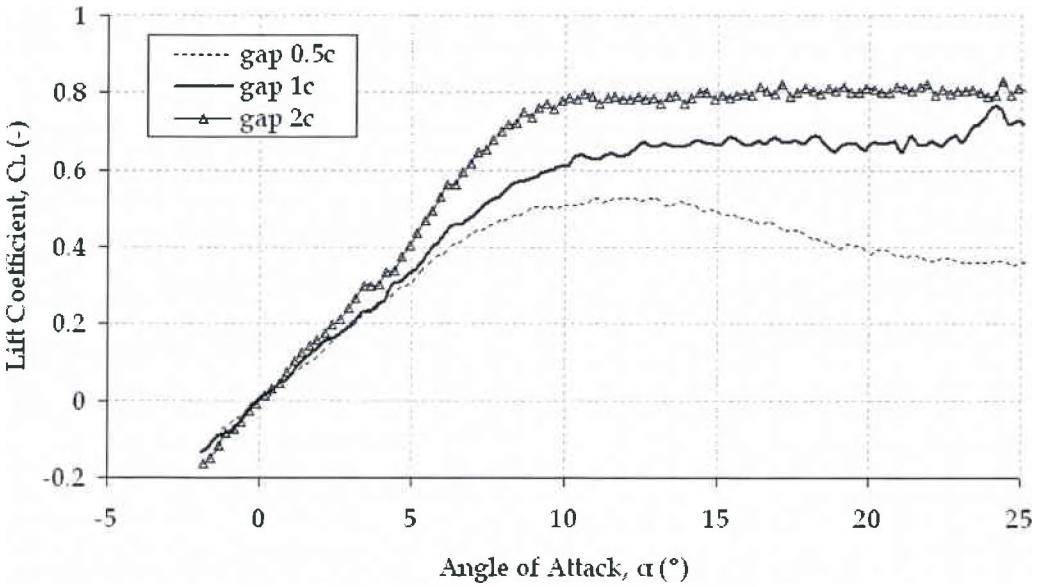

Figure 4.31: Comparison of Lift Curve with varying gap and constant stagger of -1c at Re=60,000

It can be seen that the lift coefficient increases linearly until an angle of attack around 8°. The model with lower gap shows more typical stall behavior, instead the models with higher gap do not show stall in the range of angle of attack considered. Taking a look at the lift slope it can be seen that it increases when the gap increases. Values of lift slope in the range of angle of attack between -2° and 8° are shown in Table 4.21 and Table 4.22 at two Reynolds numbers 60,000 and 120,000. The comparison between the different models is expressed in terms of a percentage which is referenced to the model with gap g = 0.5c

Table 4.21: Lift Slope for models having s=-1c at Re 60,000

Models		Speed	Lift Slope	% Variation
Gap	Stagger	Re (-)	$C_{L\alpha}$ (-)	
0.5c	-1c	60,000	0.0613	0.00
1c		60,000	0.0693	12.99
2c		60,000	0.0881	43.71

Table 4.22: Lift Slope for models having s=-1c at Re 120,000

Models		Speed	Lift Slope	% Variation
Gap	Stagger	Re (-)	$C_{L\alpha}$ (-)	
0.5c	-1c	120,000	0.0598	0.00
1c		120,000	0.0690	15.27
2c		120,000	0.0875	46.17

Figure 4.32 plots the variation of lift slope vs. gap at both Reynolds numbers.

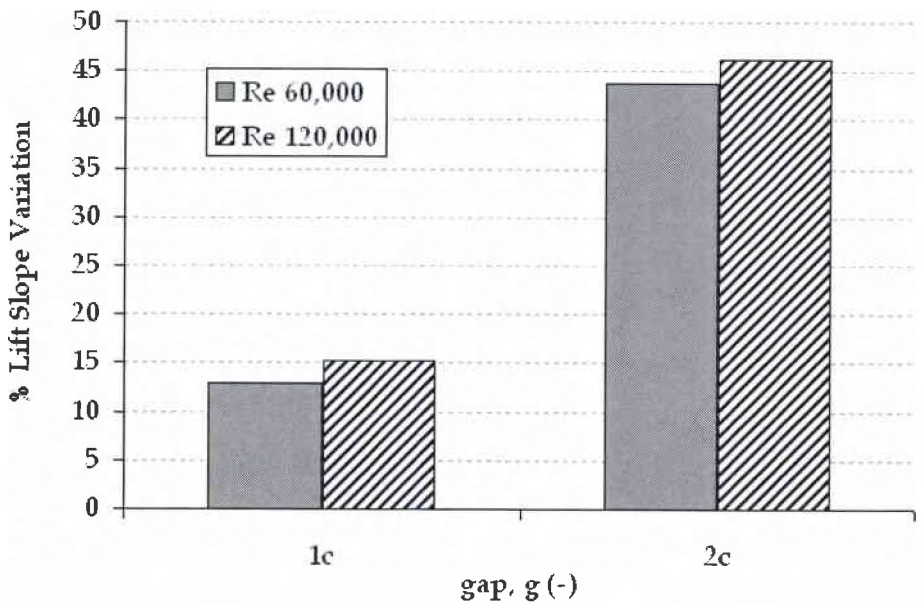

Figure 4.32: Shows the Lift Slope Variation with varying gap and constant stagger of -1c at both Reynolds numbers of 60,000 and 120,000

The lift slope is increasing by almost 15% with each 0.5c gap increment. Higher gap models experience higher lift slope. This variation of lift slope is slightly higher at higher Reynolds numbers.

Aerodynamic Efficiency

Figure 4.33 and Figure 4.34 plot the aerodynamic efficiency, or lift over drag ratio, L/D vs. α for the models having stagger s = -1c at Reynolds number 60,000 and Re 120,000.

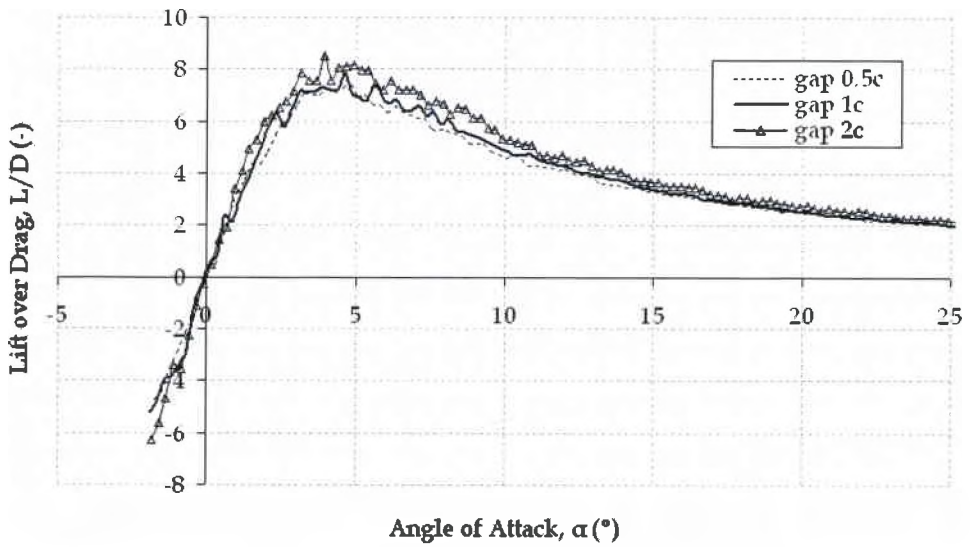

Figure 4.33: Comparison of Lift over Drag Ratio with varying gap and constant stagger of -1c at Re=60,000

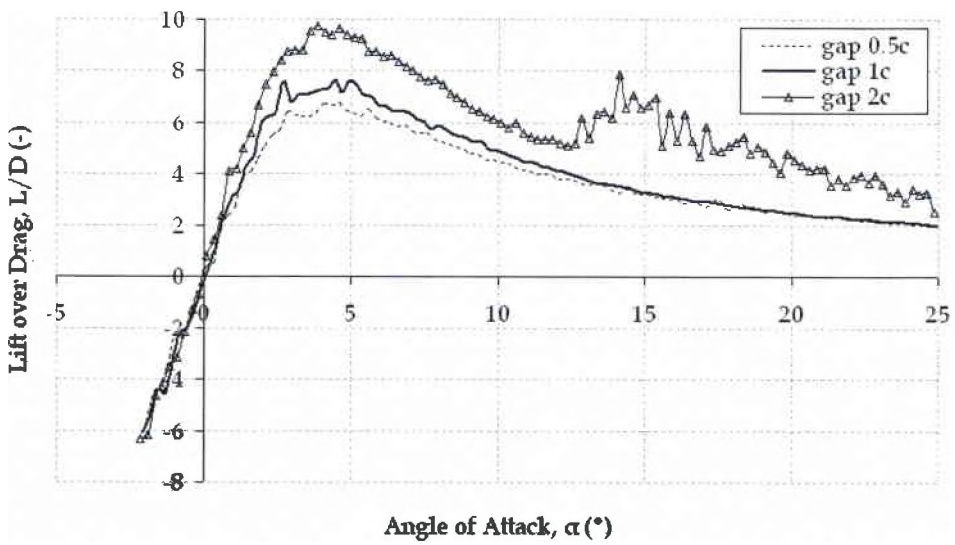

Figure 4.34: Comparison of Lift over Drag Ratio with varying gap and constant stagger of -1c at Re=120,000

It can be seen from the graphs of aerodynamic efficiency vs. angle of attack at Re 60,000 and Re 120,000 that models with larger gap experience higher lift over drag ratio. In Figure 4.34 it can be seen that the model with stagger s = -1c and gap g = 2c produces very noisy data. During the test large vibration were observed. It is believed that this may be stall flutter. At higher Reynolds number this effect becomes important and it can be seen in Table 4.23 where the variation of aerodynamic efficiency referenced to the model with stagger s = -1c is reported:

Table 4.23: Integrated Lift over Drag Ratio for models having s=-1c at Re 120,000

Model		Speed	Integrated Lift over Drag Ratio	Speed	Integrated Lift over Drag Ratio
Gap	Stagger	Re (-)	% Variation	Re (-)	% Variation
0.5c	-1c	60,000	0.00	120,000	0.00
1c		60,000	0.80	120,000	8.47
2c		60,000	11.70	120,000	38.78

At Re 120,000 the integrated lift over drag ratio of the model with gap 1c is almost 9% higher than the integrated lift over drag ratio of the model with gap 0.5c. The variation of integrated lift over drag ratio becomes equal to almost 40% when comparing the model with gap 2c to the model with gap 0.5c. This variation at Re 60,000 is equal to just 0.8% for the model with gap 1c and almost 12% for the one with gap 2c. This means that in terms of aerodynamic efficiency, the effect of changing the gap at higher Reynolds numbers is more important than the same effect at lower Reynolds numbers. The same result was obtained when considering models with no stagger and different gap configurations. Figure 4.35 plots the variation of integrated aerodynamic efficiency for models with stagger -1c.

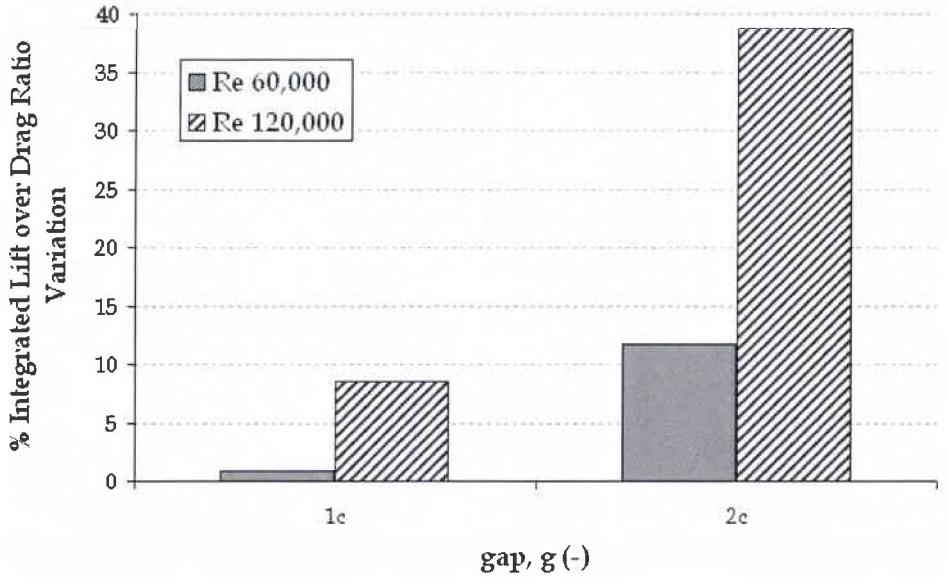

Figure 4.35: Shows the Integrated Lift over Drag Variation with varying gap and constant stagger of -1c at both Reynolds numbers of 60,000 and 120,000

Drag Polar

Figure 4.36 plots the drag polar, C_D vs. C_L, for the models having stagger s=-1c at Reynolds number 60,000.

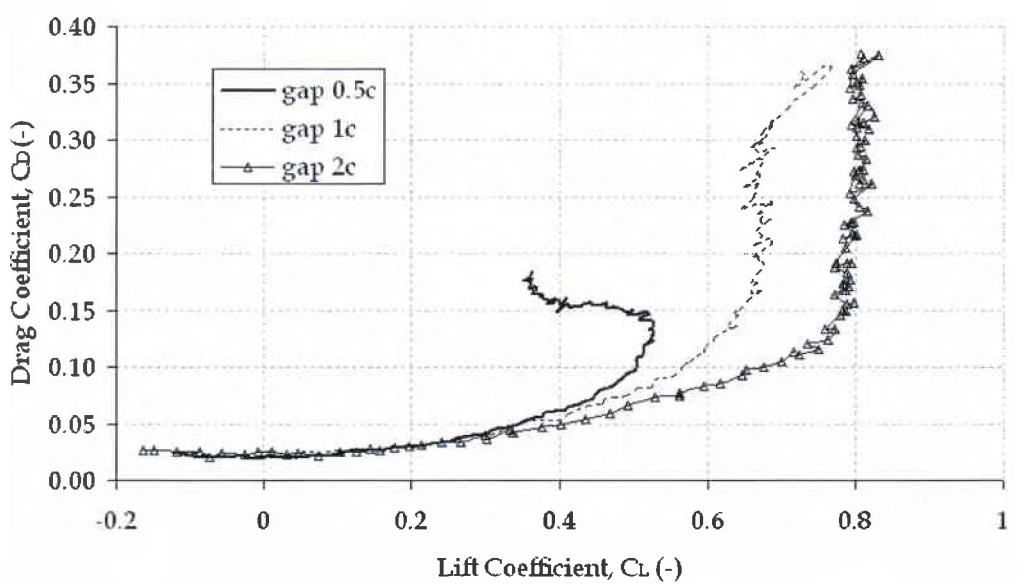

Figure 4.36: Comparison of Drag Polar with varying gap and constant stagger of -1c at Re=60,000

It can be seen that models with higher gap perform better than the model with lower gap in terms of induced drag. Table 4.24 and Table 4.25 show the induced drag over total drag ratio at both Reynolds numbers for models with stagger s = -1c.

Table 4.24: Induced Drag over Total Drag Ratio for models having s=-1c at Re 60,000

Models		Speed	Drag Coefficients			
Gap	Stagger	Re (-)	C_D (-)	C_{D0} (-)	C_{Di} (-)	$\%C_{Di}/C_D$ (-)
0.5c	-1c	60,000	0.040	0.019	0.021	53.04
1c		60,000	0.039	0.019	0.020	51.37
2c		60,000	0.036	0.020	0.015	42.44

Table 4.25: Induced Drag over Total Drag Ratio for models having s=-1c at Re 120,000

Models		Speed	Drag Coefficients			
Gap	Stagger	Re (-)	C_D (-)	C_{D0} (-)	C_{Di} (-)	$\%C_{Di}/C_D$ (-)
0.5c	-1c	120,000	0.039	0.018	0.021	53.68
1c		120,000	0.041	0.021	0.020	48.74
2c		120,000	0.031	0.020	0.011	36.44

The ratio of induced drag over total drag has been plotted versus gap in Figure 4.37 at both Reynolds numbers.

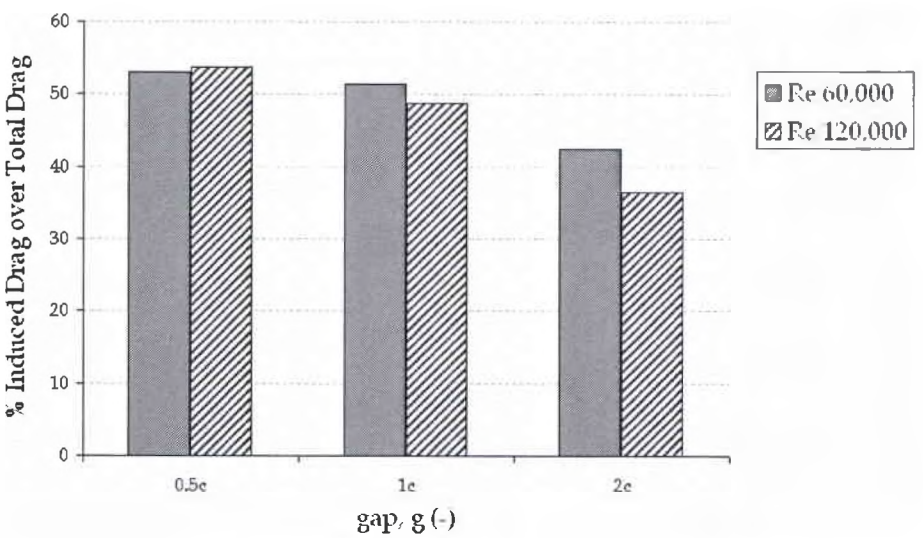

Figure 4.37: Shows the Induced Drag over Total Drag Ratio with varying gap and constant stagger of -1c at both Reynolds numbers of 60,000 and 120,000

Changing Reynolds number, the induced drag over total drag ratio is almost the same and it decreases when the gap increases.

4.4 Wind Tunnel Balance Data – Positive Versus Negative Stagger

In this section the effect of changes from positive to negative stagger on the performance of the biplane joined at the tips will be presented. For this analysis, data from models having similar gap will be presented to better understand the behaviour of such changes in stagger from a positive to a negative value. The aerodynamic performance analyzed will essentially be the lift coefficient, the drag polar, and the aerodynamic efficiency of the different models. The model with the highest change in aerodynamic performance compared to the one with same gap but opposite stagger direction, should be the model with the lowest gap where the interferences of the two wings are higher, such that the positive stagger configuration should show different behavior than the negative stagger configuration. In this section the effect of changes in stagger will be analyzed considering only two different models having similar gap g = 0.5c and two stagger configurations: the models having stagger s = -1c and the models having stagger s = 1c.

4.4.1 Gap 0.5c , Stagger ±1c

Summary

In the LSWT, an α sweep from -2° to 25° in steps of 0.25° was performed on the models having similar gap, g = 0.5c, and opposite stagger direction, s=±1c at two different speeds: Re = 60,000 $(\approx 9m/s)$, Re = 120,000 $(\approx 18m/s)$.

Lift Coefficient

Figure 4.38 plots the lift coefficient, C_L, vs. α for the models having stagger s=±1c at Reynolds number 60,000.

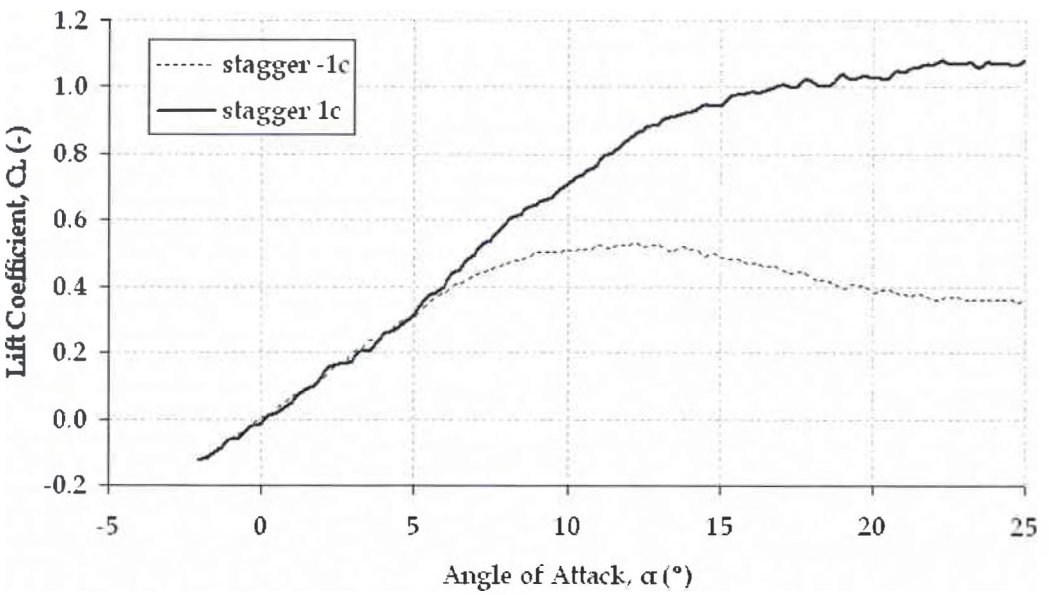

Figure 4.38: Comparison of Lift Curve positive vs. negative stagger and constant gap of 0.5c at Re=60,000

It can be seen that the model with positive stagger shows a higher lift coefficient in the entire range of angle of attack. The model with negative stagger shows the typical stall behavior, instead the model with positive stagger does not

show the stall in the range of angle of attack considered, and the lift coefficient increases linearly until an angle of attack around 12°. This means that positive stagger is a favourable condition for obtaining no stall. Taking a look at the lift slope it can be seen that it increases when the gap increases. Table 4.26 and Table 4.27 show the values of lift slope in the range of angle of attack between -2° and 8° at two Reynolds numbers 60,000 and 120,000. The comparison between the different models is expressed in terms of a percentage which is referenced to the model having negative stagger s = -1c.

Table 4.26: Lift Slope for models having g=0.5c, s=±1c at Re 60,000

Models		Speed	Lift Slope	% Variation
Gap	Stagger	Re (-)	$C_{L\alpha}$ (-)	
0.5c	-1c	60,000	0.0613	0.00
	1c	60,000	0.0701	14.41

Table 4.27: Lift Slope for models having g=0.5c, s=±1c at Re 120,000

Models		Speed	Lift Slope	% Variation
Gap	Stagger	Re (-)	$C_{L\alpha}$ (-)	
0.5c	-1c	120,000	0.0598	0.00
	1c	120,000	0.0693	15.81

The lift slope of the model with positive stagger s = 1c is always higher than the lift slope of the model with negative stagger s = -1c at both Reynolds numbers, and the variation of lift slope is almost the same in both cases and equal to ~15%.

Aerodynamic Efficiency

Figure 4.39 plots the aerodynamic efficiency, or lift over drag ratio, L/D, vs. α for the models having similar gap g=0.5c and two different stagger configurations s=-1c and s=1c at Reynolds number 60,000.

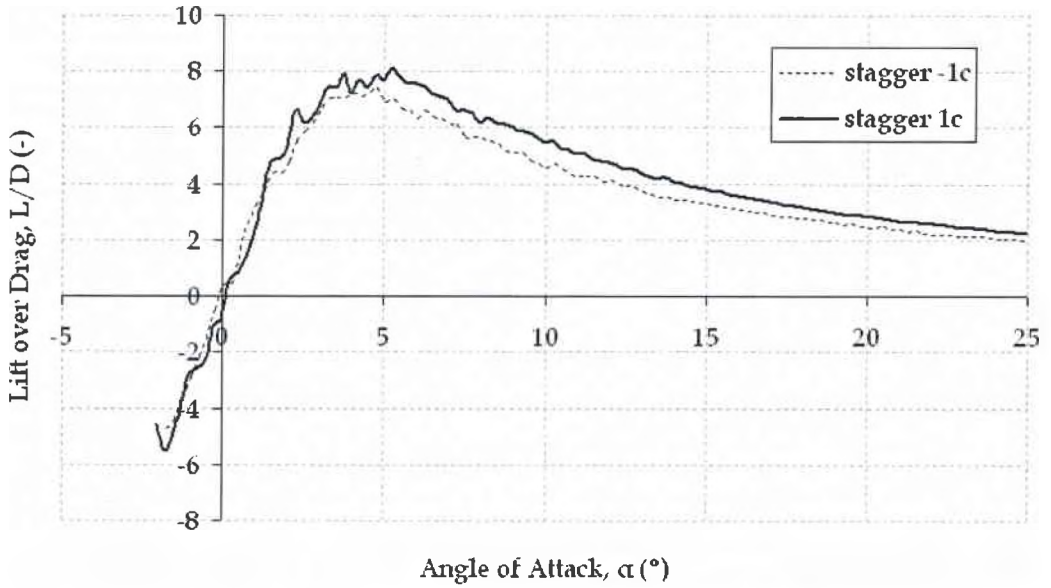

Figure 4.39: Comparison of Lift over Drag Ratio positive vs. negative stagger and constant gap of 0.5c at Re=60,000

It can be seen from the graph in Figure 4.33 of aerodynamic efficiency vs. angle of attack at Re 60,000 that the model with positive stagger experiences a higher lift over drag ratio. Table 4.28 shows the variation of aerodynamic efficiency referenced to the model with negative stagger at both Reynolds numbers:

Table 4.28: Integrated Lift over Drag Ratio for models having g=0.5c, s=±1c

Model		Speed	Integrated Lift over Drag Ratio	Speed	Integrated Lift over Drag Ratio
Gap	Stagger	Re (-)	% Variation	Re (-)	% Variation
0.5c	-1c	60,000	0.00	120,000	0.00
	1c	60,000	5.47	120,000	18.32

At Re 120,000 the integrated lift over drag ratio of the model having positive stagger is almost 18% higher than the integrated lift over drag ratio of the model with negative stagger. This variation at Re 60,000 is equal to almost 5.5%. This means that in terms of aerodynamic efficiency, models with positive stagger are

more efficient than models with negative stagger and that this behavior, and that this effect becomes more important at higher Reynolds numbers.

Drag Polar

Figure 4.40 plots the drag polar, C_D vs. C_L, for models having gap g = 0.5c and opposite stagger configuration at Reynolds number 60,000.

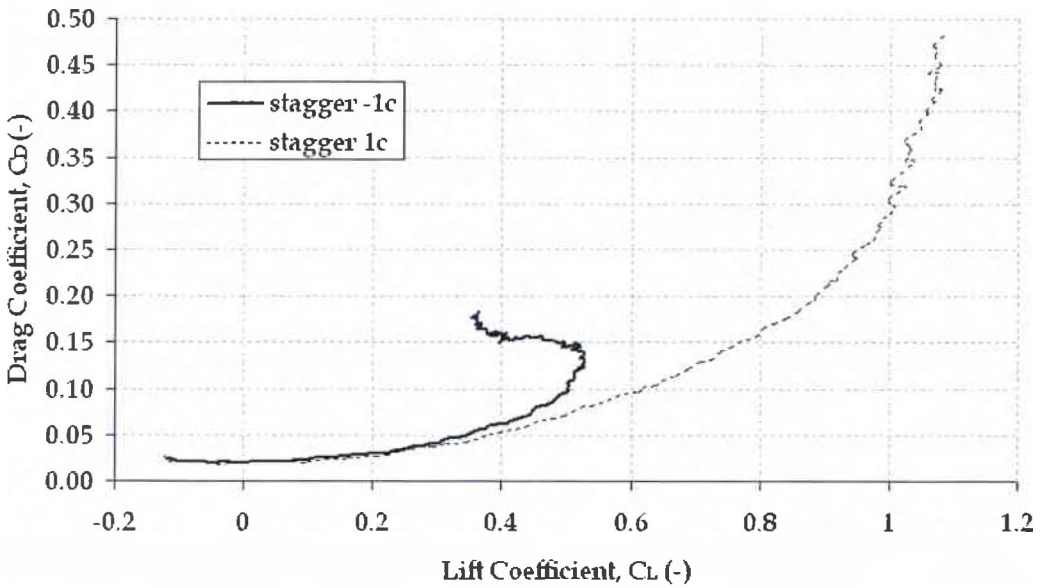

Figure 4.40: Comparison of Drag Polar positive vs. negative stagger and constant gap of 0.5c at Re=60,000

The drag polar in Figure 4.40 shows how models with positive stagger have higher drag compared to models with negative stagger. This difference can be evaluated in terms of induced drag over total drag ratio. The values of this ratio are reported in Table 4.29 and Table 4.30 at two different Reynolds numbers.

Table 4.29: Induced Drag over Total Drag Ratio for models having g=0.5c, s=±1c at Re 60,000

Models		Speed	Drag Coefficients			
Gap	Stagger	Re (-)	C_D (-)	C_{D0} (-)	C_{Di} (-)	$\%C_{Di}/C_D$ (-)
0.5c	-1c	60,000	0.040	0.019	0.021	53.04
	1c	60,000	0.042	0.018	0.024	57.38

Table 4.30: Induced Drag over Total Drag Ratio for models having g=0.5c, s=±1c at Re 120,000

Models		Speed	Drag Coefficients			
Gap	Stagger	Re (-)	C_D (-)	C_{D0} (-)	C_{Di} (-)	$\%C_{Di}/C_D$ (-)
0.5c	-1c	120,000	0.041	0.021	0.020	48.74
	1c	120,000	0.043	0.018	0.025	57.67

It can be seen from Figure 4.40 and from Table 4.29 and Table 4.30 that models with positive stagger always have higher induced drag over total drag ratio. Also, it can be seen that models with positive stagger do not change their induced drag over total drag ratio at higher Reynolds numbers, meaning that the effect of Reynolds number is less important in models with positive stagger. The opposite behavior can be seen for models with negative stagger where this ratio decreases when the Reynolds number increases.

4.5 Wind Tunnel Balance Data – Change in Lift Slope

The plot of lift coefficient, C_L, vs. angle of attack, α, in the linear regime (angle of attack between -2° and 8°) shows a change in the slope of the curve around 5° angle of attack for all the models tested in the LSWT at both Reynolds numbers. This section will provide a quantitative aspect to this analysis, showing different approaches followed for obtaining the variation in lift slope and how big this variation is compared to parameters such as stagger, gap, and angle of stagger. This section will also try to answer the question as to why this variation occurs and how the variation can be predicted and studied in future work.

Summary

In the LSWT, an α sweep from -2° to 8° in steps of 0.25° was performed on the fourteen models at two different speeds: $\mathrm{Re} = 60{,}000$ $(\approx 9 m/s)$, $\mathrm{Re} = 120{,}000$ $(\approx 18 m/s)$. Plotting lift coefficient as a function of angle of attack, a change in lift slope can be observed. The same change in lift slope was observed in previous experiments conducted on biplanes. In 1929, M. Knight and R. Noyes published a report on tests conducted on a series of biplanes, showing the effect of changes in stagger, and gap [12] [13] [14]. Using their data at Re 150,000 the change in lift slope observed was equal to almost 9% and it occurs around 0° angle of attack.

A more recent work, conducted in 2007 by D. N. Killian [20] on a biplane joined at the tips by endplates, shows a change in lift slope at Re 60,000 of almost 25% and it occurs around 2° angle of attack.

In this section of the paper, the change in the lift slope will be quantified and an hypothesis will be elaborated, using the LSWT data. There are two methods used to compute the lift slope. The graphs will be shown in this paragraph and they will allow the reader to better understand the process by which obtaining the lift slope is made possible. The two methods have been applied to all fourteen models but in this paper the model that shows the greatest change in slope will be the only one considered. This model is the model with gap g=0.5c and stagger s=1c at Re 60,000. Tables at the end of the paragraph will present the results for all fourteen models.

First Method

The first method consists of plotting the entire curve of C_L vs. α in a range of angle of attack between -2° and 8°. Then the slope has been computed across the entire range of angle of attack. Figure 4.41 shows C_L vs. α in the range of angle of attack between -2° and 8° for the model having gap g = 0.5c and stagger s = 1c at Re 60,000 and it also shows the linear curve of lift coefficient vs. angle of attack with the equation of the curve.

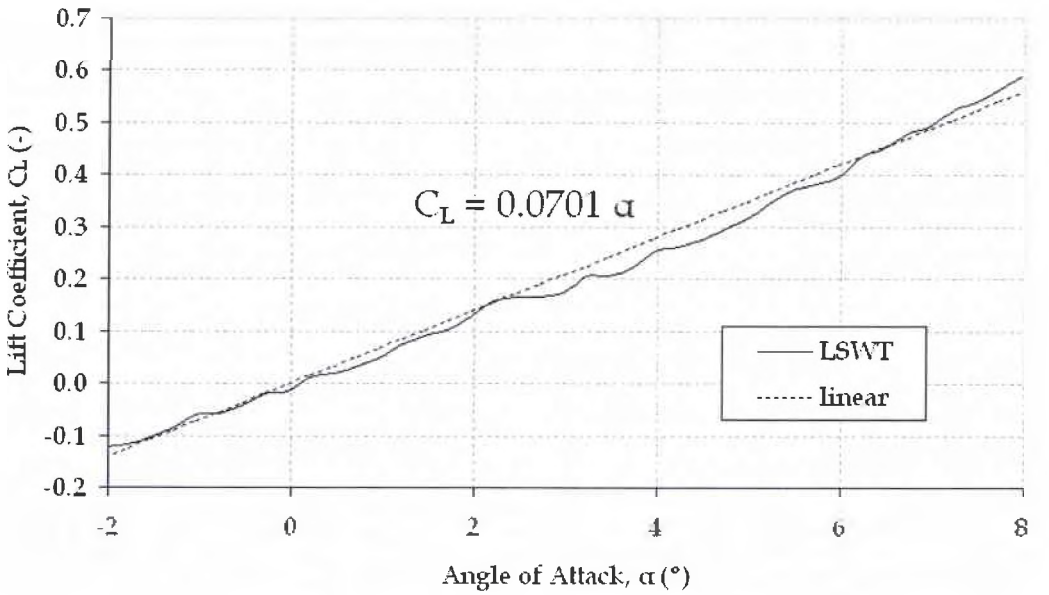

Figure 4.41: Lift Curve and linear curve in the entire region of angle of attack from -2° to 8° for the model with gap 0.5c and stagger 1c at Re 60,000

Table 4.31 shows the lift slope for the model having gap g = 0.5c and stagger s = 1c at both Reynolds numbers 60,000 and 120,000.

Table 4.31: Lift Slope for model having gap g=0.5c and stagger s=1c, First Method

Model		Speed	Lift Slope, $C_{L\alpha}$ (-)
Gap	Stagger	Re (-)	-2° < α < 8°
0.5c	1c	60,000	0.0701
		120,000	0.0693

Second Method

The second method consists of plotting the entire curve of C_L vs. α in a range of angle of attack between -2° and 8°. From each of these graphs it is possible to recognize a region of transition, where the lift slope changes from one value to another. Eliminating this region of transition, it will be possible to determine a first slope in the region before the transition, and a second slope right after the same

transition. In this method, the slope of the first region will be called first slope and the slope of the second region, second slope.

Figure 4.42 plots lift coefficient vs. angle of attack for the model having gap g = 0.5c and stagger s = 1c at Re 60,000 in the range of angle of attack before the transition, and in the range of angle of attack after the transition. For this model, at Re 60,000 the region of transition occurs between 3.22° and 4.72°.

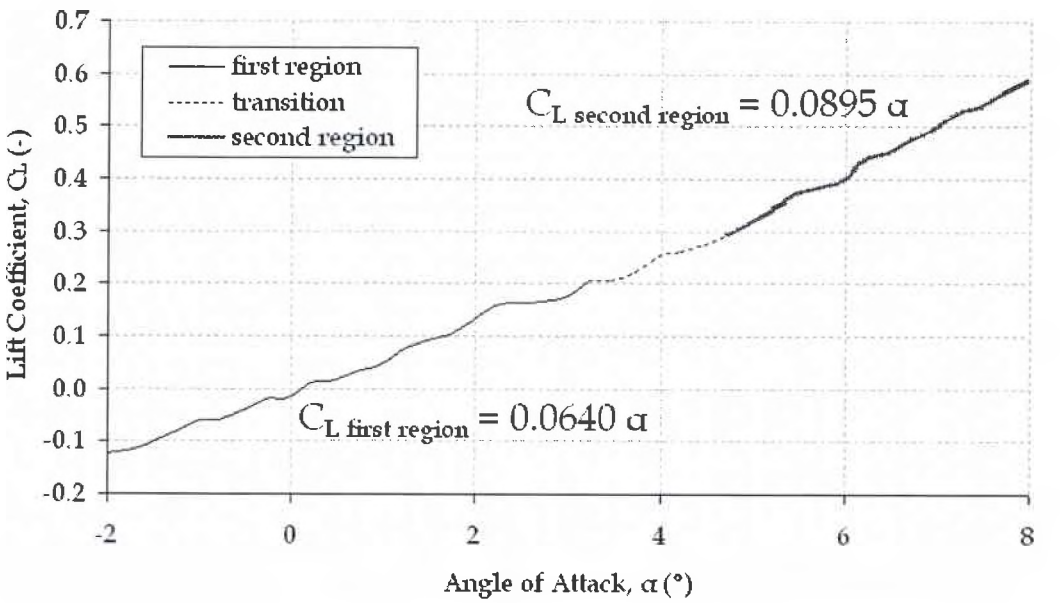

Figure 4.42: Lift Curve in the two different regions of angle of attack before and after the transition for the model with gap 0.5c and stagger 1c at Re 60,000

Then the percentage of change with respect to the first slope has been computed and it is reported in Table 4.32 for both Reynolds numbers.

Table 4.32: Lift Slope for model having gap g=0.5c and stagger s=1c, Second Method

Model		Speed	Lift Slope, $C_{L\alpha}$ (-)	Lift Slope, $C_{L\alpha}$ (-)	% Variation
Gap	Stagger	Re (-)	first slope	second slope	
0.5c	1c	60,000	0.0640	0.0895	39.87
		120,000	0.0660	0.0796	20.57

Using the second method it can be seen that at both Reynolds numbers the lift slope increases after the region of transition. This variation at Re 60,000 is equal to almost 40%, instead at Re 120,000 it is equal to almost 20.6%.

Results

Table 4.33 shows the results of the slopes at Re 60,000 and 120,000 for all fourteen models using the first method.

Table 4.33: Lift Slope all models, First Method, Re 60,000 – 120,000

Model		Speed	Lift Slope	Speed	Lift Slope
Gap	Stagger	Re (-)	$C_{L\alpha}$ (-)	Re (-)	$C_{L\alpha}$ (-)
1c	0c	60,000	0.0708	120,000	0.0693
0.5c	0c	60,000	0.0553	120,000	0.0550
0.5c	0.5c	60,000	0.0625	120,000	0.0634
0.5c	1c	60,000	0.0693	120,000	0.0701
1c	0.5c	60,000	0.0719	120,000	0.0748
1c	1c	60,000	0.0746	120,000	0.0756
2c	1c	60,000	0.0874	120,000	0.0873
1c	1.5c	60,000	0.0786	120,000	0.0803
0.5c	-0.5c	60,000	0.0569	120,000	0.0572
0.5c	-1c	60,000	0.0598	120,000	0.0613
1c	-0.5c	60,000	0.0712	120,000	0.0737
1c	-1c	60,000	0.0690	120,000	0.0693
2c	-1c	60,000	0.0875	120,000	0.0881
1c	-1.5c	60,000	0.0725	120,000	0.0697

The lift slope variation between different models having similar gap or similar stagger was discussed in each section, and reported in Figure 4.3, Figure 4.13, and Figure 4.32. Concerning the second method, Table 4.34 and Table 4.35 show the two lift slopes, first and second slopes, before and after the region of transition, at Re 60,000 and 120,000. The variation in each table represents the

percentage of change in lift slope referenced for each model to the first slope, meaning that positive variation means that the lift slope increases after the transition.

Table 4.34: Lift Slope all models, Second Method, Re 60,000

Model		Speed	Lift Slope $C_{L\alpha}$ (-)	Lift Slope $C_{L\alpha}$ (-)	% Variation
Gap	Stagger	Re (-)	first region	second region	
1c	0c	60,000	0.0631	0.0844	33.76
0.5c	0c	60,000	0.0516	0.0641	24.10
0.5c	0.5c	60,000	0.0591	0.0724	22.43
0.5c	1c	60,000	0.0640	0.0895	39.87
1c	0.5c	60,000	0.0735	0.0877	19.26
1c	1c	60,000	0.0711	0.0910	27.97
2c	1c	60,000	0.0846	0.1054	24.65
1c	1.5c	60,000	0.0777	0.0899	15.76
0.5c	-0.5c	60,000	0.0576	0.0574	-0.42
0.5c	-1c	60,000	0.0639	0.0530	-17.00
1c	-0.5c	60,000	0.0725	0.0812	12.08
1c	-1c	60,000	0.0697	0.0704	1.06
2c	-1c	60,000	0.0845	0.0948	12.19
1c	-1.5c	60,000	0.0719	0.0708	-1.51

Table 4.35: Lift Slope all models, Second Method, Re 120,000

Model		Speed	Lift Slope $C_{L\alpha}$ (-)	Lift Slope $C_{L\alpha}$ (-)	% Variation
Gap	Stagger	Re (-)	first region	second region	
1c	0c	120,000	0.0659	0.0822	24.74
0.5c	0c	120,000	0.0521	0.0677	29.77
0.5c	0.5c	120,000	0.0583	0.0628	7.82
0.5c	1c	120,000	0.0660	0.0796	20.57
1c	0.5c	120,000	0.0647	0.0824	27.35
1c	1c	120,000	0.0690	0.0889	28.82
2c	1c	120,000	0.0795	0.1010	27.07
1c	1.5c	120,000	0.0733	0.0924	25.95
0.5c	-0.5c	120,000	0.0580	0.0483	-16.72
0.5c	-1c	120,000	0.0648	0.0535	-17.35
1c	-0.5c	120,000	0.0666	0.0823	23.46
1c	-1c	120,000	0.0689	0.0642	-6.88
2c	-1c	120,000	0.0835	0.0989	18.43
1c	-1.5c	120,000	0.0716	0.0637	-11.07

To better understand this kind of behavior, a series of different tables were generated, trying to find the causes of this kind of change in the slope. The best comparison found was between the percentage change of lift slope and the angle of stagger, σ, defined before as the angle between the vertical line and the line joining the leading edges of the wings.

Table 4.36 and Table 4.37 show this comparison at Re 60,000 and Re 120,000.

Table 4.36: Lift Slope all models with Angle of Stagger, Second Method, Re 60,000

Model			Speed	Lift Slope $C_{L\alpha}$ (-)	Lift Slope $C_{L\alpha}$ (-)	% Variation
Gap	Stagger	σ (°)	Re (-)	first region	second region	
0.5c	-1c	-63.4	60,000	0.0639	0.0530	-17.00
1c	-1.5c	-56.3	60,000	0.0719	0.0708	-1.51
0.5c	-0.5c	-45	60,000	0.0576	0.0574	-0.42
1c	-1c	-45	60,000	0.0697	0.0704	1.06
1c	-0.5c	-26.6	60,000	0.0725	0.0812	12.08
2c	-1c	-26.6	60,000	0.0845	0.0948	12.19
0.5c	0c	0	60,000	0.0516	0.0641	24.10
1c	0c	0	60,000	0.0631	0.0844	33.76
1c	0.5c	26.6	60,000	0.0735	0.0877	19.26
2c	1c	26.6	60,000	0.0846	0.1054	24.65
0.5c	0.5c	45	60,000	0.0591	0.0724	22.43
1c	1c	45	60,000	0.0711	0.0910	27.97
1c	1.5c	56.3	60,000	0.0777	0.0899	15.76
0.5c	1c	63.4	60,000	0.0640	0.0895	39.87

Table 4.37: Lift Slope all models with Angle of Stagger, Second Method, Re 120,000

Model			Speed	Lift Slope $C_{L\alpha}$ (-)	Lift Slope $C_{L\alpha}$ (-)	% Variation
Gap	Stagger	σ (°)	Re (-)	first region	second region	
0.5c	-1c	-63.4	120,000	0.0648	0.0535	-17.35
1c	-1.5c	-56.3	120,000	0.0716	0.0637	-11.07
0.5c	-0.5c	-45	120,000	0.0580	0.0483	-16.72
1c	-1c	-45	120,000	0.0689	0.0642	-6.88
1c	-0.5c	-26.6	120,000	0.0666	0.0823	23.46
2c	-1c	-26.6	120,000	0.0835	0.0989	18.43
0.5c	0c	0	120,000	0.0521	0.0677	29.77
1c	0c	0	120,000	0.0659	0.0822	24.74
1c	0.5c	26.6	120,000	0.0647	0.0824	27.35
2c	1c	26.6	120,000	0.0795	0.1010	27.07
0.5c	0.5c	45	120,000	0.0583	0.0628	7.82
1c	1c	45	120,000	0.0690	0.0889	28.82
1c	1.5c	56.3	120,000	0.0733	0.0924	25.95
0.5c	1c	63.4	120,000	0.0660	0.0796	20.57

Figure 4.43 shows the percentage change of lift slope by changing the angle of stagger at Re 60,000 and 120,000.

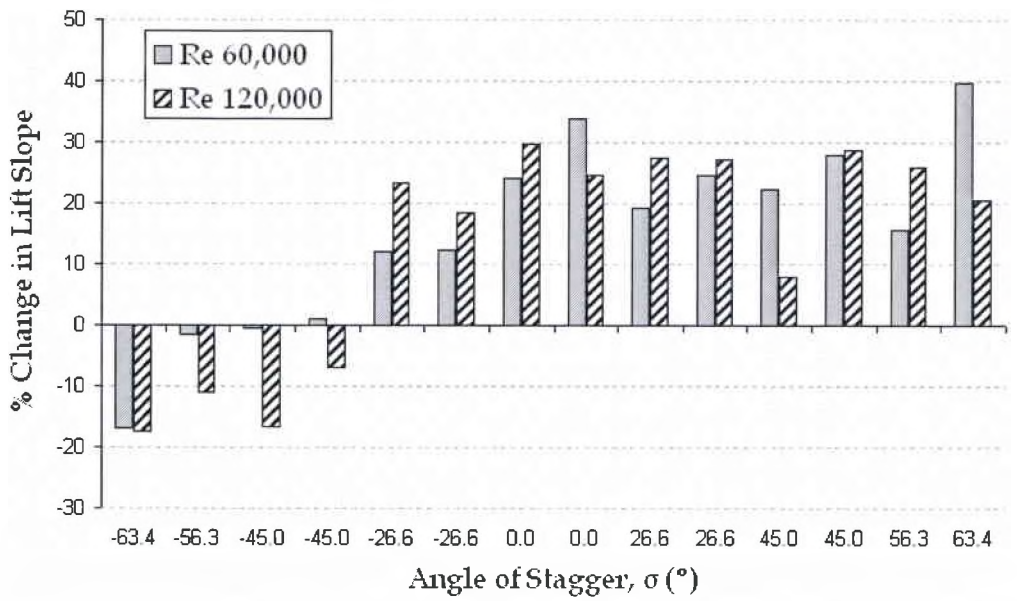

Figure 4.43: Shows the Change in Lift Slope between first and second region varying angle of stagger at both Reynolds numbers of 60,000 and 120,000

It seems that the lift slope decreases in the second region with respect to the first region, while the stagger moves in the negative direction. The largest change in slope is associated with the model having highest angle of stagger and the lowest change in slope is associated with the model having lowest angle of stagger. The only exception is given by the model with angle of stagger $\sigma = 56.3°$, that is the model with g = 1c and s = 1.5c. This model does not follow this trend. But it is still reasonable to lay down an hypothesis concerning the change in the lift slope. It can be possible that with increasing the angle of stagger, which can be realized by decreasing the gap or increasing the stagger, the model experiences a positive change in lift slope. This can be translated into a better span efficiency factor after this change has occurred.

4.6 Wind Tunnel Balance Data – Aerodynamic Hysteresis

Aerodynamic hysteresis of an airfoil refers to airfoil aerodynamic characteristics as it becomes history dependent, i.e., dependent on the sense of change in the angle of attack, near the airfoil stall angle. The coefficients of lift, and drag, of the airfoil are found to be multiple-valued rather than single-valued functions of the angle of attack. Aerodynamic hysteresis is of practical importance because it produces widely different values of lift coefficient and lift over drag ratio for a given angle of attack. It could also affect the recovery from stall conditions [21].

This section reports data obtained in the LSWT on the model with gap g=0.5c and stagger s=-1c at Reynolds numbers 60,000 and 120,000. The α sweep for this analysis is from -2° to 8° in steps of 1°.

Lift Coefficient

Figure 4.44 and Figure 4.45 show the lift coefficient vs. angle of attack for the model with gap g = 0.5c and stagger s = -1c at Re 60,000 and Re 120,000.

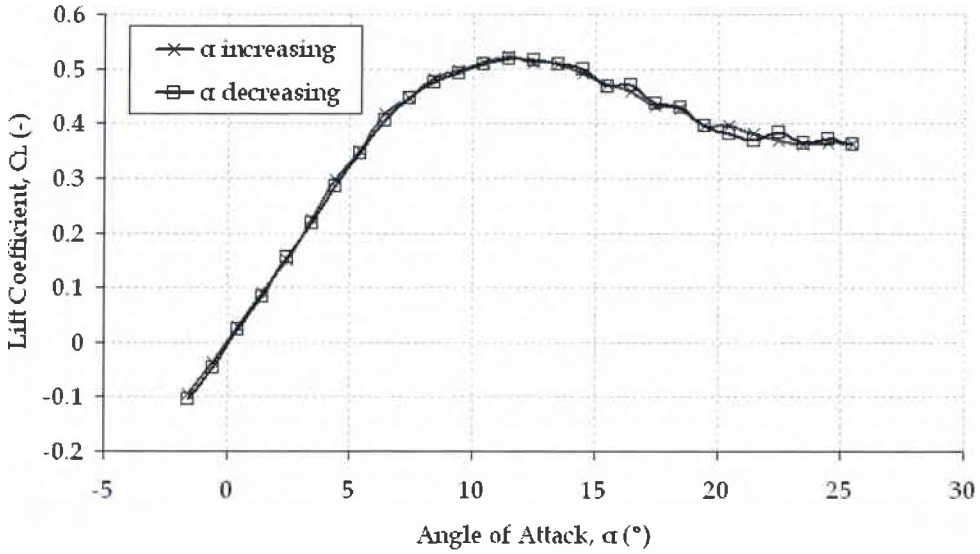

Figure 4.44: Hysteresis Analysis on Lift Curve for the model with gap 0.5c and stagger -1c at Re 60,000

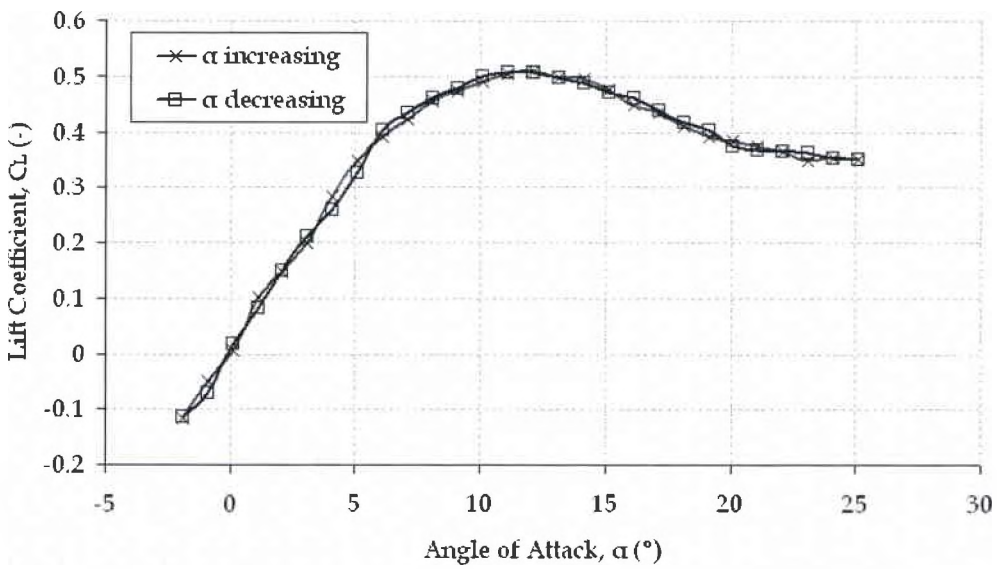

Figure 4.45: Hysteresis Analysis on Lift Curve for the model with gap 0.5c and stagger -1c at Re 120,000

From Figure 4.44 very mild hysteresis of lift coefficient at Re 60,000 can be observed for the angles of attack lying between 16° and 23°. From Figure 4.45 hysteresis of lift coefficient at Re 120,000 can be observed for the angles of attack

lying between 4° and 8°. The difference in hysteresis location can be explained considering the different kind of hysteresis loops that can occur when the flow becomes unsteady [22]. One of the most important parameters affecting the dynamic behavior of an airfoil under unsteady flow is the reduced frequency, defined as:

$$k = \frac{\omega \cdot c}{V_{\infty}}$$

where ω is the frequency of oscillation of the airfoil, c is the chord, and V_{∞} is the freestream velocity. Keeping chord length constant, small reduced frequency means high freestream velocity or small frequency of oscillation. At small angles of attack and relatively small reduced frequencies the airfoil behavior can be treated with a potential flow approach. Accordingly, the viscous effects can be neglected. The boundary layer remains attached and the airfoil generates a sinusoidal wake. The effect of the oscillating wake is to produce a time lag between the actual conditions and the state of the boundary layer. As a result the lift will be in delay, and the characteristic is a closed loop that is described clockwise. This loop can be observed clearly in Figure 4.45 for the angles of attack lying between 3° and 6°. Figure 4.46 shows a hysteresis loop in the range of angle of attack between 3° and 6° for the model with gap g = 0.5c and stagger s = -1c at Re 120,000. The hysteresis loop is clockwise and it occurs before stall.

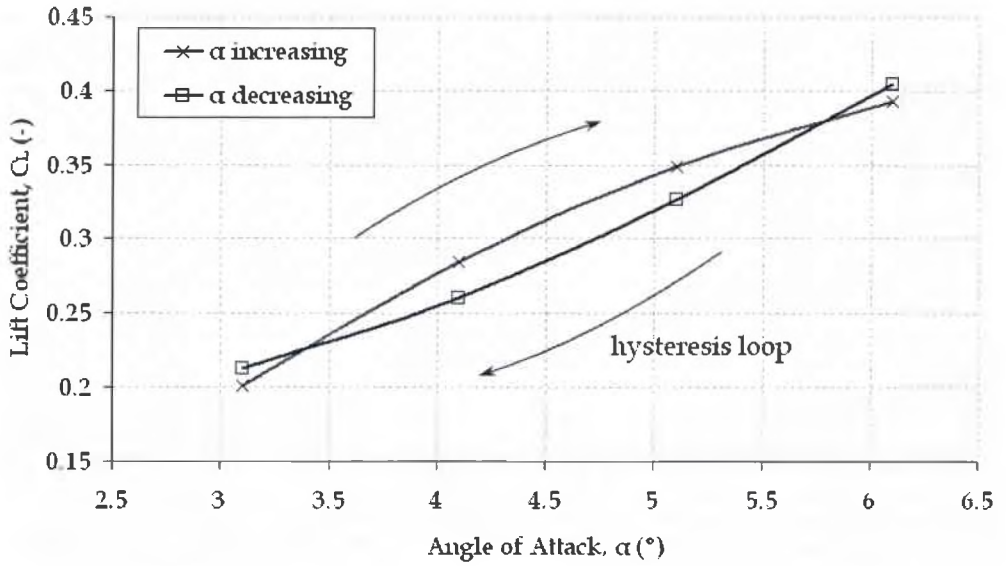

Figure 4.46: Hysteresis Loop in the range of angle of attack between 3° and 6° for the model with gap 0.5c and stagger -1c at Re 120,000

If the oscillation occurs around a mean angle of attack close to C_{Lmax} (static stall) viscous effects become predominant. Starting from the point of minimum incidence, the dynamic lift follows the static lift, until the static lift curve deflects, due to increasing trailing edge separation. The dynamic lift, instead, keeps growing almost linearly until a breakdown occurs. At the breakdown point there is massive flow separation and the lift drops to levels far below those typical of the static curve. It will take some time to recover more regular behavior, but the lift will remain below the static lift for most of the remaining loop. The increase of the lift above the static C_{Lmax} is attributed to the development of a leading edge vortex on the upper surface that grows and travels downstream. The breakdown is associated with the point when the leading edge vortex has travelled past the airfoil trailing edge. The loop is described clockwise.

From Figure 4.44 and Figure 4.45 it can be seen that there is no hysteresis around C_{Lmax}. The last kind of hysteresis loops that can occur is above C_{Lmax}. They are characteristic of a loss of energy (due to viscous dissipation) that is proportional to the area enclosed by the loop and they usually occur at high reduced frequencies, which means low Reynolds numbers. This loop can be observed clearly in Figure 4.44 for the angles of attack lying between 18° and 23°. Figure 4.47 shows a hysteresis loop in the range of angle of attack between 18° and 23° for the model with gap g=0.5c and stagger s=-1c at Re 60,000. The hysteresis loop is clockwise and it occurs after stall.

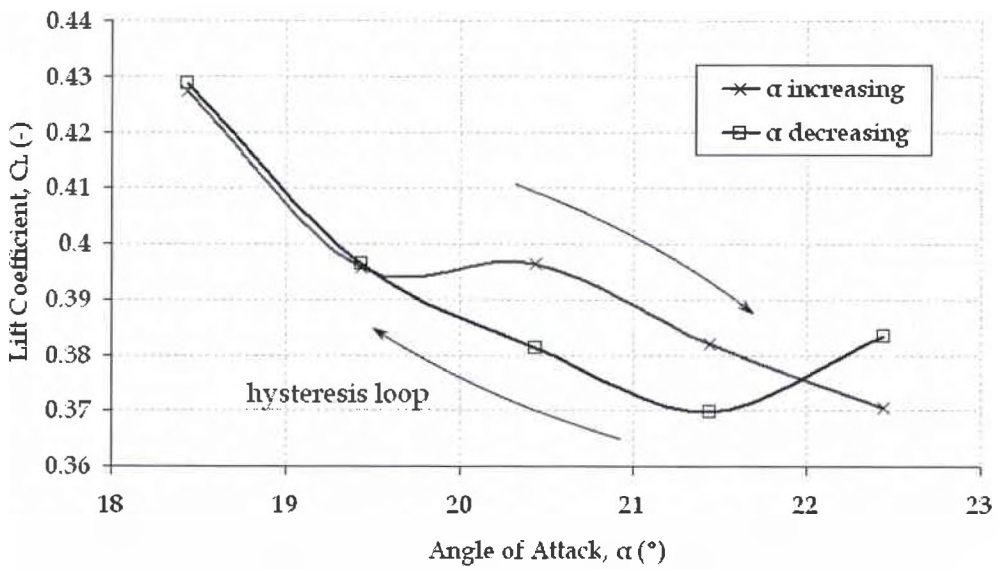

Figure 4.47: Hysteresis Loop in the range of angle of attack between 18° and 23° for the model with gap 0.5c and stagger -1c at Re 60,000

4.7 Comparison Analytical – Experimental Results

Overview

Computational analysis for the biplane configurations was carried out using AVL. This code utilizes a vortex-lattice representation of the lifting surfaces, and it assumes steady, irrotational, inviscid, incompressible attached flow. It predicts lift and induced drag coefficients only in the linear region before stall, and at low freestream velocities. In this section, analytical results of lift coefficients and induced drag coefficients, will be compared to the experimental results.

Lift Coefficient

Once the value of lift coefficient obtained from the LSWT were analyzed, it was possible to compare the results with those obtained using AVL. This code, as can only generate lift and drag coefficients in the linear region of lift coefficient. Figure 4.48 plots the lift coefficient versus angle of attack in the linear region from -2° to 10° angle of attack, for models with similar gap g = 0.5c, and both positive and negative stagger s = ±0.5c, at Re 60,000. It also plots the data of lift coefficient versus angle of attack obtained using AVL. From Table 4.1 and Table 4.2, it can be seen that the difference at Re 60,000 and 120,000 in lift slope in a range of angle of attack between -2° and 8° for the two models with similar gap g = 0.5c and stagger s = ±0.5c is really small, and equal to 1.4% for the positive stagger configuration and 0.5% for the negative stagger configuration. Due to the small difference in lift slope changing Reynolds number, for the comparison between analytical and

experimental results, the case Re 60,000 is the only one considered. Also, it is important to notice that results from AVL show no difference between positive and negative stagger.

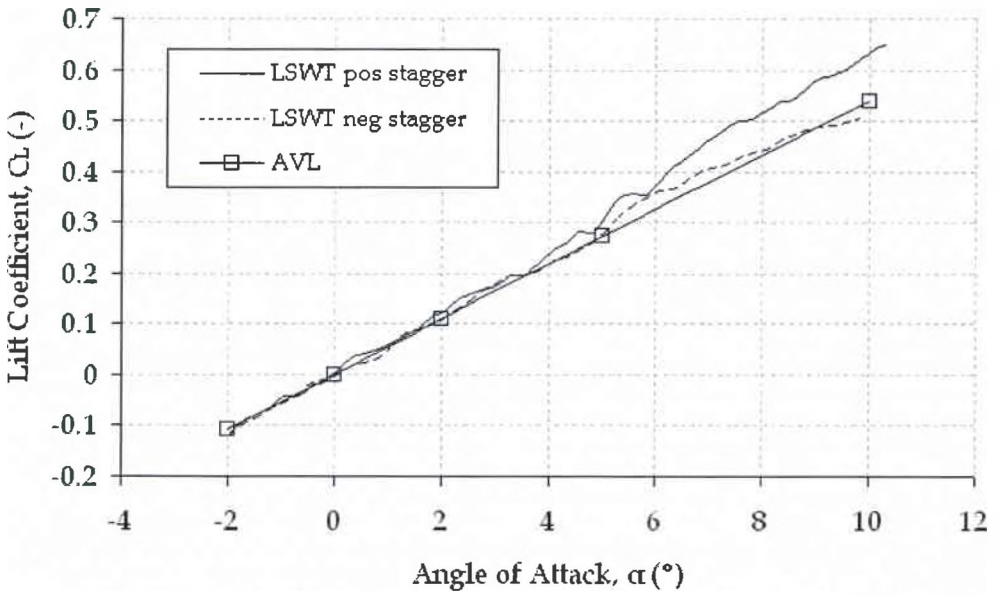

Figure 4.48: Comparison of Lift Curve between the AVL results and the LSWT data for the models with similar gap 0.5c and stagger ±0.5c at Re 60,000

The AVL results show good agreement with the LSWT data under the angle of attack range where the transition from one lift slope value to the other occurs. The change in lift slope, explained in the previous paragraph, is the only effect that causes AVL results to be different from the experimental one. All models tested show this agreement when comparing analytical and experimental results.

Induced Drag Coefficient

The induced drag coefficient, C_{Di}, was predicted theoretically using both the equivalent monoplane method (EM) by Munk and orthogonal biplane method (OB)

by Prandtl. Figure 4.49 shows the comparison between analytical and experimental induced drag coefficient, C_{Di}, versus angle of attack, α, for the models with similar gap g = 0.5c, and both positive and negative stagger s = ±0.5c at Re 60,000.

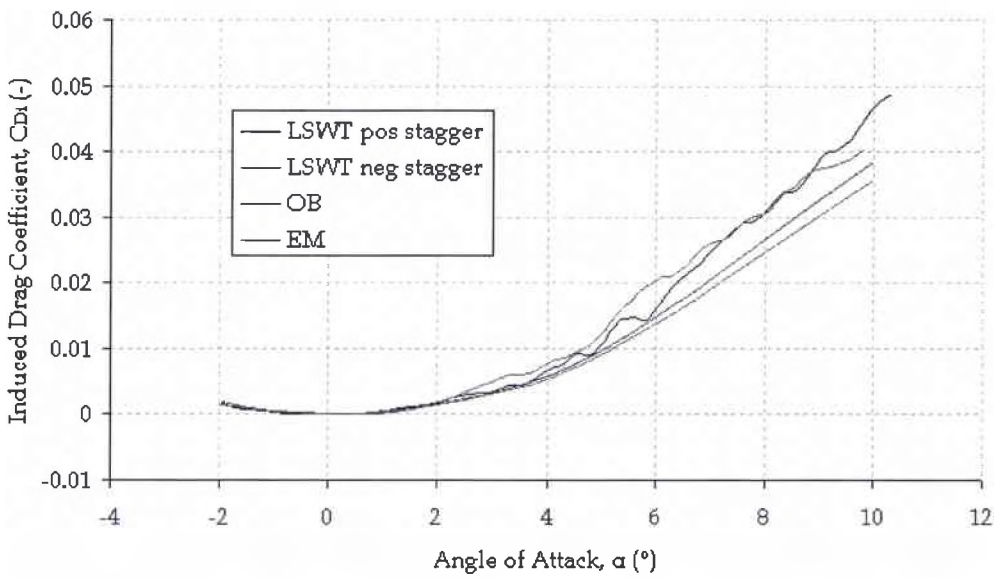

Figure 4.49: Comparison of Induced Drag Coefficient between the Orthogonal Biplane theory (OB), Equivalent Monoplane theory (EM) and the LSWT data for the models with similar gap 0.5c and stagger ±0.5c at Re 60,000

The theory shows good agreement with the experimental results. And again, from Figure 4.49, it can be seen that the theory matches the experimental curves reasonably well under the angle of attack range where the transition from one lift slope value to the other occurs. All models tested show this agreement when comparing analytical and experimental results.

4.8 Uncertainty Analysis

4.8.1 Overview

Uncertainty analysis was performed on the lift over drag ratio and on the lift coefficient for the model with gap g=0.5c and stagger s=1c.

4.8.2 Lift over Drag Ratio

In this case the quantity that we wish to determine is derived from measured quantities of lift and drag. To find the uncertainty in lift over drag ratio caused by the uncertainties in lift and drag, we consider the contribution due to the uncertainty in lift and the contribution due to the uncertainty in drag separately. Each contribution may be considered separately as long as the variables lift and drag are independent of each other. The total error is obtained by combining the individual contributions. The basic idea is to determine by how much the aerodynamic efficiency would change if lift (or drag) were changed by its uncertainty. This means we need to derive the expression of lift over drag ratio with respect to both lift and drag:

$$\frac{\partial\left(L/D\right)}{\partial L} = \frac{1}{D}$$

$$\frac{\partial\left(L/D\right)}{\partial D} = -\frac{L}{D^2}$$

Since each uncertain variable will increase, not decrease the final uncertainty, we take the absolute value of these derivatives. We can consider two different scenarios. The worst scenario is the case where each possible error occurs in the

same direction. The realistic scenario is a geometric mean of the possible errors. The uncertainty in lift over drag ratio for these two scenarios is equal to:

$$\Delta\left(L/D\right)_{worst} = \left|\frac{\partial\left(L/D\right)}{\partial L}\Delta L\right| + \left|\frac{\partial\left(L/D\right)}{\partial D}\Delta D\right| = \left|\frac{1}{D}\Delta L\right| + \left|\frac{L}{D^2}\Delta D\right| \qquad (4.1)$$

$$\Delta\left(L/D\right)_{realistic} = \sqrt{\left(\frac{\partial\left(L/D\right)}{\partial L}\Delta L\right)^2 + \left(\frac{\partial\left(L/D\right)}{\partial D}\Delta D\right)^2} = \sqrt{\left(\frac{1}{D}\Delta L\right)^2 + \left(\frac{L}{D^2}\Delta D\right)^2} \qquad (4.2)$$

where ΔL and ΔD are the possible error in the lift force and drag force measurement.

We can now compute the uncertainty in the lift over drag ratio using the values specified by the manufacturer of the balance used for taking the forces in the LSWT for ΔL and ΔD in Equations (4.1) and (4.2). These values are listed in Table 3.2 and they are both equal to 1/2560 lb, and they are considered to be conservative for actual data acquisition. The standard deviation of the force measurements at each given angle of attack can also be determined. Multiple data points are logged for each angle, therefore the actual sample variance and hence the standard deviation can be computed. Each standard deviation will be the value used for ΔL and ΔD in Equations (4.1) and (4.2).

The uncertainty analysis performed by using the balance resolution will be called conservative uncertainty analysis. The uncertainty analysis performed by using the standard deviations will be called tested uncertainty analysis, and it gives a more realistic error value.

4.8.2.1 Conservative Uncertainty Analysis

Figure 4.50 and Figure 4.51 show the lift over drag ratio vs. angle of attack for both Reynolds numbers 60,000 and 120,000 with error bars calculated using the conservative method.

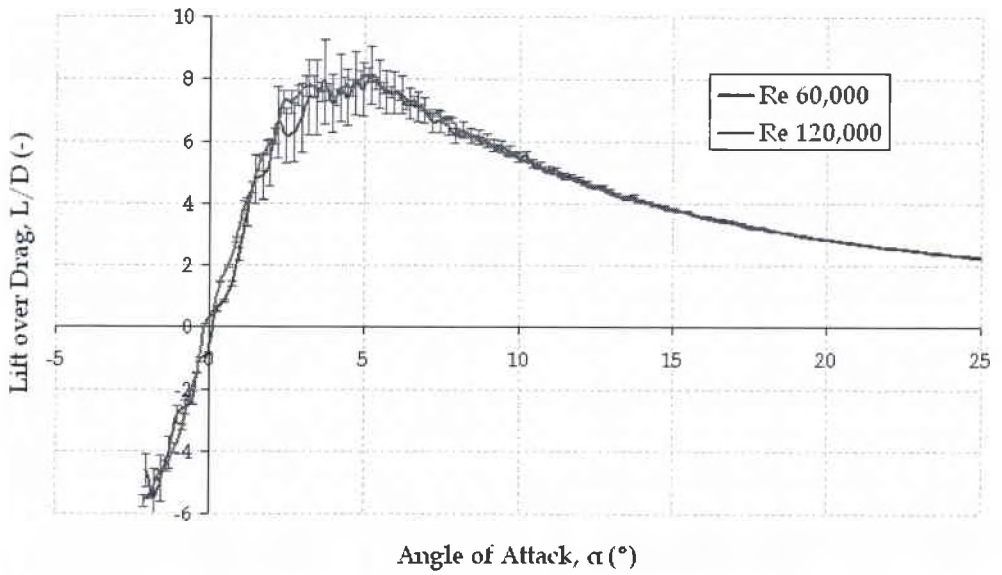

Figure 4.50: Shows the error bars of Lift over Drag Ratio for the worst case of the Conservative Uncertainty Analysis, for the model with gap 0.5c and stagger 1c at Re 60,000 – 120,000

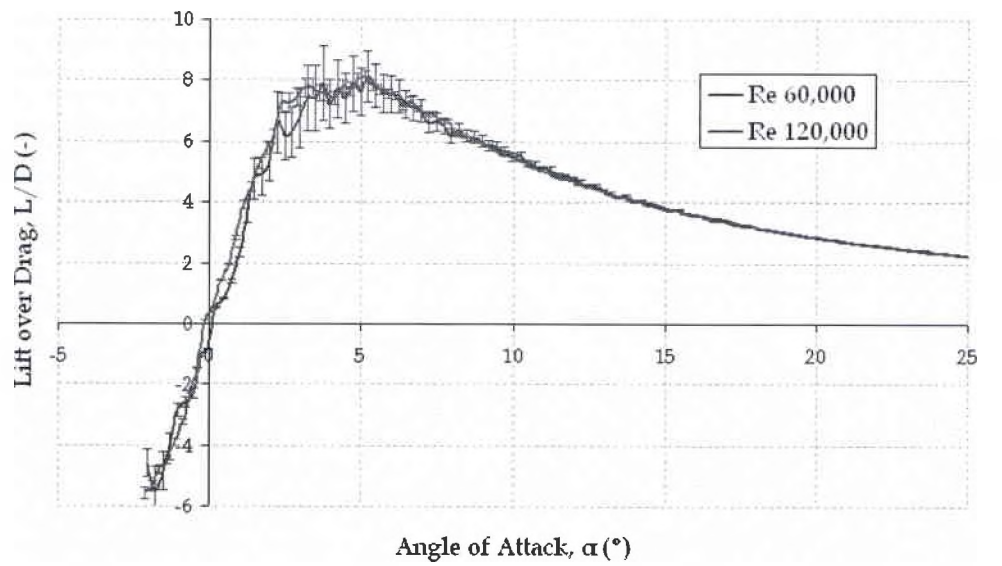

Figure 4.51: Shows the error bars of Lift over Drag Ratio for the realistic case of the Conservative Uncertainty Analysis, for the model with gap 0.5c and stagger 1c at Re 60,000 – 120,000

The results of this analysis can be seen in Table 4.38 and Table 4.39 where the percentage of error in lift over drag ratio is reported for the region where this percentage is higher. From Figure 4.50 and Figure 4.51 we can see that this region is where the lift over drag is higher which is in a range of angle of attack between 2° and 6°.

Table 4.38: Conservative Uncertainty Analysis in L/D, g=0.5c and s=1c, Re 60,000

α (°)	L/D (-)	% Worst Case Error	% Realistic Case Error
1.97	5.3214	14.0983	12.0758
2.22	6.6169	17.2616	15.1657
2.47	6.1775	14.6157	12.7431
2.72	6.2978	15.0791	13.1759
2.97	6.7500	16.2525	14.3099
3.22	7.4063	16.4045	14.5842
3.47	7.4063	16.4045	14.5842
3.72	7.9075	17.1446	15.3411
3.97	7.2115	12.6788	11.2413
4.22	7.7074	13.9027	12.4092
4.47	7.4193	12.3224	10.9570
4.72	7.8686	12.8462	11.4894
4.97	7.6472	11.3549	10.1273
5.22	8.1205	11.6498	10.4508
5.47	7.8313	10.0882	9.0185
5.72	7.5668	9.1884	8.1864
5.97	7.5533	8.8367	7.8716

Table 4.39: Conservative Uncertainty Analysis in L/D, g=0.5c and s=1c, Re 120,000

α (°)	L/D (-)	% Worst Case Error	% Realistic Case Error
2.1225	6.1613	4.1622	3.6278
2.3725	7.2590	5.0730	4.5008
2.6225	7.2567	4.9419	4.3844
2.8725	7.4566	4.4377	3.9480
3.1225	7.7592	4.2040	3.7548
3.3725	7.7592	4.2040	3.7548
3.6225	7.5785	4.0481	3.6072
3.8725	7.5787	3.6665	3.2672
4.1225	7.4027	3.3187	2.9503
4.3725	7.7980	3.3523	2.9956
4.6225	7.7070	3.1308	2.7945
4.8725	8.0231	3.0790	2.7590
5.1225	8.1167	2.8481	2.5549
5.3725	7.8609	2.4913	2.2279
5.6225	7.7031	2.3348	2.0838
5.8725	7.5696	2.1283	1.8963
6.1225	7.4864	1.9981	1.7783

In general, for the entire range of angle of attack, at Reynolds number 60,000, the worst case error ranges from 0.36% to 17.26%, and the realistic case error ranges from 0.28% to 15.34%. At Reynolds number 120,000, the worst case error ranges from 0.09% to 5.07%, and the realistic case error ranges from 0.07% to 4.50%. The error values are decreasing as the Reynolds number is increased. This is due to higher velocities producing greater balance loading and therefore, increased sensitivity. The lower loadings are closer to the balance's minimum resolution which causes the error to increase.

4.8.2.2 Tested Uncertainty Analysis

Figure 4.52 and **Figure 4.53** show the lift over drag ratio vs. angle of attack for both Reynolds numbers 60,000 and 120,000 with error bars calculated using the tested method.

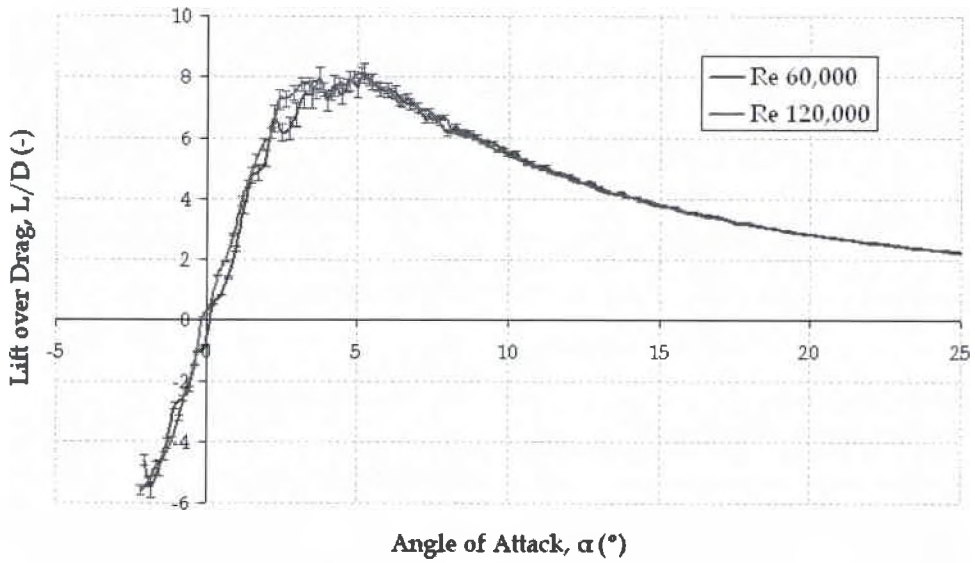

Figure 4.52: Shows the error bars of Lift over Drag Ratio for the worst case of the Tested Uncertainty Analysis, for the model with gap 0.5c and stagger 1c at Re 60,000 – 120,000

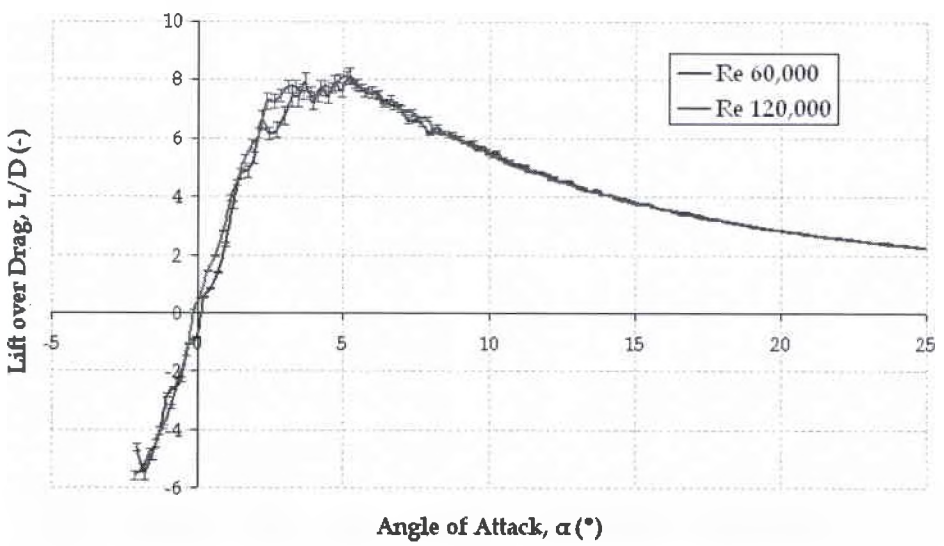

Figure 4.53: Shows the error bars of Lift over Drag Ratio for the realistic case of the Tested Uncertainty Analysis, for the model with gap 0.5c and stagger 1c at Re 60,000 – 120,000

The results of this analysis can be seen in Table 4.40 where the percentage of error in lift over drag ratio is reported for the region where this percentage is higher. From Figure 4.52 and Figure 4.53 this region is where the lift over drag is higher which is in a range of angle of attack between 2° and 6°.

Table 4.40: Tested Uncertainty Analysis in L/D, g=0.5c and s=1c, Re 60,000

α (°)	L/D (-)	% Worst Case Error	% Realistic Case Error
2.1225	6.1613	4.1622	3.6278
2.3725	7.2590	5.0730	4.5008
2.6225	7.2567	4.9419	4.3844
2.8725	7.4566	4.4377	3.9480
3.1225	7.7592	4.2040	3.7548
3.3725	7.7592	4.2040	3.7548
3.6225	7.5785	4.0481	3.6072
3.8725	7.5787	3.6665	3.2672
4.1225	7.4027	3.3187	2.9503
4.3725	7.7980	3.3523	2.9956
4.6225	7.7070	3.1308	2.7945
4.8725	8.0231	3.0790	2.7590
5.1225	8.1167	2.8481	2.5549
5.3725	7.8609	2.4913	2.2279
5.6225	7.7031	2.3348	2.0838
5.8725	7.5696	2.1283	1.8963
6.1225	7.4864	1.9981	1.7783

Table 4.41: Tested Uncertainty Analysis in L/D, g=0.5c and s=1c, Re 120,000

α (°)	L/D (-)	% Worst Case Error	% Realistic Case Error
2.1225	6.1613	4.1622	3.6278
2.3725	7.2590	5.0730	4.5008
2.6225	7.2567	4.9419	4.3844
2.8725	7.4566	4.4377	3.9480
3.1225	7.7592	4.2040	3.7548
3.3725	7.7592	4.2040	3.7548
3.6225	7.5785	4.0481	3.6072
3.8725	7.5787	3.6665	3.2672
4.1225	7.4027	3.3187	2.9503
4.3725	7.7980	3.3523	2.9956
4.6225	7.7070	3.1308	2.7945
4.8725	8.0231	3.0790	2.7590
5.1225	8.1167	2.8481	2.5549
5.3725	7.8609	2.4913	2.2279
5.6225	7.7031	2.3348	2.0838
5.8725	7.5696	2.1283	1.8963
6.1225	7.4864	1.9981	1.7783

In general, for the entire range of angle of attack, at Reynolds number 60,000, the worst case error ranges from 0.18% to 6.46%, and the realistic case error ranges from 0.13% to 4.85%. At Reynolds number 120,000, the worst case error ranges from 0.10% to 4.43%, and the realistic case error ranges from 0.08% to 3.96%. The error values are decreasing as the Reynolds number is increased. This is due to higher velocities producing greater balance loading and therefore, increased sensitivity. The lower loadings are closer to the balance's minimum resolution which causes the error to increase.

As compared to the conservative error percentages, the tested error percentages are much smaller and thus reflect the actual precision of the balance for measurements.

4.8.3 Lift Coefficient

The lift coefficient is computed using Equation (4.3):

$$C_L = \frac{L}{\frac{1}{2}\rho_{air} S V_\infty^2} \tag{4.3}$$

In this case the quantity that we wish to determine is derived from measured quantities of lift, air density, surface, and freestream velocity. As has been done before, the derivative of Equation (4.3) with respect to all the variables can be computed.

$$\frac{\partial C_L}{\partial L} = \frac{1}{\frac{1}{2}\rho_{air} S V_\infty^2}$$

$$\frac{\partial C_L}{\partial \rho_{air}} = -\frac{L}{\frac{1}{2}\rho_{air}^2 S V_\infty^2}$$

$$\frac{\partial C_L}{\partial S} = -\frac{L}{\frac{1}{2}\rho_{air} S^2 V_\infty^2}$$

$$\frac{\partial C_L}{\partial V_\infty} = -\frac{L}{\frac{1}{4}\rho_{air} S V_\infty^3}$$

The total error is obtained by combining the individual contributions. Since each uncertain variable will increase, not decrease the final uncertainty, we take the absolute value of these derivatives. For uncertainty analysis on lift coefficient, only the realistic scenario is considered in this section, and the method used is the conservative uncertainty analysis.

$$\Delta(C_L)_{realistic} = \sqrt{\left(\frac{\partial C_L}{\partial L}\Delta L\right)^2 + \left(\frac{\partial C_L}{\partial \rho_{air}}\Delta \rho_{air}\right)^2 + \left(\frac{\partial C_L}{\partial S}\Delta S\right)^2 + \left(\frac{\partial C_L}{\partial V_\infty}\Delta V_\infty\right)^2} \qquad (4.4)$$

where, for the conservative method ΔL is equal to 1/2560 lb. The other possible errors $\Delta\rho_{air}$, ΔS, and ΔV_∞ are functions of other variables, and they can be found by using the definition of air density, surface, and freestream velocity respectively.

Air density is calculated using Equation (3.2):

$$\rho_{air} = 1.2929\left(\frac{273.15}{T + 273.15}\right)\left(\frac{p_{atm} - SVP \cdot H}{760}\right)$$

Freestream velocity is calculated using Equation (3.1):

$$\mathrm{Re} = \frac{V_\infty \cdot \bar{c} \cdot \rho_{air}}{\mu_{air}}$$

$$V_\infty = \frac{\mathrm{Re} \cdot \mu_{air}}{\bar{c} \cdot \rho_{air}}$$

where it can be seen that the freestream velocity is also function of other variables, so that the error due to these variables should be considered. The air viscosity, μ_{air}, is calculated using Sutherland's formula in Equation (3.3):

$$\mu_{air} = \mu_0 \frac{T_0 + C}{T + C}\left(\frac{T}{T_0}\right)^{3/2}$$

Now, taking the derivative of air density with respect to temperature, atmospheric pressure, and humidity, the derivative of freestream velocity with respect to air viscosity, chord length, and air density, the derivative of air viscosity with respect to temperature, the possible errors associated with air density, and freestream velocity, can be computed. Using these values in Equation (4.3), the error on lift coefficient can be computed.

Figure 4.54 shows the lift coefficient vs. angle of attack for both Reynolds numbers 60,000 and 120,000 with error bars calculated using the conservative method, for the model with gap g = 0.5c and stagger s = 1c.

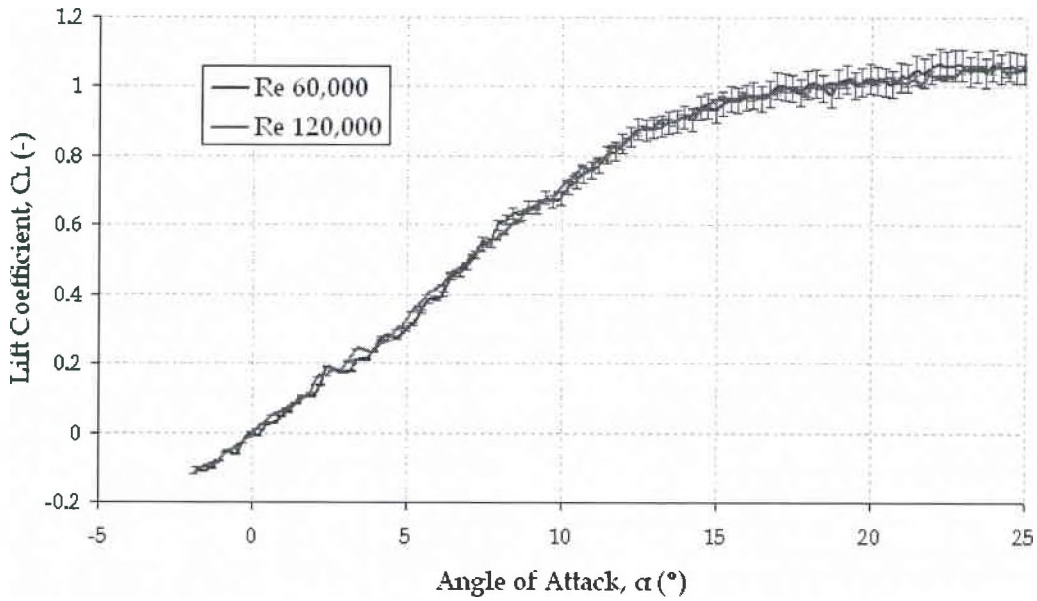

Figure 4.54: Shows the error bars of Lift Coefficient for the realistic case of the Conservative Uncertainty Analysis, for the model with gap 0.5c and stagger 1c at Re 60,000 – 120,000

In general, for the entire range of angle of attack, at Reynolds number 60,000 the realistic case error ranges from 0.08% to 4.49%. At Reynolds number 120,000 the realistic case error ranges from 0.02% to 0.72%. The error values are decreasing as the Reynolds number is increased. This is due to higher velocities producing greater balance loading and therefore, increased sensitivity. The lower loadings are closer to the balance's minimum resolution which causes the error to increase.

Bibliography

[20] Killian, D.N., "The Aerodynamic Performance of the Houck Configuration Flow Guides", Thesis, Air Force Institute of Technology, WPAFB OH, June 2007

[21] Hu, H., Yang, Z., Igarashi, H., "Aerodynamic Hysteresis of a Low Reynolds Number Airfoil", Iowa State University, Journal of Aircraft, Vol. 44, No. 6, 2007.

[22] Filippone, A. "Advanced Topics in Aerodynamics, Computational Fluid Dynamics, Aeronautics, Propulsion Systems", http://www.aerodyn.org

V. Conclusions and Recommendations

5.1 Conclusions of Research

The purpose of this study was to investigate the aerodynamic performance of a biplane joined at the tips by endplates using several biplane configurations having different stagger and gap. The models were based on rectangular flat plate profiles with the same reference planform area.

When comparing models with a gap of 0.5c, at Re 60,000 the lift slope increases by almost 5% for each 0.5c stagger increment in the negative direction, and it increases by almost 15% for each 0.5c stagger increment in the positive direction. At Re 120,000 the variation is slightly different but the trend is the same. It can be seen that at Re 120,000 the lift slope increases by almost 4% for each 0.5c stagger increment in the negative direction, and it increases by almost 13% for each 0.5c stagger increment in the positive direction. The aerodynamic efficiency, or lift over drag ratio, increases by almost 10% for the first 0.5c stagger increment in the negative direction then it increases by another 5% for the second 0.5c stagger increment in the negative direction. For the positive stagger increment it can be seen that the maximum lift over drag ratio increases by almost 10% for each 0.5c stagger increment in the positive direction. At Re 120,000 the percentages of variation between different staggers is slightly different but the trend is the same. It can be seen that at Re 120,000 the aerodynamic efficiency increases by almost 5%

for each 0.5c stagger increment in the negative direction, and it increases by almost 20% for each 0.5c stagger increment in the positive direction.

When comparing models with a gap of 1c, at Re 60,000 and Re 120,000 the variation of lift slope and aerodynamic efficiency is smaller than the case of models with a gap of 0.5c due to the fact that higher gap means less interference between the two wings.

When comparing models with a gap of 2c, at both Reynolds numbers, the variation of lift slope and aerodynamic efficiency is almost negligible due to the higher gap between the two wings. Also, models with a gap of 2c experience stall flutter after an angle of attack equal to the angle of stall.

When comparing models with a stagger of 0c, the lift slope increases by almost 26% at Re 60,000 and it increases by almost 28% at Re 120,000 for each 0.5c gap increment. The aerodynamic efficiency increases by almost 1.5% at Re 60,000 and by almost 35% at Re 120,000 for each 0.5c gap increment.

When comparing models with a stagger of -1c, the lift slope, at both Reynolds numbers, increases by almost 15% with each 0.5 gap increment. Higher gap models experience higher lift slope. At Re 120,000 the integrated lift over drag ratio of the model with a gap of 1c is almost 9% higher than the integrated lift over drag ratio of the model with gap 0.5c. The variation of integrated lift over drag ratio equals almost 40% when comparing the model with a gap of 2c to the model with gap 0.5c. This variation at Re 60,000 is equal to just 0.8% for the model with a gap of 1c and almost 12% for the one with a gap of 2c. This means that in terms of

aerodynamic efficiency, the effect of changing the gap at higher Reynolds numbers is more important than the same effect at lower Reynolds numbers. The same result was obtained when considering models with no stagger and different gap configurations.

When comparing positive versus negative stagger, the lift slope of the models with positive stagger is always higher than those with negative stagger. At both Reynolds numbers this variation is equal to almost 15%. At Re 120,000 the integrated lift over drag ratio of the model having positive stagger is almost 18% higher than the integrated lift over drag ratio of the model with negative stagger. This variation at Re 60,000 is equal to almost 5.5%. This means that in terms of aerodynamic efficiency, models with positive stagger are more efficient than models with negative stagger and that this behavior, and that this effect becomes more important at higher Reynolds numbers.

A change in lift slope was observed for all the models tested in the LSWT. The largest change in lift slope is associated with the model with the highest angle of stagger and the lowest change in lift slope is associated with the model having lowest angle of stagger. It is possible that by increasing the angle of stagger, which can be realized by decreasing the gap or increasing the stagger, the model experiences a positive change in lift slope. This can be translated into a better span efficiency factor after this change has occurred. Also, this change in lift slope occurs around the same angle of attack as maximum aerodynamic efficiency.

Aerodynamic hysteresis analysis was conducted on the model with a gap of 0.5c and a stagger of -1c. Hysteresis on lift coefficient is very mild and at Reynolds number 60,000 it occurs after the angle of stall, instead at Reynolds number 120,000 hysteresis occurs before the angle of stall.

Comparison between analytical and experimental results was conducted on all the models tested in the LSWT by using for the analytical results the code AVL. The two were found to compare quite well under some conditions, and not well under other conditions. This is due to the fact that AVL, or any other code based on Laplace's Equation, utilizes a vortex-lattice representation of the lifting surfaces, and it assumes steady, irrotational, inviscid, incompressible attached flow.

It can be seen that both stagger and gap have positive effect on the aerodynamic performance of the biplane joined at the tips by endplates. Also, despite Munk's Stagger Theorem, it can be seen that positive and negative stagger do not show the same aerodynamic performance while keeping gap constant. Positive stagger configurations always perform better than negative stagger configurations in terms of aerodynamic performance. But the most important result obtained from this research is that all the models tested in the LSWT experience a change in lift slope at the angle of attack of maximum aerodynamic efficiency. Further investigation of the biplane joined at the tips will need to be conducted to determine the reason why this change in lift slope occurs, and if it is possible to take advantage of this change.

5.2 Recommendations for Future Research

It is recommended that there be continued testing of the biplane joined at the tips by endplates in order to better understand its aerodynamic performance, and in order to study the change in lift slope observed. A deeper analysis of lift slope could be conducted by using PIV tests or CFD analysis on the biplane with endplates, around an angle of attack where the maximum aerodynamic efficiency is experienced. Also, it would be interesting to run experimental wind tunnel tests on different monoplane configurations with same reference area, or same aspect ratio of the biplane configurations tested in the LSWT and presented in this thesis. It could be interesting to run tests at higher Reynolds numbers to see if the concept of a biplane joined at the tips by endplates could be used for higher speed and/or bigger airplanes.

Analytically, a deeper study on the interference of one wing on the other, and the effect of endplates on the aerodynamic performance should be conducted, considering viscous effects that have been neglected using a vortex lattice approach.

Appendix A: ATI Gamma F/T Transducer

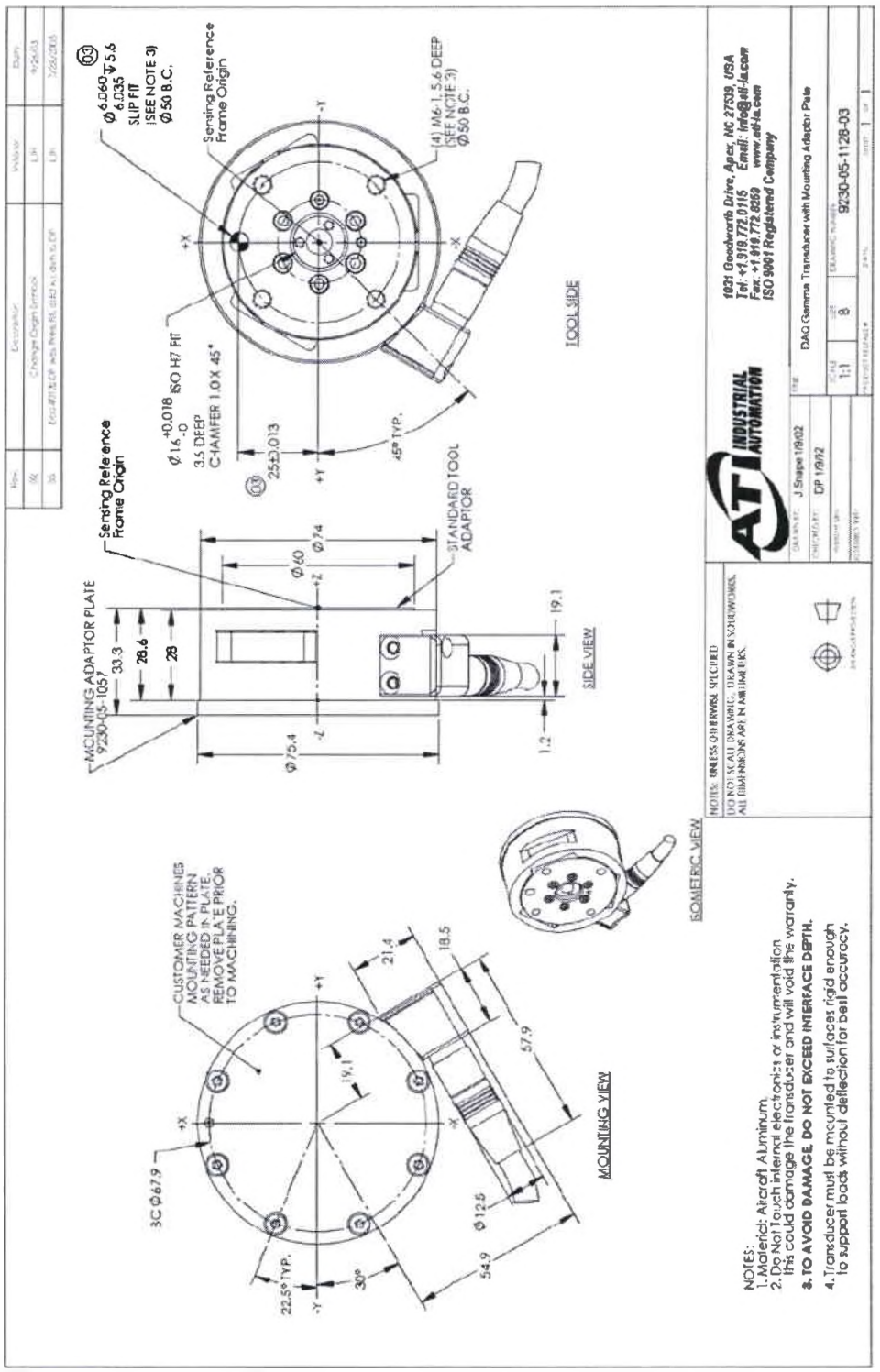

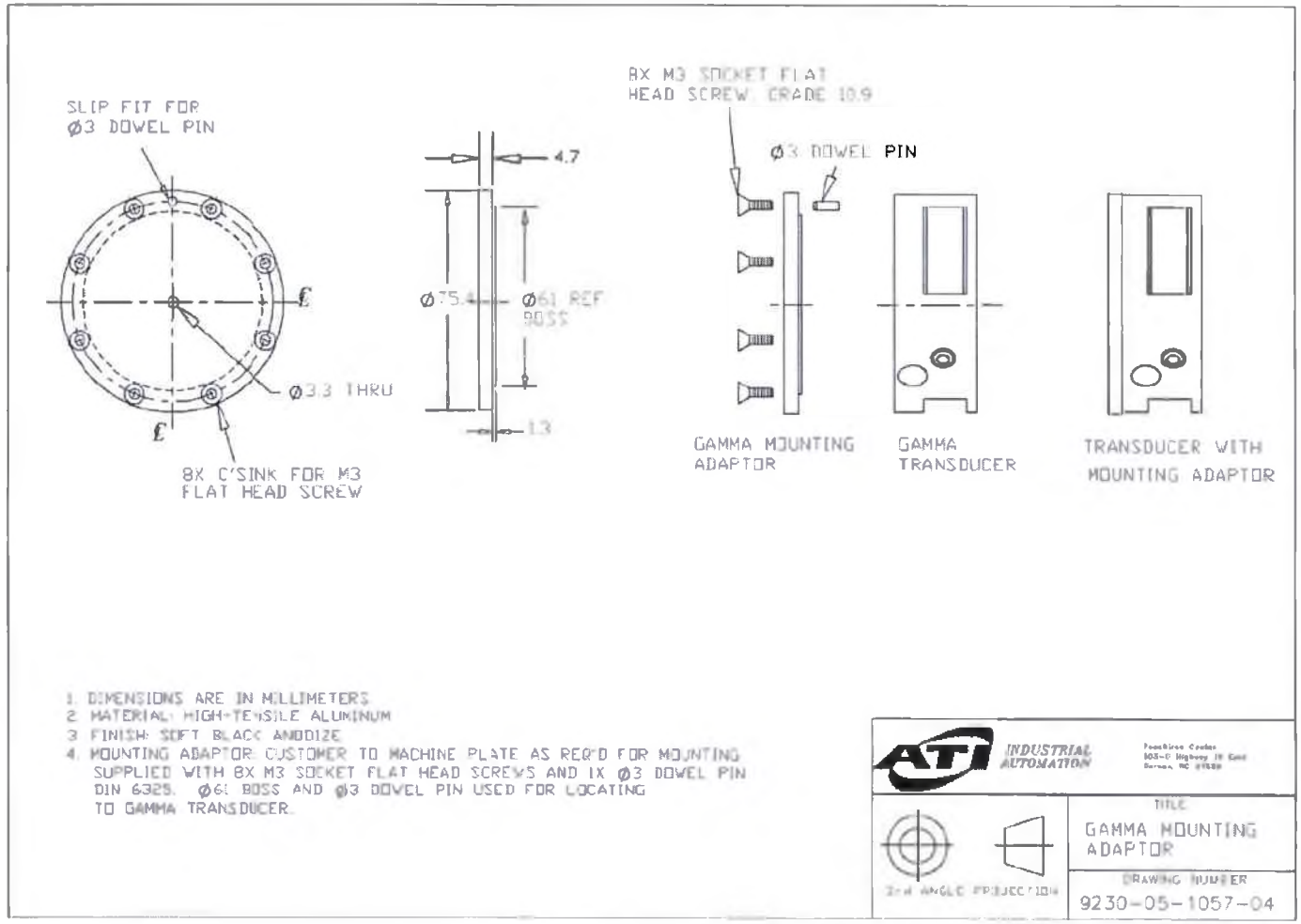

1. DIMENSIONS ARE IN MILLIMETERS.
2. MATERIAL: HIGH-TENSILE ALUMINUM
3. FINISH: SOFT BLACC ANODIZE.
4. MOUNTING ADAPTOR: CUSTOMER TO MACHINE PLATE AS REQ'D FOR MOUNTING. SUPPLIED WITH 8X M3 SOCKET FLAT HEAD SCREWS AND 1X Ø3 DOWEL PIN DIN 6325. Ø61 BOSS AND Ø3 DOWEL PIN USED FOR LOCATING TO GAMMA TRANSDUCER.

ATI INDUSTRIAL AUTOMATION

TITLE
GAMMA MOUNTING ADAPTOR

DRAWING NUMBER
9230-05-1057-04

Appendix B: Newmark RM-5 Rotary Stage

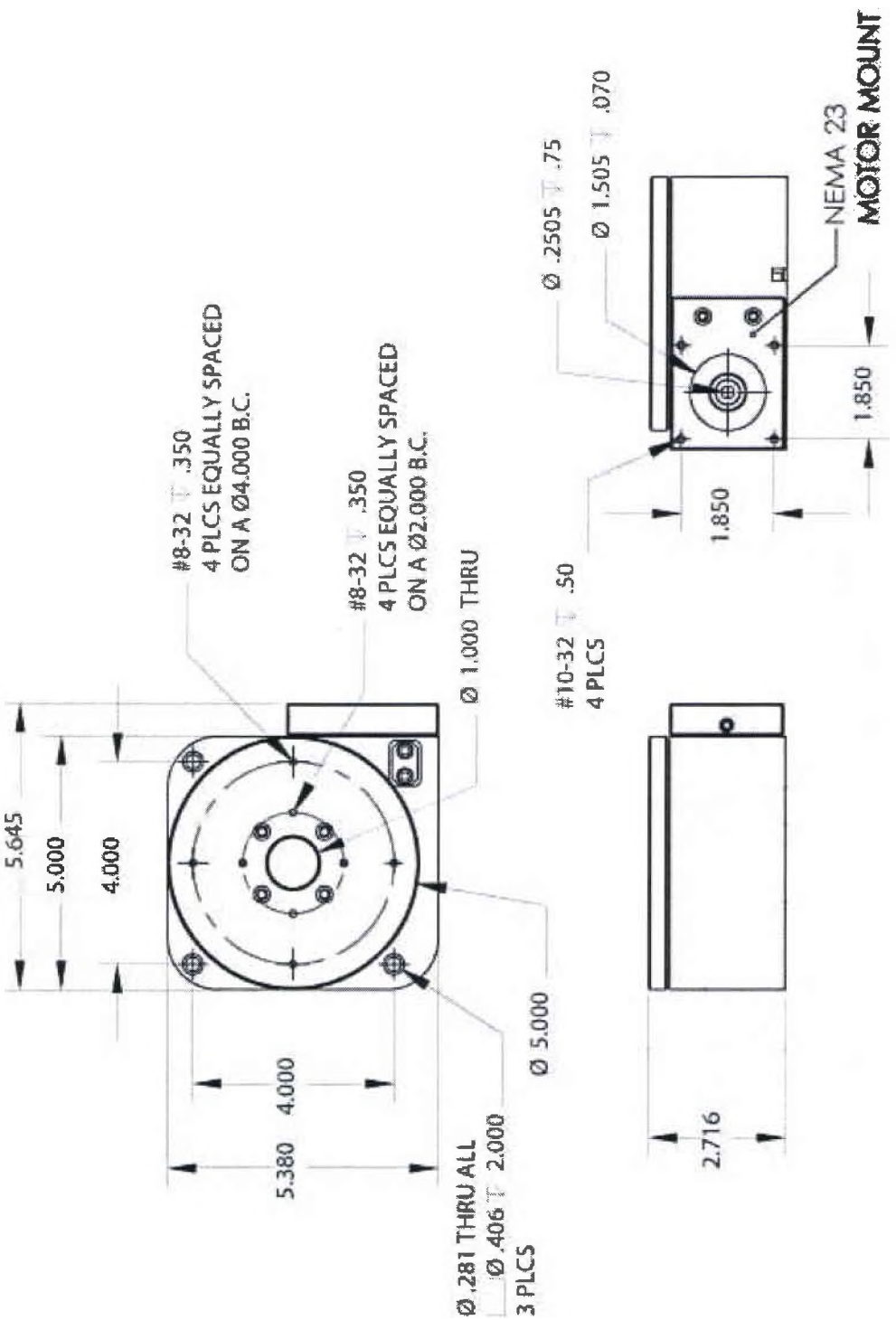

Appendix C: Wind Tunnel Conditions

Model #1 – Gap 1c, Stagger 0c

Table C.1: Model #1 Velocity, Test Dates, Temperature, Pressure, and Humidity

Model Configuration:	Model #1				
Re (-)	V (m/s)	Date	Temperature (°C)	Atmospheric Pressure	Humidity
60,000	8.83	24-jan-08	13	745.5 mmHg	52%
120,000	17.65	24-jan-08	13	745.5 mmHg	52%
60,000	9.07	28-jan-08	17	745.8 mmHg	57%
120,000	18.15	28-jan-08	17	745.8 mmHg	57%
60,000	9.46	05-feb-08	21	740.4 mmHg	82%
120,000	18.92	05-feb-08	21	740.4 mmHg	82%

Model #2 – Gap 0.5c, Stagger 0c

Table C.2: Model #2 Velocity, Test Dates, Temperature, Pressure, and Humidity

Model Configuration:	Model #2				
Re (-)	V (m/s)	Date	Temperature (°C)	Atmospheric Pressure	Humidity
60,000	8.83	24-jan-08	13	745.5 mmHg	52%
120,000	17.65	24-jan-08	13	745.5 mmHg	52%
60,000	9.07	28-jan-08	17	745.8 mmHg	57%
120,000	18.15	28-jan-08	17	745.8 mmHg	57%
60,000	9.46	05-feb-08	21	740.4 mmHg	82%
120,000	18.92	05-feb-08	21	740.4 mmHg	82%

Model #3 – Gap 0.5c, Stagger 0.5c

Table C.3: Model #3 Velocity, Test Dates, Temperature, Pressure, and Humidity

Model Configuration:	Model #3				
Re (-)	V (m/s)	Date	Temperature (°C)	Atmospheric Pressure	Humidity
60,000	8.83	24-jan-08	13	745.5 mmHg	52%
120,000	17.65	24-jan-08	13	745.5 mmHg	52%
60,000	9.07	28-jan-08	17	745.8 mmHg	57%
120,000	18.15	28-jan-08	17	745.8 mmHg	57%
60,000	9.46	05-feb-08	21	740.4 mmHg	82%
120,000	18.92	05-feb-08	21	740.4 mmHg	82%

Model #4 – Gap 0.5c, Stagger 1c

Table C.4: Model #4 Velocity, Test Dates, Temperature, Pressure, and Humidity

Model Configuration:	Model #4				
Re (-)	V (m/s)	Date	Temperature (°C)	Atmospheric Pressure	Humidity
60,000	8.82	25-jan-08	15	755 mmHg	46%
120,000	17.65	25-jan-08	15	755 mmHg	46%
60,000	9.07	28-jan-08	17	745.8 mmHg	57%
120,000	18.15	28-jan-08	17	745.8 mmHg	57%
60,000	9.46	05-feb-08	21	740.4 mmHg	82%
120,000	18.92	05-feb-08	21	740.4 mmHg	82%

Model #5 – Gap 1c, Stagger 0.5c

Table C.5: Model #5 Velocity, Test Dates, Temperature, Pressure, and Humidity

Model Configuration:	Model #5				
Re (-)	V (m/s)	Date	Temperature (°C)	Atmospheric Pressure	Humidity
60,000	8.82	25-jan-08	15	755 mmHg	46%
120,000	17.65	25-jan-08	15	755 mmHg	46%
60,000	9.07	28-jan-08	17	745.8 mmHg	57%
120,000	18.15	28-jan-08	17	745.8 mmHg	57%
60,000	9.46	05-feb-08	21	740.4 mmHg	82%
120,000	18.92	05-feb-08	21	740.4 mmHg	82%

Model #6 – Gap 1c, Stagger 1c

Table C.6: Model #6 Velocity, Test Dates, Temperature, Pressure, and Humidity

Model Configuration:	Model #6				
Re (-)	V (m/s)	Date	Temperature (°C)	Atmospheric Pressure	Humidity
60,000	8.82	25-jan-08	15	755 mmHg	46%
120,000	17.65	25-jan-08	15	755 mmHg	46%
60,000	9.07	28-jan-08	17	745.8 mmHg	57%
120,000	18.15	28-jan-08	17	745.8 mmHg	57%
60,000	9.46	05-feb-08	21	740.4 mmHg	82%
120,000	18.92	05-feb-08	21	740.4 mmHg	82%

Model #7 – Gap 2c, Stagger 1c

Table C.7: Model #7 Velocity, Test Dates, Temperature, Pressure, and Humidity

Model Configuration:	Model #7				
Re (-)	V (m/s)	Date	Temperature (°C)	Atmospheric Pressure	Humidity
60,000	8.82	25-jan-08	15	755 mmHg	46%
120,000	17.65	25-jan-08	15	755 mmHg	46%
60,000	9.21	28-jan-08	18	739.8 mmHg	56%
120,000	9.46	05-feb-08	21	740.4 mmHg	82%
60,000	18.92	05-feb-08	21	740.4 mmHg	82%
120,000	18.15	05-feb-08	21	740.4 mmHg	82%

Model #8 – Gap 1c, Stagger 1.5c

Table C.8: Model #8 Velocity, Test Dates, Temperature, Pressure, and Humidity

Model Configuration:	Model #8				
Re (-)	V (m/s)	Date	Temperature (°C)	Atmospheric Pressure	Humidity
60,000	8.82	25-jan-08	15	755 mmHg	46%
120,000	17.65	25-jan-08	15	755 mmHg	46%
60,000	9.21	28-jan-08	18	739.8 mmHg	56%
120,000	18.42	28-jan-08	18	739.8 mmHg	56%
60,000	9.49	05-feb-08	21	738.1 mmHg	81%
120,000	18.97	05-feb-08	21	738.1 mmHg	81%

Model #9 – Gap 0.5c, Stagger -0.5c

Table C.9: Model #9 Velocity, Test Dates, Temperature, Pressure, and Humidity

Model Configuration:	Model #9				
Re (-)	V (m/s)	Date	Temperature (°C)	Atmospheric Pressure	Humidity
60,000	8.83	24-jan-08	13	745.5 mmHg	52%
120,000	17.65	24-jan-08	13	745.5 mmHg	52%
60,000	9.07	28-jan-08	17	745.8 mmHg	57%
120,000	18.15	28-jan-08	17	745.8 mmHg	57%
60,000	9.46	05-feb-08	21	740.4 mmHg	82%
120,000	18.92	05-feb-08	21	740.4 mmHg	82%

Model #10 – Gap 0.5c, Stagger -1c

Table C.10: Model #10 Velocity, Test Dates, Temperature, Pressure, and Humidity

Model Configuration:	Model #10				
Re (-)	V (m/s)	Date	Temperature (°C)	Atmospheric Pressure	Humidity
60,000	8.82	25-jan-08	15	755 mmHg	46%
120,000	17.65	25-jan-08	15	755 mmHg	46%
60,000	9.07	28-jan-08	17	745.8 mmHg	57%
120,000	18.15	28-jan-08	17	745.8 mmHg	57%
60,000	9.46	05-feb-08	21	740.4 mmHg	82%
120,000	18.92	05-feb-08	21	740.4 mmHg	82%

Model #11 – Gap 1c, Stagger -0.5c

Table C.11: Model #11 Velocity, Test Dates, Temperature, Pressure, and Humidity

Model Configuration:	Model #11				
Re (-)	V (m/s)	Date	Temperature (°C)	Atmospheric Pressure	Humidity
60,000	8.82	25-jan-08	15	755 mmHg	46%
120,000	17.65	25-jan-08	15	755 mmHg	46%
60,000	9.07	28-jan-08	17	745.8 mmHg	57%
120,000	18.15	28-jan-08	17	745.8 mmHg	57%
60,000	9.46	05-feb-08	21	740.4 mmHg	82%
120,000	18.92	05-feb-08	21	740.4 mmHg	82%

Model #12 – Gap 1c, Stagger -1c

Table C.12: Model #12 Velocity, Test Dates, Temperature, Pressure, and Humidity

Model Configuration:	Model #12				
Re (-)	V (m/s)	Date	Temperature (°C)	Atmospheric Pressure	Humidity
60,000	8.82	25-jan-08	15	755 mmHg	46%
120,000	17.65	25-jan-08	15	755 mmHg	46%
60,000	9.07	28-jan-08	17	745.8 mmHg	57%
120,000	18.15	28-jan-08	17	745.8 mmHg	57%
60,000	9.46	05-feb-08	21	740.4 mmHg	82%
120,000	18.92	05-feb-08	21	740.4 mmHg	82%

Model #13 – Gap 2c, Stagger -1c

Table C.13: Model #13 Velocity, Test Dates, Temperature, Pressure, and Humidity

Model Configuration:	Model #13				
Re (-)	V (m/s)	Date	Temperature (°C)	Atmospheric Pressure	Humidity
60,000	8.82	25-jan-08	15	755 mmHg	46%
120,000	17.65	25-jan-08	15	755 mmHg	46%
60,000	9.21	28-jan-08	18	739.8 mmHg	56%
120,000	18.42	28-jan-08	18	739.8 mmHg	56%
60,000	9.46	05-feb-08	21	740.4 mmHg	82%
120,000	18.92	05-feb-08	21	740.4 mmHg	82%

Model #14 – Gap 1c, Stagger -1.5c

Table C.14: Model #14 Velocity, Test Dates, Temperature, Pressure, and Humidity

Model Configuration:	Model #14				
Re (-)	V (m/s)	Date	Temperature (°C)	Atmospheric Pressure	Humidity
60,000	8.82	25-jan-08	15	755 mmHg	46%
120,000	17.65	25-jan-08	15	755 mmHg	46%
60,000	9.21	28-jan-08	18	739.8 mmHg	56%
120,000	18.42	28-jan-08	18	739.8 mmHg	56%
60,000	9.49	05-feb-08	21	738.1 mmHg	81%
120,000	18.97	05-feb-08	21	738.1 mmHg	81%

Appendix D: Aerodynamic Data at Reynolds Number 60,000

Table D.1: Model #1, g=1c, s=0c, Aerodynamic Data at Re 60,000

α (°)	C_L (-)	C_D (-)	L/D (-)
-2.13	-0.1395	0.0262	-5.3147
-1.88	-0.1230	0.0264	-4.6535
-1.63	-0.1068	0.0272	-3.9207
-1.38	-0.0866	0.0258	-3.3618
-1.13	-0.0681	0.0257	-2.6474
-0.88	-0.0508	0.0254	-2.0024
-0.63	-0.0418	0.0239	-1.7530
-0.38	-0.0219	0.0261	-0.8382
-0.13	-0.0090	0.0242	-0.3698
0.12	-0.0063	0.0246	-0.2562
0.37	0.0172	0.0265	0.6475
0.62	0.0326	0.0246	1.3239
0.87	0.0483	0.0291	1.6580
1.12	0.0671	0.0260	2.5769
1.37	0.0864	0.0306	2.8280
1.62	0.0973	0.0275	3.5333
1.87	0.1210	0.0298	4.0611
2.12	0.1350	0.0317	4.2613
2.37	0.1683	0.0347	4.8490
2.62	0.1844	0.0358	5.1530
2.87	0.1922	0.0335	5.7276
3.12	0.2031	0.0388	5.2335
3.37	0.2031	0.0388	5.2335
3.62	0.2163	0.0392	5.5180
3.87	0.2341	0.0403	5.8138
4.12	0.2410	0.0417	5.7729
4.37	0.2612	0.0433	6.0388
4.62	0.3043	0.0451	6.7434
4.87	0.3149	0.0485	6.4865
5.12	0.3504	0.0526	6.6590
5.37	0.3672	0.0576	6.3806
5.62	0.3759	0.0612	6.1425
5.87	0.4050	0.0608	6.6580
6.12	0.4184	0.0650	6.4337
6.37	0.4301	0.0710	6.0596
6.62	0.4638	0.0747	6.2076
6.87	0.4964	0.0789	6.2901
7.12	0.5097	0.0841	6.0581
7.37	0.5448	0.0898	6.0681
7.62	0.5368	0.0897	5.9817
7.87	0.5666	0.0958	5.9168
8.12	0.5793	0.0995	5.8213
8.37	0.6054	0.1081	5.5997
8.62	0.6313	0.1171	5.3895
8.87	0.6505	0.1157	5.6230
9.12	0.6560	0.1254	5.2311
9.37	0.6784	0.1344	5.0490
9.62	0.6816	0.1278	5.3343
9.87	0.6959	0.1367	5.0923
10.12	0.7067	0.1412	5.0045
10.37	0.7156	0.1453	4.9246
10.62	0.7343	0.1539	4.7712
10.87	0.7471	0.1555	4.8035
11.12	0.7516	0.1639	4.5846
11.37	0.7338	0.1664	4.4112
11.62	0.7561	0.1775	4.2595
11.87	0.7543	0.1765	4.2749
12.12	0.7688	0.1833	4.1947
12.37	0.7508	0.1785	4.2063
12.62	0.7515	0.1833	4.0992
12.87	0.7348	0.1833	4.0079
13.12	0.7429	0.1909	3.8921
13.37	0.7349	0.1905	3.8572
13.62	0.7294	0.1966	3.7103
13.87	0.7321	0.1993	3.6740
14.12	0.7225	0.1978	3.6523
14.37	0.7190	0.2030	3.5414
14.62	0.7218	0.2054	3.5142
14.87	0.7276	0.2080	3.4979
15.12	0.7339	0.2155	3.4060
15.37	0.7251	0.2181	3.3246
15.62	0.7303	0.2208	3.3080
15.87	0.7225	0.2245	3.2180
16.12	0.7229	0.2264	3.1933
16.37	0.7263	0.2301	3.1558
16.62	0.7197	0.2320	3.1021
16.87	0.7368	0.2403	3.0654
17.12	0.7378	0.2459	3.0010
17.37	0.7316	0.2455	2.9802
17.62	0.7450	0.2531	2.9439
17.87	0.7420	0.2561	2.8977
18.12	0.7144	0.2537	2.8164
18.37	0.7316	0.2613	2.8001
18.62	0.7237	0.2616	2.7663
18.87	0.7300	0.2691	2.7127
19.12	0.7363	0.2733	2.6939
19.37	0.7341	0.2753	2.6668
19.62	0.7395	0.2809	2.6326
19.87	0.7558	0.2929	2.5803
20.12	0.7494	0.2926	2.5616
20.37	0.7504	0.2978	2.5196
20.62	0.7518	0.2997	2.5083
20.87	0.7599	0.3077	2.4696
21.12	0.7641	0.3136	2.4369
21.37	0.7521	0.3128	2.4042
21.62	0.7426	0.3133	2.3702
21.87	0.7488	0.3159	2.3703
22.12	0.7584	0.3245	2.3370
22.37	0.7644	0.3323	2.3002
22.62	0.7657	0.3369	2.2725
22.87	0.7739	0.3435	2.2533
23.12	0.7818	0.3494	2.2377
23.37	0.7871	0.3592	2.1911
23.62	0.7825	0.3626	2.1579
23.87	0.7512	0.3530	2.1278
24.12	0.7568	0.3583	2.1126
24.37	0.7874	0.3730	2.1110
24.62	0.7724	0.3730	2.0706
24.87	0.7794	0.3801	2.0505

Table D.2: Model #2, g=0.5c, s=0c, Aerodynamic Data at Re 60,000

α (°)	C_L (-)	C_D (-)	L/D (-)
-2.06	-0.1094	0.0269	-4.0691
-1.81	-0.0937	0.0252	-3.7188
-1.56	-0.0838	0.0237	-3.5351
-1.31	-0.0661	0.0232	-2.8468
-1.06	-0.0451	0.0232	-1.9394
-0.81	-0.0393	0.0225	-1.7498
-0.56	-0.0290	0.0222	-1.3076
-0.31	-0.0123	0.0232	-0.5308
-0.06	-0.0052	0.0235	-0.2226
0.19	0.0108	0.0230	0.4711
0.44	0.0273	0.0233	1.1723
0.69	0.0382	0.0236	1.6231
0.94	0.0443	0.0228	1.9455
1.19	0.0641	0.0227	2.8189
1.44	0.0776	0.0235	3.3009
1.69	0.0873	0.0245	3.5674
1.94	0.0996	0.0257	3.8827
2.19	0.1125	0.0266	4.2201
2.44	0.1252	0.0281	4.4502
2.69	0.1407	0.0286	4.9205
2.94	0.1623	0.0306	5.3068
3.19	0.1682	0.0328	5.1226
3.44	0.1682	0.0328	5.1226
3.69	0.1898	0.0322	5.8860
3.94	0.1993	0.0343	5.8184
4.19	0.2103	0.0367	5.7220
4.44	0.2235	0.0386	5.7879
4.69	0.2448	0.0396	6.1733
4.94	0.2552	0.0411	6.2066
5.19	0.2874	0.0468	6.1416
5.44	0.2869	0.0487	5.8923
5.69	0.3145	0.0512	6.1380
5.94	0.3314	0.0549	6.0395
6.19	0.3427	0.0559	6.1340
6.44	0.3586	0.0597	6.0053
6.69	0.3751	0.0640	5.8609

α (°)	C_L (-)	C_D (-)	L/D (-)
6.94	0.3911	0.0654	5.9772
7.19	0.4083	0.0718	5.6858
7.44	0.4206	0.0747	5.6278
7.69	0.4336	0.0760	5.7085
7.94	0.4459	0.0808	5.5198
8.19	0.4690	0.0848	5.5320
8.44	0.4782	0.0889	5.3764
8.69	0.4872	0.0932	5.2296
8.94	0.5089	0.0983	5.1765
9.19	0.5171	0.1013	5.1057
9.44	0.5335	0.1058	5.0405
9.69	0.5348	0.1084	4.9358
9.94	0.5502	0.1146	4.8027
10.19	0.5596	0.1189	4.7071
10.44	0.5663	0.1223	4.6291
10.69	0.5718	0.1260	4.5368
10.94	0.5854	0.1322	4.4286
11.19	0.5888	0.1353	4.3519
11.44	0.5913	0.1388	4.2606
11.69	0.6053	0.1436	4.2155
11.94	0.6060	0.1461	4.1482
12.19	0.6081	0.1502	4.0473
12.44	0.6117	0.1552	3.9408
12.69	0.6254	0.1612	3.8798
12.94	0.6253	0.1623	3.8533
13.19	0.6265	0.1672	3.7471
13.44	0.6349	0.1726	3.6795
13.69	0.6446	0.1775	3.6310
13.94	0.6467	0.1803	3.5861
14.19	0.6693	0.1885	3.5508
14.44	0.6662	0.1925	3.4613
14.69	0.6731	0.1970	3.4166
14.94	0.6857	0.2023	3.3899
15.19	0.6884	0.2092	3.2911
15.44	0.7023	0.2175	3.2296
15.69	0.7125	0.2235	3.1870

α (°)	C_L (-)	C_D (-)	L/D (-)
15.94	0.7206	0.2254	3.1965
16.19	0.7042	0.2258	3.1187
16.44	0.6974	0.2268	3.0748
16.69	0.6982	0.2299	3.0367
16.94	0.7178	0.2411	2.9770
17.19	0.7001	0.2386	2.9346
17.44	0.7255	0.2496	2.9070
17.69	0.7214	0.2490	2.8968
17.94	0.7245	0.2571	2.8180
18.19	0.7280	0.2651	2.7465
18.44	0.7197	0.2631	2.7354
18.69	0.7297	0.2710	2.6928
18.94	0.7357	0.2749	2.6765
19.19	0.7513	0.2810	2.6732
19.44	0.7479	0.2866	2.6098
19.69	0.7394	0.2855	2.5898
19.94	0.7326	0.2841	2.5783
20.19	0.7381	0.2885	2.5588
20.44	0.7258	0.2974	2.4404
20.69	0.7315	0.2961	2.4706
20.94	0.7245	0.3047	2.3777
21.19	0.7390	0.3108	2.3779
21.44	0.7264	0.3054	2.3785
21.69	0.7334	0.3127	2.3453
21.94	0.7325	0.3171	2.3098
22.19	0.7329	0.3201	2.2897
22.44	0.7158	0.3147	2.2744
22.69	0.7402	0.3279	2.2576
22.94	0.7393	0.3437	2.1513
23.19	0.7289	0.3433	2.1235
23.44	0.7248	0.3368	2.1520
23.69	0.7228	0.3464	2.0868
23.94	0.7223	0.3513	2.0558
24.19	0.7224	0.3422	2.1107
24.44	0.7279	0.3503	2.0779
24.69	0.7206	0.3558	2.0255
24.94	0.7254	0.3592	2.0196

Table D.3: Model #3, g=0.5c, s=0.5c, Aerodynamic Data at Re 60,000

α (°)	C_L (-)	C_D (-)	L/D (-)
-1.93	-0.1175	0.0257	-4.5653
-1.68	-0.0892	0.0265	-3.3603
-1.43	-0.0766	0.0269	-2.8490
-1.18	-0.0624	0.0257	-2.4278
-0.93	-0.0432	0.0269	-1.6069
-0.68	-0.0420	0.0269	-1.5621
-0.43	-0.0222	0.0238	-0.9347
-0.18	-0.0139	0.0242	-0.5736
0.07	0.0084	0.0258	0.3273
0.32	0.0338	0.0257	1.3141
0.57	0.0402	0.0254	1.5849
0.82	0.0513	0.0254	2.0226
1.07	0.0628	0.0250	2.5150
1.32	0.0776	0.0254	3.0528
1.57	0.0893	0.0254	3.5202
1.82	0.1116	0.0257	4.3389
2.07	0.1250	0.0269	4.6471
2.32	0.1500	0.0311	4.8166
2.57	0.1621	0.0311	5.2079
2.82	0.1696	0.0338	5.0201
3.07	0.1770	0.0315	5.6280
3.32	0.1956	0.0326	5.9963
3.57	0.1956	0.0326	5.9963
3.82	0.2214	0.0368	6.0185
4.07	0.2444	0.0369	6.6313
4.32	0.2588	0.0407	6.3641
4.57	0.2830	0.0426	6.6481
4.82	0.2784	0.0430	6.4786
5.07	0.3112	0.0468	6.6540
5.32	0.3479	0.0517	6.7218
5.57	0.3581	0.0545	6.5763
5.82	0.3529	0.0544	6.4893
6.07	0.3822	0.0605	6.3124
6.32	0.4117	0.0632	6.5181
6.57	0.4293	0.0697	6.1588
6.82	0.4453	0.0689	6.4601
7.07	0.4686	0.0720	6.5051
7.32	0.4853	0.0800	6.0672
7.57	0.5005	0.0839	5.9685
7.82	0.5034	0.0862	5.8427
8.07	0.5206	0.0900	5.7875
8.32	0.5390	0.0942	5.7233
8.57	0.5426	0.0972	5.5821
8.82	0.5642	0.1030	5.4774
9.07	0.5840	0.1107	5.2768
9.32	0.5899	0.1117	5.2793
9.57	0.6010	0.1152	5.2159
9.82	0.6227	0.1232	5.0533
10.07	0.6390	0.1286	4.9681
10.32	0.6481	0.1317	4.9205
10.57	0.6532	0.1344	4.8614
10.82	0.6701	0.1413	4.7437
11.07	0.6807	0.1428	4.7678
11.32	0.6840	0.1481	4.6183
11.57	0.7058	0.1546	4.5659
11.82	0.7148	0.1585	4.5102
12.07	0.7198	0.1635	4.4037
12.32	0.7253	0.1665	4.3569
12.57	0.7332	0.1703	4.3064
12.82	0.7335	0.1760	4.1673
13.07	0.7391	0.1786	4.1372
13.32	0.7499	0.1840	4.0755
13.57	0.7652	0.1928	3.9680
13.82	0.7708	0.1993	3.8671
14.07	0.7766	0.2005	3.8741
14.32	0.7880	0.2112	3.7316
14.57	0.7857	0.2111	3.7218
14.82	0.7823	0.2142	3.6516
15.07	0.7967	0.2207	3.6098
15.32	0.7890	0.2207	3.5752
15.57	0.7969	0.2276	3.5011
15.82	0.8172	0.2368	3.4508
16.07	0.8120	0.2409	3.3702
16.32	0.8025	0.2393	3.3529
16.57	0.8025	0.2416	3.3216
16.82	0.8053	0.2474	3.2553
17.07	0.8303	0.2574	3.2258
17.32	0.8260	0.2604	3.1724
17.57	0.8472	0.2720	3.1152
17.82	0.8308	0.2676	3.1044
18.07	0.8224	0.2689	3.0581
18.32	0.8170	0.2733	2.9891
18.57	0.8349	0.2814	2.9667
18.82	0.8594	0.2910	2.9528
19.07	0.8538	0.2956	2.8878
19.32	0.8480	0.2971	2.8541
19.57	0.8616	0.3063	2.8132
19.82	0.8685	0.3144	2.7621
20.07	0.8655	0.3160	2.7392
20.32	0.8552	0.3146	2.7185
20.57	0.8629	0.3234	2.6679
20.82	0.8560	0.3261	2.6249
21.07	0.8600	0.3288	2.6154
21.32	0.8724	0.3372	2.5868
21.57	0.8883	0.3476	2.5551
21.82	0.8889	0.3522	2.5239
22.07	0.8899	0.3569	2.4936
22.32	0.8990	0.3634	2.4735
22.57	0.8767	0.3590	2.4424
22.82	0.8848	0.3668	2.4124
23.07	0.8778	0.3662	2.3972
23.32	0.8981	0.3791	2.3688
23.57	0.8820	0.3789	2.3278
23.82	0.9241	0.4008	2.3057
24.07	0.9212	0.4022	2.2905
24.32	0.8756	0.3858	2.2694
24.57	0.9103	0.4075	2.2341
24.82	0.8768	0.3969	2.2094
25.07	0.8826	0.4025	2.1927

Table D.4: Model #4, g=0.5c, s=1c, Aerodynamic Data at Re 60,000

α (°)	C_L (-)	C_D (-)	L/D (-)
-2.03	-0.1223	0.0267	-4.5880
-1.78	-0.1164	0.0212	-5.4945
-1.53	-0.1034	0.0212	-4.8713
-1.28	-0.0844	0.0208	-4.0489
-1.03	-0.0611	0.0216	-2.8240
-0.78	-0.0590	0.0228	-2.5897
-0.53	-0.0414	0.0181	-2.2882
-0.28	-0.0204	0.0197	-1.0325
-0.03	-0.0164	0.0197	-0.8337
0.22	0.0111	0.0209	0.5307
0.47	0.0187	0.0224	0.8358
0.72	0.0328	0.0232	1.4142
0.97	0.0482	0.0205	2.3547
1.22	0.0759	0.0205	3.7079
1.47	0.0922	0.0193	4.7760
1.72	0.1013	0.0209	4.8575
1.97	0.1296	0.0243	5.3232
2.22	0.1590	0.0240	6.6257
2.47	0.1649	0.0267	6.1814
2.72	0.1655	0.0263	6.2963
2.97	0.1747	0.0259	6.7523
3.22	0.2060	0.0279	7.3962
3.47	0.2060	0.0279	7.3962
3.72	0.2231	0.0282	7.9136
3.97	0.2537	0.0352	7.2112
4.22	0.2622	0.0340	7.7047
4.47	0.2750	0.0371	7.4161
4.72	0.2948	0.0375	7.8636
4.97	0.3160	0.0413	7.6449
5.22	0.3450	0.0425	8.1246
5.47	0.3722	0.0476	7.8227
5.72	0.3829	0.0506	7.5611
5.97	0.3968	0.0526	7.5450
6.22	0.4368	0.0584	7.4848
6.47	0.4513	0.0627	7.2029
6.72	0.4775	0.0673	7.0958

α (°)	C_L (-)	C_D (-)	L/D (-)
6.97	0.4948	0.0707	6.9940
7.22	0.5235	0.0793	6.5997
7.47	0.5386	0.0812	6.6346
7.72	0.5641	0.0867	6.5087
7.97	0.5898	0.0955	6.1762
8.22	0.6114	0.0960	6.3715
8.47	0.6181	0.1002	6.1683
8.72	0.6371	0.1040	6.1257
8.97	0.6474	0.1079	6.0015
9.22	0.6615	0.1129	5.8606
9.47	0.6690	0.1148	5.8283
9.72	0.6885	0.1217	5.6557
9.97	0.7080	0.1295	5.4673
10.22	0.7239	0.1310	5.5252
10.47	0.7382	0.1396	5.2895
10.72	0.7540	0.1445	5.2175
10.97	0.7664	0.1511	5.0721
11.22	0.7935	0.1569	5.0567
11.47	0.8043	0.1650	4.8730
11.72	0.8225	0.1701	4.8358
11.97	0.8407	0.1767	4.7584
12.22	0.8593	0.1844	4.6601
12.47	0.8729	0.1929	4.5256
12.72	0.8836	0.1952	4.5276
12.97	0.8868	0.2021	4.3882
13.22	0.9032	0.2106	4.2899
13.47	0.9079	0.2176	4.1730
13.72	0.9176	0.2175	4.2185
13.97	0.9201	0.2264	4.0642
14.22	0.9286	0.2303	4.0314
14.47	0.9485	0.2403	3.9468
14.72	0.9449	0.2422	3.9007
14.97	0.9433	0.2473	3.8144
15.22	0.9633	0.2566	3.7545
15.47	0.9753	0.2604	3.7459
15.72	0.9785	0.2700	3.6245

α (°)	C_L (-)	C_D (-)	L/D (-)
15.97	0.9851	0.2758	3.5712
16.22	0.9811	0.2774	3.5367
16.47	0.9886	0.2851	3.4676
16.72	0.9996	0.2890	3.4588
16.97	1.0075	0.2959	3.4045
17.22	1.0006	0.2998	3.3372
17.47	0.9989	0.3064	3.2603
17.72	1.0236	0.3172	3.2274
17.97	1.0183	0.3199	3.1832
18.22	1.0010	0.3211	3.1175
18.47	1.0014	0.3252	3.0795
18.72	1.0145	0.3330	3.0465
18.97	1.0379	0.3465	2.9954
19.22	1.0235	0.3457	2.9608
19.47	1.0275	0.3535	2.9067
19.72	1.0315	0.3578	2.8830
19.97	1.0276	0.3627	2.8329
20.22	1.0283	0.3650	2.8170
20.47	1.0217	0.3685	2.7726
20.72	1.0479	0.3812	2.7488
20.97	1.0444	0.3878	2.6929
21.22	1.0581	0.3983	2.6563
21.47	1.0560	0.4009	2.6339
21.72	1.0680	0.4106	2.6011
21.97	1.0645	0.4126	2.5797
22.22	1.0807	0.4248	2.5437
22.47	1.0689	0.4238	2.5223
22.72	1.0697	0.4287	2.4950
22.97	1.0682	0.4352	2.4546
23.22	1.0731	0.4431	2.4219
23.47	1.0583	0.4410	2.3997
23.72	1.0777	0.4500	2.3950
23.97	1.0699	0.4585	2.3336
24.22	1.0681	0.4612	2.3160
24.47	1.0711	0.4678	2.2895
24.72	1.0669	0.4716	2.2620
24.97	1.0831	0.4832	2.2417

Table D.5: Model #5, g=1c, s=0.5c, Aerodynamic Data at Re 60,000

α (°)	C_L (-)	C_D (-)	L/D (-)
-1.89	-0.1382	0.0449	-3.0740
-1.64	-0.1296	0.0462	-2.8064
-1.39	-0.1107	0.0452	-2.4491
-1.14	-0.0928	0.0440	-2.1062
-0.89	-0.0720	0.0449	-1.6051
-0.64	-0.0464	0.0438	-1.0596
-0.39	-0.0343	0.0413	-0.8294
-0.14	-0.0174	0.0412	-0.4217
0.11	0.0046	0.0418	0.1103
0.36	0.0233	0.0420	0.5550
0.61	0.0441	0.0435	1.0133
0.86	0.0673	0.0406	1.6566
1.11	0.0730	0.0426	1.7152
1.36	0.0933	0.0448	2.0814
1.61	0.1144	0.0478	2.3919
1.86	0.1374	0.0476	2.8841
2.11	0.1313	0.0431	3.0449
2.36	0.1645	0.0464	3.5468
2.61	0.1916	0.0502	3.8148
2.86	0.2095	0.0509	4.1146
3.11	0.2259	0.0516	4.3785
3.36	0.2404	0.0547	4.3922
3.61	0.2404	0.0547	4.3922
3.86	0.2575	0.0564	4.5672
4.11	0.2748	0.0562	4.8896
4.36	0.2935	0.0603	4.8654
4.61	0.3275	0.0627	5.2265
4.86	0.3343	0.0643	5.1974
5.11	0.3495	0.0646	5.4093
5.36	0.3874	0.0710	5.4594
5.61	0.4144	0.0749	5.5310
5.86	0.4395	0.0784	5.6058
6.11	0.4611	0.0820	5.6217
6.36	0.4761	0.0848	5.6155
6.61	0.4962	0.0888	5.5858
6.86	0.5247	0.0910	5.7676
7.11	0.5442	0.0966	5.6314
7.36	0.5524	0.0988	5.5891
7.61	0.5740	0.1041	5.5140
7.86	0.6079	0.1110	5.4784
8.11	0.6323	0.1152	5.4868
8.36	0.6345	0.1171	5.4190
8.61	0.6591	0.1247	5.2843
8.86	0.6647	0.1284	5.1771
9.11	0.6900	0.1351	5.1060
9.36	0.7033	0.1378	5.1046
9.61	0.7212	0.1410	5.1142
9.86	0.7473	0.1520	4.9173
10.11	0.7651	0.1584	4.8307
10.36	0.7689	0.1597	4.8147
10.61	0.7782	0.1669	4.6634
10.86	0.7938	0.1687	4.7054
11.11	0.8056	0.1759	4.5811
11.36	0.8213	0.1837	4.4707
11.61	0.8308	0.1879	4.4203
11.86	0.8276	0.1926	4.2968
12.11	0.8421	0.1985	4.2420
12.36	0.8498	0.2037	4.1715
12.61	0.8624	0.2076	4.1533
12.86	0.8632	0.2100	4.1103
13.11	0.8665	0.2167	3.9980
13.36	0.8709	0.2201	3.9566
13.61	0.8828	0.2268	3.8923
13.86	0.8923	0.2342	3.8104
14.11	0.8882	0.2368	3.7514
14.36	0.8983	0.2446	3.6720
14.61	0.8992	0.2479	3.6265
14.86	0.8990	0.2508	3.5845
15.11	0.9058	0.2557	3.5416
15.36	0.9026	0.2594	3.4794
15.61	0.9028	0.2643	3.4155
15.86	0.9003	0.2690	3.3465
16.11	0.9069	0.2721	3.3327
16.36	0.9046	0.2786	3.2472
16.61	0.9039	0.2806	3.2214
16.86	0.9058	0.2840	3.1899
17.11	0.9150	0.2923	3.1306
17.36	0.9130	0.2969	3.0752
17.61	0.9096	0.2966	3.0671
17.86	0.9196	0.3058	3.0073
18.11	0.9180	0.3069	2.9912
18.36	0.9125	0.3094	2.9489
18.61	0.9300	0.3203	2.9036
18.86	0.9217	0.3224	2.8587
19.11	0.9184	0.3204	2.8664
19.36	0.9177	0.3275	2.8020
19.61	0.9295	0.3357	2.7692
19.86	0.9294	0.3386	2.7453
20.11	0.9348	0.3482	2.6849
20.36	0.9310	0.3470	2.6826
20.61	0.9459	0.3579	2.6427
20.86	0.9315	0.3619	2.5742
21.11	0.9345	0.3629	2.5755
21.36	0.9431	0.3696	2.5519
21.61	0.9321	0.3761	2.4784
21.86	0.9503	0.3847	2.4700
22.11	0.9450	0.3837	2.4628
22.36	0.9620	0.3949	2.4361
22.61	0.9476	0.3960	2.3931
22.86	0.9524	0.3975	2.3959
23.11	0.9560	0.4074	2.3464
23.36	0.9594	0.4112	2.3335
23.61	0.9542	0.4134	2.3081
23.86	0.9659	0.4225	2.2861
24.11	0.9714	0.4303	2.2577
24.36	0.9809	0.4409	2.2247
24.61	0.9728	0.4387	2.2173
24.86	0.9709	0.4471	2.1718
25.11	0.9809	0.4526	2.1674

Table D.6: Model #6, g=1c, s=1c, Aerodynamic Data at Re 60,000

α (°)	C_L (-)	C_D (-)	L/D (-)
-2.03	-0.1580	0.0246	-6.4227
-1.78	-0.1316	0.0276	-4.7698
-1.53	-0.1272	0.0250	-5.0968
-1.28	-0.1054	0.0250	-4.2244
-1.03	-0.1055	0.0250	-4.2166
-0.78	-0.0673	0.0220	-3.0624
-0.53	-0.0414	0.0262	-1.5837
-0.28	-0.0261	0.0223	-1.1712
-0.03	-0.0034	0.0197	-0.1738
0.22	0.0211	0.0212	0.9949
0.47	0.0303	0.0209	1.4536
0.72	0.0439	0.0197	2.2251
0.97	0.0684	0.0220	3.1070
1.22	0.0609	0.0208	2.9291
1.47	0.0857	0.0216	3.9684
1.72	0.1087	0.0220	4.9419
1.97	0.1274	0.0227	5.6107
2.22	0.1425	0.0280	5.0966
2.47	0.1552	0.0296	5.2496
2.72	0.1810	0.0299	6.0592
2.97	0.2085	0.0336	6.2020
3.22	0.2255	0.0340	6.6296
3.47	0.2255	0.0340	6.6296
3.72	0.2420	0.0367	6.5993
3.97	0.2663	0.0378	7.0456
4.22	0.2784	0.0404	6.8889
4.47	0.2967	0.0404	7.3460
4.72	0.3170	0.0434	7.3043
4.97	0.3205	0.0467	6.8603
5.22	0.3686	0.0512	7.1952
5.47	0.3752	0.0524	7.1626
5.72	0.4046	0.0516	7.8393
5.97	0.4347	0.0622	6.9911
6.22	0.4564	0.0651	7.0109
6.47	0.4794	0.0659	7.2730
6.72	0.4971	0.0685	7.2533
6.97	0.5180	0.0756	6.8499
7.22	0.5411	0.0779	6.9430
7.47	0.5708	0.0843	6.7710
7.72	0.5912	0.0892	6.6306
7.97	0.6002	0.0967	6.2076
8.22	0.6200	0.1004	6.1759
8.47	0.6320	0.1041	6.0699
8.72	0.6380	0.1094	5.8309
8.97	0.6744	0.1143	5.8984
9.22	0.7072	0.1233	5.7356
9.47	0.7113	0.1286	5.5317
9.72	0.7360	0.1315	5.5960
9.97	0.7393	0.1382	5.3481
10.22	0.7511	0.1402	5.3580
10.47	0.7677	0.1466	5.2363
10.72	0.7909	0.1518	5.2099
10.97	0.7996	0.1593	5.0180
11.22	0.8105	0.1668	4.8587
11.47	0.8231	0.1709	4.8153
11.72	0.8252	0.1752	4.7112
11.97	0.8294	0.1792	4.6281
12.22	0.8295	0.1830	4.5335
12.47	0.8476	0.1875	4.5207
12.72	0.8480	0.1924	4.4073
12.97	0.8517	0.1976	4.3104
13.22	0.8452	0.2040	4.1426
13.47	0.8628	0.2093	4.1228
13.72	0.8717	0.2126	4.0998
13.97	0.8723	0.2206	3.9550
14.22	0.8703	0.2239	3.8864
14.47	0.8730	0.2314	3.7725
14.72	0.8776	0.2313	3.7942
14.97	0.8818	0.2393	3.6843
15.22	0.8850	0.2438	3.6296
15.47	0.8863	0.2463	3.5980
15.72	0.8990	0.2516	3.5728
15.97	0.8851	0.2546	3.4763
16.22	0.8882	0.2550	3.4829
16.47	0.8878	0.2659	3.3390
16.72	0.8901	0.2715	3.2783
16.97	0.8953	0.2726	3.2844
17.22	0.8828	0.2741	3.2208
17.47	0.8816	0.2801	3.1470
17.72	0.8811	0.2821	3.1235
17.97	0.8898	0.2918	3.0492
18.22	0.9104	0.3008	3.0265
18.47	0.9177	0.3045	3.0136
18.72	0.9019	0.3083	2.9252
18.97	0.9211	0.3188	2.8893
19.22	0.8960	0.3151	2.8436
19.47	0.8974	0.3187	2.8155
19.72	0.9224	0.3305	2.7911
19.97	0.9210	0.3314	2.7787
20.22	0.9291	0.3383	2.7466
20.47	0.9306	0.3428	2.7146
20.72	0.9147	0.3388	2.6997
20.97	0.9272	0.3485	2.6607
21.22	0.9258	0.3545	2.6117
21.47	0.9395	0.3582	2.6228
21.72	0.9341	0.3646	2.5618
21.97	0.9274	0.3657	2.5358
22.22	0.9375	0.3765	2.4901
22.47	0.9283	0.3758	2.4702
22.72	0.9362	0.3864	2.4231
22.97	0.9418	0.3882	2.4263
23.22	0.9382	0.3984	2.3547
23.47	0.9360	0.4032	2.3212
23.72	0.9386	0.4069	2.3066
23.97	0.9442	0.4129	2.2869
24.22	0.9553	0.4221	2.2635
24.47	0.9569	0.4253	2.2502
24.72	0.9420	0.4257	2.2127
24.97	0.9491	0.4310	2.2023

Table D.7: Model #7, g=2c, s=1c, Aerodynamic Data at Re 60,000

α (°)	C_L (-)	C_D (-)	L/D (-)
-2.14	-0.1938	0.0341	-5.6899
-1.89	-0.1679	0.0333	-5.0394
-1.64	-0.1388	0.0315	-4.4012
-1.39	-0.1295	0.0321	-4.0370
-1.14	-0.1079	0.0283	-3.8101
-0.89	-0.0877	0.0260	-3.3690
-0.64	-0.0698	0.0273	-2.5569
-0.39	-0.0443	0.0303	-1.4627
-0.14	-0.0204	0.0271	-0.7552
0.11	0.0061	0.0305	0.2008
0.36	0.0256	0.0282	0.9075
0.61	0.0390	0.0285	1.3666
0.86	0.0658	0.0283	2.3258
1.11	0.0903	0.0266	3.4004
1.36	0.1070	0.0266	4.0273
1.61	0.1226	0.0292	4.1955
1.86	0.1379	0.0331	4.1710
2.11	0.1695	0.0315	5.3831
2.36	0.1929	0.0305	6.3149
2.61	0.2153	0.0387	5.5570
2.86	0.2306	0.0395	5.8433
3.11	0.2451	0.0438	5.6013
3.36	0.2451	0.0438	5.6013
3.61	0.2675	0.0428	6.2574
3.86	0.2927	0.0429	6.8212
4.11	0.3164	0.0452	6.9928
4.36	0.3443	0.0467	7.3717
4.61	0.3530	0.0514	6.8735
4.86	0.3719	0.0534	6.9664
5.11	0.4222	0.0593	7.1199
5.36	0.4413	0.0596	7.4076
5.61	0.4760	0.0658	7.2363
5.86	0.5039	0.0681	7.4006
6.11	0.5260	0.0743	7.0832
6.36	0.5486	0.0780	7.0353
6.61	0.5776	0.0809	7.1415

α (°)	C_L (-)	C_D (-)	L/D (-)
6.86	0.5993	0.0859	6.9757
7.11	0.6277	0.0899	6.9860
7.36	0.6563	0.0954	6.8810
7.61	0.6817	0.1003	6.7947
7.86	0.6955	0.1030	6.7557
8.11	0.7078	0.1128	6.2732
8.36	0.7299	0.1104	6.6127
8.61	0.7420	0.1239	5.9889
8.86	0.7555	0.1255	6.0202
9.11	0.7724	0.1293	5.9736
9.36	0.7792	0.1350	5.7717
9.61	0.7776	0.1404	5.5376
9.86	0.7950	0.1445	5.5006
10.11	0.7984	0.1498	5.3291
10.36	0.8133	0.1566	5.1950
10.61	0.8028	0.1627	4.9333
10.86	0.8193	0.1665	4.9220
11.11	0.8247	0.1684	4.8966
11.36	0.8156	0.1668	4.8898
11.61	0.8319	0.1737	4.7885
11.86	0.8414	0.1778	4.7316
12.11	0.8279	0.1790	4.6254
12.36	0.8322	0.1861	4.4707
12.61	0.8468	0.1893	4.4734
12.86	0.8553	0.1965	4.3528
13.11	0.8337	0.1966	4.2400
13.36	0.8427	0.2063	4.0853
13.61	0.8421	0.2130	3.9530
13.86	0.8402	0.2134	3.9368
14.11	0.8293	0.2122	3.9072
14.36	0.8406	0.2197	3.8265
14.61	0.8475	0.2227	3.8052
14.86	0.8430	0.2315	3.6416
15.11	0.8450	0.2270	3.7224
15.36	0.8565	0.2382	3.5956
15.61	0.8733	0.2425	3.6014

α (°)	C_L (-)	C_D (-)	L/D (-)
15.86	0.8677	0.2433	3.5667
16.11	0.8756	0.2478	3.5343
16.36	0.8609	0.2519	3.4177
16.61	0.8841	0.2601	3.3993
16.86	0.8689	0.2631	3.3018
17.11	0.8669	0.2615	3.3156
17.36	0.8693	0.2646	3.2854
17.61	0.8804	0.2736	3.2176
17.86	0.8968	0.2791	3.2133
18.11	0.8827	0.2823	3.1270
18.36	0.8721	0.2872	3.0366
18.61	0.9020	0.2969	3.0376
18.86	0.8956	0.2940	3.0461
19.11	0.8765	0.2997	2.9248
19.36	0.8798	0.3034	2.8996
19.61	0.8838	0.3118	2.8349
19.86	0.8708	0.3108	2.8013
20.11	0.8800	0.3182	2.7653
20.36	0.8812	0.3196	2.7572
20.61	0.8974	0.3237	2.7723
20.86	0.8909	0.3274	2.7209
21.11	0.8930	0.3351	2.6645
21.36	0.8897	0.3364	2.6448
21.61	0.8922	0.3406	2.6192
21.86	0.8964	0.3514	2.5507
22.11	0.9205	0.3548	2.5944
22.36	0.8921	0.3561	2.5055
22.61	0.9112	0.3614	2.5211
22.86	0.8893	0.3633	2.4479
23.11	0.8972	0.3709	2.4187
23.36	0.8857	0.3720	2.3810
23.61	0.8992	0.3736	2.4068
23.86	0.9113	0.3826	2.3817
24.11	0.8971	0.3854	2.3275
24.36	0.9030	0.3918	2.3046
24.61	0.9162	0.4020	2.2792
24.86	0.9384	0.4050	2.3172

Table D.8: Model #8, g=1c, s=1.5c, Aerodynamic Data at Re 60,000

α (°)	C_L (-)	C_D (-)	L/D (-)
-2.42	-0.1897	0.0290	-6.5323
-2.17	-0.1676	0.0308	-5.4385
-1.92	-0.1492	0.0288	-5.1827
-1.67	-0.1334	0.0280	-4.7600
-1.42	-0.1004	0.0245	-4.1048
-1.17	-0.0853	0.0257	-3.3141
-0.92	-0.0787	0.0252	-3.1213
-0.67	-0.0529	0.0224	-2.3614
-0.42	-0.0337	0.0222	-1.5225
-0.17	-0.0116	0.0222	-0.5235
0.08	0.0070	0.0258	0.2715
0.33	0.0247	0.0242	1.0223
0.58	0.0426	0.0256	1.6616
0.83	0.0583	0.0249	2.3401
1.08	0.0917	0.0249	3.6770
1.33	0.1006	0.0259	3.8804
1.58	0.1182	0.0274	4.3087
1.83	0.1433	0.0241	5.9460
2.08	0.1597	0.0285	5.6118
2.33	0.1879	0.0301	6.2405
2.58	0.2064	0.0313	6.6033
2.83	0.2257	0.0307	7.3451
3.08	0.2257	0.0307	7.3451
3.33	0.2482	0.0383	6.4852
3.58	0.2585	0.0362	7.1326
3.83	0.2893	0.0390	7.4123
4.08	0.3017	0.0401	7.5248
4.33	0.3289	0.0454	7.2506
4.58	0.3497	0.0458	7.6350
4.83	0.3882	0.0504	7.6954
5.08	0.4030	0.0553	7.2868
5.33	0.4235	0.0526	8.0554
5.58	0.4549	0.0608	7.4786
5.83	0.4751	0.0644	7.3814
6.08	0.5036	0.0694	7.2526
6.33	0.5057	0.0711	7.1130
6.58	0.5194	0.0737	7.0522
6.83	0.5527	0.0795	6.9525
7.08	0.5860	0.0837	7.0014
7.33	0.6106	0.0912	6.6968
7.58	0.6267	0.0921	6.8087
7.83	0.6297	0.0995	6.3286
8.08	0.6583	0.1064	6.1885
8.33	0.6797	0.1119	6.0748
8.58	0.6996	0.1134	6.1716
8.83	0.7095	0.1229	5.7749
9.08	0.7334	0.1271	5.7685
9.33	0.7511	0.1309	5.7392
9.58	0.7551	0.1338	5.6426
9.83	0.7753	0.1412	5.4911
10.08	0.7749	0.1448	5.3522
10.33	0.7990	0.1518	5.2648
10.58	0.8103	0.1588	5.1031
10.83	0.8237	0.1639	5.0268
11.08	0.8264	0.1649	5.0126
11.33	0.8264	0.1751	4.7182
11.58	0.8499	0.1778	4.7793
11.83	0.8539	0.1859	4.5923
12.08	0.8619	0.1882	4.5804
12.33	0.8505	0.1905	4.4645
12.58	0.8547	0.1980	4.3173
12.83	0.8654	0.1992	4.3443
13.08	0.8605	0.2041	4.2162
13.33	0.8775	0.2123	4.1326
13.58	0.8892	0.2171	4.0952
13.83	0.8734	0.2207	3.9579
14.08	0.8804	0.2254	3.9054
14.33	0.8779	0.2275	3.8591
14.58	0.8654	0.2327	3.7186
14.83	0.8827	0.2355	3.7486
15.08	0.8859	0.2387	3.7109
15.33	0.8806	0.2438	3.6124
15.58	0.8889	0.2477	3.5881
15.83	0.8875	0.2545	3.4876
16.08	0.9026	0.2558	3.5285
16.33	0.9090	0.2651	3.4285
16.58	0.8958	0.2658	3.3704
16.83	0.9094	0.2733	3.3274
17.08	0.8887	0.2735	3.2497
17.33	0.9004	0.2764	3.2581
17.58	0.9092	0.2889	3.1468
17.83	0.9060	0.2929	3.0930
18.08	0.9062	0.2922	3.1009
18.33	0.9099	0.2985	3.0483
18.58	0.9188	0.3073	2.9900
18.83	0.9185	0.3076	2.9860
19.08	0.9151	0.3153	2.9027
19.33	0.9092	0.3196	2.8447
19.58	0.9109	0.3249	2.8038
19.83	0.9111	0.3246	2.8072
20.08	0.9361	0.3333	2.8090
20.33	0.9380	0.3445	2.7230
20.58	0.9258	0.3452	2.6819
20.83	0.9393	0.3537	2.6558
21.08	0.9374	0.3558	2.6346
21.33	0.9395	0.3578	2.6261
21.58	0.9333	0.3656	2.5528
21.83	0.9419	0.3702	2.5444
22.08	0.9340	0.3720	2.5109
22.33	0.9354	0.3771	2.4804
22.58	0.9449	0.3840	2.4606
22.83	0.9334	0.3850	2.4246
23.08	0.9454	0.3919	2.4125
23.33	0.9399	0.3966	2.3699
23.58	0.9358	0.4005	2.3363
23.83	0.9478	0.4085	2.3201
24.08	0.9494	0.4126	2.3008
24.33	0.9486	0.4170	2.2750
24.58	0.9594	0.4263	2.2506

Table D.9: Model #9, g=0.5c, s=-0.5c, Aerodynamic Data at Re 60,000

α (°)	C_L (-)	C_D (-)	L/D (-)
-1.93	-0.1136	0.0249	-4.5684
-1.68	-0.0957	0.0245	-3.9096
-1.43	-0.0828	0.0234	-3.5436
-1.18	-0.0654	0.0226	-2.8904
-0.93	-0.0526	0.0205	-2.5671
-0.68	-0.0384	0.0227	-1.6935
-0.43	-0.0183	0.0220	-0.8323
-0.18	-0.0105	0.0194	-0.5403
0.07	-0.0007	0.0201	-0.0333
0.32	0.0175	0.0226	0.7730
0.57	0.0248	0.0216	1.1476
0.82	0.0327	0.0208	1.5714
1.07	0.0605	0.0212	2.8515
1.32	0.0805	0.0226	3.5546
1.57	0.0901	0.0230	3.9209
1.82	0.0990	0.0219	4.5232
2.07	0.1125	0.0226	4.9750
2.32	0.1315	0.0263	5.0056
2.57	0.1489	0.0266	5.5999
2.82	0.1701	0.0291	5.8373
3.07	0.1814	0.0281	6.4589
3.32	0.1955	0.0306	6.3894
3.57	0.1955	0.0306	6.3894
3.82	0.2053	0.0310	6.6261
4.07	0.2241	0.0331	6.7642
4.32	0.2322	0.0343	6.7738
4.57	0.2464	0.0368	6.6960
4.82	0.2601	0.0372	6.9879
5.07	0.2838	0.0426	6.6539
5.32	0.3134	0.0437	7.1708
5.57	0.3322	0.0474	7.0084
5.82	0.3498	0.0518	6.7575
6.07	0.3634	0.0506	7.1798
6.32	0.3670	0.0561	6.5420
6.57	0.3808	0.0586	6.4947
6.82	0.3984	0.0630	6.3264
7.07	0.4076	0.0652	6.2514
7.32	0.4131	0.0689	5.9996
7.57	0.4289	0.0732	5.8591
7.82	0.4376	0.0769	5.6916
8.07	0.4431	0.0769	5.7637
8.32	0.4604	0.0802	5.7433
8.57	0.4691	0.0838	5.5991
8.82	0.4829	0.0878	5.5010
9.07	0.4877	0.0929	5.2472
9.32	0.4914	0.0929	5.2898
9.57	0.4968	0.0976	5.0883
9.82	0.5068	0.1009	5.0235
10.07	0.5210	0.1039	5.0137
10.32	0.5228	0.1082	4.8302
10.57	0.5298	0.1112	4.7650
10.82	0.5405	0.1170	4.6213
11.07	0.5436	0.1200	4.5314
11.32	0.5482	0.1218	4.5018
11.57	0.5606	0.1270	4.4153
11.82	0.5586	0.1287	4.3403
12.07	0.5670	0.1341	4.2264
12.32	0.5802	0.1400	4.1453
12.57	0.5748	0.1407	4.0858
12.82	0.5773	0.1462	3.9486
13.07	0.5787	0.1469	3.9384
13.32	0.5892	0.1531	3.8490
13.57	0.5921	0.1571	3.7683
13.82	0.5904	0.1575	3.7482
14.07	0.5923	0.1615	3.6662
14.32	0.5913	0.1655	3.5724
14.57	0.5988	0.1703	3.5167
14.82	0.5886	0.1692	3.4786
15.07	0.5936	0.1739	3.4135
15.32	0.5936	0.1765	3.3628
15.57	0.5880	0.1805	3.2584
15.82	0.6091	0.1874	3.2496
16.07	0.5991	0.1905	3.1442
16.32	0.5949	0.1900	3.1315
16.57	0.5910	0.1947	3.0360
16.82	0.5988	0.1957	3.0600
17.07	0.6015	0.2012	2.9903
17.32	0.5939	0.1997	2.9735
17.57	0.6036	0.2064	2.9241
17.82	0.5989	0.2067	2.8970
18.07	0.5942	0.2075	2.8633
18.32	0.5994	0.2169	2.7634
18.57	0.6096	0.2185	2.7897
18.82	0.5882	0.2158	2.7256
19.07	0.5953	0.2198	2.7088
19.32	0.5971	0.2238	2.6687
19.57	0.5907	0.2247	2.6284
19.82	0.6041	0.2315	2.6095
20.07	0.5838	0.2312	2.5251
20.32	0.5940	0.2382	2.4942
20.57	0.5937	0.2374	2.5011
20.82	0.5833	0.2396	2.4346
21.07	0.5706	0.2363	2.4146
21.32	0.5681	0.2367	2.3998
21.57	0.5738	0.2433	2.3589
21.82	0.5708	0.2465	2.3155
22.07	0.5757	0.2494	2.3086
22.32	0.5619	0.2476	2.2694
22.57	0.5555	0.2458	2.2599
22.82	0.5695	0.2571	2.2151
23.07	0.5591	0.2540	2.2010
23.32	0.5582	0.2597	2.1494
23.57	0.5717	0.2669	2.1424
23.82	0.5584	0.2616	2.1348
24.07	0.5468	0.2612	2.0935
24.32	0.5504	0.2670	2.0619
24.57	0.5426	0.2603	2.0847
24.82	0.5358	0.2618	2.0469
25.07	0.5333	0.2652	2.0111

Table D.10: Model #10, g=0.5c, s=-1c, Aerodynamic Data at Re 60,000

α (°)	C_L (-)	C_D (-)	L/D (-)
-1.71	-0.1190	0.0251	-4.7427
-1.46	-0.0950	0.0216	-4.4050
-1.21	-0.0729	0.0205	-3.5509
-0.96	-0.0591	0.0205	-2.8746
-0.71	-0.0432	0.0202	-2.1361
-0.46	-0.0323	0.0215	-1.5029
-0.21	-0.0087	0.0190	-0.4585
0.04	0.0086	0.0215	0.3972
0.29	0.0099	0.0210	0.4691
0.54	0.0356	0.0210	1.6912
0.79	0.0544	0.0210	2.5891
1.04	0.0690	0.0212	3.2513
1.29	0.0827	0.0220	3.7670
1.54	0.0963	0.0219	4.3919
1.79	0.1090	0.0250	4.3621
2.04	0.1258	0.0260	4.8375
2.29	0.1484	0.0270	5.5044
2.54	0.1643	0.0279	5.8877
2.79	0.1809	0.0292	6.1884
3.04	0.2039	0.0304	6.6980
3.29	0.2146	0.0304	7.0563
3.54	0.2376	0.0337	7.0477
3.79	0.2376	0.0337	7.0477
4.04	0.2553	0.0354	7.2027
4.29	0.2710	0.0380	7.1393
4.54	0.2922	0.0402	7.2690
4.79	0.2998	0.0404	7.4151
5.04	0.3106	0.0448	6.9385
5.29	0.3369	0.0480	7.0196
5.54	0.3548	0.0533	6.6572
5.79	0.3752	0.0568	6.6097
6.04	0.3802	0.0601	6.3305
6.29	0.4046	0.0613	6.5992
6.54	0.4116	0.0646	6.3750
6.79	0.4255	0.0676	6.2960
7.04	0.4387	0.0715	6.1360
7.29	0.4449	0.0726	6.1324
7.54	0.4535	0.0798	5.6814
7.79	0.4636	0.0816	5.6838
8.04	0.4691	0.0831	5.6441
8.29	0.4780	0.0863	5.5391
8.54	0.4831	0.0888	5.4399
8.79	0.4933	0.0956	5.1602
9.04	0.5040	0.0979	5.1453
9.29	0.5026	0.0982	5.1201
9.54	0.5044	0.1044	4.8294
9.79	0.5030	0.1064	4.7261
10.04	0.5073	0.1102	4.6037
10.29	0.5093	0.1082	4.7045
10.54	0.5138	0.1136	4.5246
10.79	0.5139	0.1190	4.3180
11.04	0.5270	0.1228	4.2909
11.29	0.5173	0.1213	4.2656
11.54	0.5222	0.1223	4.2704
11.79	0.5251	0.1286	4.0842
12.04	0.5250	0.1269	4.1354
12.29	0.5278	0.1325	3.9839
12.54	0.5192	0.1320	3.9347
12.79	0.5260	0.1353	3.8875
13.04	0.5258	0.1406	3.7391
13.29	0.5089	0.1409	3.6123
13.54	0.5083	0.1429	3.5570
13.79	0.5206	0.1467	3.5488
14.04	0.5129	0.1485	3.4533
14.29	0.5098	0.1474	3.4576
14.54	0.4929	0.1453	3.3917
14.79	0.4985	0.1502	3.3183
15.04	0.4894	0.1484	3.2987
15.29	0.4842	0.1506	3.2142
15.54	0.4817	0.1519	3.1716
15.79	0.4762	0.1515	3.1443
16.04	0.4710	0.1525	3.0883
16.29	0.4650	0.1523	3.0541
16.54	0.4632	0.1550	2.9877
16.79	0.4640	0.1563	2.9687
17.04	0.4501	0.1548	2.9083
17.29	0.4430	0.1553	2.8522
17.54	0.4447	0.1555	2.8591
17.79	0.4393	0.1572	2.7949
18.04	0.4258	0.1529	2.7843
18.29	0.4203	0.1545	2.7199
18.54	0.4149	0.1522	2.7258
18.79	0.4086	0.1553	2.6315
19.04	0.3955	0.1487	2.6601
19.29	0.4086	0.1614	2.5310
19.54	0.4019	0.1560	2.5765
19.79	0.3990	0.1590	2.5102
20.04	0.3835	0.1559	2.4596
20.29	0.3913	0.1604	2.4392
20.54	0.3922	0.1574	2.4922
20.79	0.3814	0.1593	2.3945
21.04	0.3791	0.1587	2.3894
21.29	0.3751	0.1622	2.3122
21.54	0.3771	0.1626	2.3187
21.79	0.3708	0.1645	2.2538
22.04	0.3624	0.1640	2.2094
22.29	0.3657	0.1674	2.1850
22.54	0.3696	0.1680	2.2002
22.79	0.3677	0.1716	2.1425
23.04	0.3611	0.1691	2.1358
23.29	0.3613	0.1698	2.1282
23.54	0.3595	0.1691	2.1258
23.79	0.3615	0.1730	2.0896
24.04	0.3593	0.1758	2.0435
24.29	0.3628	0.1769	2.0508
24.54	0.3600	0.1763	2.0419
24.79	0.3529	0.1760	2.0054
25.04	0.3595	0.1792	2.0062
25.29	0.3641	0.1838	1.9808

Table D.11: Model #11, g=1c, s=-0.5c, Aerodynamic Data at Re 60,000

α (°)	C_L (-)	C_D (-)	L/D (-)
-2.07	-0.1402	0.0305	-4.5939
-1.82	-0.1258	0.0314	-4.0036
-1.57	-0.1037	0.0312	-3.3253
-1.32	-0.0907	0.0302	-3.0064
-1.07	-0.0702	0.0319	-2.1996
-0.82	-0.0373	0.0285	-1.3099
-0.57	-0.0329	0.0332	-0.9903
-0.32	-0.0213	0.0311	-0.6858
-0.07	0.0026	0.0267	0.0980
0.18	0.0108	0.0288	0.3749
0.43	0.0324	0.0303	1.0689
0.68	0.0597	0.0285	2.0952
0.93	0.0738	0.0287	2.5725
1.18	0.0873	0.0277	3.1567
1.43	0.1191	0.0288	4.1343
1.68	0.1290	0.0303	4.2626
1.93	0.1462	0.0328	4.4543
2.18	0.1614	0.0341	4.7273
2.43	0.1823	0.0342	5.3225
2.68	0.2067	0.0376	5.5006
2.93	0.2248	0.0405	5.5545
3.18	0.2442	0.0416	5.8662
3.43	0.2442	0.0416	5.8662
3.68	0.2717	0.0433	6.2794
3.93	0.2789	0.0435	6.4163
4.18	0.2894	0.0496	5.8352
4.43	0.3135	0.0507	6.1820
4.68	0.3301	0.0524	6.2968
4.93	0.3549	0.0574	6.1867
5.18	0.3872	0.0621	6.2371
5.43	0.4145	0.0657	6.3076
5.68	0.4405	0.0661	6.6611
5.93	0.4510	0.0701	6.4301
6.18	0.4698	0.0752	6.2439
6.43	0.4737	0.0813	5.8280
6.68	0.5041	0.0855	5.8991

α (°)	C_L (-)	C_D (-)	L/D (-)
6.93	0.5332	0.0889	6.0002
7.18	0.5430	0.0924	5.8748
7.43	0.5449	0.0941	5.7883
7.68	0.5714	0.0997	5.7300
7.93	0.6103	0.1095	5.5749
8.18	0.6191	0.1123	5.5114
8.43	0.6251	0.1174	5.3229
8.68	0.6472	0.1244	5.2005
8.93	0.6655	0.1297	5.1322
9.18	0.6748	0.1315	5.1301
9.43	0.6823	0.1347	5.0636
9.68	0.6817	0.1389	4.9071
9.93	0.6930	0.1423	4.8705
10.18	0.6944	0.1462	4.7494
10.43	0.6986	0.1525	4.5820
10.68	0.7171	0.1609	4.4571
10.93	0.7115	0.1654	4.3012
11.18	0.7111	0.1654	4.2999
11.43	0.7165	0.1728	4.1461
11.68	0.7149	0.1768	4.0431
11.93	0.7115	0.1810	3.9311
12.18	0.7142	0.1802	3.9646
12.43	0.7151	0.1867	3.8293
12.68	0.7087	0.1856	3.8181
12.93	0.7141	0.1930	3.6997
13.18	0.7085	0.1954	3.6259
13.43	0.6989	0.1963	3.5602
13.68	0.7011	0.1966	3.5658
13.93	0.7138	0.2047	3.4876
14.18	0.7171	0.2126	3.3724
14.43	0.6995	0.2100	3.3307
14.68	0.7060	0.2161	3.2670
14.93	0.7069	0.2193	3.2241
15.18	0.7154	0.2259	3.1666
15.43	0.7088	0.2257	3.1410
15.68	0.7022	0.2256	3.1121

α (°)	C_L (-)	C_D (-)	L/D (-)
15.93	0.7206	0.2360	3.0533
16.18	0.7169	0.2401	2.9864
16.43	0.7146	0.2424	2.9478
16.68	0.7147	0.2461	2.9042
16.93	0.7294	0.2540	2.8719
17.18	0.7112	0.2522	2.8201
17.43	0.7159	0.2608	2.7449
17.68	0.7065	0.2586	2.7325
17.93	0.7121	0.2630	2.7074
18.18	0.7154	0.2706	2.6432
18.43	0.7329	0.2782	2.6346
18.68	0.7248	0.2803	2.5856
18.93	0.7168	0.2791	2.5684
19.18	0.7184	0.2865	2.5075
19.43	0.7290	0.2891	2.5215
19.68	0.7115	0.2912	2.4433
19.93	0.7212	0.2979	2.4211
20.18	0.7243	0.3024	2.3954
20.43	0.7338	0.3095	2.3711
20.68	0.7362	0.3112	2.3658
20.93	0.7217	0.3097	2.3306
21.18	0.7201	0.3167	2.2738
21.43	0.7225	0.3192	2.2632
21.68	0.7269	0.3229	2.2507
21.93	0.7280	0.3289	2.2134
22.18	0.7320	0.3332	2.1970
22.43	0.7179	0.3360	2.1362
22.68	0.7184	0.3351	2.1442
22.93	0.7169	0.3391	2.1144
23.18	0.7226	0.3475	2.0794
23.43	0.7217	0.3534	2.0424
23.68	0.7201	0.3517	2.0473
23.93	0.7201	0.3566	2.0195
24.18	0.7151	0.3568	2.0041
24.43	0.7081	0.3598	1.9683
24.68	0.7124	0.3659	1.9470
24.93	0.7128	0.3668	1.9434

Table D.12: Model #12, g=1c, s=-1c, Aerodynamic Data at Re 60,000

α (°)	C_L (-)	C_D (-)	L/D (-)
-1.89	-0.1364	0.0262	-5.2140
-1.64	-0.1192	0.0247	-4.8274
-1.39	-0.0960	0.0242	-3.9613
-1.14	-0.0847	0.0224	-3.7864
-0.89	-0.0761	0.0228	-3.3402
-0.64	-0.0572	0.0201	-2.8419
-0.39	-0.0240	0.0217	-1.1073
-0.14	-0.0050	0.0209	-0.2418
0.11	0.0123	0.0224	0.5498
0.36	0.0204	0.0220	0.9281
0.61	0.0453	0.0191	2.3735
0.86	0.0530	0.0250	2.1179
1.11	0.0748	0.0243	3.0797
1.36	0.0995	0.0269	3.6953
1.61	0.1175	0.0261	4.5011
1.86	0.1340	0.0258	5.1896
2.11	0.1542	0.0265	5.8112
2.36	0.1627	0.0258	6.3127
2.61	0.1724	0.0299	5.7634
2.86	0.1885	0.0288	6.5409
3.11	0.2030	0.0284	7.1538
3.36	0.2298	0.0322	7.1392
3.61	0.2298	0.0322	7.1392
3.86	0.2465	0.0337	7.3213
4.11	0.2643	0.0366	7.2188
4.36	0.3020	0.0419	7.2046
4.61	0.3078	0.0392	7.8496
4.86	0.3262	0.0457	7.1438
5.11	0.3405	0.0490	6.9434
5.36	0.3641	0.0535	6.8001
5.61	0.3965	0.0536	7.4007
5.86	0.4125	0.0591	6.9737
6.11	0.4395	0.0659	6.6668
6.36	0.4577	0.0671	6.8241
6.61	0.4584	0.0712	6.4423
6.86	0.4737	0.0734	6.4512

α (°)	C_L (-)	C_D (-)	L/D (-)
7.11	0.4906	0.0746	6.5804
7.36	0.5068	0.0821	6.1744
7.61	0.5231	0.0817	6.4046
7.86	0.5289	0.0896	5.9045
8.11	0.5523	0.0911	6.0629
8.36	0.5654	0.1001	5.6498
8.61	0.5692	0.1023	5.5660
8.86	0.5761	0.1049	5.4901
9.11	0.5855	0.1091	5.3679
9.36	0.5954	0.1136	5.2399
9.61	0.5978	0.1177	5.0784
9.86	0.6080	0.1226	4.9588
10.11	0.6107	0.1267	4.8190
10.36	0.6363	0.1350	4.7136
10.61	0.6389	0.1357	4.7073
10.86	0.6321	0.1339	4.7209
11.11	0.6291	0.1380	4.5606
11.36	0.6381	0.1436	4.4435
11.61	0.6418	0.1455	4.4114
11.86	0.6361	0.1477	4.3074
12.11	0.6431	0.1511	4.2546
12.36	0.6554	0.1593	4.1146
12.61	0.6730	0.1676	4.0152
12.86	0.6598	0.1654	3.9899
13.11	0.6640	0.1718	3.8661
13.36	0.6670	0.1736	3.8419
13.61	0.6610	0.1755	3.7669
13.86	0.6595	0.1751	3.7658
14.11	0.6680	0.1826	3.6581
14.36	0.6766	0.1900	3.5603
14.61	0.6700	0.1935	3.4632
14.86	0.6693	0.1973	3.3925
15.11	0.6623	0.1974	3.3559
15.36	0.6873	0.2080	3.3037
15.61	0.6829	0.2134	3.1997
15.86	0.6686	0.2081	3.2138

α (°)	C_L (-)	C_D (-)	L/D (-)
16.11	0.6639	0.2077	3.1958
16.36	0.6744	0.2152	3.1335
16.61	0.6674	0.2201	3.0318
16.86	0.6860	0.2302	2.9802
17.11	0.6750	0.2269	2.9746
17.36	0.6724	0.2307	2.9142
17.61	0.6751	0.2362	2.8581
17.86	0.6685	0.2348	2.8473
18.11	0.6858	0.2453	2.7959
18.36	0.6862	0.2437	2.8160
18.61	0.6646	0.2438	2.7254
18.86	0.6464	0.2401	2.6925
19.11	0.6636	0.2508	2.6459
19.36	0.6674	0.2610	2.5571
19.61	0.6689	0.2618	2.5553
19.86	0.6502	0.2588	2.5122
20.11	0.6708	0.2671	2.5114
20.36	0.6678	0.2723	2.4525
20.61	0.6661	0.2704	2.4632
20.86	0.6736	0.2832	2.3786
21.11	0.6441	0.2740	2.3502
21.36	0.6905	0.2925	2.3607
21.61	0.6681	0.2888	2.3135
21.86	0.6651	0.2969	2.2401
22.11	0.6734	0.2973	2.2649
22.36	0.6591	0.2937	2.2440
22.61	0.6774	0.3025	2.2390
22.86	0.6889	0.3174	2.1708
23.11	0.6717	0.3042	2.2080
23.36	0.7080	0.3281	2.1582
23.61	0.7172	0.3354	2.1384
23.86	0.7415	0.3474	2.1346
24.11	0.7660	0.3636	2.1063
24.36	0.7565	0.3651	2.0721
24.61	0.7174	0.3464	2.0713
24.86	0.7292	0.3573	2.0407
25.11	0.7180	0.3616	1.9857

Table D.13: Model #13, g=2c, s=-1c, Aerodynamic Data at Re 60,000

α (°)	C_L (-)	C_D (-)	L/D (-)
-1.83	-0.1629	0.0261	-6.2491
-1.58	-0.1486	0.0265	-5.6049
-1.33	-0.1172	0.0250	-4.6899
-1.08	-0.0850	0.0250	-3.3943
-0.83	-0.0723	0.0205	-3.5302
-0.58	-0.0557	0.0247	-2.2539
-0.33	-0.0252	0.0232	-1.0878
-0.08	-0.0073	0.0254	-0.2873
0.17	0.0117	0.0250	0.4688
0.42	0.0321	0.0227	1.4151
0.67	0.0460	0.0239	1.9267
0.92	0.0736	0.0216	3.4100
1.17	0.1030	0.0250	4.1117
1.42	0.1255	0.0254	4.9454
1.67	0.1446	0.0273	5.2902
1.92	0.1563	0.0261	5.9809
2.17	0.1770	0.0285	6.2154
2.42	0.1975	0.0302	6.5291
2.67	0.2132	0.0314	6.7953
2.92	0.2425	0.0337	7.1943
3.17	0.2675	0.0340	7.8595
3.42	0.2999	0.0397	7.5491
3.67	0.2999	0.0397	7.5491
3.92	0.3023	0.0356	8.5015
4.17	0.3341	0.0442	7.5523
4.42	0.3375	0.0419	8.0541
4.67	0.3763	0.0465	8.0996
4.92	0.4024	0.0492	8.1837
5.17	0.4354	0.0547	7.9546
5.42	0.4674	0.0585	7.9895
5.67	0.4928	0.0660	7.4626
5.92	0.5294	0.0732	7.2312
6.17	0.5627	0.0743	7.5684
6.42	0.5620	0.0777	7.2326
6.67	0.5950	0.0826	7.2035
6.92	0.6178	0.0856	7.2157
7.17	0.6475	0.0924	7.0054
7.42	0.6515	0.0979	6.6522
7.67	0.6767	0.1002	6.7572
7.92	0.7008	0.1047	6.6923
8.17	0.7165	0.1137	6.3002
8.42	0.7232	0.1111	6.5099
8.67	0.7494	0.1153	6.5019
8.92	0.7344	0.1202	6.1086
9.17	0.7631	0.1243	6.1382
9.42	0.7710	0.1342	5.7435
9.67	0.7585	0.1339	5.6630
9.92	0.7790	0.1461	5.3323
10.17	0.7870	0.1495	5.2646
10.42	0.7835	0.1503	5.2132
10.67	0.7975	0.1568	5.0848
10.92	0.7888	0.1555	5.0722
11.17	0.7724	0.1641	4.7074
11.42	0.7870	0.1679	4.6878
11.67	0.7898	0.1716	4.6033
11.92	0.7827	0.1671	4.6829
12.17	0.7846	0.1738	4.5135
12.42	0.7916	0.1773	4.4652
12.67	0.7837	0.1736	4.5145
12.92	0.7875	0.1827	4.3114
13.17	0.7715	0.1880	4.1033
13.42	0.7892	0.1910	4.1324
13.67	0.7940	0.1921	4.1340
13.92	0.7739	0.1914	4.0424
14.17	0.7859	0.2043	3.8459
14.42	0.7998	0.2159	3.7039
14.67	0.8010	0.2169	3.6923
14.92	0.7827	0.2137	3.6624
15.17	0.7958	0.2183	3.6449
15.42	0.7852	0.2249	3.4919
15.67	0.7933	0.2261	3.5086
15.92	0.7967	0.2277	3.4995
16.17	0.7934	0.2283	3.4753
16.42	0.8168	0.2379	3.4335
16.67	0.8054	0.2404	3.3503
16.92	0.7981	0.2476	3.2233
17.17	0.8220	0.2611	3.1487
17.42	0.7917	0.2533	3.1250
17.67	0.7999	0.2683	2.9814
17.92	0.8105	0.2653	3.0547
18.17	0.8058	0.2616	3.0808
18.42	0.7966	0.2728	2.9205
18.67	0.8108	0.2735	2.9646
18.92	0.8042	0.2734	2.9418
19.17	0.8140	0.2826	2.8807
19.42	0.8027	0.2871	2.7956
19.67	0.8021	0.2930	2.7373
19.92	0.8114	0.3000	2.7051
20.17	0.8066	0.2944	2.7396
20.42	0.8019	0.3041	2.6371
20.67	0.8019	0.3105	2.5821
20.92	0.8175	0.3094	2.6418
21.17	0.8113	0.3153	2.5732
21.42	0.8039	0.3167	2.5385
21.67	0.8151	0.3301	2.4691
21.92	0.8243	0.3204	2.5727
22.17	0.7931	0.3135	2.5303
22.42	0.8083	0.3324	2.4318
22.67	0.7960	0.3356	2.3721
22.92	0.8062	0.3400	2.3713
23.17	0.8053	0.3482	2.3128
23.42	0.8083	0.3548	2.2783
23.67	0.8004	0.3501	2.2860
23.92	0.7921	0.3461	2.2889
24.17	0.7948	0.3579	2.2210
24.42	0.8313	0.3745	2.2198
24.67	0.7944	0.3626	2.1907
24.92	0.8103	0.3728	2.1734
25.17	0.8063	0.3756	2.1465

Table D.14: Model #14, g=1c, s=-1.5c, Aerodynamic Data at Re 60,000

α (°)	C_L (-)	C_D (-)	L/D (-)
-1.88	-0.1382	0.0257	-5.3788
-1.63	-0.1116	0.0247	-4.5153
-1.38	-0.1037	0.0217	-4.7879
-1.13	-0.0770	0.0230	-3.3519
-0.88	-0.0575	0.0235	-2.4497
-0.63	-0.0404	0.0203	-1.9897
-0.38	-0.0239	0.0190	-1.2595
-0.13	-0.0046	0.0234	-0.1946
0.12	0.0107	0.0231	0.4643
0.37	0.0191	0.0224	0.8521
0.62	0.0430	0.0264	1.6276
0.87	0.0649	0.0231	2.8043
1.12	0.0813	0.0242	3.3527
1.37	0.0985	0.0244	4.0402
1.62	0.1177	0.0277	4.2405
1.87	0.1392	0.0276	5.0421
2.12	0.1550	0.0275	5.6302
2.37	0.1754	0.0271	6.4749
2.62	0.1838	0.0301	6.1164
2.87	0.2090	0.0360	5.8075
3.12	0.2181	0.0293	7.4525
3.37	0.2401	0.0377	6.3743
3.62	0.2401	0.0377	6.3743
3.87	0.2617	0.0380	6.8797
4.12	0.2836	0.0400	7.0966
4.37	0.3010	0.0430	7.0065
4.62	0.3057	0.0427	7.1536
4.87	0.3370	0.0481	7.0017
5.12	0.3492	0.0504	6.9325
5.37	0.3766	0.0573	6.5708
5.62	0.3982	0.0600	6.6332
5.87	0.4178	0.0628	6.6501
6.12	0.4424	0.0670	6.6069
6.37	0.4546	0.0685	6.6410
6.62	0.4699	0.0746	6.3023
6.87	0.4788	0.0753	6.3572
7.12	0.4966	0.0830	5.9828
7.37	0.5153	0.0881	5.8520
7.62	0.5219	0.0883	5.9113
7.87	0.5475	0.0956	5.7265
8.12	0.5648	0.1038	5.4390
8.37	0.5652	0.1001	5.6465
8.62	0.5858	0.1053	5.5618
8.87	0.5986	0.1145	5.2270
9.12	0.6069	0.1132	5.3601
9.37	0.6199	0.1208	5.1315
9.62	0.6204	0.1257	4.9350
9.87	0.6246	0.1257	4.9709
10.12	0.6309	0.1329	4.7475
10.37	0.6395	0.1406	4.5494
10.62	0.6532	0.1447	4.5147
10.87	0.6490	0.1459	4.4477
11.12	0.6511	0.1455	4.4736
11.37	0.6530	0.1537	4.2484
11.62	0.6576	0.1554	4.2319
11.87	0.6571	0.1573	4.1786
12.12	0.6763	0.1646	4.1083
12.37	0.6661	0.1641	4.0599
12.62	0.6838	0.1782	3.8378
12.87	0.6864	0.1756	3.9092
13.12	0.6725	0.1771	3.7964
13.37	0.6919	0.1857	3.7258
13.62	0.6909	0.1883	3.6688
13.87	0.6897	0.1921	3.5910
14.12	0.6991	0.1964	3.5593
14.37	0.6921	0.2007	3.4487
14.62	0.6914	0.2009	3.4411
14.87	0.6881	0.2027	3.3941
15.12	0.6967	0.2078	3.3528
15.37	0.6873	0.2099	3.2753
15.62	0.6920	0.2158	3.2058
15.87	0.6819	0.2218	3.0745
16.12	0.7036	0.2241	3.1398
16.37	0.7040	0.2342	3.0059
16.62	0.7176	0.2428	2.9550
16.87	0.6965	0.2335	2.9836
17.12	0.7015	0.2396	2.9283
17.37	0.7128	0.2407	2.9618
17.62	0.7151	0.2523	2.8342
17.87	0.6881	0.2434	2.8272
18.12	0.6760	0.2391	2.8273
18.37	0.6782	0.2428	2.7929
18.62	0.6757	0.2461	2.7455
18.87	0.6556	0.2463	2.6616
19.12	0.6735	0.2561	2.6304
19.37	0.6786	0.2636	2.5747
19.62	0.6789	0.2697	2.5175
19.87	0.6544	0.2521	2.5963
20.12	0.6548	0.2642	2.4782
20.37	0.6522	0.2625	2.4844
20.62	0.6650	0.2745	2.4227
20.87	0.6579	0.2796	2.3528
21.12	0.6479	0.2761	2.3465
21.37	0.6552	0.2840	2.3071
21.62	0.6372	0.2755	2.3127
21.87	0.6285	0.2759	2.2782
22.12	0.6767	0.2958	2.2878
22.37	0.6719	0.2983	2.2523
22.62	0.6689	0.3076	2.1748
22.87	0.6713	0.3036	2.2110
23.12	0.6610	0.3037	2.1767
23.37	0.6237	0.2979	2.0934
23.62	0.6749	0.3190	2.1154
23.87	0.6743	0.3239	2.0816
24.12	0.6801	0.3279	2.0739
24.37	0.6318	0.3065	2.0616
24.62	0.6186	0.3078	2.0096
24.87	0.6440	0.3270	1.9695
25.12	0.5852	0.2949	1.9843

Appendix E: Aerodynamic Data at Reynolds Number 120,000

Table E.1: Model #1, g=1c, s=0c, Aerodynamic Data at Re 120,000

α (°)	C_L (-)	C_D (-)	L/D (-)
-1.70	-0.1018	0.0195	-5.2293
-1.45	-0.0931	0.0158	-5.8821
-1.20	-0.0720	0.0127	-5.6646
-0.95	-0.0646	0.0139	-4.6380
-0.70	-0.0570	0.0138	-4.1208
-0.45	-0.0303	0.0136	-2.2236
-0.20	-0.0148	0.0137	-1.0840
0.05	0.0019	0.0132	0.1452
0.30	0.0261	0.0159	1.6375
0.55	0.0382	0.0166	2.2965
0.80	0.0565	0.0173	3.2734
1.05	0.0639	0.0175	3.6456
1.30	0.0862	0.0149	5.7888
1.55	0.1026	0.0146	7.0062
1.80	0.1230	0.0170	7.2382
2.05	0.1444	0.0191	7.5749
2.30	0.1517	0.0201	7.5332
2.55	0.1687	0.0219	7.7136
2.80	0.1827	0.0236	7.7522
3.05	0.2134	0.0262	8.1348
3.30	0.2276	0.0278	8.1728
3.55	0.2461	0.0291	8.4637
3.80	0.2461	0.0291	8.4637
4.05	0.2618	0.0279	9.3987
4.30	0.2697	0.0325	8.3028
4.55	0.2998	0.0369	8.1215
4.80	0.3170	0.0399	7.9408
5.05	0.3306	0.0408	8.1115
5.30	0.3446	0.0422	8.1726
5.55	0.4012	0.0496	8.0916
5.80	0.4159	0.0562	7.4060
6.05	0.4216	0.0589	7.1577
6.30	0.4475	0.0649	6.8948
6.55	0.4611	0.0661	6.9710
6.80	0.4879	0.0717	6.8042
7.05	0.4992	0.0772	6.4623
7.30	0.5220	0.0812	6.4272
7.55	0.5484	0.0874	6.2758
7.80	0.5722	0.0938	6.1026
8.05	0.5875	0.0981	5.9874
8.30	0.5988	0.1023	5.8511
8.55	0.6191	0.1064	5.8198
8.80	0.6503	0.1156	5.6245
9.05	0.6449	0.1190	5.4200
9.30	0.6742	0.1282	5.2572
9.55	0.6942	0.1347	5.1545
9.80	0.7131	0.1418	5.0290
10.05	0.7310	0.1469	4.9750
10.30	0.7422	0.1534	4.8375
10.55	0.7449	0.1527	4.8788
10.80	0.7532	0.1619	4.6525
11.05	0.7636	0.1677	4.5545
11.30	0.7763	0.1743	4.4528
11.55	0.7869	0.1848	4.2575
11.80	0.7914	0.1819	4.3515
12.05	0.8017	0.1930	4.1539
12.30	0.8074	0.1961	4.1177
12.55	0.8142	0.2035	4.0000
12.80	0.8182	0.2094	3.9078
13.05	0.8199	0.2118	3.8719
13.30	0.8197	0.2143	3.8259
13.55	0.8180	0.2201	3.7169
13.80	0.8252	0.2267	3.6397
14.05	0.8171	0.2261	3.6140
14.30	0.8174	0.2341	3.4909
14.55	0.8141	0.2358	3.4521
14.80	0.8152	0.2390	3.4100
15.05	0.8073	0.2423	3.3316
15.30	0.8030	0.2453	3.2742
15.55	0.7936	0.2472	3.2099
15.80	0.7931	0.2483	3.1941
16.05	0.7826	0.2494	3.1374
16.30	0.7840	0.2541	3.0849
16.55	0.7833	0.2578	3.0383
16.80	0.7743	0.2582	2.9985
17.05	0.7855	0.2673	2.9390
17.30	0.7852	0.2707	2.9010
17.55	0.7825	0.2750	2.8454
17.80	0.7801	0.2772	2.8140
18.05	0.7720	0.2780	2.7767
18.30	0.7748	0.2844	2.7238
18.55	0.7691	0.2859	2.6901
18.80	0.7653	0.2896	2.6427
19.05	0.7603	0.2892	2.6287
19.30	0.7501	0.2893	2.5928
19.55	0.7511	0.2938	2.5568
19.80	0.7431	0.2970	2.5020
20.05	0.7474	0.2999	2.4921
20.30	0.7377	0.3032	2.4334
20.55	0.7323	0.3027	2.4197
20.80	0.7472	0.3126	2.3906
21.05	0.7350	0.3121	2.3555
21.30	0.7500	0.3220	2.3288
21.55	0.7463	0.3232	2.3092
21.80	0.7479	0.3269	2.2874
22.05	0.7355	0.3263	2.2543
22.30	0.7477	0.3361	2.2245
22.55	0.7526	0.3409	2.2078
22.80	0.7489	0.3430	2.1832
23.05	0.7407	0.3441	2.1526
23.30	0.7518	0.3507	2.1435
23.55	0.7556	0.3593	2.1030
23.80	0.7600	0.3633	2.0919
24.05	0.7496	0.3625	2.0680
24.30	0.7579	0.3705	2.0453
24.55	0.7517	0.3726	2.0176
24.80	0.7607	0.3798	2.0028
25.05	0.7467	0.3776	1.9776
25.30	0.7545	0.3860	1.9549

Table E.2: Model #2, g=0.5c, s=0c, Aerodynamic Data at Re 120,000

α (°)	C_L (-)	C_D (-)	L/D (-)
-2.24	-0.1139	0.0224	-5.0781
-1.99	-0.1037	0.0218	-4.7506
-1.74	-0.0829	0.0209	-3.9744
-1.49	-0.0911	0.0226	-4.0280
-1.24	-0.0677	0.0205	-3.3088
-0.99	-0.0512	0.0193	-2.6524
-0.74	-0.0405	0.0211	-1.9238
-0.49	-0.0290	0.0211	-1.3788
-0.24	-0.0135	0.0207	-0.6518
0.01	0.0005	0.0209	0.0256
0.26	0.0237	0.0209	1.1352
0.51	0.0229	0.0199	1.1516
0.76	0.0357	0.0209	1.7133
1.01	0.0507	0.0213	2.3867
1.26	0.0612	0.0224	2.7310
1.51	0.0815	0.0224	3.6334
1.76	0.0910	0.0236	3.8577
2.01	0.1071	0.0257	4.1645
2.26	0.1145	0.0251	4.5551
2.51	0.1313	0.0240	5.4746
2.76	0.1315	0.0263	4.9963
3.01	0.1630	0.0281	5.8076
3.26	0.1630	0.0281	5.8076
3.51	0.1682	0.0296	5.6798
3.76	0.1931	0.0308	6.2733
4.01	0.1873	0.0308	6.0837
4.26	0.2143	0.0335	6.3962
4.51	0.2338	0.0374	6.2510
4.76	0.2464	0.0401	6.1418
5.01	0.2669	0.0428	6.2281
5.26	0.2715	0.0444	6.1150
5.51	0.3029	0.0487	6.2208
5.76	0.3007	0.0483	6.2266
6.01	0.3377	0.0553	6.1064
6.26	0.3482	0.0563	6.1876
6.51	0.3752	0.0627	5.9853
6.76	0.3877	0.0677	5.7222
7.01	0.4042	0.0691	5.8487
7.26	0.4110	0.0728	5.6453
7.51	0.4307	0.0777	5.5448
7.76	0.4394	0.0806	5.4526
8.01	0.4509	0.0839	5.3745
8.26	0.4554	0.0847	5.3779
8.51	0.4766	0.0911	5.2317
8.76	0.4980	0.0991	5.0265
9.01	0.4997	0.1000	4.9951
9.26	0.5266	0.1067	4.9371
9.51	0.5235	0.1072	4.8812
9.76	0.5418	0.1154	4.6941
10.01	0.5398	0.1170	4.6150
10.26	0.5585	0.1222	4.5694
10.51	0.5560	0.1228	4.5271
10.76	0.5610	0.1294	4.3348
11.01	0.5620	0.1319	4.2591
11.26	0.5742	0.1368	4.1973
11.51	0.5735	0.1395	4.1098
11.76	0.5791	0.1428	4.0541
12.01	0.5937	0.1495	3.9723
12.26	0.5902	0.1522	3.8782
12.51	0.6032	0.1570	3.8411
12.76	0.5978	0.1590	3.7599
13.01	0.6165	0.1666	3.7007
13.26	0.5993	0.1650	3.6319
13.51	0.6155	0.1732	3.5538
13.76	0.6268	0.1767	3.5472
14.01	0.6211	0.1790	3.4694
14.26	0.6299	0.1847	3.4109
14.51	0.6381	0.1905	3.3492
14.76	0.6462	0.1960	3.2978
15.01	0.6281	0.1915	3.2804
15.26	0.6394	0.1975	3.2374
15.51	0.6338	0.2012	3.1499
15.76	0.6303	0.2059	3.0614
16.01	0.6421	0.2103	3.0527
16.26	0.6406	0.2129	3.0091
16.51	0.6419	0.2148	2.9882
16.76	0.6474	0.2220	2.9159
17.01	0.6493	0.2267	2.8644
17.26	0.6476	0.2271	2.8518
17.51	0.6536	0.2323	2.8133
17.76	0.6538	0.2353	2.7792
18.01	0.6643	0.2456	2.7053
18.26	0.6591	0.2454	2.6860
18.51	0.6612	0.2496	2.6485
18.76	0.6637	0.2510	2.6443
19.01	0.6676	0.2586	2.5817
19.26	0.6655	0.2617	2.5428
19.51	0.6847	0.2699	2.5372
19.76	0.6678	0.2697	2.4763
20.01	0.6672	0.2710	2.4617
20.26	0.6735	0.2773	2.4289
20.51	0.6781	0.2804	2.4186
20.76	0.6682	0.2810	2.3782
21.01	0.6801	0.2880	2.3616
21.26	0.6744	0.2899	2.3263
21.51	0.6949	0.3020	2.3010
21.76	0.6791	0.2996	2.2664
22.01	0.6834	0.3008	2.2718
22.26	0.6717	0.3031	2.2158
22.51	0.6836	0.3123	2.1889
22.76	0.6865	0.3168	2.1672
23.01	0.6997	0.3273	2.1381
23.26	0.6791	0.3212	2.1140
23.51	0.6684	0.3216	2.0782
23.76	0.6785	0.3284	2.0659
24.01	0.6935	0.3374	2.0555
24.26	0.6857	0.3374	2.0324
24.51	0.6882	0.3409	2.0190
24.76	0.6818	0.3434	1.9854

Table E.3: Model #3, g=0.5c, s=0.5c, Aerodynamic Data at Re 120,000

α (°)	C_L (-)	C_D (-)	L/D (-)
-1.61	-0.0919	0.0251	-3.6626
-1.36	-0.0718	0.0233	-3.0793
-1.11	-0.0607	0.0233	-2.6040
-0.86	-0.0491	0.0234	-2.0960
-0.61	-0.0394	0.0224	-1.7603
-0.36	-0.0191	0.0224	-0.8503
-0.11	-0.0068	0.0222	-0.3051
0.14	0.0086	0.0223	0.3876
0.39	0.0273	0.0214	1.2765
0.64	0.0393	0.0211	1.8609
0.89	0.0604	0.0223	2.7125
1.14	0.0729	0.0222	3.2785
1.39	0.0796	0.0210	3.7980
1.64	0.0922	0.0226	4.0851
1.89	0.1127	0.0228	4.9319
2.14	0.1329	0.0229	5.8034
2.39	0.1409	0.0240	5.8784
2.64	0.1558	0.0259	6.0153
2.89	0.1691	0.0251	6.7461
3.14	0.1856	0.0257	7.2245
3.39	0.2038	0.0276	7.3712
3.64	0.2149	0.0294	7.3005
3.89	0.2149	0.0294	7.3005
4.14	0.2447	0.0310	7.9006
4.39	0.2499	0.0325	7.6981
4.64	0.2706	0.0353	7.6649
4.89	0.2807	0.0387	7.2488
5.14	0.2977	0.0399	7.4530
5.39	0.3110	0.0406	7.6602
5.64	0.3602	0.0498	7.2275
5.89	0.3710	0.0505	7.3413
6.14	0.3943	0.0534	7.3867
6.39	0.4052	0.0570	7.1134
6.64	0.4272	0.0597	7.1520
6.89	0.4383	0.0618	7.0919
7.14	0.4500	0.0656	6.8621

α (°)	C_L (-)	C_D (-)	L/D (-)
7.39	0.4693	0.0691	6.7867
7.64	0.4862	0.0738	6.5899
7.89	0.5052	0.0781	6.4658
8.14	0.5146	0.0827	6.2231
8.39	0.5311	0.0847	6.2682
8.64	0.5406	0.0890	6.0744
8.89	0.5643	0.0955	5.9116
9.14	0.5735	0.0978	5.8650
9.39	0.5963	0.1037	5.7496
9.64	0.6071	0.1078	5.6323
9.89	0.6163	0.1120	5.5030
10.14	0.6267	0.1149	5.4519
10.39	0.6427	0.1230	5.2271
10.64	0.6532	0.1261	5.1788
10.89	0.6534	0.1273	5.1315
11.14	0.6697	0.1327	5.0477
11.39	0.6752	0.1374	4.9128
11.64	0.6913	0.1440	4.8003
11.89	0.7006	0.1490	4.7009
12.14	0.7019	0.1511	4.6462
12.39	0.7176	0.1591	4.5096
12.64	0.7309	0.1645	4.4426
12.89	0.7336	0.1690	4.3416
13.14	0.7474	0.1737	4.3037
13.39	0.7459	0.1778	4.1951
13.64	0.7508	0.1793	4.1884
13.89	0.7487	0.1823	4.1064
14.14	0.7689	0.1928	3.9874
14.39	0.7700	0.1945	3.9597
14.64	0.7851	0.2009	3.9072
14.89	0.7762	0.2037	3.8098
15.14	0.7869	0.2083	3.7776
15.39	0.7927	0.2135	3.7134
15.64	0.7977	0.2198	3.6289
15.89	0.8041	0.2254	3.5673
16.14	0.8017	0.2284	3.5106

α (°)	C_L (-)	C_D (-)	L/D (-)
16.39	0.8123	0.2332	3.4837
16.64	0.8229	0.2383	3.4529
16.89	0.8181	0.2422	3.3780
17.14	0.8197	0.2463	3.3275
17.39	0.8286	0.2519	3.2889
17.64	0.8271	0.2557	3.2349
17.89	0.8357	0.2637	3.1687
18.14	0.8381	0.2683	3.1234
18.39	0.8296	0.2665	3.1133
18.64	0.8497	0.2775	3.0626
18.89	0.8499	0.2822	3.0118
19.14	0.8416	0.2841	2.9624
19.39	0.8353	0.2819	2.9636
19.64	0.8635	0.2973	2.9045
19.89	0.8562	0.2989	2.8643
20.14	0.8609	0.3045	2.8276
20.39	0.8826	0.3180	2.7753
20.64	0.8731	0.3173	2.7521
20.89	0.8509	0.3125	2.7230
21.14	0.8838	0.3267	2.7055
21.39	0.8821	0.3304	2.6701
21.64	0.8696	0.3308	2.6291
21.89	0.8772	0.3364	2.6076
22.14	0.8928	0.3473	2.5707
22.39	0.8887	0.3492	2.5448
22.64	0.8797	0.3492	2.5190
22.89	0.8879	0.3577	2.4820
23.14	0.8918	0.3617	2.4656
23.39	0.8848	0.3650	2.4243
23.64	0.8810	0.3662	2.4059
23.89	0.8791	0.3704	2.3737
24.14	0.8875	0.3758	2.3615
24.39	0.9131	0.3909	2.3361
24.64	0.8963	0.3873	2.3143
24.89	0.9226	0.4046	2.2799
25.14	0.9126	0.4050	2.2531
25.39	0.9232	0.4153	2.2230

Table E.4: Model #4, g=0.5c, s=1c, Aerodynamic Data at Re 120,000

α (°)	C_L (-)	C_D (-)	L/D (-)
-2.13	-0.1312	0.0235	-5.5901
-1.88	-0.1204	0.0226	-5.3193
-1.63	-0.1015	0.0212	-4.7967
-1.38	-0.0907	0.0202	-4.4922
-1.13	-0.0750	0.0192	-3.9032
-0.88	-0.0602	0.0187	-3.2240
-0.63	-0.0449	0.0199	-2.2556
-0.38	-0.0280	0.0192	-1.4538
-0.13	0.0022	0.0184	0.1198
0.12	0.0101	0.0198	0.5087
0.37	0.0279	0.0190	1.4708
0.62	0.0398	0.0203	1.9631
0.87	0.0589	0.0208	2.8332
1.12	0.0724	0.0184	3.9466
1.37	0.0929	0.0206	4.5116
1.62	0.1026	0.0194	5.2750
1.87	0.1287	0.0221	5.8140
2.12	0.1440	0.0233	6.1716
2.37	0.1605	0.0221	7.2744
2.62	0.1646	0.0226	7.2697
2.87	0.1928	0.0258	7.4603
3.12	0.2194	0.0283	7.7660
3.37	0.2194	0.0283	7.7660
3.62	0.2179	0.0287	7.5803
3.87	0.2406	0.0317	7.5841
4.12	0.2542	0.0343	7.4153
4.37	0.2776	0.0355	7.8103
4.62	0.2907	0.0377	7.7155
4.87	0.3191	0.0397	8.0311
5.12	0.3523	0.0434	8.1237
5.37	0.3792	0.0482	7.8680
5.62	0.3895	0.0506	7.7012
5.87	0.4132	0.0546	7.5719
6.12	0.4313	0.0576	7.4865
6.37	0.4497	0.0629	7.1518
6.62	0.4686	0.0639	7.3380
6.87	0.4928	0.0697	7.0661
7.12	0.5078	0.0736	6.9002
7.37	0.5259	0.0762	6.9001
7.62	0.5399	0.0809	6.6718
7.87	0.5565	0.0836	6.6601
8.12	0.5778	0.0932	6.1972
8.37	0.5894	0.0953	6.1840
8.62	0.6171	0.1012	6.0949
8.87	0.6263	0.1046	5.9866
9.12	0.6453	0.1104	5.8453
9.37	0.6570	0.1144	5.7448
9.62	0.6758	0.1208	5.5931
9.87	0.7063	0.1256	5.6235
10.12	0.7194	0.1336	5.3861
10.37	0.7353	0.1384	5.3124
10.62	0.7357	0.1433	5.1337
10.87	0.7518	0.1490	5.0474
11.12	0.7684	0.1547	4.9671
11.37	0.7908	0.1625	4.8651
11.62	0.7961	0.1667	4.7762
11.87	0.8200	0.1724	4.7556
12.12	0.8336	0.1813	4.5979
12.37	0.8506	0.1876	4.5336
12.62	0.8606	0.1920	4.4818
12.87	0.8680	0.1977	4.3908
13.12	0.8781	0.2058	4.2676
13.37	0.8801	0.2104	4.1837
13.62	0.8912	0.2144	4.1566
13.87	0.8977	0.2211	4.0596
14.12	0.9121	0.2254	4.0469
14.37	0.9219	0.2347	3.9276
14.62	0.9261	0.2396	3.8647
14.87	0.9399	0.2477	3.7939
15.12	0.9468	0.2540	3.7284
15.37	0.9473	0.2539	3.7319
15.62	0.9424	0.2588	3.6418
15.87	0.9503	0.2668	3.5614
16.12	0.9538	0.2709	3.5204
16.37	0.9648	0.2780	3.4701
16.62	0.9619	0.2850	3.3748
16.87	0.9718	0.2856	3.4033
17.12	0.9733	0.2922	3.3309
17.37	0.9757	0.3000	3.2526
17.62	0.9697	0.3038	3.1923
17.87	0.9823	0.3042	3.2292
18.12	0.9854	0.3120	3.1579
18.37	0.9929	0.3183	3.1193
18.62	0.9867	0.3233	3.0517
18.87	0.9865	0.3259	3.0267
19.12	0.9980	0.3381	2.9523
19.37	0.9921	0.3392	2.9251
19.62	1.0070	0.3492	2.8833
19.87	0.9898	0.3474	2.8494
20.12	1.0010	0.3545	2.8237
20.37	0.9997	0.3601	2.7764
20.62	0.9965	0.3635	2.7415
20.87	0.9962	0.3702	2.6906
21.12	1.0016	0.3742	2.6765
21.37	0.9959	0.3783	2.6326
21.62	1.0156	0.3886	2.6137
21.87	1.0073	0.3913	2.5743
22.12	1.0046	0.3964	2.5346
22.37	1.0056	0.3995	2.5171
22.62	1.0155	0.4066	2.4978
22.87	1.0223	0.4166	2.4541
23.12	1.0333	0.4233	2.4410
23.37	1.0303	0.4300	2.3960
23.62	1.0237	0.4359	2.3487
23.87	1.0340	0.4420	2.3394
24.12	1.0249	0.4446	2.3050
24.37	1.0339	0.4508	2.2933
24.62	1.0367	0.4584	2.2614
24.87	1.0422	0.4666	2.2337

Table E.5: Model #5, g=1c, s=0.5c, Aerodynamic Data at Re 120,000

α (°)	C_L (-)	C_D (-)	L/D (-)
-1.76	-0.0987	0.0331	-2.9805
-1.51	-0.1015	0.0329	-3.0836
-1.26	-0.0795	0.0318	-2.5023
-1.01	-0.0623	0.0299	-2.0820
-0.76	-0.0482	0.0297	-1.6222
-0.51	-0.0294	0.0305	-0.9653
-0.26	-0.0152	0.0288	-0.5257
-0.01	0.0032	0.0298	0.1069
0.25	0.0155	0.0286	0.5422
0.50	0.0352	0.0301	1.1707
0.75	0.0559	0.0315	1.7726
1.00	0.0805	0.0302	2.6684
1.25	0.0726	0.0304	2.3896
1.50	0.0946	0.0315	2.9988
1.75	0.1070	0.0308	3.4685
2.00	0.1313	0.0316	4.1512
2.25	0.1536	0.0326	4.7147
2.50	0.1661	0.0333	4.9809
2.75	0.1819	0.0355	5.1262
3.00	0.1969	0.0358	5.5006
3.25	0.2151	0.0389	5.5264
3.50	0.2404	0.0396	6.0699
3.75	0.2404	0.0396	6.0699
4.00	0.2570	0.0408	6.2961
4.25	0.2728	0.0439	6.2092
4.50	0.2886	0.0451	6.3996
4.75	0.3075	0.0480	6.4049
5.00	0.3348	0.0494	6.7798
5.25	0.3556	0.0530	6.7051
5.50	0.4001	0.0577	6.9390
5.75	0.4121	0.0628	6.5622
6.00	0.4330	0.0632	6.8464
6.25	0.4454	0.0647	6.8881
6.50	0.4729	0.0690	6.8569
6.75	0.4965	0.0760	6.5351
7.00	0.5137	0.0802	6.4047
7.25	0.5318	0.0859	6.1910
7.50	0.5465	0.0862	6.3395
7.75	0.5787	0.0919	6.2975
8.00	0.5956	0.0998	5.9665
8.25	0.6138	0.1022	6.0064
8.50	0.6220	0.1050	5.9231
8.75	0.6547	0.1120	5.8454
9.00	0.6615	0.1155	5.7275
9.25	0.6974	0.1247	5.5944
9.50	0.6955	0.1286	5.4073
9.75	0.7331	0.1348	5.4387
10.00	0.7267	0.1371	5.3016
10.25	0.7585	0.1467	5.1697
10.50	0.7668	0.1496	5.1269
10.75	0.7903	0.1590	4.9705
11.00	0.7943	0.1608	4.9397
11.25	0.8138	0.1667	4.8822
11.50	0.8161	0.1718	4.7503
11.75	0.8220	0.1759	4.6732
12.00	0.8319	0.1823	4.5635
12.25	0.8369	0.1909	4.3844
12.50	0.8328	0.1894	4.3977
12.75	0.8389	0.1953	4.2944
13.00	0.8346	0.1985	4.2053
13.25	0.8375	0.2040	4.1045
13.50	0.8463	0.2084	4.0610
13.75	0.8434	0.2107	4.0024
14.00	0.8447	0.2168	3.8959
14.25	0.8435	0.2183	3.8648
14.50	0.8384	0.2221	3.7751
14.75	0.8311	0.2225	3.7361
15.00	0.8499	0.2298	3.6990
15.25	0.8389	0.2321	3.6138
15.50	0.8465	0.2384	3.5505
15.75	0.8413	0.2409	3.4924
16.00	0.8455	0.2457	3.4417
16.25	0.8578	0.2515	3.4107
16.50	0.8456	0.2541	3.3277
16.75	0.8563	0.2596	3.2986
17.00	0.8574	0.2636	3.2533
17.25	0.8615	0.2700	3.1911
17.50	0.8561	0.2708	3.1617
17.75	0.8472	0.2711	3.1254
18.00	0.8587	0.2809	3.0572
18.25	0.8522	0.2802	3.0410
18.50	0.8565	0.2856	2.9992
18.75	0.8582	0.2905	2.9545
19.00	0.8681	0.2976	2.9170
19.25	0.8533	0.2959	2.8842
19.50	0.8615	0.3050	2.8246
19.75	0.8515	0.3054	2.7881
20.00	0.8579	0.3114	2.7555
20.25	0.8588	0.3175	2.7052
20.50	0.8582	0.3191	2.6900
20.75	0.8633	0.3234	2.6696
21.00	0.8800	0.3346	2.6303
21.25	0.8712	0.3346	2.6042
21.50	0.8820	0.3422	2.5774
21.75	0.8776	0.3457	2.5387
22.00	0.8705	0.3448	2.5244
22.25	0.8858	0.3553	2.4934
22.50	0.8893	0.3602	2.4687
22.75	0.8954	0.3697	2.4222
23.00	0.8928	0.3710	2.4065
23.25	0.9071	0.3791	2.3930
23.50	0.8872	0.3760	2.3599
23.75	0.8838	0.3812	2.3186
24.00	0.8890	0.3863	2.3011
24.25	0.8948	0.3921	2.2821
24.50	0.9081	0.4026	2.2558
24.75	0.8954	0.4005	2.2357
25.00	0.9028	0.4089	2.2080
25.25	0.9029	0.4141	2.1803

Table E.6: Model #6, g=1c, s=1c, Aerodynamic Data at Re 120,000

α (°)	C_L (-)	C_D (-)	L/D (-)
-1.90	-0.1435	0.0248	-5.7852
-1.65	-0.1193	0.0227	-5.2446
-1.40	-0.1061	0.0230	-4.6042
-1.15	-0.0901	0.0221	-4.0785
-0.90	-0.0731	0.0215	-3.4038
-0.65	-0.0523	0.0208	-2.5157
-0.40	-0.0331	0.0204	-1.6220
-0.15	-0.0074	0.0197	-0.3745
0.10	0.0019	0.0209	0.0924
0.35	0.0248	0.0191	1.2999
0.60	0.0378	0.0222	1.7043
0.85	0.0476	0.0199	2.3870
1.10	0.0773	0.0216	3.5820
1.35	0.0898	0.0208	4.3095
1.60	0.1006	0.0217	4.6330
1.85	0.1274	0.0222	5.7282
2.10	0.1350	0.0232	5.8096
2.35	0.1550	0.0242	6.4194
2.60	0.1631	0.0253	6.4526
2.85	0.1832	0.0270	6.7775
3.10	0.2116	0.0271	7.8045
3.35	0.2227	0.0293	7.6122
3.60	0.2227	0.0293	7.6122
3.85	0.2409	0.0286	8.4358
4.10	0.2704	0.0323	8.3758
4.35	0.2880	0.0358	8.0506
4.60	0.3017	0.0359	8.4076
4.85	0.3225	0.0394	8.1850
5.10	0.3479	0.0427	8.1438
5.35	0.3726	0.0455	8.1889
5.60	0.4034	0.0499	8.0811
5.85	0.4245	0.0532	7.9793
6.10	0.4451	0.0581	7.6580
6.35	0.4768	0.0617	7.7264
6.60	0.4906	0.0650	7.5460
6.85	0.5197	0.0689	7.5381

α (°)	C_L (-)	C_D (-)	L/D (-)
7.10	0.5381	0.0711	7.5691
7.35	0.5451	0.0768	7.0952
7.60	0.5735	0.0811	7.0694
7.85	0.5905	0.0918	6.4300
8.10	0.6289	0.0951	6.6106
8.35	0.6562	0.1041	6.3040
8.60	0.6622	0.1042	6.3547
8.85	0.6782	0.1104	6.1403
9.10	0.7037	0.1109	6.3467
9.35	0.7226	0.1196	6.0438
9.60	0.7359	0.1308	5.6255
9.85	0.7462	0.1301	5.7362
10.10	0.7762	0.1413	5.4944
10.35	0.8042	0.1445	5.5665
10.60	0.8146	0.1500	5.4296
10.85	0.8319	0.1579	5.2690
11.10	0.8451	0.1633	5.1763
11.35	0.8510	0.1674	5.0830
11.60	0.8579	0.1741	4.9281
11.85	0.8748	0.1821	4.8033
12.10	0.8678	0.1826	4.7532
12.35	0.8650	0.1906	4.5394
12.60	0.8712	0.1920	4.5384
12.85	0.8790	0.1995	4.4063
13.10	0.8838	0.2044	4.3237
13.35	0.8835	0.2106	4.1946
13.60	0.8755	0.2113	4.1434
13.85	0.8778	0.2148	4.0875
14.10	0.8731	0.2158	4.0465
14.35	0.8661	0.2177	3.9785
14.60	0.8710	0.2259	3.8553
14.85	0.8681	0.2274	3.8177
15.10	0.8736	0.2315	3.7739
15.35	0.8605	0.2347	3.6659
15.60	0.8842	0.2430	3.6387
15.85	0.8769	0.2431	3.6070

α (°)	C_L (-)	C_D (-)	L/D (-)
16.10	0.8870	0.2517	3.5244
16.35	0.8769	0.2523	3.4751
16.60	0.8760	0.2553	3.4312
16.85	0.8756	0.2606	3.3603
17.10	0.8853	0.2665	3.3222
17.35	0.8856	0.2717	3.2598
17.60	0.8870	0.2745	3.2313
17.85	0.8818	0.2785	3.1666
18.10	0.8809	0.2827	3.1162
18.35	0.8848	0.2883	3.0693
18.60	0.8847	0.2908	3.0420
18.85	0.8857	0.2971	2.9812
19.10	0.8932	0.3009	2.9683
19.35	0.8838	0.3056	2.8916
19.60	0.8869	0.3074	2.8849
19.85	0.8890	0.3152	2.8202
20.10	0.8929	0.3207	2.7841
20.35	0.8961	0.3231	2.7732
20.60	0.9005	0.3291	2.7360
20.85	0.8991	0.3322	2.7064
21.10	0.9056	0.3382	2.6777
21.35	0.8919	0.3393	2.6290
21.60	0.9161	0.3479	2.6337
21.85	0.9184	0.3537	2.5965
22.10	0.8975	0.3520	2.5496
22.35	0.8930	0.3547	2.5178
22.60	0.9041	0.3634	2.4877
22.85	0.9045	0.3688	2.4527
23.10	0.9185	0.3783	2.4276
23.35	0.9227	0.3853	2.3948
23.60	0.9052	0.3816	2.3717
23.85	0.9270	0.3974	2.3327
24.10	0.9335	0.4006	2.3303
24.35	0.9315	0.4046	2.3021
24.60	0.9295	0.4093	2.2710
24.85	0.9222	0.4095	2.2521
25.10	0.9281	0.4184	2.2183

Table E.7: Model #7, g=2c, s=1c, Aerodynamic Data at Re 120,000

α (°)	C_L (-)	C_D (-)	L/D (-)
-2.08	-0.1552	0.0281	-5.5224
-1.83	-0.1349	0.0288	-4.6813
-1.58	-0.1187	0.0288	-4.1197
-1.33	-0.1010	0.0285	-3.5473
-1.08	-0.0738	0.0281	-2.6282
-0.83	-0.0571	0.0278	-2.0542
-0.58	-0.0401	0.0263	-1.5222
-0.33	-0.0151	0.0280	-0.5416
-0.08	-0.0025	0.0284	-0.0867
0.17	0.0081	0.0286	0.2825
0.42	0.0562	0.0282	1.9923
0.67	0.0607	0.0275	2.2110
0.92	0.0835	0.0276	3.0274
1.17	0.1082	0.0287	3.7687
1.42	0.1192	0.0284	4.1923
1.67	0.1496	0.0273	5.4835
1.92	0.1495	0.0295	5.0616
2.17	0.1870	0.0303	6.1719
2.42	0.2034	0.0326	6.2334
2.67	0.2206	0.0320	6.9023
2.92	0.2351	0.0340	6.9079
3.17	0.2627	0.0368	7.1408
3.42	0.2627	0.0368	7.1408
3.67	0.2954	0.0383	7.7220
3.92	0.3200	0.0409	7.8221
4.17	0.3329	0.0415	8.0164
4.42	0.3540	0.0446	7.9329
4.67	0.3948	0.0488	8.0913
4.92	0.4056	0.0496	8.1741
5.17	0.4501	0.0568	7.9215
5.42	0.4703	0.0606	7.7654
5.67	0.5080	0.0644	7.8900
5.92	0.5340	0.0700	7.6318
6.17	0.5629	0.0730	7.7123
6.42	0.5735	0.0760	7.5490
6.67	0.6064	0.0821	7.3882
6.92	0.6395	0.0874	7.3151
7.17	0.6555	0.0923	7.1017
7.42	0.6731	0.0952	7.0702
7.67	0.6937	0.1006	6.8954
7.92	0.7171	0.1083	6.6212
8.17	0.7276	0.1120	6.4962
8.42	0.7484	0.1186	6.3111
8.67	0.7589	0.1245	6.0959
8.92	0.7675	0.1290	5.9507
9.17	0.7817	0.1339	5.8370
9.42	0.7926	0.1405	5.6394
9.67	0.7908	0.1412	5.6023
9.92	0.8000	0.1472	5.4335
10.17	0.8073	0.1521	5.3064
10.42	0.8120	0.1565	5.1891
10.67	0.8139	0.1601	5.0828
10.92	0.8246	0.1645	5.0124
11.17	0.8124	0.1679	4.8373
11.42	0.8282	0.1737	4.7678
11.67	0.8260	0.1737	4.7540
11.92	0.8278	0.1741	4.7554
12.17	0.8196	0.1662	4.9316
12.42	0.8313	0.1677	4.9562
12.67	0.8305	0.1682	4.9371
12.92	0.8300	0.1765	4.7013
13.17	0.8302	0.1675	4.9569
13.42	0.8440	0.1796	4.6985
13.67	0.8167	0.1724	4.7381
13.92	0.8275	0.1749	4.7311
14.17	0.8432	0.1778	4.7426
14.42	0.8298	0.1751	4.7402
14.67	0.8437	0.1857	4.5442
14.92	0.8530	0.1946	4.3833
15.17	0.8259	0.1884	4.3829
15.42	0.8371	0.1925	4.3491
15.67	0.8390	0.2081	4.0326
15.92	0.8499	0.2111	4.0251
16.17	0.8636	0.2090	4.1321
16.42	0.8599	0.2095	4.1036
16.67	0.8509	0.2181	3.9021
16.92	0.8665	0.2303	3.7619
17.17	0.8753	0.2438	3.5897
17.42	0.8554	0.2416	3.5405
17.67	0.8702	0.2348	3.7070
17.92	0.8849	0.2445	3.6188
18.17	0.8635	0.2556	3.3781
18.42	0.8514	0.2568	3.3158
18.67	0.8824	0.2695	3.2739
18.92	0.8791	0.2674	3.2877
19.17	0.8621	0.2596	3.3207
19.42	0.8819	0.2707	3.2574
19.67	0.8765	0.2886	3.0376
19.92	0.8589	0.2697	3.1841
20.17	0.8571	0.2722	3.1494
20.42	0.8804	0.2841	3.0986
20.67	0.8632	0.2870	3.0080
20.92	0.8588	0.2827	3.0384
21.17	0.8694	0.2879	3.0195
21.42	0.8682	0.2945	2.9476
21.67	0.8456	0.2971	2.8465
21.92	0.8888	0.3006	2.9565
22.17	0.8564	0.3052	2.8065
22.42	0.8651	0.3146	2.7496
22.67	0.8723	0.3100	2.8138
22.92	0.8767	0.3297	2.6593
23.17	0.8509	0.3246	2.6218
23.42	0.8867	0.3301	2.6864
23.67	0.8909	0.3205	2.7799
23.92	0.9021	0.3362	2.6833
24.17	0.9071	0.3416	2.6550
24.42	0.9090	0.3577	2.5415
24.67	0.8861	0.3476	2.5493
24.92	0.8881	0.3533	2.5135

Table E.8: Model #8, g=1c, s=1.5c, Aerodynamic Data at Re 120,000

α (°)	C_L (-)	C_D (-)	L/D (-)
-2.07	-0.1469	0.0257	-5.7056
-1.82	-0.1309	0.0258	-5.0727
-1.57	-0.1126	0.0246	-4.5790
-1.32	-0.0991	0.0240	-4.1361
-1.07	-0.0804	0.0226	-3.5593
-0.82	-0.0552	0.0210	-2.6265
-0.57	-0.0583	0.0207	-2.8194
-0.32	-0.0394	0.0225	-1.7524
-0.07	-0.0093	0.0227	-0.4116
0.19	0.0174	0.0226	0.7704
0.44	0.0320	0.0232	1.3756
0.69	0.0517	0.0224	2.3075
0.94	0.0572	0.0225	2.5363
1.19	0.0833	0.0217	3.8402
1.44	0.0995	0.0241	4.1352
1.69	0.1248	0.0231	5.4102
1.94	0.1384	0.0252	5.4841
2.19	0.1647	0.0250	6.5881
2.44	0.1788	0.0255	7.0114
2.69	0.1978	0.0267	7.4096
2.94	0.2122	0.0275	7.7073
3.19	0.2384	0.0304	7.8404
3.44	0.2384	0.0304	7.8404
3.69	0.2679	0.0322	8.3289
3.94	0.2835	0.0336	8.4321
4.19	0.3081	0.0363	8.4768
4.44	0.3186	0.0392	8.1364
4.69	0.3305	0.0401	8.2429
4.94	0.3563	0.0447	7.9649
5.19	0.4001	0.0491	8.1470
5.44	0.4201	0.0515	8.1605
5.69	0.4450	0.0568	7.8319
5.94	0.4695	0.0599	7.8340
6.19	0.4802	0.0628	7.6525
6.44	0.5031	0.0659	7.6372
6.69	0.5456	0.0744	7.3367
6.94	0.5573	0.0762	7.3181
7.19	0.5862	0.0826	7.0924
7.44	0.6036	0.0874	6.9087
7.69	0.6005	0.0880	6.8278
7.94	0.6392	0.0959	6.6652
8.19	0.6514	0.1000	6.5141
8.44	0.6679	0.1061	6.2949
8.69	0.6986	0.1137	6.1433
8.94	0.7090	0.1170	6.0611
9.19	0.7489	0.1258	5.9508
9.44	0.7624	0.1329	5.7374
9.69	0.7757	0.1367	5.6758
9.94	0.8069	0.1446	5.5813
10.19	0.8168	0.1492	5.4740
10.44	0.8418	0.1565	5.3792
10.69	0.8508	0.1603	5.3068
10.94	0.8597	0.1691	5.0848
11.19	0.8810	0.1766	4.9898
11.44	0.8941	0.1807	4.9474
11.69	0.9027	0.1850	4.8808
11.94	0.9169	0.1937	4.7322
12.19	0.9074	0.1955	4.6424
12.44	0.9166	0.2022	4.5340
12.69	0.9228	0.2067	4.4646
12.94	0.9251	0.2103	4.3992
13.19	0.9252	0.2179	4.2469
13.44	0.9179	0.2195	4.1813
13.69	0.9118	0.2212	4.1227
13.94	0.9226	0.2250	4.1003
14.19	0.8999	0.2275	3.9551
14.44	0.9091	0.2327	3.9064
14.69	0.9037	0.2359	3.8305
14.94	0.8979	0.2381	3.7715
15.19	0.9015	0.2440	3.6942
15.44	0.9025	0.2453	3.6795
15.69	0.8997	0.2490	3.6128
15.94	0.8963	0.2531	3.5405
16.19	0.8954	0.2597	3.4476
16.44	0.8793	0.2590	3.3947
16.69	0.8919	0.2663	3.3489
16.94	0.8997	0.2720	3.3076
17.19	0.9089	0.2743	3.3137
17.44	0.9032	0.2817	3.2059
17.69	0.9197	0.2875	3.1991
17.94	0.9078	0.2913	3.1166
18.19	0.9113	0.2968	3.0709
18.44	0.9033	0.2961	3.0510
18.69	0.8966	0.2989	2.9994
18.94	0.9103	0.3066	2.9686
19.19	0.9059	0.3074	2.9468
19.44	0.9204	0.3150	2.9219
19.69	0.9072	0.3177	2.8552
19.94	0.8863	0.3175	2.7915
20.19	0.8914	0.3223	2.7660
20.44	0.9199	0.3354	2.7425
20.69	0.8995	0.3301	2.7249
20.94	0.9184	0.3415	2.6889
21.19	0.9156	0.3468	2.6400
21.44	0.9091	0.3451	2.6346
21.69	0.9186	0.3544	2.5920
21.94	0.9269	0.3591	2.5807
22.19	0.9387	0.3666	2.5607
22.44	0.9239	0.3680	2.5105
22.69	0.9067	0.3706	2.4462
22.94	0.9142	0.3736	2.4467
23.19	0.9164	0.3823	2.3970
23.44	0.9244	0.3880	2.3824
23.69	0.9222	0.3915	2.3555
23.94	0.9174	0.3922	2.3392
24.19	0.9503	0.4089	2.3242
24.44	0.9156	0.4046	2.2631
24.69	0.9472	0.4161	2.2765
24.94	0.9361	0.4187	2.2359

Table E.9: Model #9, g=0.5c, s=-0.5c, Aerodynamic Data at Re 120,000

α (°)	C_L (-)	C_D (-)	L/D (-)
-2.48	-0.1435	0.0246	-5.8345
-2.23	-0.1212	0.0242	-5.0143
-1.98	-0.1106	0.0230	-4.8021
-1.73	-0.0935	0.0228	-4.1019
-1.48	-0.0831	0.0225	-3.6954
-1.23	-0.0751	0.0221	-3.4013
-0.98	-0.0592	0.0222	-2.6670
-0.73	-0.0374	0.0217	-1.7254
-0.48	-0.0336	0.0229	-1.4685
-0.23	-0.0107	0.0215	-0.4986
0.03	0.0033	0.0229	0.1426
0.28	0.0169	0.0216	0.7858
0.53	0.0360	0.0233	1.5463
0.78	0.0501	0.0230	2.1768
1.03	0.0580	0.0243	2.3900
1.28	0.0736	0.0238	3.0956
1.53	0.0927	0.0246	3.7696
1.78	0.1115	0.0258	4.3157
2.03	0.1221	0.0270	4.5262
2.28	0.1269	0.0278	4.5613
2.53	0.1503	0.0281	5.3420
2.78	0.1609	0.0304	5.2889
3.03	0.1609	0.0304	5.2889
3.28	0.1637	0.0305	5.3731
3.53	0.1874	0.0334	5.6048
3.78	0.2007	0.0340	5.9002
4.03	0.2167	0.0359	6.0274
4.28	0.2280	0.0375	6.0885
4.53	0.2468	0.0399	6.1817
4.78	0.2729	0.0432	6.3236
5.03	0.3014	0.0469	6.4319
5.28	0.3122	0.0500	6.2487
5.53	0.3284	0.0520	6.3111
5.78	0.3352	0.0551	6.0884
6.03	0.3525	0.0585	6.0309
6.28	0.3667	0.0606	6.0555
6.53	0.3729	0.0644	5.7886
6.78	0.3846	0.0683	5.6289
7.03	0.4048	0.0714	5.6677
7.28	0.4080	0.0731	5.5846
7.53	0.4206	0.0760	5.5309
7.78	0.4289	0.0806	5.3191
8.03	0.4423	0.0841	5.2604
8.28	0.4547	0.0870	5.2255
8.53	0.4570	0.0904	5.0564
8.78	0.4680	0.0941	4.9740
9.03	0.4752	0.0970	4.8985
9.28	0.4858	0.1022	4.7549
9.53	0.4886	0.1046	4.6711
9.78	0.4929	0.1074	4.5892
10.03	0.5025	0.1106	4.5458
10.28	0.5104	0.1155	4.4212
10.53	0.5193	0.1206	4.3050
10.78	0.5213	0.1220	4.2722
11.03	0.5236	0.1251	4.1857
11.28	0.5314	0.1294	4.1063
11.53	0.5358	0.1325	4.0450
11.78	0.5348	0.1355	3.9473
12.03	0.5434	0.1399	3.8852
12.28	0.5479	0.1431	3.8288
12.53	0.5524	0.1471	3.7561
12.78	0.5585	0.1505	3.7104
13.03	0.5623	0.1541	3.6482
13.28	0.5637	0.1589	3.5471
13.53	0.5638	0.1606	3.5098
13.78	0.5563	0.1627	3.4200
14.03	0.5600	0.1648	3.3977
14.28	0.5632	0.1698	3.3166
14.53	0.5675	0.1709	3.3211
14.78	0.5693	0.1758	3.2385
15.03	0.5678	0.1789	3.1748
15.28	0.5642	0.1794	3.1447
15.53	0.5702	0.1854	3.0758
15.78	0.5790	0.1918	3.0189
16.03	0.5808	0.1931	3.0077
16.28	0.5645	0.1920	2.9405
16.53	0.5624	0.1928	2.9163
16.78	0.5693	0.1995	2.8530
17.03	0.5637	0.1994	2.8278
17.28	0.5721	0.2042	2.8013
17.53	0.5828	0.2114	2.7565
17.78	0.5797	0.2147	2.7001
18.03	0.5774	0.2158	2.6748
18.28	0.5741	0.2165	2.6516
18.53	0.5794	0.2226	2.6033
18.78	0.5698	0.2207	2.5820
19.03	0.5607	0.2201	2.5470
19.28	0.5770	0.2312	2.4952
19.53	0.5700	0.2314	2.4635
19.78	0.5665	0.2305	2.4578
20.03	0.5764	0.2375	2.4265
20.28	0.5695	0.2350	2.4228
20.53	0.5650	0.2411	2.3431
20.78	0.5722	0.2464	2.3221
21.03	0.5702	0.2488	2.2920
21.28	0.5643	0.2474	2.2808
21.53	0.5689	0.2520	2.2574
21.78	0.5660	0.2586	2.1890
22.03	0.5722	0.2596	2.2038
22.28	0.5669	0.2641	2.1463
22.53	0.5542	0.2591	2.1387
22.78	0.5564	0.2610	2.1313
23.03	0.5487	0.2632	2.0844
23.28	0.5420	0.2626	2.0639
23.53	0.5465	0.2666	2.0498
23.78	0.5415	0.2679	2.0214
24.03	0.5365	0.2684	1.9990
24.28	0.5366	0.2707	1.9819
24.53	0.5353	0.2763	1.9375

Table E.10: Model #10, g=0.5c, s=-1c, Aerodynamic Data at Re 120,000

α (°)	C_L (-)	C_D (-)	L/D (-)
-1.90	-0.1271	0.0227	-5.6082
-1.65	-0.1094	0.0242	-4.5131
-1.40	-0.0940	0.0230	-4.0880
-1.15	-0.0718	0.0226	-3.1764
-0.90	-0.0460	0.0213	-2.1596
-0.65	-0.0506	0.0211	-2.4011
-0.40	-0.0300	0.0232	-1.2948
-0.15	-0.0077	0.0216	-0.3569
0.10	0.0098	0.0230	0.4277
0.35	0.0121	0.0214	0.5669
0.60	0.0417	0.0215	1.9382
0.85	0.0568	0.0241	2.3609
1.10	0.0659	0.0238	2.7665
1.35	0.0906	0.0237	3.8285
1.60	0.1022	0.0247	4.1387
1.85	0.1170	0.0254	4.6107
2.10	0.1319	0.0259	5.0943
2.35	0.1530	0.0278	5.5090
2.60	0.1690	0.0297	5.6941
2.85	0.1859	0.0288	6.4569
3.10	0.1973	0.0314	6.2747
3.35	0.2113	0.0338	6.2488
3.60	0.2113	0.0338	6.2488
3.85	0.2299	0.0359	6.3964
4.10	0.2527	0.0374	6.7514
4.35	0.2575	0.0385	6.6827
4.60	0.2801	0.0411	6.8080
4.85	0.2846	0.0439	6.4791
5.10	0.3035	0.0473	6.4093
5.35	0.3344	0.0534	6.2629
5.60	0.3568	0.0545	6.5447
5.85	0.3613	0.0585	6.1804
6.10	0.3776	0.0623	6.0638
6.35	0.3924	0.0656	5.9778
6.60	0.4035	0.0692	5.8310
6.85	0.4184	0.0709	5.9003
7.10	0.4223	0.0748	5.6466
7.35	0.4318	0.0773	5.5871
7.60	0.4366	0.0783	5.5764
7.85	0.4492	0.0843	5.3296
8.10	0.4515	0.0859	5.2543
8.35	0.4628	0.0900	5.1402
8.60	0.4634	0.0916	5.0613
8.85	0.4707	0.0946	4.9741
9.10	0.4772	0.0994	4.7985
9.35	0.4833	0.1013	4.7735
9.60	0.4865	0.1070	4.5486
9.85	0.4951	0.1090	4.5417
10.10	0.4941	0.1104	4.4767
10.35	0.4972	0.1122	4.4306
10.60	0.5004	0.1169	4.2808
10.85	0.4941	0.1189	4.1556
11.10	0.5017	0.1223	4.1023
11.35	0.5063	0.1254	4.0379
11.60	0.5090	0.1273	3.9991
11.85	0.5099	0.1281	3.9794
12.10	0.5040	0.1316	3.8300
12.35	0.5061	0.1320	3.8347
12.60	0.5054	0.1343	3.7616
12.85	0.5059	0.1388	3.6441
13.10	0.5021	0.1411	3.5593
13.35	0.5032	0.1386	3.6320
13.60	0.4991	0.1401	3.5618
13.85	0.5026	0.1469	3.4202
14.10	0.4941	0.1499	3.2961
14.35	0.4986	0.1464	3.4058
14.60	0.4890	0.1483	3.2974
14.85	0.4847	0.1508	3.2131
15.10	0.4843	0.1499	3.2303
15.35	0.4778	0.1534	3.1146
15.60	0.4748	0.1534	3.0948
15.85	0.4668	0.1537	3.0365
16.10	0.4617	0.1522	3.0345
16.35	0.4565	0.1588	2.8743
16.60	0.4525	0.1542	2.9352
16.85	0.4524	0.1565	2.8900
17.10	0.4361	0.1586	2.7502
17.35	0.4329	0.1466	2.9534
17.60	0.4317	0.1452	2.9728
17.85	0.4228	0.1614	2.6197
18.10	0.4126	0.1502	2.7468
18.35	0.4115	0.1459	2.8210
18.60	0.4045	0.1527	2.6486
18.85	0.4080	0.1552	2.6290
19.10	0.3942	0.1570	2.5103
19.35	0.3893	0.1521	2.5591
19.60	0.3871	0.1497	2.5853
19.85	0.3831	0.1540	2.4879
20.10	0.3775	0.1575	2.3965
20.35	0.3775	0.1584	2.3823
20.60	0.3767	0.1549	2.4313
20.85	0.3664	0.1561	2.3473
21.10	0.3706	0.1575	2.3536
21.35	0.3605	0.1582	2.2785
21.60	0.3602	0.1541	2.3376
21.85	0.3508	0.1572	2.2315
22.10	0.3533	0.1584	2.2299
22.35	0.3528	0.1625	2.1712
22.60	0.3461	0.1572	2.2016
22.85	0.3484	0.1629	2.1381
23.10	0.3429	0.1603	2.1389
23.35	0.3473	0.1657	2.0963
23.60	0.3398	0.1634	2.0797
23.85	0.3529	0.1680	2.1005
24.10	0.3433	0.1682	2.0413
24.35	0.3454	0.1688	2.0457
24.60	0.3465	0.1747	1.9829
24.85	0.3482	0.1743	1.9977
25.10	0.3429	0.1753	1.9560

Table E.11: Model #11, g=1c, s=-0.5c, Aerodynamic Data at Re 120,000

α (°)	C_L (-)	C_D (-)	L/D (-)
-2.03	-0.1404	0.0256	-5.4801
-1.78	-0.1268	0.0237	-5.3408
-1.53	-0.1108	0.0237	-4.6730
-1.28	-0.0973	0.0249	-3.9159
-1.03	-0.0687	0.0245	-2.8021
-0.78	-0.0566	0.0227	-2.4940
-0.53	-0.0377	0.0225	-1.6751
-0.28	-0.0225	0.0242	-0.9289
-0.03	-0.0064	0.0223	-0.2867
0.22	0.0046	0.0232	0.1988
0.47	0.0203	0.0225	0.9017
0.72	0.0319	0.0225	1.4153
0.97	0.0607	0.0218	2.7854
1.22	0.0660	0.0240	2.7492
1.47	0.0918	0.0239	3.8455
1.72	0.1028	0.0263	3.9069
1.97	0.1237	0.0258	4.7887
2.22	0.1392	0.0258	5.3977
2.47	0.1584	0.0276	5.7335
2.72	0.1817	0.0305	5.9635
2.97	0.1940	0.0318	6.0984
3.22	0.2089	0.0331	6.3054
3.47	0.2089	0.0331	6.3054
3.72	0.2314	0.0354	6.5374
3.97	0.2419	0.0373	6.4774
4.22	0.2576	0.0380	6.7838
4.47	0.2938	0.0407	7.2191
4.72	0.3153	0.0451	6.9845
4.97	0.3200	0.0471	6.7957
5.22	0.3574	0.0535	6.6805
5.47	0.3853	0.0568	6.7837
5.72	0.4019	0.0590	6.8075
5.97	0.4218	0.0630	6.6943
6.22	0.4433	0.0671	6.6110
6.47	0.4622	0.0725	6.3789
6.72	0.4799	0.0776	6.1823
6.97	0.4984	0.0796	6.2653
7.22	0.5058	0.0840	6.0222
7.47	0.5306	0.0889	5.9662
7.72	0.5591	0.0942	5.9343
7.97	0.5798	0.0995	5.8291
8.22	0.5845	0.1033	5.6578
8.47	0.6111	0.1096	5.5735
8.72	0.6225	0.1160	5.3680
8.97	0.6439	0.1204	5.3473
9.22	0.6678	0.1283	5.2042
9.47	0.6750	0.1319	5.1180
9.72	0.6931	0.1387	4.9962
9.97	0.7032	0.1429	4.9195
10.22	0.7019	0.1457	4.8186
10.47	0.7211	0.1514	4.7642
10.72	0.7298	0.1583	4.6100
10.97	0.7389	0.1627	4.5426
11.22	0.7445	0.1671	4.4553
11.47	0.7505	0.1736	4.3239
11.72	0.7540	0.1770	4.2595
11.97	0.7547	0.1805	4.1815
12.22	0.7572	0.1860	4.0706
12.47	0.7525	0.1892	3.9766
12.72	0.7536	0.1906	3.9543
12.97	0.7539	0.1947	3.8725
13.22	0.7569	0.1995	3.7938
13.47	0.7499	0.2024	3.7045
13.72	0.7452	0.2040	3.6529
13.97	0.7388	0.2070	3.5683
14.22	0.7296	0.2068	3.5288
14.47	0.7294	0.2100	3.4739
14.72	0.7360	0.2160	3.4079
14.97	0.7259	0.2161	3.3594
15.22	0.7200	0.2191	3.2858
15.47	0.7106	0.2216	3.2068
15.72	0.7050	0.2212	3.1874
15.97	0.6941	0.2229	3.1142
16.22	0.7024	0.2278	3.0842
16.47	0.6848	0.2268	3.0190
16.72	0.6859	0.2298	2.9847
16.97	0.6754	0.2307	2.9278
17.22	0.6762	0.2339	2.8906
17.47	0.6663	0.2357	2.8270
17.72	0.6824	0.2445	2.7909
17.97	0.6797	0.2454	2.7696
18.22	0.6879	0.2531	2.7175
18.47	0.6792	0.2540	2.6735
18.72	0.6830	0.2569	2.6583
18.97	0.6789	0.2582	2.6293
19.22	0.6797	0.2623	2.5909
19.47	0.6888	0.2687	2.5640
19.72	0.6892	0.2711	2.5425
19.97	0.6871	0.2780	2.4711
20.22	0.6966	0.2831	2.4607
20.47	0.6879	0.2827	2.4333
20.72	0.6847	0.2859	2.3951
20.97	0.6820	0.2896	2.3551
21.22	0.6800	0.2895	2.3485
21.47	0.6857	0.2957	2.3189
21.72	0.6812	0.2994	2.2750
21.97	0.6742	0.3003	2.2450
22.22	0.6780	0.3051	2.2219
22.47	0.6797	0.3105	2.1893
22.72	0.6743	0.3092	2.1811
22.97	0.6586	0.3056	2.1549
23.22	0.6687	0.3143	2.1277
23.47	0.6683	0.3185	2.0983
23.72	0.6671	0.3190	2.0911
23.97	0.6815	0.3308	2.0604
24.22	0.6767	0.3295	2.0536
24.47	0.6807	0.3370	2.0199
24.72	0.6826	0.3414	1.9995
24.97	0.6743	0.3401	1.9828

Table E.12: Model #12, g=1c, s=-1c, Aerodynamic Data at Re 120,000

α (°)	C_L (-)	C_D (-)	L/D (-)
-2.03	-0.1370	0.0226	-6.0702
-1.78	-0.1167	0.0217	-5.3775
-1.53	-0.0990	0.0225	-4.4084
-1.28	-0.0899	0.0198	-4.5519
-1.03	-0.0681	0.0204	-3.3444
-0.78	-0.0450	0.0201	-2.2349
-0.53	-0.0429	0.0214	-2.0000
-0.28	-0.0256	0.0211	-1.2130
-0.03	-0.0051	0.0181	-0.2785
0.22	0.0102	0.0194	0.5259
0.47	0.0253	0.0205	1.2360
0.72	0.0504	0.0215	2.3403
0.97	0.0624	0.0202	3.0875
1.22	0.0762	0.0223	3.4182
1.47	0.0917	0.0210	4.3732
1.72	0.1124	0.0233	4.8183
1.97	0.1392	0.0237	5.8795
2.22	0.1575	0.0253	6.2376
2.47	0.1728	0.0269	6.4312
2.72	0.1987	0.0262	7.5815
2.97	0.2102	0.0311	6.7629
3.22	0.2225	0.0314	7.0761
3.47	0.2225	0.0314	7.0761
3.72	0.2525	0.0351	7.1938
3.97	0.2481	0.0341	7.2799
4.22	0.2631	0.0358	7.3434
4.47	0.3012	0.0392	7.6888
4.72	0.3020	0.0420	7.1817
4.97	0.3377	0.0444	7.6087
5.22	0.3685	0.0496	7.4319
5.47	0.3800	0.0536	7.0924
5.72	0.4117	0.0589	6.9920
5.97	0.4155	0.0624	6.6565
6.22	0.4400	0.0662	6.6502
6.47	0.4532	0.0702	6.4563
6.72	0.4659	0.0716	6.5096
6.97	0.4804	0.0750	6.4079
7.22	0.4979	0.0811	6.1429
7.47	0.5132	0.0848	6.0527
7.72	0.5272	0.0919	5.7345
7.97	0.5510	0.0938	5.8756
8.22	0.5628	0.0977	5.7585
8.47	0.5768	0.1035	5.5705
8.72	0.5873	0.1077	5.4545
8.97	0.6044	0.1121	5.3916
9.22	0.6100	0.1161	5.2531
9.47	0.6229	0.1189	5.2393
9.72	0.6171	0.1248	4.9433
9.97	0.6299	0.1287	4.8922
10.22	0.6329	0.1317	4.8042
10.47	0.6381	0.1361	4.6872
10.72	0.6418	0.1390	4.6185
10.97	0.6457	0.1442	4.4780
11.22	0.6508	0.1460	4.4582
11.47	0.6505	0.1505	4.3217
11.72	0.6503	0.1520	4.2782
11.97	0.6486	0.1562	4.1529
12.22	0.6526	0.1592	4.0980
12.47	0.6481	0.1621	3.9970
12.72	0.6459	0.1651	3.9126
12.97	0.6462	0.1694	3.8133
13.22	0.6551	0.1752	3.7390
13.47	0.6510	0.1790	3.6371
13.72	0.6531	0.1805	3.6194
13.97	0.6553	0.1837	3.5679
14.22	0.6437	0.1831	3.5152
14.47	0.6481	0.1877	3.4528
14.72	0.6655	0.1969	3.3797
14.97	0.6522	0.1989	3.2792
15.22	0.6586	0.2010	3.2770
15.47	0.6647	0.2063	3.2224
15.72	0.6360	0.2021	3.1465
15.97	0.6338	0.2032	3.1186
16.22	0.6498	0.2102	3.0915
16.47	0.6470	0.2149	3.0103
16.72	0.6465	0.2205	2.9320
16.97	0.6545	0.2248	2.9115
17.22	0.6532	0.2247	2.9075
17.47	0.6529	0.2273	2.8722
17.72	0.6596	0.2337	2.8231
17.97	0.6553	0.2370	2.7652
18.22	0.6556	0.2400	2.7316
18.47	0.6384	0.2373	2.6907
18.72	0.6477	0.2408	2.6903
18.97	0.6475	0.2463	2.6287
19.22	0.6524	0.2508	2.6015
19.47	0.6438	0.2486	2.5895
19.72	0.6327	0.2513	2.5181
19.97	0.6476	0.2603	2.4877
20.22	0.6402	0.2592	2.4700
20.47	0.6421	0.2642	2.4304
20.72	0.6417	0.2666	2.4069
20.97	0.6475	0.2751	2.3540
21.22	0.6700	0.2858	2.3441
21.47	0.6559	0.2834	2.3142
21.72	0.6760	0.2897	2.3339
21.97	0.6853	0.3002	2.2830
22.22	0.6878	0.3054	2.2523
22.47	0.6645	0.2996	2.2179
22.72	0.6984	0.3149	2.2183
22.97	0.6811	0.3123	2.1809
23.22	0.7075	0.3315	2.1343
23.47	0.7205	0.3384	2.1288
23.72	0.6992	0.3297	2.1208
23.97	0.7231	0.3466	2.0865
24.22	0.7176	0.3442	2.0850
24.47	0.7347	0.3612	2.0338
24.72	0.7048	0.3431	2.0544
24.97	0.7138	0.3554	2.0084

Table E.13: Model #13, g=2c, s=-1c, Aerodynamic Data at Re 120,000

α (°)	C_L (-)	C_D (-)	L/D (-)
-2.13	-0.1713	0.0271	-6.3167
-1.88	-0.1590	0.0258	-6.1559
-1.63	-0.1226	0.0263	-4.6577
-1.38	-0.1057	0.0246	-4.2929
-1.13	-0.0903	0.0259	-3.4942
-0.88	-0.0757	0.0240	-3.1497
-0.63	-0.0530	0.0247	-2.1449
-0.38	-0.0302	0.0238	-1.2697
-0.13	-0.0150	0.0227	-0.6618
0.12	0.0177	0.0222	0.7973
0.37	0.0310	0.0216	1.4395
0.62	0.0519	0.0216	2.4084
0.87	0.0819	0.0200	4.0984
1.12	0.0914	0.0216	4.2303
1.37	0.1187	0.0238	4.9956
1.62	0.1346	0.0241	5.5778
1.87	0.1669	0.0249	6.7079
2.12	0.1830	0.0244	7.4912
2.37	0.1990	0.0249	7.9923
2.62	0.2262	0.0269	8.4047
2.87	0.2508	0.0287	8.7471
3.12	0.2591	0.0294	8.8238
3.37	0.2591	0.0294	8.8238
3.62	0.2921	0.0306	9.5388
3.87	0.3071	0.0314	9.7692
4.12	0.3208	0.0338	9.4856
4.37	0.3477	0.0369	9.4219
4.62	0.3766	0.0390	9.6649
4.87	0.3977	0.0423	9.3949
5.12	0.4369	0.0470	9.3016
5.37	0.4765	0.0515	9.2468
5.62	0.4956	0.0566	8.7547
5.87	0.5294	0.0605	8.7458
6.12	0.5469	0.0638	8.5685
6.37	0.5774	0.0672	8.5911
6.62	0.6096	0.0726	8.3924
6.87	0.6167	0.0753	8.1942
7.12	0.6380	0.0797	8.0038
7.37	0.6630	0.0851	7.7919
7.62	0.6801	0.0890	7.6427
7.87	0.6923	0.0902	7.6778
8.12	0.7283	0.0974	7.4740
8.37	0.7351	0.1027	7.1548
8.62	0.7559	0.1086	6.9620
8.87	0.7803	0.1151	6.7804
9.12	0.7881	0.1202	6.5589
9.37	0.8062	0.1248	6.4582
9.62	0.8031	0.1288	6.2373
9.87	0.8067	0.1316	6.1323
10.12	0.8139	0.1361	5.9823
10.37	0.8112	0.1401	5.7912
10.62	0.8198	0.1371	5.9808
10.87	0.8237	0.1472	5.5969
11.12	0.8352	0.1534	5.4433
11.37	0.8278	0.1542	5.3684
11.62	0.8243	0.1539	5.3573
11.87	0.8170	0.1530	5.3412
12.12	0.8149	0.1573	5.1796
12.37	0.8109	0.1593	5.0889
12.62	0.7975	0.1539	5.1812
12.87	0.7976	0.1291	6.1790
13.12	0.8052	0.1486	5.4196
13.37	0.8031	0.1265	6.3465
13.62	0.8072	0.1253	6.4438
13.87	0.8025	0.1293	6.2041
14.12	0.8065	0.1026	7.8589
14.37	0.7944	0.1204	6.5956
14.62	0.7698	0.1088	7.0754
14.87	0.7944	0.1210	6.5657
15.12	0.8142	0.1214	6.7070
15.37	0.7940	0.1139	6.9693
15.62	0.7820	0.1526	5.1229
15.87	0.8103	0.1271	6.3728
16.12	0.7907	0.1489	5.3103
16.37	0.7987	0.1256	6.3602
16.62	0.7947	0.1502	5.2895
16.87	0.7868	0.1667	4.7214
17.12	0.7944	0.1360	5.8413
17.37	0.7706	0.1548	4.9769
17.62	0.7947	0.1615	4.9214
17.87	0.7832	0.1533	5.1105
18.12	0.7933	0.1504	5.2734
18.37	0.8249	0.1507	5.4748
18.62	0.8018	0.1666	4.8135
18.87	0.8096	0.1605	5.0439
19.12	0.8015	0.1658	4.8355
19.37	0.7965	0.1783	4.4679
19.62	0.7802	0.1913	4.0775
19.87	0.8226	0.1719	4.7853
20.12	0.8277	0.1813	4.5652
20.37	0.8139	0.1872	4.3468
20.62	0.8096	0.1942	4.1687
20.87	0.8372	0.1979	4.2316
21.12	0.8597	0.2047	4.1989
21.37	0.8004	0.2242	3.5695
21.62	0.8380	0.2204	3.8026
21.87	0.7989	0.2242	3.5632
22.12	0.8354	0.2146	3.8918
22.37	0.8619	0.2179	3.9565
22.62	0.8039	0.2196	3.6602
22.87	0.8070	0.2046	3.9442
23.12	0.8287	0.2300	3.6030
23.37	0.7747	0.2456	3.1540
23.62	0.7882	0.2380	3.3117
23.87	0.7435	0.2552	2.9129
24.12	0.8365	0.2438	3.4304
24.37	0.7909	0.2454	3.2226
24.62	0.8222	0.2523	3.2584
24.87	0.7860	0.3081	2.5513

Table E.14: Model #14, g=1c, s=-1.5c, Aerodynamic Data at Re 120,000

α (°)	C_L (-)	C_D (-)	L/D (-)
-2.06	-0.1498	0.0255	-5.8804
-1.81	-0.1305	0.0236	-5.5397
-1.56	-0.1096	0.0235	-4.6586
-1.31	-0.1014	0.0230	-4.4065
-1.06	-0.0712	0.0232	-3.0744
-0.81	-0.0540	0.0241	-2.2366
-0.56	-0.0375	0.0229	-1.6392
-0.31	-0.0232	0.0231	-1.0074
-0.06	-0.0004	0.0220	-0.0160
0.19	0.0092	0.0240	0.3830
0.44	0.0300	0.0220	1.3636
0.69	0.0473	0.0232	2.0365
0.94	0.0739	0.0237	3.1141
1.19	0.0865	0.0245	3.5313
1.44	0.1040	0.0234	4.4371
1.69	0.1156	0.0257	4.4922
1.94	0.1393	0.0257	5.4236
2.19	0.1546	0.0267	5.7879
2.44	0.1805	0.0289	6.2464
2.69	0.1837	0.0296	6.1983
2.94	0.2108	0.0303	6.9580
3.19	0.2275	0.0330	6.8843
3.44	0.2275	0.0330	6.8843
3.69	0.2354	0.0335	7.0242
3.94	0.2708	0.0353	7.6638
4.19	0.2833	0.0396	7.1551
4.44	0.2978	0.0420	7.0867
4.69	0.3233	0.0438	7.3759
4.94	0.3351	0.0465	7.2070
5.19	0.3792	0.0509	7.4514
5.44	0.4107	0.0563	7.2952
5.69	0.4233	0.0602	7.0298
5.94	0.4400	0.0621	7.0799
6.19	0.4580	0.0680	6.7339
6.44	0.4819	0.0729	6.6112
6.69	0.4963	0.0758	6.5483
6.94	0.5104	0.0802	6.3652
7.19	0.5239	0.0843	6.2150
7.44	0.5382	0.0881	6.1121
7.69	0.5571	0.0922	6.0408
7.94	0.5632	0.0946	5.9559
8.19	0.5843	0.1014	5.7613
8.44	0.5908	0.1042	5.6710
8.69	0.6083	0.1119	5.4374
8.94	0.6287	0.1179	5.3319
9.19	0.6354	0.1217	5.2193
9.44	0.6574	0.1279	5.1383
9.69	0.6527	0.1284	5.0836
9.94	0.6519	0.1320	4.9369
10.19	0.6850	0.1416	4.8374
10.44	0.6836	0.1449	4.7179
10.69	0.6946	0.1487	4.6699
10.94	0.6905	0.1525	4.5274
11.19	0.7125	0.1604	4.4408
11.44	0.7223	0.1666	4.3348
11.69	0.7245	0.1679	4.3143
11.94	0.7201	0.1711	4.2093
12.19	0.7275	0.1780	4.0862
12.44	0.7170	0.1770	4.0513
12.69	0.7390	0.1871	3.9497
12.94	0.7336	0.1889	3.8836
13.19	0.7244	0.1899	3.8141
13.44	0.7180	0.1916	3.7482
13.69	0.7183	0.1953	3.6782
13.94	0.7219	0.1981	3.6434
14.19	0.7421	0.2103	3.5287
14.44	0.6976	0.2005	3.4793
14.69	0.7070	0.2064	3.4258
14.94	0.7050	0.2082	3.3856
15.19	0.7085	0.2168	3.2674
15.44	0.6951	0.2118	3.2819
15.69	0.7042	0.2220	3.1729
15.94	0.6915	0.2218	3.1172
16.19	0.7152	0.2311	3.0947
16.44	0.7008	0.2319	3.0221
16.69	0.6821	0.2278	2.9947
16.94	0.6864	0.2316	2.9640
17.19	0.6858	0.2351	2.9168
17.44	0.7131	0.2485	2.8691
17.69	0.7002	0.2467	2.8383
17.94	0.7127	0.2524	2.8238
18.19	0.6879	0.2475	2.7797
18.44	0.6789	0.2470	2.7484
18.69	0.6868	0.2561	2.6819
18.94	0.6679	0.2528	2.6418
19.19	0.6821	0.2610	2.6132
19.44	0.6698	0.2560	2.6168
19.69	0.6667	0.2606	2.5588
19.94	0.6744	0.2715	2.4843
20.19	0.6966	0.2874	2.4240
20.44	0.6948	0.2796	2.4847
20.69	0.7303	0.2965	2.4630
20.94	0.6863	0.2819	2.4348
21.19	0.6692	0.2805	2.3859
21.44	0.6834	0.2933	2.3304
21.69	0.7463	0.3059	2.4402
21.94	0.7189	0.3106	2.3148
22.19	0.7581	0.3204	2.3663
22.44	0.6982	0.3077	2.2693
22.69	0.6806	0.3087	2.2048
22.94	0.6939	0.3256	2.1314
23.19	0.6577	0.2959	2.2226
23.44	0.6323	0.2879	2.1963
23.69	0.5896	0.2843	2.0739
23.94	0.6200	0.3054	2.0298
24.19	0.5813	0.2828	2.0552
24.44	0.5855	0.2841	2.0611
24.69	0.5911	0.2748	2.1506
24.94	0.5915	0.3132	1.8883

Appendix F: Stall Flutter

Overview

This section is intended to clarify the behavior seen in Figure 4.22 and Figure 4.34. Most of this section will discuss how flutter occurs and the effect that it can have on the structure, such as wings and airplanes.

Introduction

Flutter is a dangerous phenomenon encountered in flexible structures subjected to aerodynamic forces. This includes aircraft, buildings, telegraph wires, stop signs, and bridges. Flutter occurs as a result of interactions between aerodynamics, stiffness, and inertial forces on a structure. In an aircraft, as the speed of the wind increases, there may be a point at which the structural damping is insufficient to damp out the motions which are increasing due to aerodynamic energy being added to the structure. This vibration can cause structural failure and therefore considering flutter characteristics is an essential part of designing an aircraft.

Flutter Motion

The basic type of flutter seen in aircraft wings is described here. Flutter may be initiated by a rotation of the airfoil (see t=0 in Figure F.1). As the increased force causes the airfoil to rise, the torsional stiffness of the structure returns the airfoil to zero rotation (t=T/4 in Figure F.1). The bending stiffness of the structure tries to

return the airfoil to the neutral position, but now the airfoil rotates in a nose-down position (t=T/2 in Figure F.1). Again the increased force causes the airfoil to plunge and the torsional stiffness returns the airfoil to zero rotation (t=3T/4). The cycle is completed when the airfoil returns to the neutral position with a nose-up rotation. Notice that the maximum rotation leads the maximum rise or plunge by 90 degrees (T/4). As time increases, the plunge motion tends to damp out, but the rotational motion diverges. If the motion is allowed to continue, the forces due to rotation will cause the structure to fail.

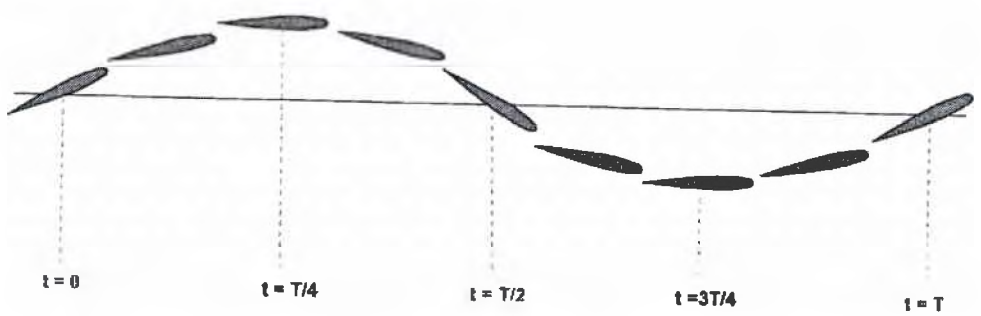

Figure F.1: Rotation and Plunge Motion for an Airfoil Exhibiting Flutter

This flutter is caused by the coalescence of two structural modes – pitch and plunge (or wing-bending) motion. This example wing has two basic degrees of freedom or natural modes of vibration: pitch and plunge (bending). The pitch mode is rotational and the bending mode is a vertical up and down motion at the wing tip. As the airfoil flies at increasing speed, the frequencies of these modes coalesce to create one mode at the flutter frequency and flutter condition. This is

flutter resonance. Stall flutter is a torsional mode of flutter that occurs on wings at high loading conditions near the stall speed. Because the airflow separates during stall, this single degree-of-freedom flutter cannot be explained by classical flutter theory. Figure 4.22 and Figure 4.34 show the aerodynamic efficiency of models tested in the LSWT. It can be seen that the region where the data of lift over drag ratio begin to oscillate is the region where the same model reaches the highest C_L, that is the region of stall.

Classical Flutter Definition

The following example of a simple two degree-of-freedom model is fundamental to understanding flutter behavior. Aerodynamic forces excite the structural spring/mass system. The plunge spring represents the bending stiffness of the structure and the rotation spring represents the torsional stiffness. The shape of the airfoil determines the aerodynamic center. The center of gravity is determined by the mass distribution of the cross-section (that is, how the airfoil is constructed).

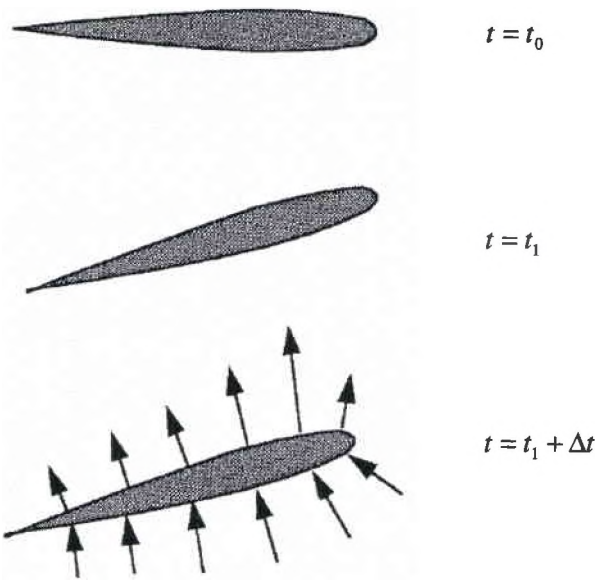

Figure F.2: Aerodynamic Lag

In Figure F.2, at time $t = t_0$ no angle of attack means symmetrical pressures on the upper and lower surfaces. At $t = t_1$ the airfoil has an angle of attack. No circulation nor pressures have built up. At $t = t_1 + \Delta t$ aero pressures have fully developed. When this last situation occurs, the airfoil, at certain velocities, can pitch and plunge. Figure F.3 and Figure F.4 represent two modes, plunge and pitch.

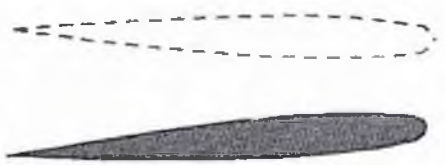

Figure F.3: Mode 1 – Plunge

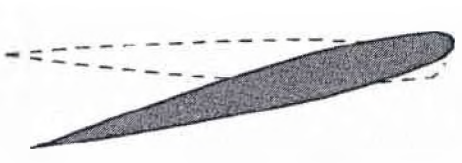

Figure F.4: Mode 2 – Pitch

As we said before, the flutter is caused by the coalescence of these structural modes – pitch and plunge. The frequencies of these modes can coalesce and generate flutter resonance.

BIBLIOGRAPHY

[1] Kang, H., Bichal, A., Altman, A., "Aerodynamic Effects of End Plates on Biplane Wings", AIAA 2008-317, 46th AIAA Aerospace Science Meeting and Exhibit, Reno, Nevada, 2008

[2] Wolkovitch, J., "The Joined Wing: An Overview", Journal of Aircraft, Vol. 23, 1986

[3] Raymer, D.P., "Aircraft Design: A Conceptual Approach", AIAA Education Series, 1999

[4] Anderson, J.D. Jr., "Fundamentals of Aerodynamics", McGraw-Hill, 1984

[5] Milne – Thomson, L.M., "Theoretical Aerodynamics", MacMillan Co., London, 1966

[6] Munk, M.M., "General Biplane Theory", NACA TR 151, 1922

[7] Prandtl, L., "Induced Drag of Multiplanes", NACA TN 182, 1924

[8] http://web.mit.edu/drela/Public/web/avl/

[9] Hunsaker, J.C., "Experimental Analysis of Inherent Longitudinal Stability for a Typical Biplane", NACA TR 1, 1915

[10] Norton, F.H., "The Effect of Staggering a Biplane", NACA TN 70, 1921

[11] Glauert, H., "Theoretical Relationships for a Biplane" R&M 901, British A.R.C., 1923

[12] Knight, M., Noyes, R.W., "Wind Tunnel Pressure Distribution Tests on a Series of Biplane Wing Models. Part I: Effects of Changes in Stagger and Gap", NACA TR 310, 1929

[13] Knight, M., Noyes, R.W., "Wind Tunnel Pressure Distribution Tests on a Series of Biplane Wing Models. Part II: Effects of Changes in Decalage, Dihedral, Sweepback, and Overhang", NACA TR 325, 1929

[14] Knight, M., Noyes, R.W., "Wind Tunnel Pressure Distribution Tests on a Series of Biplane Wing Models. Part III: Effects of Changes in Various Combinations of Stagger, Gap, Sweepback, and Decalage", NACA TR 330, 1929

[15] Munk, M.M., "The Air Forces on a Systematic Series of Biplane and Triplane Cellule Models", NACA TR 256, 1922

[16] Millikan, C.B., "Extended Theory of Thin Airfoils and its Application to the Biplane Problem", NACA TR 362, 1930

[17] Diehl, W.S., "Relative Loading on Biplane Wings", NACA TR 458, 1933

[18] Olson, E.C., Selberg, B.P., "Experimental Determination of Improved Aerodynamic Characteristics Utilizing Biplane Wing Configurations", University of Missouri-Rolla, Journal of Aircraft, Vol. 13, No. 4, 1974

[19] Barlow, J.B., Rae , W.H.R., Pope, A., "Low-Speed Wind Tunnel Testing", Wiley-Interscience, Third Edition, 1999

[20] Killian, D.N., "The Aerodynamic Performance of the Houck Configuration Flow Guides", Thesis, Air Force Institute of Technology, WPAFB OH, June 2007

[21] Hu, H., Yang, Z., Igarashi, H., "Aerodynamic Hysteresis of a Low Reynolds Number Airfoil", Iowa State University, Journal of Aircraft, Vol. 44, No. 6, 2007.

[22] Filippone, A. "Advanced Topics in Aerodynamics, Computational Fluid Dynamics, Aeronautics, Propulsion Systems", http://www.aerodyn.org

[23] Melin, T., "A Vortex Lattice Implementation for Linear Aerodynamic Wing Applications", Master Thesis, Royal Institute of Technology (KTH), 2000

[24] Bertin, J.J., and Smith, M.L., "Aerodynamics for Engineers", Prentice-Hall, Inc., Englewood Cliffs, 2nd Ed., 1989

VITA

Nicola Genco was born in Altamura (BA), Italy, on the 20th of February, 1984. He graduated from Galileo Galilei High School in chemistry, in Altamura (BA), Italy, in 2003. He went on to earn a Bachelors degree in Aerospace Engineering from the University of Rome "La Sapienza", Italy from 2003 to 2006, with a thesis in Propulsion on "The Hollow Cathode". In January 2007 he began attending the University of Dayton, Ohio for completion of his Masters Degree in Aerospace Engineering. During graduation, he presented his research project on biplane joined at the tips by endplates at DCASS (Dayton-Cincinnati Aerospace Sciences Symposium) and at two regional student conferences hosted by AIAA. He won the first place in the 2008 Regional Student Paper Competition for the Graduate division, and he will participate in the AIAA Foundation International Student Conference, part of the AIAA Aerospace Sciences Meeting, held in Orlando, Florida, 5 January 2009.